

**DENSITY FUNCTIONAL THEORY
INVESTIGATION OF WATER
ADSORPTION ON THE
 $\text{Fe}_3\text{O}_4(001)$ SURFACE**

By
Narasimham Mulakaluri

PhD Thesis
SUBMITTED IN PARTIAL FULFILLMENT
OF THE REQUIREMENTS FOR THE DEGREE OF
Dr. rer. nat.



Fakultät für Geowissenschaften
Ludwig-Maximilians-Universität München

May, 2010

- 1. Supervisor PD Dr. Rossitza Pentcheva
- 2. Co-Supervisor Prof. Dr. Wolfgang Moritz
- Date of oral examination 14-07-2010

..... This PhD thesis is dedicated to my parents and to my master Sri Satya Sai Baba.....

Ehrenwörtliche Versicherung

Ich versichere hiermit ehrenwörtlich, dass die Dissertation von mir selbständig und ohne Beihilfe angefertigt worden ist.

Narasimham Mulakaluri
München, May 2010

Erklärung

Hiermit erkläre ich, dass die Dissertation noch nicht in einem anderen Prüfungsverfahren vorgelegt und bewertet wurde.

Hiermit erkläre ich, dass ich mich nicht anderweitig einer Doktorprüfung ohne Erfolg unterzogen habe.

Narasimham Mulakaluri
München, May 2010

Contents

List of Publications	xix
Abstract	xxi
1 Introduction	1
2 Theoretical Background	5
2.1 Density Functional Theory	7
2.2 Methods for band structure calculation	11
2.3 Structure of the Wien2k code	15
2.4 <i>Ab-initio</i> atomistic thermodynamics	15
2.5 Surface core level shifts	20
2.6 Molecular orbitals of H ₂ O and OH	22
3 Computational Details	25
3.1 Surface slab setup	25
3.2 Surface and adsorption models	26
3.3 Surface and adsorption energetics	27
3.4 Technical parameters and accuracy	28
4 Monomer Adsorption	31
4.1 Adsorption models and energetic stability	32
4.2 Analysis of the electronic structure	34
4.3 Structural properties	40
4.4 Summary	44

5	Adsorption on a Defective Surface	47
5.1	Formation of a F-center	47
5.2	Adsorption models and energetic stability	49
5.3	Analysis of the electronic structure	50
5.4	Structural properties	55
5.5	Summary	60
6	Dimer Adsorption	61
6.1	Adsorption models and energetic stability	61
6.2	Analysis of the electronic structure	65
6.3	Structural properties	72
6.4	Summary	76
7	Saturation Coverage	77
7.1	Adsorption models and energetic stability	77
7.2	Analysis of the electronic structure	81
7.3	Structural details	93
7.4	Hydroxylation and hydrogenation	100
7.5	0.5 ML A layer termination	100
7.6	Coverage vs. E_{ads} and $\Delta\Phi$	101
7.7	Summary	103
8	Surface Phase Diagram	105
8.1	Compilation of the surface phase diagram	106
8.2	Discussion	107
8.3	Summary	111
9	Magnetic Properties and Charge/Orbital Ordering	115
9.1	Change in magnetic properties	116
9.2	Adsorbate induced CO/OO	118
9.3	Summary	120
10	Surface Core Level Shifts	121
10.1	Origin and factors contributing to SCLS	122
10.2	SCLS of H ₂ O on Fe ₃ O ₄ (001)	122
10.3	Summary	127
11	Low Energy Electron Diffraction	129
11.1	Experimental set up	129
11.2	Experimental procedure	130
11.3	Results and discussion	131

11.4 Summary	135
12 Conclusions and Outlook	137
A Reference energies	141
Bibliography	143
Manuscript A	151
Manuscript B	157
Manuscript C	169
Acknowledgment	181
Curriculum Vitae	183

List of Figures

2.1	Division of space in a unit cell within the FP-LAPW method as muffin tin region and interstitial region	12
2.2	Wien2k flow chart	14
2.3	The molecular orbitals of a gas phase H ₂ O molecule	22
2.4	The molecular orbitals of an OH group	23
3.1	Fe ₃ O ₄ (001) slab with seven B layers and six A layers	26
4.1	Tilt angle α between the H ₂ O molecule and the surface	32
4.2	1 H ₂ O coverage: adsorption models vs. E_{ads}	33
4.3	1b ₁ , 3a ₁ and 1b ₂ MO shapes of a H ₂ O molecule	35
4.4	GGA+ U : Electron density redistribution plots of 1U and 1F	35
4.5	GGA and GGA+ U : DOS and PDOS of 1U and 1F	36
4.6	GGA and GGA+ U : DOS, PDOS and electron density redistribution plots of 1D-1	38
4.7	Top view of the surface B-layer from 1D-1	40
4.8	Side view of 1U and 1F along with bond lengths	41
4.9	Side view of 1D-1 and 1D-2 along with bond lengths	42
4.10	Side view of 1D-2 and 1D-OH along bond lengths	44
5.1	Various surface oxygen sites chosen for vacancy creation	48
5.2	Top views of all the adsorption models considered vs. E_{ads}	49
5.3	DOS and PDOS in the case of B+V _O	51
5.4	DOS and PDOS in the case of 1F _V and 1F	53
5.5	DOS, PDOS and electron density redistribution plots from 1D _V -3	54
5.6	Top view of B+V _O and 1D _V -3 with lateral bond lengths	55
5.7	Side view of B+V _O and 1F _V along with bond lengths	56
5.8	Side view of 1D _V -1 and 1D _V -3 along with bond lengths	58
5.9	Side view of 1D _V -2 along with bond lengths	59

6.1	2 H ₂ O coverage: adsorption models vs. E_{ads}	62
6.2	2 H ₂ O coverage: other adsorbate geometries	63
6.3	DOS and PDOS of 2T-1	66
6.4	2D-1: DOS, PDOS and electron density redistribution plots	67
6.5	DOS and PDOS in the case of 2D-1	68
6.6	2M-4: DOS, PDOS and electron density redistribution plots	70
6.7	2M-4: Charge density plots	71
6.8	2M-4: surface B-layer	72
6.9	Side view of 2T-1 and 2F-2	72
6.10	Side view of 2M-4 and 2D-1	74
7.1	4 H ₂ O coverage: Adsorbate configurations vs. E_{ads}	78
7.2	4 H ₂ O coverage: other adsorbate models	79
7.3	DOS and PDOS of 4U, 2U-1 and 1U	82
7.4	4F-2: electronic structure within GGA and GGA+ U	83
7.5	4D-2: electronic structure within GGA and GGA+ U	85
7.6	GGA+ U : Electron density redistribution plots of 4M	86
7.7	GGA: DOS, PDOS and charge density plots of 4M	88
7.8	GGA: DOS, PDOS of 4M, 2M-4, 1D-1 and 1F	89
7.9	GGA+ U : DOS, PDOS and charge density plots of 4M	91
7.10	GGA+ U : DOS, PDOS of 4M, 2M-4, 1D-1 and 1F	92
7.11	4M: schematic top view	93
7.12	Side view with characteristic bond lengths of 4F-2 and 4D-2	94
7.13	Side view with characteristic bond lengths of 4M	98
7.14	Top view of the hydroxylated and hydrogenated surface	100
7.15	Adsorption energies vs. coverage	101
7.16	Work function vs. coverage	103
8.1	A three-dimensional view of the surface phase diagram	106
8.2	GGA: surface phase diagram of H ₂ O and O ₂ on Fe ₃ O ₄ (001)	108
8.3	GGA+ U : surface phase diagram of H ₂ O and O ₂ on Fe ₃ O ₄ (001)	109
8.4	Surface phase diagram of O ₂ and H ₂ on Fe ₃ O ₄ (001) within GGA and GGA+ U	110
8.5	A two-dimensional view of the surface phase diagram in H ₂ O poor condition	112
8.6	A two-dimensional surface phase diagram in the rich limit of μ_{H}	113
9.1	Electron density plots representing Fe ²⁺ orbitals	119
9.2	U vs. charge and magnetic moment	120
10.1	Top view of the most stable surface terminations of H ₂ O ad- sorbed Fe ₃ O ₄ (001)	123
10.2	PDOS of different Oxygens	126
11.1	Schematic diagram of LEED setup	130
11.2	LEED patterns obtained from different experiments	132

11.3	LEED $I(V)$ curves at different temperatures	133
11.4	LEED $I(V)$ curves of the water adsorption at 273 K and calculated curves	134

List of Tables

4.1	Surface atoms relaxation of the 1U and 1F configurations . . .	41
4.2	Surface atoms relaxation of the 1D-1 configuration	43
5.1	Relaxation of the surface atoms in B+V _O	57
5.2	Relaxation of the surface atoms in 1F _V and 1D _V -1	58
5.3	Relaxation of the surface atoms in 1D _V -3	59
6.1	Surface atom relaxation for 2T-1 and 2F-2	73
6.2	Surface atom relaxation for 2M-4 and 2D-1	75
7.1	Surface atom relaxations of 4F-2	95
7.2	Surface atom relaxations of 4D-2	96
7.3	Surface atom relaxations of 4M	97
7.4	Adsorbate-substrate bond lengths and angles in the case of 1D-1, 1D _V -3, 2D-2, 2D-3, 4D-2, 2M-3, 4M	99
7.5	Adsorbate-substrate bond lengths and angles in the case of 1F-1, 2F-3, 4F-2, 2M-3, 4M	99
9.1	Magnetic moments (μ_B) of the surface and sub surface layer . .	117
10.1	Surface core level shifts of O1s and Fe $2p_{\frac{1}{2}}$ and $2p_{\frac{3}{2}}$ for modified B-layer, 1F and 1D-1	124
10.2	Surface core level shifts of O1s and Fe $2p_{\frac{1}{2}}$ and $2p_{\frac{3}{2}}$ for B+V _O and 1D _V -3	125
10.3	O1s, Fe $2p_{\frac{1}{2}}$ and $2p_{\frac{3}{2}}$ surface core level shifts of 2M-3 and 4M . .	125

List of Publications

- Adsorbate Induced Semiconductor-Half Metal Transition at the $\text{Fe}_3\text{O}_4(001)$ Surface. G. S. Parkinson, **N. Mulakaluri**, Y. Losovyj, P. Jacobson¹, R. Pentcheva and U. Diebold, **Phys. Rev. B** 82, 115420 (2010).
- Coverage dependent adsorption mode of water on $\text{Fe}_3\text{O}_4(001)$: Insights from first principles. **N. Mulakaluri**, R. Pentcheva and M. Scheffler, **J. Phy. Chem. C** 114, 11148 (2010).
- Partial dissociation of water on $\text{Fe}_3\text{O}_4(001)$: Adsorbate induced charge and orbital order. **N. Mulakaluri**, R. Pentcheva, M. Wieland, W. Moritz, and M. Scheffler, **Phys. Rev. Lett.** 103, 176102 (2009).
- Compensation mechanisms and functionality of transition metal oxide surfaces and Interfaces: A density functional theory study. *In: High Performance Computing in Science and Engineering.*, R. Pentcheva, R., **N. Mulakaluri**, W.E. Pickett, H.-G. Kleinhenz, W. Moritz, and M. Scheffler: Editors-(Eds.) S. Wagner, M. Steinmetz, A. Bode, and M. Brehm. Springer Berlin Heidelberg 2009, 709-717.
- Theoretical evidence of a mixed adsorption mode of water on $\text{Fe}_3\text{O}_4(001)$. **N. Mulakaluri**, R. Pentcheva, M. Wieland, W. Moritz, and M. Scheffler, **Geochim. Cosmochim. Acta** 73(13), A913.
- **N. Mulakaluri** (2003), Study of Electrospinning: A Process used to produce polymer nanofibers. Masters Thesis at IITM Chennai, India

Manuscripts in preparation

- Photoemission study of the reaction of water vapor with the $\text{Fe}_3\text{O}_4(001)$ Surface at near ambient conditions. T. Kendelewicz, S. Kaya, J. E. Newberg, H. Bluhm, **N. Mulakaluri**, R. Pentcheva, W. Moritz, A. Nilsson, and G. E. Brown, Jr.

Abstract

Magnetite (Fe_3O_4) plays a significant role in geophysics and mineralogy and it is a potential spintronics material. Additionally, it exhibits interesting catalytic properties. As both in nature and technology, these catalytic reactions typically take place at the interface with water, it is important to gain a fundamental understanding of these processes at the atomistic level. This work comprises the first systematic investigation of the water adsorption on the $\text{Fe}_3\text{O}_4(001)$ surface based on large scale density functional theory (DFT) calculations. The influence of electronic correlations was explored within the LDA/GGA+ U approach.

A variety of concentrations and configurations of H_2O molecules on the surface with and without defects were studied to explore the underlying adsorption energetics. The DFT results were extended to finite temperatures (T) and pressures (p) of the surrounding gas phase molecules by compiling a surface phase diagram within the framework of *ab initio* atomistic thermodynamics. This phase diagram reveals a dissociative mode of adsorption for an isolated H_2O molecule, especially at oxygen vacancies. With increasing coverage, a crossover from dissociative to partial dissociation of H_2O molecules on the surface is predicted. This is attributed to adsorbate-adsorbate interactions stabilized by hydrogen bond formation between the linear chains of alternating H_2O and OH groups. This partially dissociated termination is stable across a wide range of water vapor and oxygen partial pressures and confirmed by a quantitative low energy electron diffraction (LEED) analysis. In addition, the LEED pattern also indicates a lifting of the $(\sqrt{2} \times \sqrt{2})R45^\circ$ surface reconstruction.

The DFT results reveal that defects and adsorbates induce a unique charge and orbital order (CO/OO) on the $\text{Fe}_3\text{O}_4(001)$ surface. This provides a novel way to alter the catalytic properties of the $\text{Fe}_3\text{O}_4(001)$ surface. While the CO/OO in the sub-surface layers lead to an insulating character of the clean surface, a transition to half-metallic behavior with the adsorption of H_2O molecules is predicted. This insulating to half-metal transition can be explored for applications in spintronics. The calculated surface core level shifts are used to interpret the X-ray photoemission spectroscopy data, disclosing the major contribution of the screening effects.

Introduction

Magnetite (Fe_3O_4) is the oldest (1500 B.C.) known magnetic material. It is a common accessory mineral present in rocks and is an important iron ore [1]. Magnetotactic bacteria, birds and honey bees use magnetite particles to orient themselves for navigation [2]. It is used in many applications like in pigments, catalysts, magnetic filed sensors and is a component of ferrofluids and magnetorheological fluids [1]. In addition, it has biomedical applications [3] and is also found in human tissue [2]. At room temperature this transition metal oxide, black in color, crystallizes in an inverse spinel structure [1, 4]. The oxygen atoms form a closely packed distorted cubic lattice and the cations (i.e the iron atoms) occupy the octahedral (six-fold coordinated) and tetrahedral (four-fold coordinated) interstices which are referred to as B and A sites respectively. Fe_3O_4 differs from other iron oxides since it contains iron in Fe^{2+} and Fe^{3+} oxidation states. All the A sites are occupied by Fe^{3+} while the B sites are occupied by both Fe^{2+} and Fe^{3+} . The usual chemical formula is written as: $\text{Fe}_A^{3+}[\text{Fe}^{2+}, \text{Fe}^{3+}]_B\text{O}_4$.

At around 120 K, magnetite shows a first order phase transition known as the Verwey transition [5]. During this transition, the conductivity abruptly decreases by two orders of magnitude and is accompanied by a structural change from cubic to monoclinic [6]. Based on the assumption that at high temperatures, the conductivity in magnetite is due to the fast hopping of electrons between Fe_B^{2+} and Fe_B^{3+} sites, Verwey explained this metal to insulator transition in terms of charge ordering of Fe^{2+} and Fe^{3+} on the B sublattice in successive planes along [001]. Both the type of transition (metal-to-insulator vs. semiconductor-to-semiconductor [7, 8]) and the type of charge (CO) and orbital ordering (OO) at the octahedral iron sites in the low temperature phase are subject of an ongoing debate [6, 9–11]. On the other hand, the high temperature phase of magnetite is predicted to be a half-metallic ferrimagnet [12] with a high magnetic ordering temperature ($T_C=858$ K). These properties make it a potential candidate for magneto- and spin-electronics, apart from the existing usage in magnetic recording and storage devices.

The surface properties of a material can differ significantly from that of the bulk due to different surface geometry and stoichiometry. The $\text{Fe}_3\text{O}_4(001)$

surface has two bulk terminations: it either terminates with an octahedral iron (B sites) and oxygen layer known as the B layer termination or with a tetrahedral iron (A sites) layer referred to as the A layer termination. Both bulk truncations, either with an A- or a B-layer are polar of type three according to the classification of Tasker [13]. Polar surfaces are unstable in nature and, therefore, they often exhibit surface reconstruction or surface faceting in order to attain stability [14]. In the present case the clean $\text{Fe}_3\text{O}_4(001)$ shows a $(\sqrt{2} \times \sqrt{2})R45^\circ$ -surface reconstruction [15–23]. Previously, the origin of the surface reconstruction was thought to be due to ordering of surface defects (e.g. [21, 24]). Recently, DFT calculations [25, 26] have shown that the symmetry lowering at $\text{Fe}_3\text{O}_4(001)$ is achieved rather by a distorted B-layer, supported also by surface x-ray diffraction [25], low energy electron diffraction (LEED) [27] and scanning tunneling microscopy (STM) [28].

Transition metal oxide surfaces play an important role in heterogeneous catalysis. Fe_3O_4 is used as a catalyst e.g. in the Fischer-Tropsch synthesis¹ [1], in environmental redox reactions [29, 30] wherein the toxic heavy metal ions like As(V) or Cr(IV) are adsorbed and reduced, and in the high temperature water gas phase shift reaction² [31]. Typically, all these reactions involve H_2O , prompting the need to understand how water interacts with the Fe_3O_4 surface. The study of aqueous interface with a mineral surface is a subject of great importance in the field of geochemistry, environmental sciences, corrosion and heterogeneous catalysis [32–34]. The water molecule acts as a probe for surface properties like chemical reactivity, redox processes, site distribution [32] and can also alter these properties.

Some of the primary questions addressed in this work are:

- the mode of adsorption: molecular (intact water molecule) or dissociative (splitting of the water molecule in OH and H)
- binding strength of adsorbates
- orientation of the H_2O molecule and adsorption site
- possibility for the formation of hydrogen bonded networks

All these issues can significantly affect the surface properties and availability of reaction sites which result in a complex surface chemistry [32, 33]. Usually, the water molecule binds via the oxygen atom to the metal oxide substrate or in specific to the cation site, which acts as a Lewis acid that attracts the oxygen lone pair orbital.

Despite intensive research on the clean $\text{Fe}_3\text{O}_4(001)$ surface, there are only a few studies on its interaction with water. The first set of experiments on Fe_3O_4 dates back to 1991-92 where authors used incoherent neutron scattering [35] and x-ray photoemission spectroscopy (XPS) [36]. However, the orientation

¹ $(2n + 1) \text{H}_2 + n \text{CO} \xrightarrow{\text{Fe}_3\text{O}_4} \text{C}_n\text{H}_{2n+2} + n \text{H}_2\text{O}$: where $n \geq 1$ and integer

² $\text{CO} + \text{H}_2\text{O} \xrightarrow{\text{Fe}_3\text{O}_4} \text{CO}_2 + \text{H}_2\text{O}$

of crystal face was not specified. In the former case, an ice like structure was reported, while in the latter case dissociation of water molecules was found. Kendelewicz *et al.* [37] measured oxygen 1s core level shifts with XPS. For low water vapor pressures, the spectra were interpreted as a dissociative adsorption related to surface defects. Beyond water vapor pressures of 10^{-3} – 10^{-4} mbar, an extensive hydroxylation was observed. The onset pressure is similar to values reported for the $\text{Fe}_3\text{O}_4(111)$ [37] and $\alpha\text{-Fe}_2\text{O}_3(0001)$ [38] surfaces. On the other hand, water immersed surfaces showed smaller chemical shifts. A broad feature at 1.6 eV was observed in the O1s spectra and it is attributed to hydroxyl groups at nonequivalent sites. Furthermore, no sign of formation of a surface oxyhydroxide was found in near edge extended X-ray adsorption fine spectra (NEXAFS) of the Fe *L* edge. In thermal programmed desorption (TPD) experiments of epitaxially grown $\text{Fe}_3\text{O}_4(001)$ films on a $\text{MgO}(001)$ -substrate three desorption peaks were observed at 320, 280 and 225 K [24]. These were associated with different chemisorbed states, but the exact adsorbate configurations and their relative stability cannot be directly accessed from experiment. On the theoretical side, the water adsorption on $\text{Fe}_3\text{O}_4(001)$ has been studied by molecular dynamics (MD) with empirical potentials [39, 40]. These studies point at a dissociative adsorption. However, a termination with a 0.5 ML (monolayers) of tetrahedral iron (0.5 A-layer) was assumed for the $\text{Fe}_3\text{O}_4(001)$ surface, which according to DFT calculations is energetically unfavorable [25].

First principles calculations have proven very useful to resolve the energetic stability and structural properties of different adsorbate geometries, but are lacking so far due to the complexity of the Fe_3O_4 surface. We have investigated the water adsorption on $\text{Fe}_3\text{O}_4(001)$ surface using DFT calculations with the full-potential linear augmented plane wave method (FP-LAPW) [41] as implemented in Wien2k [42]. As an all electron method with no approximation made for the shape of the potential this code is most reliable. We have not only used generalized gradient approximation (GGA) [44] for exchange-correlation potential but also considered an on-site Coulomb repulsion term within $\text{GGA}+U$ [43] to describe the electronic correlations of the localized 3d orbitals of the transition metal (Fe). The distorted B layer termination (modified B-layer) and the B-layer with an oxygen vacancy termination ($\text{B}+\text{V}_\text{O}$) are used as starting surface models for the adsorption. We vary the configuration and concentration of H_2O and OH on the surface in order to get the most stable termination. In order to further determine stability of different surface terminations as a function of temperature and pressure of the surrounding gas phase molecule, we compile a surface phase diagram within the framework of *ab initio* atomistic thermodynamics [45, 46].

Outline of the thesis

The thesis is organized as follows: **Chapter 2** describes the theoretical background of the calculations. It includes a brief review of the basic concepts of

density functional theory (DFT), *ab initio* atomistic thermodynamics as well as the approach to calculate spectroscopic properties such as surface core level shifts. The Wien2k [42] code used in the calculations is also described briefly.

In **Chapter 3**, the setup and technical parameters of the calculations as well as the nomenclature of the adsorption models are described. Here various important formulations used in the analysis of the results are mentioned as well.

The adsorption of an isolated single H₂O molecule on the Fe₃O₄(001) surface is discussed in **Chapter 4**. The stability of various adsorbate configurations is discussed based on their adsorption energies. The trend in the adsorption energy is analyzed with the help of density of states (DOS) and electron density redistribution plots. The effect of the water adsorption on the structural properties of the surface is also described. **Chapter 5** deals with the adsorption of water molecules on the defective surface. The analysis is done using similar methods as discussed in **Chapter 4**.

The coverage regime of two H₂O molecules is described in **Chapter 6**. The important aspect of adsorbate-adsorbate bonding is also taken into account. In this Chapter, the energetic trends are explained with the help of DOS and electron density redistribution plots.

In **Chapter 7**, the coverage is extended to four H₂O molecules, thereby saturating all the available surface cation sites. In this Chapter, not only the adsorption related energetics, electronic and structural properties are discussed with the help of DOS and electron density redistribution plots, but also the coverage dependent adsorption trends are analyzed.

The stability of the different surface terminations as a function of temperature and pressure of the molecules in the gas phase is the topic of **Chapter 8**. Here we present a surface phase diagram compiled within the framework of *ab initio* atomistic thermodynamics. The surface phase diagram is presented both w.r.t the H₂O and O₂ and w.r.t the H₂ and O₂ partial pressures in the gas phase.

Chapter 9 explores the change in magnetic properties with the adsorption of H₂O molecules. The coverage dependent trend is also analyzed. In addition another interesting aspect discussed in this Chapter, is how the charge and orbital ordering (CO-OO) of the Fe₃O₄(001) surface is influenced by the adsorbates.

In **Chapter 10** the surface core level shifts upon adsorption are discussed. These are related to X-ray photoemission measurements [37]. Finally, in **Chapter 11**, the low energy electron diffraction (LEED) measurements and quantitative analysis are described. In this Chapter a brief introduction to the method, theory and experimental procedure is presented. The LEED results are also compared with the DFT results and they show good agreement. Finally a brief summary of the main findings is presented in **Chapter 12**.

Theoretical Background

In this Chapter we will discuss the theoretical background behind the electronic structure calculations. Typically, to study the adsorption process on the surface and its effects, one needs to understand it from an atomistic view. The modern Density Functional Theory is the right kind of tool to deal with this problem. We start by introducing the Hamiltonian for a many body system, written as:

$$\hat{H} = -\frac{\hbar^2}{2m_e} \sum_i \nabla_i^2 - \frac{\hbar^2}{2M_I} \sum_I \nabla_I^2 - \sum_{i,I}^N \frac{Z_I e^2}{|\mathbf{r}_i - \mathbf{R}_I|} + \frac{1}{2} \sum_{i \neq j} \frac{e^2}{|\mathbf{r}_i - \mathbf{r}_j|} + \frac{1}{2} \sum_{I \neq J} \frac{Z_I Z_J e^2}{|\mathbf{R}_I - \mathbf{R}_J|}, \quad (2.1)$$

where m_e is the mass of an electron with charge e and M is the mass of the nucleus with charge Ze . The first term denotes the kinetic energy operator for the electrons and the second term that of the nuclei. The last three terms depict the electron-nucleus, electron-electron and nucleus-nucleus interaction.

The first approximation made in the electronic structure theory is the Born-Oppenheimer(BO) [47] or adiabatic approximation, which leads to the decoupling of electronic and nuclear motions. The electrons move instantaneously to any given nuclei displacement due to their relatively low mass and therefore, the electrons are considered to be moving in a potential generated by the nucleus. Following the approximation, we can ignore the kinetic energy term of the nucleus and the nucleus-nucleus interaction resulting in the so-called electronic Hamiltonian:

$$\hat{H}_e = \hat{T}_e + \hat{V}_{ext} + \hat{V}_{int}. \quad (2.2)$$

By adopting the Hartree atomic units $\hbar = m_e = e = \frac{4\pi}{\epsilon_0} = 1$, the terms in

Eq. 2.2 are easy to handle. The kinetic energy operator is given by:

$$\hat{T} = \sum -\frac{1}{2}\nabla_i^2, \quad (2.3)$$

where \hat{V}_{ext} is the potential of the nuclei acting on electrons:

$$\hat{V}_{ext} = \sum_{i,I} V(\mathbf{r}_i - \mathbf{R}_I), \quad (2.4)$$

\hat{V}_{int} is the electron-electron interaction:

$$\hat{V}_{int} = \frac{1}{2} \sum_{i \neq j} V(\mathbf{r}_i - \mathbf{r}_j). \quad (2.5)$$

The time independent Schrödinger equation [48] for electrons is:

$$\hat{H}_e \Psi(\mathbf{r}_1, \mathbf{r}_2, \dots \mathbf{r}_N) = E_e \Psi(\mathbf{r}_1, \mathbf{r}_2, \dots \mathbf{r}_N), \quad (2.6)$$

where $\Psi(\mathbf{r}_1, \mathbf{r}_2, \dots \mathbf{r}_N)$ is the many electron wave function and \mathbf{r}_i represents the position and spin coordinates of the electron. It is not practical to solve Eq. 2.6 by substituting \hat{H} from Eq. 2.2 for any large system.

The proper description of $\Psi(\mathbf{r}_1, \mathbf{r}_2, \dots \mathbf{r}_N)$ is the desired final output of any electronic structure method. In the present form, it is still difficult to solve the Schrödinger equation (Eq. 2.6). The first attempt to calculate Ψ was made by Hartree. In this approach, the many-electron wave function Ψ is approximated by the product of one-electron wave functions (ϕ) for each of the N electrons:

$$\Psi(\mathbf{r}_1, \mathbf{r}_2, \dots \mathbf{r}_N) = \phi_1(\mathbf{r}_1)\phi_2(\mathbf{r}_2) \dots \phi_N(\mathbf{r}_N). \quad (2.7)$$

Since then, many improvements were made as in the Hartree-Fock (HF) theory [49, 50], to accommodate Pauli's principle by determining an antisymmetric wavefunction. The HF theory is quite accurate to describe atoms and molecules but less appropriate for periodic solids. A more powerful theory for solids is the density functional theory.

2.1 Density Functional Theory

Density functional theory (DFT) was developed by Hohenberg and Kohn in 1964 [51]. In this work, it was stated that the density of particles can be considered as a “basic variable” ,i.e., all other properties of the system can be considered as an unique functional of the ground state density. In fact, this concept goes back to the work of Thomas and Fermi.

A *functional* is defined as a function of functions. In general, a function maps the value of a variable to a singular number. In a similar way, a functional maps the function to a singular value. For example:

$$F[f(r)] = \int_1^1 f(x)dx \quad (2.8)$$

is a functional of the function $f(x)$.

2.1.1 Hohenberg-Kohn theorems

Hohenberg-Kohn (HK) theorems applies to a system of interacting particles in an external potential $\hat{V}_{ext}(\mathbf{r})$ where the Hamiltonian is written as in Eq. 2.2.

Theorem 1 For any system of interacting particles in an external potential $\hat{V}_{ext}(\mathbf{r})$, the potential $\hat{V}_{ext}(r)$ is determined uniquely, except for a constant, by the ground state particle density $n_o(\mathbf{r})$.

This means that all the system properties are completely determined by the ground state particle density $n_o(\mathbf{r})$.

Theorem 2 A universal functional of the energy $E[n]$ in terms of the density $n(\mathbf{r})$ be defined, valid for any external potential $\hat{V}_{ext}(\mathbf{r})$. For any particular value of $\hat{V}_{ext}(\mathbf{r})$, the exact ground state energy of the system is the global minimum value of this functional, and the density $n(\mathbf{r})$ that minimizes the functional is the exact ground state density $n_o(\mathbf{r})$.

The functional $E[n]$ alone is sufficient to determine the exact ground state density. The excited states must be found by some other means.

The HK theorems do not provide a practical way for solving the Schrödinger equation for a many electron system. It was the Kohn-Sham formulation of DFT which led to the realisation of practically solvable equations. It also became the basis for all the modern density functional theory (DFT) codes. Kohn-Sham converted the interacting many particle problem to a system of non-interacting particles with an effective potential. The potential includes the exchange-correlation effects as considered for a real interacting particle system.

The two assumptions in the Kohn-Sham's [52] approach are:

- The exact ground state density can be represented by the ground state density of an auxiliary system of non-interacting particles.
- The auxiliary Hamiltonian is chosen to have the usual kinetic operator and an effective local potential $V_{eff}^\sigma(\mathbf{r})$ acting on an electron of spin σ at point (\mathbf{r})

The calculations are performed on a non-interacting system of N particles (auxiliary system) with an auxiliary Hamiltonian:

$$\hat{H} = -\frac{1}{2}\nabla_i^2 + V_{eff}^\sigma(\mathbf{r}). \quad (2.9)$$

The density of the auxiliary system is given by the sum of the squares of the orbitals for each spin:

$$n(\mathbf{r}) = \sum_{\sigma} n(\mathbf{r}, \sigma) = \sum_{\sigma} \sum_{i=1}^{N_{\sigma}} |\psi_i^{\sigma}(\mathbf{r})|^2 \quad (2.10)$$

and the independent particle kinetic energy T_s is given by:

$$T_s = -\frac{1}{2} \sum_{\sigma} \sum_{i=1}^{N_{\sigma}} \langle \psi_i^{\sigma} | \nabla^2 | \psi_i^{\sigma} \rangle = -\frac{1}{2} \sum_{\sigma} \sum_{i=1}^{N_{\sigma}} \int d^3r |\nabla \psi_i^{\sigma}(\mathbf{r})|^2. \quad (2.11)$$

Finally, the Hartree energy term, which defines the average Coulomb interaction between electrons in terms of electron density $n(\mathbf{r})$ is written as:

$$E_{Hartree}[n] = \frac{1}{2} \int d^3r d^3r' \frac{n(\mathbf{r})n(\mathbf{r}')}{|\mathbf{r} - \mathbf{r}'|}. \quad (2.12)$$

The Kohn-Sham formulation modified the Hohenberg-Kohn's interacting many body expression for the ground the state energy as:

$$E_{KS} = T_s[n] + \int d\mathbf{r} V_{ext}(\mathbf{r})n(\mathbf{r}) + E_{Hartree}[n] + E_{II} + E_{xc}[n], \quad (2.13)$$

where $V_{ext}(\mathbf{r})$ includes the external potential due to the nuclei and any other external fields and E_{II} is the nucleus-nucleus interaction. The independent particle kinetic energy $T_s[n]$ is given as a functional of the orbitals. However, T_s for each spin σ must be an unique functional of the density $n(\mathbf{r}, \sigma)$ due to

the HK theorems. All the many body effects of exchange and correlation are accounted in the exchange-correlation energy E_{xc} . Comparing the total energy expression of Hohenberg-Kohn and Kohn-Sham, the exchange correlation energy can be written as:

$$E_{xc}[n] = F_{HK}[n] - (T_s[n] + E_{Hartree}[n]) \quad (2.14)$$

and in a more simple way as:

$$E_{xc}[n] = \langle \hat{T} \rangle - T_s[n] + \langle \hat{V}_{int} \rangle - E_{Hartree}[n]. \quad (2.15)$$

Here $[n]$ represents the density $n(\mathbf{r})$ which depends on both the position \mathbf{r} and the spin σ . From Eq. 2.15 it can be noted that $E_{xc}[n]$ explicitly depends on the difference between the kinetic energies of a system of interacting and non-interacting particles and the difference of internal interaction energies between the real system and the fictitious independent particle system with the electron-electron interaction replaced by the Hartree energy.

The solution of Kohn-Sham system Eq. 2.9 for the ground state can be seen as the problem of minimisation with respect to either the density $n(\mathbf{r})$ or the effective potential $V_{ext}(\mathbf{r})$. Since $T_s[n]$ is explicitly expressed as a functional of the orbital and all other terms are considered as a functional of the density, one can vary the wavefunction using the variational principle. The wavefunction should follow the orthonormalisation constraint given by:

$$\langle \psi_i^\sigma | \psi_j^\sigma \rangle = \delta_{i,j} \delta_{\sigma,\sigma}. \quad (2.16)$$

With the application of the variational principle and the Lagrange multiplier method one arrives at the Kohn-Sham equations which are like usual Schrödinger Eq.:

$$(H_{KS}^\sigma - \epsilon_i^\sigma) \psi_i(\mathbf{r}) = 0, \quad (2.17)$$

where ϵ_i are the eigenvalues and H_{ks} is the effective Hamiltonian:

$$H_{KS}^\sigma(\mathbf{r}) = -\frac{1}{2} \nabla_i^2 + V_{KS}^\sigma \mathbf{r}, \quad (2.18)$$

with:

$$V_{KS}^\sigma(\mathbf{r}) = V_{ext}(\mathbf{r}) + \frac{\delta E_{Hartree}}{\delta n(\mathbf{r}, \sigma)} + \frac{\delta E_{xc}}{\delta n(\mathbf{r}, \sigma)} = V_{ext}(\mathbf{r}) + V_{Hartree}(\mathbf{r}) + V_{xc}^\sigma(\mathbf{r}). \quad (2.19)$$

The resulting density $n(\mathbf{r})$ and the total energy E_{ks} are given by Eq. 2.11

and Eq. 2.13. The Eq. 2.17 have the form of independent particle equations with a potential that must be found self-consistently with the resulting density.

The Eq. 2.17 is solved as a secular equation similar to the Hartree-Fock equation. The wave function $\psi_i(\mathbf{r})$ is expanded in a given basis set ϕ_p^b as:

$$\psi_i(\mathbf{r}) = \sum_{p=1}^P c_p^m \phi_p^b, \quad (2.20)$$

where P is the dimensionality of the basis set. The main task consists of determining the coefficients c_p^m .

2.1.2 Exchange correlation potential

The form of E_{xc} is not exactly known and therefore approximations are necessary to be made. The most well known approximation for the E_{xc} is the local density approximation (LDA) or more generally known as **local spin density approximation** (L(S)DA). Only in the case of homogenous electron gas [53], the exchange and correlation energy are known to a very high accuracy. The idea to use this model for approximating E_{xc} for the Kohn-Sham scheme was already suggested by Kohn & Sham in their pioneering work. The effect of exchange-correlation is local within this limit and it is calculated by integrating the exchange-correlation energy density over the whole space assuming that at each point E_{xc} is same as E_{xc} of a homogenous gas. The generalised expression can be written as:

$$E_{xc}^{LSDA}[n \uparrow, n \downarrow] = \int d^3r n(\mathbf{r}) \epsilon_{xc}^{hom}(n \uparrow(\mathbf{r}), n \downarrow(\mathbf{r})). \quad (2.21)$$

The exchange energy for a homogeneous electron gas is known and given by an analytic expression whereas the correlation energy is approximated from Monte Carlo simulations. Among the drawbacks of LDA are the spurious self-interaction term and over-binding effects [54]. Due to the latter, cohesive energy turn out to be too large when compared to experiments for e.g. the binding energy of an O₂ molecule [54]. This overbinding also leads to lattice constants and bond lengths that are smaller compared to the experimental values.

An attempt to improve the LDA is the **Generalized Gradient Approximation** (GGA). Within this approximation, the ϵ_{xc} is a function of the electron density and its gradient. It is defined as:

$$E_{xc}^{GGA}[n \uparrow, n \downarrow] = \int d^3r n(\mathbf{r}) \epsilon_{xc}^{hom}(n \uparrow(\mathbf{r}), n \downarrow(\mathbf{r}), \nabla \uparrow, \nabla \downarrow). \quad (2.22)$$

Numerous variations of this approximation [44, 55–59] have been proposed and the most commonly used ones are those of Perdew and Wang (PW91) [58], Perdew, Burke and Ernzerhof (PBE) [44], and the revised PBE functional (RPBE) [59]. We have used PBE in our calculations. GGA overcomes many shortcomings of LDA especially for systems with strong variations of electron density e.g surfaces, adsorbates and gives reasonable results which are comparable with experiments. One of the shortcomings of both LDA and GGA is the poor description of the electronic structure of strongly correlated materials [54], like in transition metal oxides (TMO). GGA fails to predict the insulating character of oxides and often wrongly predicts metallic character. Therefore, a further improvement is necessary.

LDA/GGA+ U : An additional term is required to deal with the highly localized electron orbitals whose strong interactions produce a metal to insulator transition. This is done by including an orbital dependent Hubbard U term in the calculation to the LDA terms. This method is not truly *ab initio*, as it contains the parameters U and J . The Coulomb interaction term U is physically equivalent to the amount of energy needed to add an extra d(f electron) onto an atomic site. This is reflected in the splitting between the occupied and unoccupied states of the d(f) band thus producing an insulating state. The U term is only applied to the highly localized orbital such as the $3d$ orbital in Fe. We have used the implementation of Ref. [43]. Within this approach, the self interaction term is also subtracted. The LDA+ U total energy is given by:

$$E_{LDA+U} = E_{LDA} + \frac{1}{2}U \sum_{m,\acute{m},\sigma} n_{m\sigma}n_{\acute{m}\sigma} + \frac{1}{2}(U - J) \sum_{m \neq \acute{m}, \acute{m}, \sigma} n_{m\sigma}n_{\acute{m}\sigma} - UN(N - 1)/2 - JN(N - 2)/4. \quad (2.23)$$

2.2 Methods for band structure calculation

Augmented Plane Wave Method (APW)

The solution of the Schrödinger equation at zero potential is a plane wave. The electrons far from the nuclei behave as free particles and can be represented by plane waves. The electrons close to the nucleus behave as in a free atom and hence, atomic like functions can be used to represent them. This is used in the augmented plane wave (APW) [41, 60] method. The space is divided into two regions as shown in Fig. 2.24. One is called the muffin tin region wherein the wave function is expanded in atomic like functions and the rest of the space called the interstitial which is described by the plane waves composed part of the wave function. The augmented plane wave (APW) [41, 60] used in the expansion of $\Psi_{\vec{k}}^k(\vec{r}, E)$ is defined as:

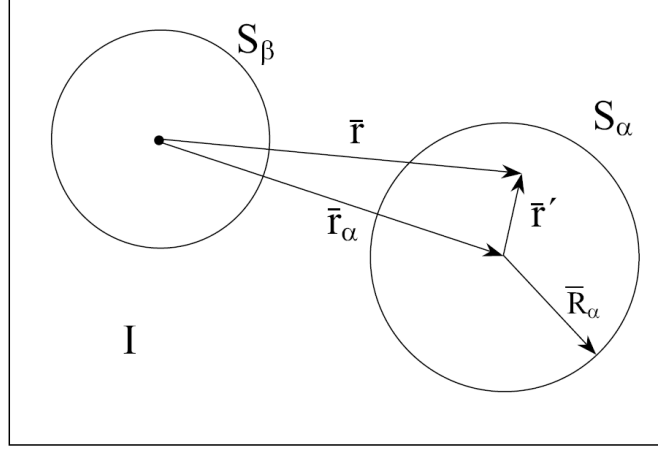


Figure 2.1: In FP-LAPW method, the unit cell space is divided into two regions namely muffin tin region and interstitial region [41]

$$\Psi_K^k(\vec{r}, E) = \begin{cases} \frac{1}{\sqrt{V}} e^{i(\vec{k} + \vec{K}) \cdot \vec{r}} & \vec{r} \in I \\ \sum_{l,m} A_{lm}^{\alpha, (\vec{k} + \vec{K})} u_l^\alpha(r', E) Y_m^l(\hat{r}') & \vec{r} \in S_\alpha, \end{cases} \quad (2.24)$$

where \vec{k} is the wave vector and \vec{K} is the reciprocal lattice vector. \vec{r} is used to represent the position vector and V represents volume of the unit cell in this section. The APW basis set is \vec{k} -dependent. The $Y_m^l(\theta, \phi)$ are the spherical harmonics. The parameters $A_{lm}^{\alpha, (\vec{k} + \vec{K})}$ and E are to be determined. The $u_l^\alpha(r', E)$ are the solutions of the radial part of the Schrödinger equation for a free atom at energy E . On the other hand, this implies that the wave function inside the muffin tin sphere depends on the energy parameter E . The plane waves which form the part of the wavefunction in the interstitial region are \vec{K} -dependent. The eigenfunction cannot be discontinuous at the sphere boundary. This imposes a condition of continuity (in value, not slope) for the plane waves outside sphere and the functions inside the sphere, and allows determination of A_{lm}^α . The energy E is the eigenvalue of the Schrödinger equation. This value needs a guess and a subsequent improvement with the self-consistent (scf) cycles.

Linear Augmented Plane Wave Method (LAPW)

The shortcoming of the APW method was the construction of the $u_l^\alpha(r', E)$ with the yet to be searched eigenvalues $E = \epsilon_n^k$. This has been resolved in the

LAPW method [41, 61] by Taylor expanding the u_l^α around an energy E_0 :

$$u_l^\alpha(r', E) = u_l^\alpha(r', E_0) + (E_0 - \epsilon_n^k) \frac{\partial u_l^\alpha(r', E)}{\partial E} + O(E_0 - \epsilon_n^k)^2. \quad (2.25)$$

Eq. 2.25 enables a larger flexibility in the choice of E_0 . The first two terms are the additional parameters included from the APW expansion to form a LAPW basis set at a fixed energy E_0 :

$$\Psi_K^k(\vec{r}', E) = \begin{cases} \frac{1}{\sqrt{V}} e^{i(\vec{k} + \vec{K}) \cdot \vec{r}'} & \vec{r}' \in I \\ \sum_{l,m} \left\{ A_{lm}^{\alpha, (\vec{k} + \vec{K})} u_l^\alpha(r', E_0) \right. \\ \left. + B_{lm}^{\alpha, (\vec{k} + \vec{K})} \dot{u}_l^\alpha(r', E_0) \right\} Y_m^l(\hat{r}') & \vec{r}' \in S_\alpha, \end{cases} \quad (2.26)$$

where $(E_0 - \epsilon_n^k) = B_{lm}^{\alpha, (\vec{k} + \vec{K})}$ and $\frac{\partial u_l^\alpha(r', E)}{\partial E} = \dot{u}_l^\alpha(r', E_0)$. The coefficients $A_{lm}^{\alpha, (\vec{k} + \vec{K})}$ and $B_{lm}^{\alpha, (\vec{k} + \vec{K})}$ are determined from the boundary condition. In this case the basis set must match both in value and slope at the sphere boundary.

The core states that lie high in energy and are close to the valence states are called semi-core states. The problem with these states is that they are highly bound and sometime go beyond the muffin tin region. States having the same l but different principal quantum number n (valence and semicore states) should be treated with care. This treatment comes in the form of LAPW+LO [41]. LO means a local orbital which is zero in the interstitial region as well in other muffin tins region. It is localized within the muffin sphere. The implementation of this set is done by including an extra radial term $C_{lm}^{\alpha, (\vec{k} + \vec{K})} u_l^\alpha(r', E_{1,l})$ in the muffin tin sphere region. Now there are three terms to be determined. These are obtained from the boundary conditions and normalisation.

Similar to LAPW+LO, the APW basis set has been improved by including the concept of fixed energies and local orbitals, leading to a APW+lo orbital [41]. Here the lo is used to enhance the power of the basis set, still the first derivative is discontinuous as in APW.

Full-Potential Liner Augmented Plane Wave Method (FP-LAPW)

The FP-LAPW method combines the LAPW basis set with a full potential and charge density of the system. This means there is no shape approximation of interstitial potential (V_I^0) and muffin tin potential ($V_{MT}^0(\vec{r}')$) as done e.g. in

APW. This is achieved by relating the constant interstitial potential V_I^0 and the muffin tin potential $V_{MT}^0(\vec{r})$ due to the inclusion of a wrapped potential $\sum_K V_I^K e^{iK \cdot \vec{r}}$ and the non-spherical terms in the muffin tin region as:

$$V(\vec{r}) = \begin{cases} \sum_{LM} V_{LM}(\vec{r}) Y_{LM}(\vec{r}) & \vec{r} \in S_\alpha \\ \sum_K V_K e^{iK \cdot \vec{r}} & \vec{r} \in I. \end{cases} \quad (2.27)$$

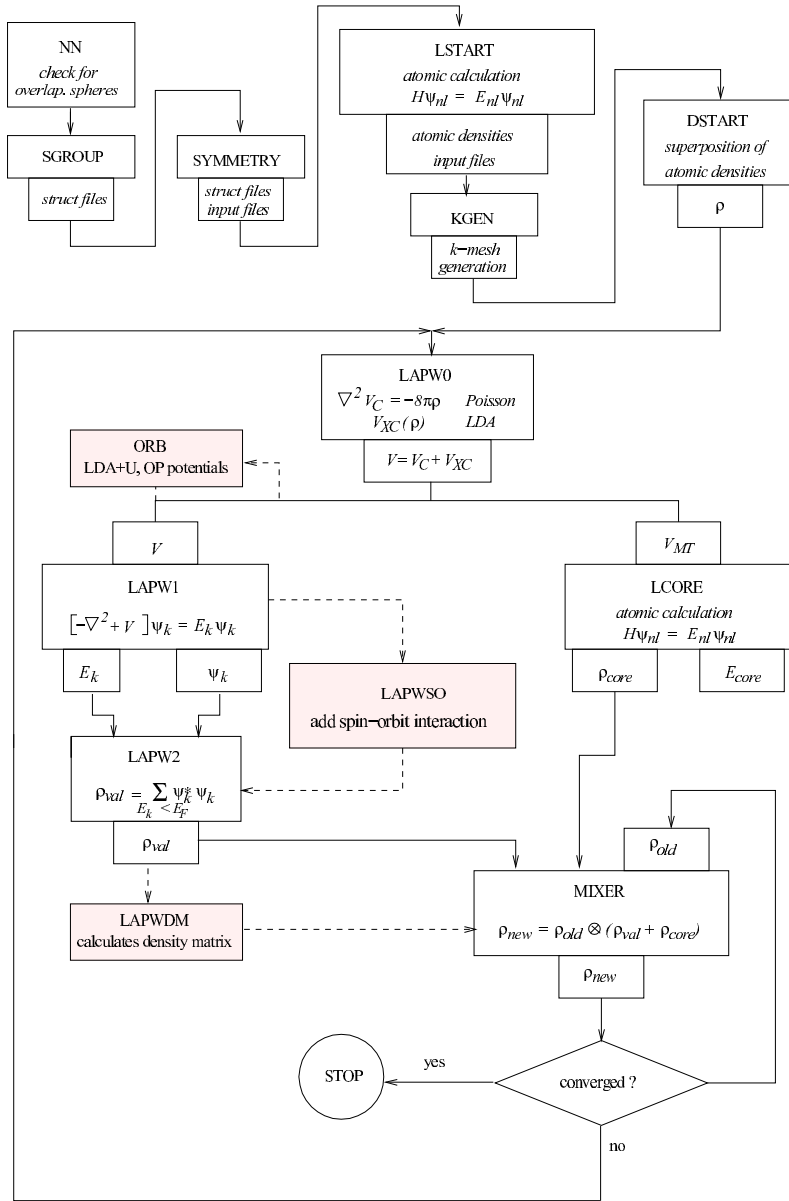


Figure 2.2: Wien2k flow chart [42].

2.3 Structure of the Wien2k code

All the calculations are done primarily using the WIEN2K code [42]. In this Section we will briefly introduce the program. The WIEN2k code is based on the full potential (L)APW+lo method to describe crystalline materials. The program is divided into two parts 1) initialisation and 2) self consistent calculation. The initialisation includes setting up of the crystal structure file and checking its symmetry related information with SGROUP and SYMMETRY. In the next step, using LSTART, atomic densities are generated from the input files. The starting charge density for the scf cycle is generated as a superposition of the atomic density using the DSTART routine as shown in the flow chart of Fig. 2.2. In the self-consistent calculation, first the LAPW0 routine generates the potential for the calculation from the charge density, secondly the LAPW1 routine calculates the eigenvectors and eigenvalues for the valence band by diagonalizing the matrix. Usually this is most time consuming part in the calculation. In the next step the LAPW2 routine generates the valence density from the eigenvectors, LCORE calculates the core states and density for a spherical symmetric potential and finally the MIXER mixes the input and output density to generate the input for the next cycle and checks the convergence criteria. The whole process is also depicted in the flow chart of WIEN2K given in Fig. 2.2.

2.4 *Ab-initio* atomistic thermodynamics

DFT is known as a zero temperature and zero pressure (ground state) technique. To study any material under realistic conditions, inclusion of environmental conditions are crucial. The most common parameters are the temperature, pressure and the surrounding gas phase. To extend the predictive power of *ab-initio* calculations to finite temperature and pressures, *ab-initio* atomistic thermodynamics was formulated [45,62–66]. The basic idea is to interpret the DFT values in terms of a thermodynamic potential. If any one of the thermodynamic potentials is known from the DFT calculations, then, within the existing framework of thermodynamics other properties can be related.

The surface is assumed to be in equilibrium with the gas atmosphere and with the underlying bulk. If two components are in thermodynamic equilibrium, then the individual chemical potentials (μ) have to be equal. The bulk of the solid and the gaseous atmosphere are essentially treated as reservoir of particles. The most appropriate thermodynamic potential for a given (T,p) would be Gibbs's free energy (\mathbf{G}). We also define g which is the free energy per formula unit or per particle. In case of a homogeneous and infinite reservoir g is same as the chemical potential μ .

For a solid system in contact with a surrounding gas phase, the Gibbs free

energy of the whole system can be written as:

$$G = G_{solid} + G_{gas} + \Delta G_{surf}. \quad (2.28)$$

The contributions are separated into solid, gas and the surface. If the surface is homogenous, like in a single crystal surface, the surface contribution will scale with the area A . This introduces the surface energy term γ as:

$$\gamma = \frac{1}{A}(G - G_{solid} - G_{gas}), \quad (2.29)$$

where γ is defined in terms of the finite part of the total (infinite) system and G is the total energy which contains the contribution from the bulk and the gas phase. In Eq. 2.29, equivalent amounts of these homogeneous system contributions G_{solid} , G_{gas} are subtracted to have an exclusive contribution from the surface. Now, if we assume that the surface contains N_{Fe} iron atoms and N_O oxygen atoms per surface area, Eq. 2.29 can be written as:

$$\gamma(T, p) = \frac{1}{A}(G(T, p, N_{Fe}, N_O) - N_{Fe}g_{Fe}(T, p) - N_O\mu_O(T, p)), \quad (2.30)$$

where g_{Fe} is the Gibbs free energy per Fe atom in the bulk bcc Fe, and μ_O is the gas phase oxygen chemical potential.

In a more general way, Eq. 2.30 can be written for a multicomponent (for example when the gas phase contains many components) system as:

$$\gamma(T, p_k) = \frac{1}{A}(G^{surf} - \sum_k N_k\mu_k(T, p_k)), \quad (2.31)$$

where G^{surf} is the Gibbs free energy of the solid including the surface and $\mu_k(T, p_k)$ are the chemical potential of the various species present in the system.

Since we are mostly interested in the relative stability of the surface, it is useful to take the reference Gibbs free energy from that of a clean surface:

$$\gamma_{clean}(T, p) = \frac{1}{A}(G(T, p, N'_{Fe}, N'_O) - N'_{Fe}g_{Fe}(T, p) - N'_O\mu_O(T, p)). \quad (2.32)$$

Defining the change in the Gibbs free surface energy $\Delta\gamma(T, p)$ as the dif-

ference between Eq. 2.30 and Eq. 2.32 as:

$$\begin{aligned} \Delta\gamma(T, p) = & \frac{1}{A}(G(T, p, N_{\text{Fe}}, N_{\text{O}}) - G(T, p, N'_{\text{Fe}}, N'_{\text{O}})^{clean} \\ & - (N_{\text{Fe}} - N'_{\text{Fe}})g_{\text{Fe}}(T, p) - (N_{\text{O}} - N'_{\text{O}})\mu_{\text{O}}(T, p)). \end{aligned} \quad (2.33)$$

If the difference is negative ($\Delta\gamma(T, p)$), then the surface is more stable than the reference surface. In principle the Gibbs free energy has several contributions which must be considered as:

$$G = E^{total} + F^{vib} + F^{conf} + pV, \quad (2.34)$$

where E^{total} is the total internal energy, F^{vib} is the vibrational free energy, and F^{conf} is the configurational free energy and pV is the volume effect. The internal energy E^{total} is the total energy from the DFT calculations. The vibrational energy contribution can also be estimated as shown in Ref. [66]. Though the changes are typically within $\pm 5 \text{ meV}/\text{\AA}^2$ but in some cases they can be significant. The other contributions from the configuration and volume energies are largely canceled as in Eq. 2.33 only the difference in Gibbs free energy is considered. Finally, with all the approximations considered above, the Gibbs free energy in Eq. 2.33 is replaced by the total energy from the DFT calculations E^{total} . The configuration that minimizes Eq. 2.33 is the most stable configuration at a given T and p.

Now we apply the above discussed formalism of *ab-initio* atomistic thermodynamics to account for water additional to the O_2 in the atmosphere on a $\text{Fe}_3\text{O}_4(001)$ surface. In the case of Fe_3O_4 we can relate the Gibbs free energy as:

$$N_{\text{Fe}}^b \mu_{\text{Fe}} + N_{\text{O}}^b \mu_{\text{O}} = g_{\text{bulk}}^{\text{Fe}_3\text{O}_4}, \quad (2.35)$$

where μ_{Fe} and μ_{O} are the chemical potentials of oxygen and iron atoms respectively and $g_{\text{bulk}}^{\text{Fe}_3\text{O}_4}$ is the Gibbs free energy of formation of bulk Fe_3O_4 . N_{Fe}^b and N_{O}^b are the number of iron and oxygen atoms in the bulk. In a similar way, the surrounding gas phase of oxygen and hydrogen is assumed to be in equilibrium with each other as well as with the surface. The thermodynamic equilibrium between oxygen and hydrogen cannot rule out the formation of water vapour [67]. The chemical potential of oxygen and hydrogen can be related as:

$$\mu_{\text{H}_2\text{O}} = 2\mu_{\text{H}} + \mu_{\text{O}}, \quad (2.36)$$

where $\mu_{\text{H}_2\text{O}}$, μ_{H} and μ_{O} are the chemical potential of water, hydrogen and oxygen respectively. Eq. 2.31 can be rewritten for the present system with two

components (μ_{H_2O}, μ_O):

$$\begin{aligned} \gamma(T, p) = \frac{1}{2A} & (G^{slab}(T, p, N_{Fe}, N_O) - N_{Fe}\mu_{Fe}(T, p) \\ & - N_O\mu_O(T, p) - N_{H_2O}\mu_{H_2O}(T, p)). \end{aligned} \quad (2.37)$$

In this equation we see an additional factor of 2 with the surface area. This is because of the two surfaces of a slab will be explained in Chapter 4. Combining Eq. 2.35 and Eq. 2.36 with Eq. 2.37 we end up with the following expression for the surface energy ($\gamma(T, p)$):

$$\gamma(T, p) = \frac{1}{2A} (G^{slab}(T, p, N_{Fe}^s, N_O^s) - [N_O^s - \frac{N_H^s}{2}]\mu_H - \frac{N_H^s}{2}\mu_{H_2O}). \quad (2.38)$$

2.4.1 Range of the chemical potentials

The limits of μ_{H_2O} and μ_O in principle can vary from minus to plus infinity but to represent a realistic picture we need to choose a meaningful range. For μ_O the *oxygen poor limit* will decompose the metal oxide into pure metal and oxygen. This means that:

$$\max[\mu_{Fe}(T, p)] = g_{Fe}^{bulk}(T, p). \quad (2.39)$$

Substituting $\max[\mu_{Fe}(T, p)]$ in Eq. 2.35 we get the μ_O poor limit as:

$$\mu_O = \frac{1}{N_O} [g_{bulk}^{Fe_3O_4} - N_{Fe}^b \cdot g_{Fe}^{bulk}] \quad (2.40)$$

The oxygen rich limit is defined as the limit where the oxygen starts to condense on the surface. The approximation for the rich limit is given by :

$$\max[\mu_O(T, p)] \simeq 1/2 E_{O_2}^{total}. \quad (2.41)$$

Combining Eq. 2.40 and Eq. 2.41 we can show the range varies as:

$$\frac{1}{2} \Delta G_f(0, 0) < \mu_O(T, p) - \frac{1}{2} E_{O_2}^{total} < 0, \quad (2.42)$$

where $\Delta G_f(0, 0)$ is the Gibbs formation energy of the bulk oxide. In a similar

way the range of $\mu_{\text{H}_2\text{O}}$ and μ_{H} is defined as:

$$-E_f \leq \mu_{\text{H}_2\text{O}} \leq 0 \quad (2.43)$$

and

$$-E_f \leq \mu_{\text{H}} \leq 0, \quad (2.44)$$

where E_f is the formation energy. In order to derive surface energy in the oxygen poor limit we combine Eq. 2.38 and Eq. 2.40 as:

$$\begin{aligned} \gamma(T, p) = \frac{1}{2A} \left[E^{\text{slab}}(T, p, N_{\text{Fe}}^s, N_{\text{O}}^s) - \left(N_{\text{Fe}}^s - \frac{N_{\text{Fe}}^b N_{\text{O}}^s}{N_{\text{O}}^b} - \frac{N_{\text{H}}^s N_{\text{Fe}}^b}{2N_{\text{O}}^b} \mu_{\text{Fe}} \right) \right. \\ \left. - \left(\frac{N_{\text{O}}^s}{N_{\text{O}}^b} - \frac{N_{\text{H}}^s}{2N_{\text{O}}^b} \right) E_{\text{bulk}}^{\text{Fe}_3\text{O}_4} - \frac{N_{\text{H}}}{2} \mu_{\text{H}_2\text{O}} \right]. \end{aligned} \quad (2.45)$$

On the other hand, the surface energy in the oxygen rich limit is:

$$\gamma(T, p) = \gamma_{\text{poor}} - \frac{1}{2A} \left(\frac{N_{\text{Fe}}^s}{N_{\text{Fe}}^b} - \frac{N_{\text{O}}^s}{2N_{\text{O}}^b} \mu_{\text{Fe}} \right) \Delta G_f(0, 0). \quad (2.46)$$

2.4.2 Temperature and pressure dependence of $\mu(T, p)$

In the Eq. 2.45, Eq. 2.46, we relate surface energy to the chemical potential of $\mu_{\text{H}_2\text{O}}$ and μ_{O} . Now in the next step we need to relate these chemical potential values to temperature (T) and pressure (p). The dependence is given as [66]:

$$\mu_{\text{O}}(T, p) = \mu_{\text{O}}(T, p^o) + 1/2 K_B T \ln \left(\frac{p}{p^o} \right), \quad (2.47)$$

where for a given T, p the $\mu_{\text{O}}(T, p^o)$ is calculated using the thermodynamic relation $G = H - TS$ in the following way:

$$\begin{aligned} \mu_{\text{O}}(T, p^o) = \left[\frac{1}{2} [H(T, p^o, \text{O}_2) - H(0\text{K}, p^o, \text{O}_2)] \right] \\ - \left[\frac{1}{2} T [S(T, p^o, \text{O}_2) - S(0\text{K}, p^o, \text{O}_2)] \right]. \end{aligned} \quad (2.48)$$

For standard pressure $p^o=1$ atm, the values of H and S are listed in thermochemical tables [68]. By inserting these values we get the required $\mu_{\text{O}}(T, p^o)$ and together with Eq. 2.47 we can calculate chemical potential of oxygen at

any given T and p . In a similar way chemical potential of H_2O and H are also obtained.

2.5 Surface core level shifts

Core level binding energies are very sensitive to the chemical environment [69–71]. The shifts in the binding energies are usually considered with respect to a reference system: $E_{\text{CLS}}^{\text{exp}} = E_{\text{B}} - E_{\text{B}}^{\text{ref}}$. Here the reference system is an isolated free atom. The core level binding energy in a free atom is calculated w.r.t vacuum and that in a solid w.r.t the Fermi level. Therefore one needs to be careful with the reference level in consideration. The core level binding energy shift between a metal and a free atom can be extended to account changes on a surface. In this case the surface core level shifts (SCLS) are given by:

$$\Delta^{\text{SCLS}} = [E^{\text{S}}(n_c - 1) - E^{\text{S}}(n_c)] - [E^{\text{B}}(n_c - 1) - E^{\text{B}}(n_c)], \quad (2.49)$$

where $E^{\text{S}}(n_c)$ is the binding energy of the surface slab with n_c electrons at a particular core level and $E^{\text{B}}(n_c)$ is that of the bulk. The bulk atom acts as reference in this case. The surface atom is under-coordinated compared to the bulk atom which means a different local potential and chemical environment is seen by the core electrons. This in turn affects the binding energies resulting in a shift (Δ^{SCLS}). This shift can be measured by highly sensitive XPS (X-ray photoemission spectroscopy) [69, 71, 72]. A similar quantity known as the chemical shift is given by electron spectroscopy for chemical analysis (ESCA). There are several methods to extract Δ^{SCLS} from DFT code as:

1. Initial state approximation
2. Transition state model

In the following we briefly describe both the approaches. When a core electron is removed or excited to the Fermi level, a relaxation effect takes place in the system which includes the screening of the core hole by the other valence electrons. Core level shift energy values can be divided into an initial state effect and final state effect. The former does not contain the screening contribution. To calculate the initial effect we expand the energy from Eq. 2.49 in a Taylor expansion [69]:

$$E(n_c - \delta n_c) - E(n_c) = -\frac{\partial E(n_c)}{\partial n_c} \delta n_c + \frac{1}{2} \partial^2 E(n_c) \partial^2 n_c (\delta n_c)^2 + \dots \quad (2.50)$$

In DFT, the partial derivative of the total energy w.r.t the occupation number is given by the orbital energy, therefore:

$$\partial E(n_c) \partial n_c = \epsilon_c. \quad (2.51)$$

Substituting Eq. 2.51 in Eq. 2.50, we refine the equation as:

$$\Delta^{SCLS} = -(\epsilon_c^S - \epsilon_c^B) - \frac{1}{2} \frac{\partial}{\partial n_c} \epsilon_c^B + \frac{1}{2} \partial n_c \epsilon_c^S + \dots \quad (2.52)$$

The higher order terms are neglected in the initial state approximation and hence the $\Delta_{initial}^{SCLS}$ is given by:

$$\Delta_{initial}^{SCLS} = -(\epsilon_c^S - \epsilon_c^B). \quad (2.53)$$

The orbital energy ϵ in DFT is given by the Kohn-Sham orbital energies. The higher order terms in Eq. 2.50 represent the final state effects which can also be calculated using the transition state method [71, 72]. In this method an impurity (core hole) is introduced once in a bulk atom and once in a surface atom as given in Eq. 2.49. The total energy difference in Eq. 2.49 is evaluated in this method by the Slater-Janak transition state approach [73]. Applying the mean value of integration, the energy difference is written as:

$$E(n_c - 1) - E(n_c) = \int_{n_c}^{n_c-1} \frac{\partial E(\acute{n})}{\partial \acute{n}} d\acute{n} \approx -\epsilon_c \left(n_c - \frac{1}{2} \right). \quad (2.54)$$

Substituting Eq. 2.54 in Eq. 2.49 along with Eq. 2.53 we can calculate not only the initial state but also include the final state effects. This total Δ^{SCLS} is more appropriate to compare with experimental shifts.

We calculate SCLS for oxygen 1s and iron 2p states of Fe_A and Fe_B . The reference system is the corresponding atom in the bulk unit cell of Fe_3O_4 . The initial state contribution (Eq. 2.53) can be directly calculated from the Kohn-Sham eigenvalues after a full self-consistent convergence. For the final state calculation (2.54) half of the electron is taken from core level and kept in a valence level so as to maintain the charge neutrality of the atoms. In many of the cases care has been taken to avoid any core-hole:core-hole interaction by choosing distant atomic sites.

2.6 Molecular orbitals of H₂O and OH

In this Section we will describe briefly the molecular orbitals (MO) of H₂O and OH which will be frequently used during the interpretation of results in the later Chapters.

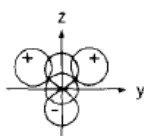
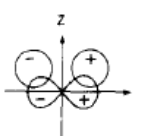
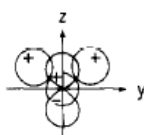
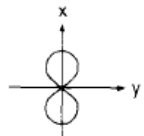
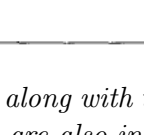
Orbital	Atomic equivalent	Description	Energy (eV)	Depiction
(1a ₁) ²	(1s _O) ²	Nonbonding (core level)	539.7 (559.6)	
(2a ₁) ²	[c ₁ (2s _O) + c ₂ (2p _{z,0}) + c ₃ (1s _{H_A} + 1s _{H_B})] ²	Partly bonding and partly nonbonding (lone pair)	32.2 (36.8)	
(1b ₂) ²	[c ₄ (1s _{H_A} - 1s _{H_B}) + c ₅ (2p _{y,0})] ²	Bonding	18.5 (19.5)	
(3a ₁) ²	[c ₆ (1s _{H_A} + 1s _{H_B}) + c ₇ (2s _O) + c ₈ (2p _{z,0})] ²	Partly bonding and partly nonbonding (lone pair)	14.7 (15.9)	
(1b ₁) ²	(2p _{x,0}) ²	Nonbonding (lone pair)	12.6 (13.9)	

Figure 2.3: The molecular orbitals of a gas phase H₂O molecule along with the participating atomic orbitals. The bonding and non-bonding orbitals are also indicated. This figure is taken from Ref. [32] and references therein.

The well known Atomic orbitals (AO) like s and p orbital are used in a linear combination of atomic orbitals (LCAO) to generate the MO. The H₂O molecule has a C_{2v} point group symmetry and the LCAO combination is considered resulting in molecular orbitals shown in table of Fig. 2.3.

The 1b₁ is the highest occupied molecular orbital (HOMO) and 2b₁ is the lowest unoccupied molecular orbital (LUMO). During the adsorption process mainly the 1b₁ and 3a₁ participates. These have non-bonding and bonding character, respectively.

In the case of a OH group, the MO are represented by those of hydrogen fluoride which is isoelectronic. The MO are shown in Fig. 2.4. The 1π orbital is the non-bonding orbital but it is also degenerate as shown in the Fig. 2.4. The 3σ orbital is of bonding nature and is also the HOMO. During the adsorption process both the 1π and 3σ orbital participate.

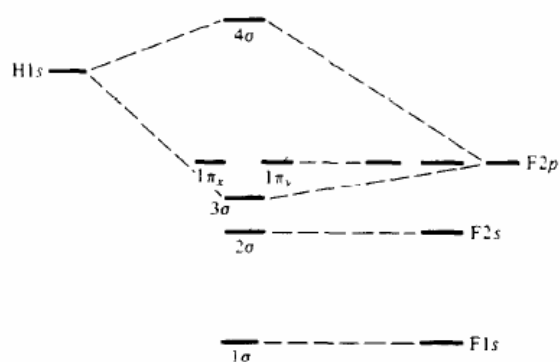


Figure 2.4: *The molecular orbitals of OH group is similar to that of HF as both are isoelectronic. This figure is taken from Ref. [32] and reference therein.*

Computational Details

The properties of solids can be calculated or understood in a better way if we can simulate a given material in real conditions. In general as we know an ordered solid is made up of repetitive arrays of unit cell in all three directions. This is exactly what a usual periodic DFT code will do to simulate a bulk solid. At an oxide surface, there is no repetition of the unit cell in the direction normal to the surface. The surface is simulated by a finite slab. In this scheme the main factors that determine the accuracy of the calculation are: thickness of the slab and vacuum. Slabs are separated on either side by vacuum region to avoid the interaction between them. This results in the creation of two surfaces one on each side. In this way we calculate surface properties using a periodic DFT code. The thickness of vacuum generally varies from 10-15 Å. The slab thickness is another important parameter which determines the reliability of results and has been tested carefully. Fig. 3.1 shows the surface slab setup of $\text{Fe}_3\text{O}_4(001)$.

3.1 Surface slab setup

We have simulated the $\text{Fe}_3\text{O}_4(001)$ surface with a slab consisting of 7-B layers and 6-A layers with a vacuum thickness of 10–12 Å as shown in Fig 3.1. In this setup the central 3-B/2-A layers represent the bulk material while the outer 2-B/1-A layers are the surface region. We allow the surface layers along with adsorbate layers to relax fully during structural optimisation, while the central layers are kept fixed.

While choosing the slab thickness we have also tested a smaller slab of 5-B layers and 4-A layers along with 10 Å of vacuum. In this regime of slab thickness we found that the central layers possess appreciable forces during the optimisation procedure. This indicates that bulk part is influenced by the spurious interactions between the opposite faces of the slabs. For a higher thickness of slab the forces at the central layers are reduced appreciably.

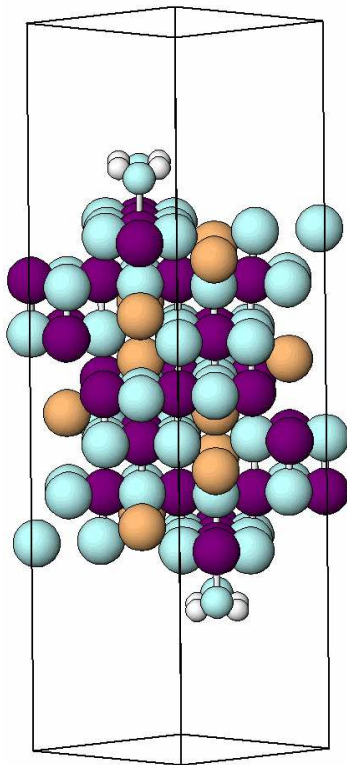


Figure 3.1: Slab with seven B layers and six A layers used to simulate the $\text{Fe}_3\text{O}_4(001)$ surface. The vacuum between the slabs is $\sim 10\text{--}12 \text{ \AA}$.

3.2 Surface and adsorption models

Before proceeding with the surface calculations, we have to carefully choose the clean $\text{Fe}_3\text{O}_4(001)$ surface termination. As discussed in Chapter 1 and Chapter 8 modified B-layer [25] is the most stable surface termination under a wide range of partial pressure of oxygen p_{O_2} while at low oxygen partial pressures other stable phase termination stabilizes i.e. the B-layer with an oxygen vacancy (B+V_O). Both these terminations along with a 0.5 A layer termination is considered for the water adsorption. The 0.5 A layer termination has been proposed in literature [20] following the autocompensation rule [74], and therefore we have also taken into account 0.5 A-layer terminated surface.

The B-layer termination is used to adsorb H_2O , OH and H. The geometry and concentration of these species is varied on the surface from a single molecule to full saturation where all the surface cation sites are covered.

The mode of adsorption for a single water molecule can be molecular or dissociative. With the inclusion of higher number of water molecules we have considered a mixed mode (dissociative and molecular) of adsorption. In this way we can ascertain which adsorption mode is more favorable. In all the coverages, molecular, tilted and dissociative configurations are denoted by F/U, T

and D respectively. U denotes molecular adsorption in an upright orientation and F denotes molecule lying parallel to the surface as will be explained in Chapter 4. In the T configuration, the H₂O molecule is tilted from its upright geometry. The suffix to these letters gives the number of water molecules and prefix shows the variation in the geometry. Naming scheme of the adsorption models is: (No. of H₂O molecules)(Mode of adsorption like M/F/D)-(Model number) e.g. 1D-2 is interpreted as, in a one water molecule coverage with dissociated mode of adsorption, the model number of the configuration is two as shown in Fig. 4.2.

3.3 Surface and adsorption energetics

The truncation of a bulk crystal to form a surface retains the 2-D periodicity intact. The atoms near the surface are under-coordinated when compared to the bulk atoms due to the break in translational symmetry along the z direction. We consider the \hat{z} unit vector to be parallel to the surface normal. The surface atoms often exhibit relaxations to gain stability.

The binding of an ad-atom to the surface is described by the adsorption energy:

$$E_{\text{ads}} = \frac{1}{n}(E_{\text{nH}_2\text{O:Fe}_3\text{O}_4(001)} - E_{\text{Fe}_3\text{O}_4(001)} - nE_{\text{H}_2\text{O}}), \quad (3.1)$$

where $E_{\text{nH}_2\text{O:Fe}_3\text{O}_4(001)}$ and $E_{\text{Fe}_3\text{O}_4(001)}$ are the total energies of the system with adsorbates and the clean surface, $E_{\text{H}_2\text{O}}$ is the energy of a gas phase H₂O molecule and n is the number of water molecules adsorbed. We have also calculated the energetics of H₂O, O₂ and H₂ molecule and verified their description within DFT-GGA, details are given in Appendix A. It is to be noted here that throughout this thesis we are referring to the E_{ads} per molecule as defined in Eq. 3.1. There are two regimes of adsorption based on the value of E_{ads} [54, 75]: if $E_{\text{ads}} \leq 0.5$ eV we are in regime of physisorption and ≥ 0.5 eV corresponds to chemisorption [54, 75]. In the former case the effect on the electronic structure is less compared to the latter one. Water adsorption falls mostly in the limit of physi-and chemi-sorption [32].

Another aspect which can give further insight into the adsorption process is the change in electrostatic potential i.e. change in the work function. The work function is defined as the energy needed to remove an electron from the solid to vacuum at 0 K. In our calculations we determine the work function by taking the difference between the electrostatic potential from the center of the vacuum and Fermi level.

To shed more light on the adsorption mode and the binding mechanism, we have analyzed the electron density redistribution ($\Delta\rho$) upon adsorption for

different adsorbate configurations. $\Delta\rho$ is defined as:

$$\Delta\rho = \rho_{\text{nH}_2\text{O:Fe}_3\text{O}_4(001)} - \rho_{\text{Fe}_3\text{O}_4(001)} - \rho_{\text{nH}_2\text{O}}, \quad (3.2)$$

where $\rho_{\text{H}_2\text{O:Fe}_3\text{O}_4(001)}$, $\rho_{\text{Fe}_3\text{O}_4(001)}$ and $\rho_{\text{nH}_2\text{O}}$ are the electron densities of the system with adsorbates, the clean $\text{Fe}_3\text{O}_4(001)$ surface and water molecules, respectively. In the reference systems, the positions of the atoms correspond to the system with adsorbates.

3.4 Technical parameters and accuracy

Density functional theory calculations were performed using the FP-LAPW (full potential linear augmented plane wave) method in the WIEN2k [42] implementation. The generalised gradient approximation (GGA) [44] of the exchange-correlation potential is used. Since Fe_3O_4 is a strongly correlated material we have also considered the influence of electronic correlations within the LDA/GGA+ U [43] approximation.

We have used $U = 5$ eV and $J = 1$ eV, similar to the values used for bulk Fe_3O_4 [9,10]. With these values an insulating band gap of 0.3 eV is calculated for the modified B-layer in agreement with the scanning tunneling spectroscopy (STS) [118] measurements and a previous DFT calculation [26]. In order to check the dependence of results on the chosen U value we have varied the U from 2 eV to 8 eV. As discussed in Chapter 8, we find that for $U \geq 2$ eV the pattern of charge order almost remains the same as shown in Fig. 9.2.

The use of two approximations for the exchange correlation potential makes our results more reliable and qualitative and therefore a substantial part of the thesis discusses the agreements/discrepancies between the two approximations and analyze them. This also brings out the limitation in the applicability of the two approximations.

We have used the following RMT's: $R_{\text{Fe}}^{MT} = 1.90$, $R_{\text{O}}^{MT} = 1.10$ and $R_{\text{H}}^{MT} = 0.60$ Bohr. A mixed augmented plane wave (APW+lo) and linear augmented plane wave (LAPW) basis sets is used. Inside the MTs the wave function are expanded in spherical harmonics up to $l_{\text{max}}^{wf} = 10$ and non-spherical contribution to the electron density as well as potential are considered up to $l_{\text{max}}^{\text{pot}} = 6$. The energy cut off for the plane wave representation and potential are $E_{\text{max}}^{wf} = 25$ Ry and $E_{\text{max}}^{\text{pot}} = 196$ Ry, respectively. For the integration in the Brillouin zone 16 $k||$ -points were used. The accuracy of the calculations using Wien2k for the energy is 10^{-4} Ryd.

The systems contain typically 100-130 atoms which results in a high numerical demand with matrix sizes for the diagonalisation of up to 31000×31000 . To reduce the computational cost and to search more efficiently for the most favorable adsorbate geometries we have performed for some of the systems a struc-

tural optimisation using the Vienna *ab-initio* Simulation Package (VASP) [76] with a default cutoff energy for the plane-wave basis and a force relaxation up to 0.01 eV/Å. Using these geometries several further relaxation steps were done subsequently with the Wien2k code.

The description of the Van-der Waals interaction by DFT is not significantly correct. However in a systematic study done on water clusters [77, 78] using different exchange-correlation functionals it was found that GGA (PBE) describes the hydrogen bond well for equilibrium geometries. The error of overbinding which can be as large as 20 meV/bond will not affect our conclusions as the hydrogen bond contribution derived from our calculations is 0.37 eV per hydrogen bond. A recent DFT investigation within GGA for water adsorption on Al₂O₃(0001) [79] has used the PBE description for the hydrogen bonds.

Monomer Adsorption

Understanding how a single water molecule interacts with a mineral surface is the starting point of the investigation. This is because water molecules tend to diffuse on the surface and form clusters which in turn masks the water substrate interaction [34, 80]. Experimentally it is hardly possible to reach the single H₂O molecule limit which means very low coverages and temperatures $\ll 100$ K to limit the aggregation. Scanning tunneling microscopy (STM) is reliable in studying water monomer species and some attempts are made to visualize the same [81–83] but there are some difficulties associated with it like perturbing the water molecule by the tunneling current [34, 80]. Even with real time STM data, it is difficult to determine the orientation and the binding site in a definitive manner [34, 80]. This is where DFT calculations are useful and contribute towards a better understanding. DFT calculations on water monomer adsorption have been done for many transition metal (Rh(111), Pd(111)) and noble metal surfaces (Au(111), Ag(111)) [34, 80]. To our knowledge there are few metal oxides e.g. NiO(100) [84], Fe₂O₃(0001) [85], Fe₃O₄(111) [86], Al₂O₃(0001) [87] and MgO [88] on which similar studies were carried out. There are only few experimental studies existing on the H₂O interaction with Fe₃O₄(001) surface. The XPS (X-ray photoemission spectroscopy) measurements indicate a dissociative adsorption of H₂O molecules while the TPD (temperature programmed desorption) measurements show three desorption peaks which are assigned to water adsorption on three different iron sites. Lack of a clear picture from the existing results, motivated us to take up this problem. We have studied the adsorption of H₂O molecules in various geometrical configurations. Section 4.1 describes the stability of each configuration in terms of E_{ads} as calculated from Eq. 3.1. To understand the energetic trends we have analysed electronic properties in Section 4.2 with probable explanation for the observed results and differences between GGA and GGA+ U . The structural relaxations and bond lengths upon adsorption of H₂O molecule is discussed in Section 4.3.

4.1 Adsorption models and energetic stability

In this Section we will discuss the different configurations¹ that were considered for an isolated water molecule adsorbed on the $\text{Fe}_3\text{O}_4(001)$ surface. Among all studied geometries we concentrate on some important ones. In Fig. 4.1, we define the tilt angle α between the H_2O molecule and the surface. We define all our molecular adsorption models based on this angle. In an upright configuration $\alpha=90^\circ$ while in the flat/tilted configuration $\alpha=0^\circ$. We have optimized the tilt angle as well.

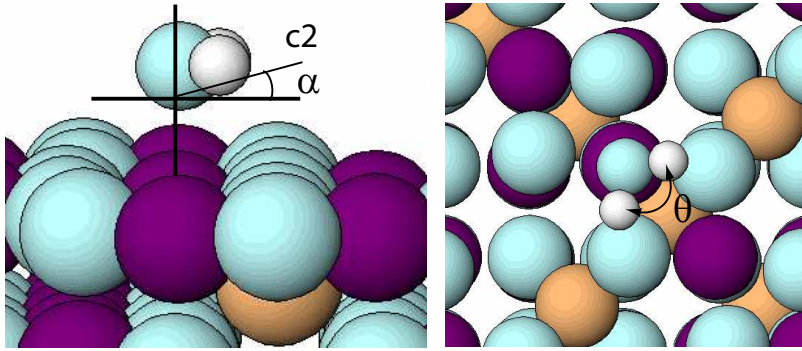


Figure 4.1: *Right panel: Tilt angle α between the H_2O molecule and the surface. Left panel: Angle θ is between $\text{H}-\text{O}^w-\text{H}$ of the H_2O molecule. Positions of oxygen, Fe_B , Fe_A and H are marked by cyan, purple, orange and white circles. The oxygens of the adsorbate are marked by smaller circles.*

Besides the molecular adsorption we have studied dissociated configurations, where the hydroxyl group binds to the surface cation (surface Fe_B) and the hydrogen binds to a nearby surface oxygen atom ($\text{O}(\text{S})$) forming $\text{O}(\text{S})-\text{H}$. The possibility that the H atom diffuses on the surface is also taken into account by adsorbing the hydrogen atom on more distant $\text{O}(\text{S})$ namely T2 and T3, as shown in Fig. 4.2. The three $\text{O}(\text{S})$ sites T1, T2, T3 give rise to three distinct dissociated configurations 1D-1, 1D-2 and 1D-3 respectively. The top view of 1D-1, 1D-2 and 1D-3 are shown in Fig. 4.2.

GGA: Fig. 4.2 shows adsorption of a water molecule in 1F configuration is most favorable with an adsorption energy of -0.70 eV. It is followed in stability by the dissociated configuration 1D-1 with an E_{ads} of -0.66 eV, 0.04 eV less favorable than 1F. The upright adsorption of water (1U) is less favorable by 0.08 eV than 1F. The diffusion of hydrogen to a distant surface oxygen site was found to be 0.44 eV less favorable. For a water molecule two types of dissociation are possible namely heterolytic and homolytic. In the heterolytic mode (1D-1) water splits as $\text{H}_2\text{O} \Rightarrow \text{OH}^- + \text{H}^+$. In the homolytic mode (1D-OH) water splits as $\text{H}_2\text{O} \Rightarrow \text{H}\dot{\text{O}} + 1/2\text{H}_2$. The $\text{H}\dot{\text{O}}$ in homolytic fission signifies the

¹Naming scheme: (No. of H_2O molecules)(Mode of adsorption like M/F/D)-(Model number)

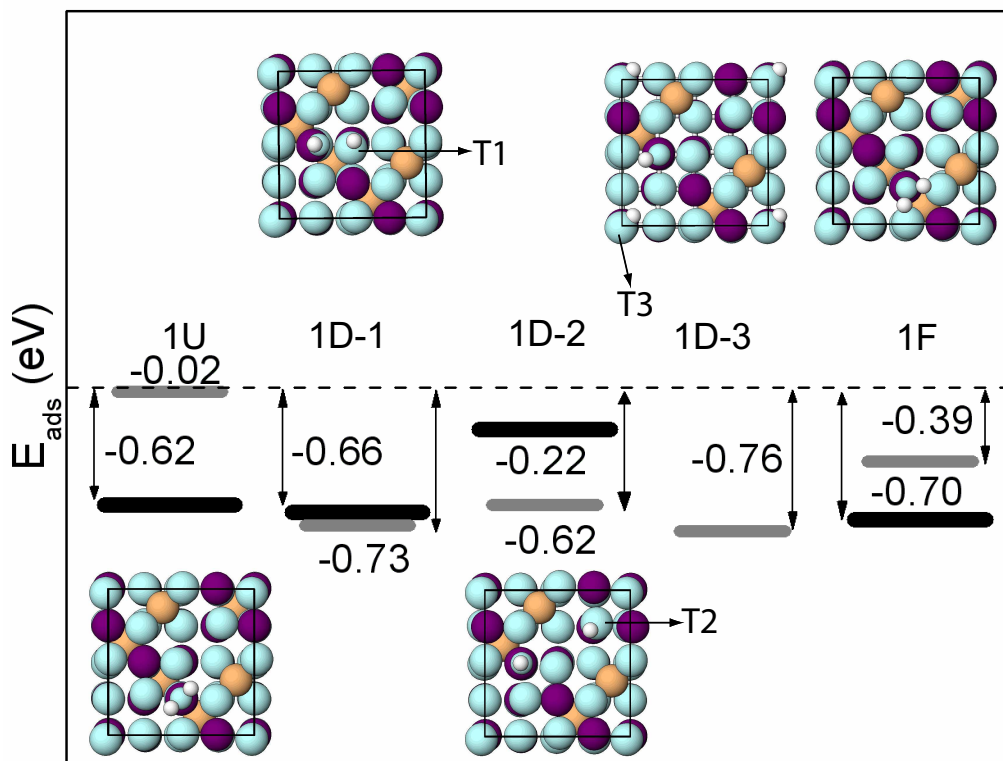


Figure 4.2: Top view of different adsorbate geometries of a single water molecule per $(\sqrt{2} \times \sqrt{2})R45^\circ$ -unit cell. The diagram shows the corresponding adsorption energies (in eV per molecule). GGA (GGA+U) results are given by a solid black (grey) line. Different hydrogen adsorption sites are marked as T1, T2 and T3. Positions of oxygen, Fe_B , Fe_A and H are marked by cyan, purple, orange and white circles. The oxygens of the adsorbate are marked by smaller circles.

bond cleavage is isoelectronic i.e. the hydrogen atom retains its electron and finally desorbs as $1/2H_2$. Our calculation shows that the homolytic mode of dissociation is endothermic with E_{ads} of 0.56 eV. The side view of 1D-OH is shown in the right panel of Fig. 4.10.

GGA+U: The influence of correlation effects is explored with the inclusion of an onsite Coulomb repulsion term within the GGA+U approach. A change in the mode of adsorption from that of GGA is observed as shown in the Fig. 4.2. The dissociative adsorption(1D-1) is now most favorable with an E_{ads} of -0.73 eV, while the 1F configuration is now less favorable by 0.34 eV. Interestingly we find that 1U configuration which was competing with 1F within GGA is now highly unfavorable with a vanishing E_{ads} . Another prominent feature is the binding position of the H atom which now has equal probability to adsorb at a distant O(S) sites (1D-2 and 1D-3). We observe that the total energies of all the dissociated configurations are nearly degenerate. The homolytic dissociation is not considered within GGA+U as it was already found to be unfavorable within GGA.

In order to understand the nature of interaction between the OH and O(S)-H on the surface we have calculated the interaction energy $E_{\text{OH:H}}$ as:

$$E_{\text{OH:H}} = \frac{1}{2}(E_{\text{H+OH:Fe}_3\text{O}_4(001)} + E_{\text{Fe}_3\text{O}_4(001)} - E_{\text{OH:Fe}_3\text{O}_4(001)} - E_{\text{H:Fe}_3\text{O}_4(001)}) \quad (4.1)$$

Where $E_{\text{H+OH:Fe}_3\text{O}_4(001)}$ is the total energy of 1D-1, $E_{\text{OH:Fe}_3\text{O}_4(001)}$ is the total energy of OH on $\text{Fe}_3\text{O}_4(001)$ (fully relaxed), $E_{\text{H:Fe}_3\text{O}_4(001)}$ is the total energy of $\text{Fe}_3\text{O}_4(001)$ with adsorbed H atom (fully relaxed) and $E_{\text{Fe}_3\text{O}_4(001)}$ is the total energy of the clean surface. The interaction energy was calculated only for the case of 1D-1 as -0.14 eV (GGA). The sign of $E_{\text{OH:H}}$ is negative which indicates attractive interaction. We can substantiate the attractive nature of interaction by the following argument: The OH group is electronegative and the H atom which loosely binds on a O(S) (O(S)-H) forms a positive charge hence an attractive interaction evolves between them. Further, the $\angle(\text{Fe}_B(\text{S}-1)\text{-O(S)-H})$ which takes on a value of 111.5° , 105.6° and 105.8° for 1D-1, 1D-2 and 1D-3 respectively supports the argument in the following way: The $\angle(\text{Fe}_B(\text{S}-1)\text{-O(S)-H})$ in 1D-1 is high because the T1 site is adjacent to Fe_B^{OH} and hence it has a higher interaction. At T2 and T3 the distance between the Fe_B^{OH} and O(S)-H increases and the interaction energy decreases, thus the angle decreases.

4.2 Analysis of the electronic structure

In order to understand the energetic trends as well as the reason for the discrepancy between GGA and GGA+ U results, we have analysed the electronic structure based on density of states (DOS), difference density plots and molecular orbital analysis. In Fig. 4.3 we show the MO of H_2O which are involved in the interaction with the surface as we will see below.

Before proceeding further, we will discuss here briefly the factors behind the bonding of water with a transition metal/metal-oxide substrate. The binding energy depends on long range electrostatic interactions and short range Pauli repulsion due to overlap between the oxygen lone pair orbital ($1b_1$) with the cation d orbital. Electrostatic interactions include: 1) water dipole interaction with its image dipole in the substrate, 2) polarisation of s, p electrons in the case of metals which reduces Pauli repulsion and enables dative bond formation between the $1b_1$ and d orbital, and 3) the spacial redistribution of charge in different d orbitals to reduce Pauli repulsion resulting in formation of dative bond [89, 90]. The contribution of water dipole and image dipole interaction is usually not enough to overcome Pauli repulsion [90] while dative or covalent bond formation can. The charge redistribution in different spatially oriented d

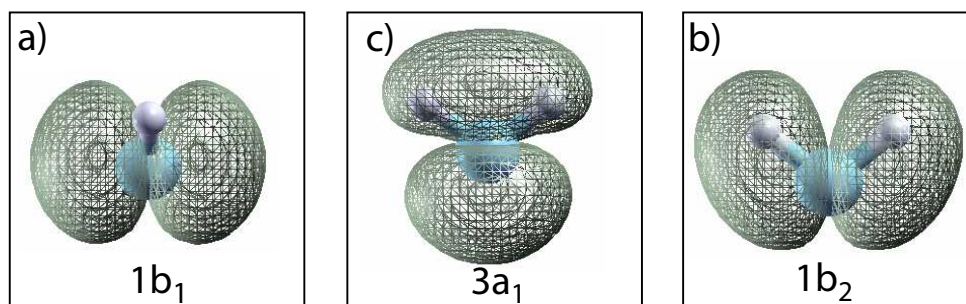


Figure 4.3: *Molecular orbitals of an isolated water molecule calculated from DFT. a) $1b_1$ b) $3a_1$ c) $1b_2$.*

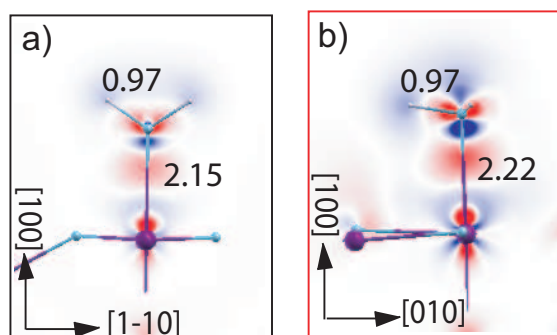


Figure 4.4: *Electron density redistribution ($\Delta\rho$) obtained within GGA+U upon adsorption of a single water molecule in an a) upright and b) flat geometry. Electron accumulation (depletion) is shown in red (blue). Positions of O, Fe_B , and H are marked by cyan, purple and white circles*

orbitals is usually energetically favorable than charge transfer from one atom to another [91]. This factor plays an important role in the case of Fe_3O_4 as s, p electrons of Fe are far below the Fermi energy.

1U and 1F (One H_2O molecule upright and flat/tilted configuration): At first we address why 1F is preferred over 1U. Figure 4.4a,b shows the electron density redistribution upon adsorption for both configurations within GGA+U. We note that both GGA and GGA+U show similar features for the electron density redistribution and hence the GGA result is not shown here. In 1F (Fig. 4.4b) we observe a stronger charge accumulation between $Fe_B(S)$ and the water molecule than in 1U (Fig. 4.4a). 1F also exhibits hydrogen bond between $O(S)$ and H^w which enhances its stability. On the other hand the H^w in 1U points away from the surface and therefore is less preferable. Both in 1U and 1F we notice an accumulation of charge in the d_{z^2} orbital of $Fe_B(S)$ towards the adsorbate indicating its primary role in bonding. Charge redistribution also takes place in the H_2O molecule specially depletion of charge in $1b_1$ MO which reduces Pauli repulsion. Also depletion of charge near the H^w indicates weakening of the OH bond.

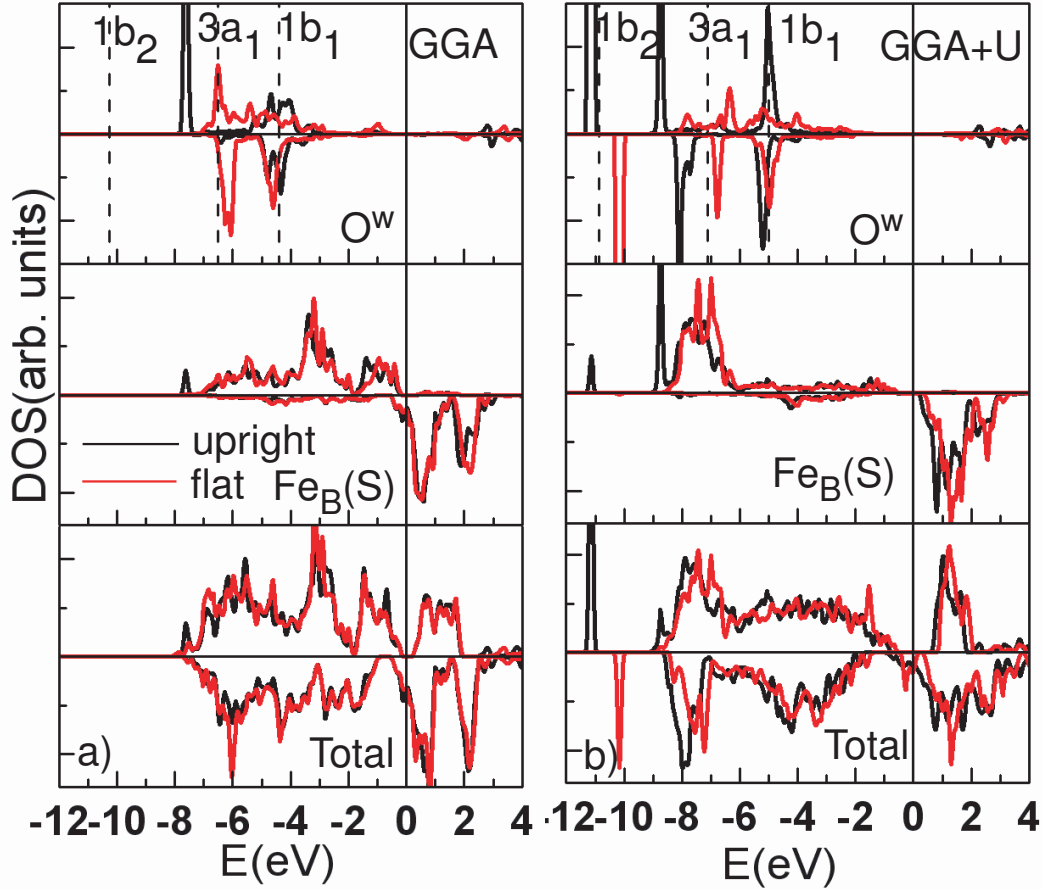


Figure 4.5: Total and projected DOS (PDOS) for the 1U (black) and 1F (red) configurations within a) GGA and b) GGA+U. Top panel: PDOS of O^w , Middle panel: PDOS of $Fe_B(S)$ which stabilizes water molecule on top, Bottom panel: total DOS of the unit cell. The dotted vertical lines represent the energy levels of the molecular orbitals (MOs) of an isolated gas phase water molecule ($1b_1$, $3a_1$, $1b_2$).

The energetic stability of the 1U configuration is different in GGA and in GGA+U. Fig. 4.2 shows that within GGA, H_2O in 1U is strongly bound to the surface by -0.62 eV whereas with the inclusion of a Coulomb repulsion term the E_{ads} is nearly zero. A possible explanation for this discrepancy can be seen from the DOS plot shown in Fig. 4.5a and b for GGA and GGA+U, respectively. The main effects expected due to the interaction with the substrate are a shift of position and change in width of the molecular levels of the adsorbate [92, 93]. The broadening of electronic states as seen in DOS are a result of hybridisation and also reduces Pauli repulsion [94]. To estimate the effect of adsorption on the MOs of H_2O we have indicated the reference energy levels of an isolated gas phase H_2O molecule with vertical dotted lines. These are derived by aligning the $2a_1$ core energy level of the gas phase molecule with that of the adsorbed molecule [80, 95]. This procedure is followed throughout

the thesis wherever we compare the MOs and will not be explicitly mentioned elsewhere. If we now look at the GGA+ U DOS of O^w in Fig. 4.5b top panel, we find the MOs ($1b_1, 3a_1, 1b_2$) of the adsorbed water molecule are highly localized and retain their molecular character. Except for a slight shift of $3a_1$ to lower energy, the degree of hybridisation/interaction between $Fe_B(S)$ - $3d$ orbitals which spans from -8 eV to -6 eV and the $1b_1$ is quite low. This results in an almost vanishing absorption energy within GGA+ U . On the other hand the energetic stability of 1U within GGA comes from the strong hybridisation of $Fe_B(S)$ - $3d$ orbitals, which spans from -7 eV to Fermi level, with the $1b_1$ and $3a_1$ MOs. Fig. 4.5a (top panel) shows broadening and splitting of the $1b_1$ MO into bonding/antibonding states. Since $1b_1$ is close to the Fermi level, our calculation shows that it plays a major role in bonding and hence lower adsorption energy is obtained within GGA. Thus, the different position and width of the Fe_B - $3d$ band within GGA and GGA+ U determines whether or not there is the hybridisation with the $1b_1$ MO and results in different binding strength.

Considering the shape of the molecular orbitals of a water molecule as shown in Fig. 4.3, we realize that in the 1U configuration, the $1b_1$ molecular orbital cannot hybridize strongly with surface states. Using the same geometrical argument we can infer that in the 1F configuration, $1b_1$ and $3a_1$ can strongly interact with the Fe_B - $3d$ orbitals. This is clearly seen in Fig. 4.5a and b, where both the MOs ($1b_1, 3a_1$) are broadened and splitting into bonding/antibonding states takes place. This indicates stronger hybridisation. The water molecule prefers to adsorb in such a way so as to maximize the interaction of MOs with the cation $3d$ orbitals and in the present case the 1F configuration facilitates that. The preference by the H_2O molecule to adsorb in a flat/tilted orientation is also observed on many metal surfaces [34, 80] and in the case of NiO(100) [84]. At this point we can say that GGA+ U gives better description of the electronic structure than GGA.

1D-1 (One H_2O molecule in dissociated configuration): Next we discuss the dissociated case 1D-1. The energetic stability of 1D-1 also varies with and without the use of an on-site Coulomb repulsion term U . The difference in the E_{ads} is 0.07 eV. In 1D-1, two hydroxyl groups are created on the surface one from the OH group of the water molecule and the other one by the protonation of O(S). The former is named basic hydroxyl group OH_b due to its electronegative behavior and the latter one as acidic hydroxyl OH_a due to its electropositive behavior [96]. As mentioned in Section 2.6, the partially occupied 1π orbital of OH is the HOMO which participates in bonding together with the 3σ orbital. In general, the reaction of OH with a metal or metal oxide surface involves accumulation of charge in the 1π orbital [32] and simultaneous depletion of charge in the d_{z^2} orbital if a transition metal like Cu(110) [97] is involved. In fact we also observe the same but since the $3d$ -band of Fe is half filled unlike Cu where it is fully filled, we notice some back donation of charge from the OH group to the surface from DOS and electron density

redistribution plots. A similar scenario of charge donation (from the adsorbate to the surface) and charge back donation (from the surface to the adsorbate) for adsorbate molecules like CO on metal surface and H₂ on transition metal surface is discussed in literature [75, 89]. In our case the charge donation stabilises the system more than the back donation. This will be explained in the following.

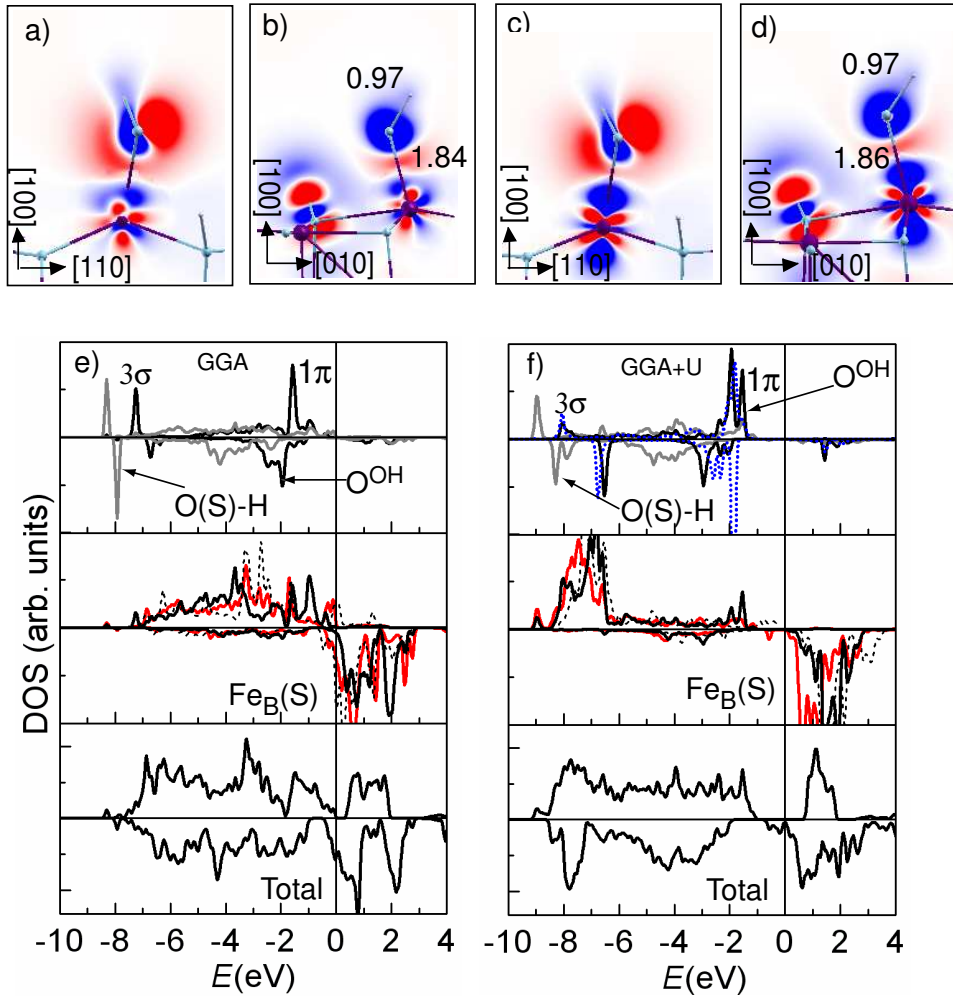


Figure 4.6: Electron density redistribution plots and density of states (DOS) for the dissociative adsorption (1D-1) of an isolated H₂O molecule within GGA (left panels) and GGA+U (right panels). In a) and b) $\Delta\rho$ is shown in a plane perpendicular to the surface, along the [110] direction, while c) and d) show a cut along the [010]-direction where both the OH group on top of a surface Fe_B and the protonated neighboring O(S) are visible. e) and f) contain the total and projected DOS, top panel: PDOS of oxygen of the OH group on top of Fe_B (black line) and that of O(S)-H (grey line), middle panel: PDOS of Fe_B-3d states with (solid black) and without (solid red line) an OH group on top and for comparison the PDOS of Fe_B on the clean Fe₃O₄(001) surface is shown with a dashed line, and finally the DOS of the total unit cell is shown in the bottom panel.

Fig. 4.6 a,b shows the electron density redistribution upon adsorption within GGA and c,d within GGA+ U . The most prominent difference between GGA and GGA+ U is observed at the $\text{Fe}_B(\text{S})$ sites where orbitals of different character (t_{2g} vs. d_{z^2}) are depleted. A stronger electron density redistribution is observed in the dissociated case than in the molecular case. Fig. 4.6c shows charge accumulation in the 1π orbital of OH group and depletion in d_{z^2} orbital confirms the charge back donation. On the other hand electron depletion in the 3σ -orbital of the OH group and weak accumulation in $d_{xz,yz}$ orbitals of $\text{Fe}_B(\text{S})$ confirms the charge donation mechanism. Fig. 4.6d shows charge accumulation in the 3σ -orbital of the $\text{O}_s\text{-H}$ group explaining its electropositive nature.

The density of states (DOS) in Fig. 4.6e and f within GGA and GGA+ U support the charge redistribution pattern. The DOS in the minority spin states show broad features for the MO of OH. This shows very weak hybridisation with the nearly vanishing $\text{Fe}_B(\text{S})\text{-}3d$ electronic states in the minority spin. The energy levels of these MOs are higher than their counterparts in the majority spin states and thus they can serve as reference levels to determine the extent of hybridisation in majority spin channel. The position and width of the $\text{Fe}_B\text{-}3d$ band is similar to the molecular adsorption case. Within GGA the strongest hybridisation occurs between -3 and -1 eV with the 1π -OH-states. As a result we notice bonding/antibonding splitting of both 1π and $\text{Fe}_B\text{-}3d$ states. Within GGA+ U , the $\text{Fe}_B\text{-}3d$ band splits into a lower Hubbard band and a upper Hubbard band due to the Coloumb repulsion term U as shown in Fig. 4.6f. The lower Hubbard band hybridizes mainly with the 3σ -orbital, which now shows a much stronger bonding/antibonding splitting than within GGA. If we consider the extent of hybridisation of $\text{Fe}_B(\text{S})(3d)\text{-OH}(\text{MOs})$ along with the difference in E_{ads} between GGA and GGA+ U , we realise that the 1π orbital does not play a significant role in bonding. On the other hand the extent of hybridisation of the 3σ -orbital with that of the $\text{Fe}_B\text{-}3d$ -band, which represents charge donation, determines the stability of dissociated configuration, which is more in the case of GGA+ U thus lowering the E_{ads} than within GGA.

We also notice a shift of $\text{Fe}_B(\text{S})\text{-}3d$ band to lower energy when compared to the clean surface in both approximations. The 3σ peaks of the $\text{O}(\text{S})\text{-H}$ are lower in energy than in OH and the 1π peak is quite broad. Fig. 4.6f top panel also highlights the change in DOS with $\angle\text{Fe}_B(\text{S})\text{-O}^{\text{OH}}\text{-H}$. The blue curve represents the $\angle\text{Fe}_B(\text{S})\text{-O}^{\text{OH}}\text{-H}$ of 130.1° and black with that of 120.9° . We notice splitting of the 1π peak in the majority spin channel whereas the energy of 3σ largely remains the same. With decreasing angle the $\text{O}^{\text{OH}}\text{-H}(\text{O}(\text{S})\text{-H})$ bond length is elongated thereby reducing their interaction. Hence interaction of 1π orbital with the substrate leads to peak splitting. The peak splitting is discussed in detail in Chapter 6. This change in the structure lowers the E_{ads} by 0.23 eV. The details of the interaction of O^{OH} and $\text{O}(\text{S})\text{-H}$ were discussed in the previous Section. We also notice from the Fig. 4.6f that dissociative mode of adsorption leads to a half metallic character within GGA+ U . In the

case of dissociated configuration, electronic structure is well described within GGA+ U than within GGA.

In this Section we realize that different position and width of the Fe^{3+} - $3d$ band within GGA and GGA+ U leads to a hybridisation with different types of orbitals of the adsorbate species thus resulting in different binding strength.

Tilt angle and energetic stability

The adsorption energy shows a strong dependence on the tilt angle α defined in Section 4.1. We have varied the angle $\angle\text{Fe}_B(\text{S})\text{-O}^w\text{-H}$ from -30° to 90° and found a tilt angle α of $11 - 12^\circ$ minimising the energy. We have noticed that within GGA+ U the total energy is more sensitive to the variation in tilt angle e.g a change of 0.27 eV in the total energy is found with α changing by 2° . Another parameter is the angle θ between $\angle\text{H-O}^w\text{-H}$ which in a gas phase molecule has a value of 104.5° . In the case of 1F it changes to 105.6° and 106.5° within GGA and GGA+ U , respectively. A similar increase ($\angle\text{H-O}^w\text{-H}$) is also observed in the case of NiO(100) [84] and for some metal surfaces [80]. In the case of 1U configuration the angle θ expands further to a value of 110.5° and 111.25° .

4.3 Structural properties

In this Section we will discuss the structural changes induced by water adsorption. These changes can be correlated to the electronic structure described in the previous Section. Table 4.1 and 4.2 list all the relaxations in the adsorbate and the surface layer and Fig. 4.7 shows a top view of the surface B-layer. The

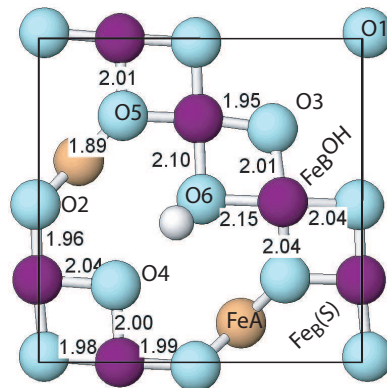


Figure 4.7: Top view of the surface B-layer from 1D-1 is shown along with all its lateral bond lengths. This schematic view marks all the surface atoms. The bond lengths are given in Å.

results discussed in this Section are obtained within GGA+ U while wherever needed GGA values are explicitly mentioned and compared.

1U and 1F (One H_2O molecule upright and flat/tilted configuration): Fig. 4.8 left and right panels show the side view of 1U and 1F respectively along with some characteristic bond lengths. Table 4.1 lists all the surface relaxations. The $\text{Fe}_B^{\text{H}_2\text{O}}$ in 1U relaxes towards the surface while in 1F it relaxes outwards. The magnitude of Δz is quite small (~ 0.05 Å) and in addition there is no lateral relaxation. The $\text{Fe}_B(\text{S})$ sites with no adsorbates on top relax towards the surface as seen also in the case of clean surface [27]. The sign of Δz is a further sign of the extent of hybridisation of H_2O with $\text{Fe}_B(\text{S})$. This can be seen in the case of 1U where Δz of $\text{Fe}_B^{\text{H}_2\text{O}}$ and $\text{Fe}_B(\text{S})$ is

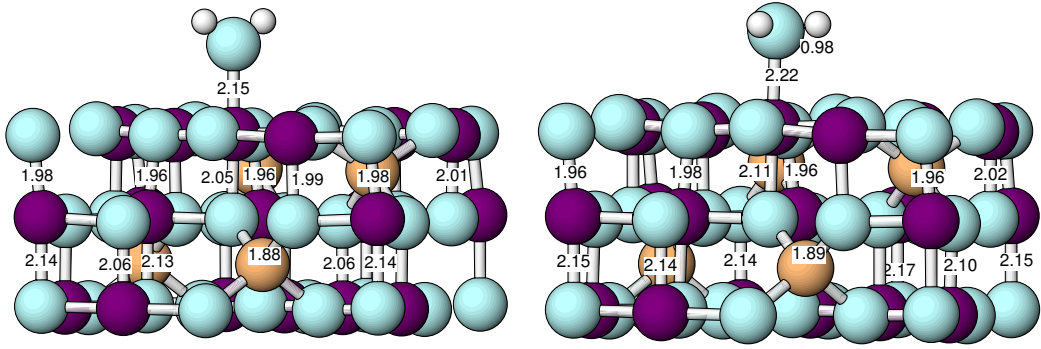


Figure 4.8: Side view of the relaxed 1U (left panel) and 1F (right panel) along with surface and sub-surface bond lengths. All bond lengths are given in Å and are obtained within GGA+ U .

Table 4.1: Atomic relaxations of the surface layer obtained within GGA+ U in the case of 1U and 1F are listed. The values in the parenthesis are obtained within GGA. The Δz values typically represent relaxation along the surface normal, negative values indicate an outward while the positive means inward relaxation. The numbering of the atom corresponds to those shown in Fig. 10.1. All distances are in Å.

	1U			1F		
	Δx	Δy	Δz	Δx	Δy	Δz
$\text{Fe}_A(\text{S})$	-0.01 (-0.01)	-0.00 (0.00)	-0.12 (-0.10)	0.00 (-0.01)	-0.02 (0.00)	-0.18 (-0.13)
O1	-0.10 (-0.20)	-0.08 (-0.08)	0.02 (0.01)	-0.09 (-0.21)	-0.09 (-0.09)	0.03 (0.00)
O2	0.04 (0.03)	0.07 (0.07)	0.05 (0.07)	0.05 (0.02)	0.06 (0.08)	-0.03 (0.03)
O3	0.11 (0.22)	0.06 (0.05)	0.05 (0.04)	0.11 (0.22)	0.08 (0.05)	0.02 (0.02)
O4	0.08 (0.08)	0.10 (0.21)	0.02 (0.02)	0.10 (0.08)	0.10 (0.20)	-0.03 (0.02)
O5	-0.07 (-0.07)	-0.04 (-0.03)	0.05 (0.07)	-0.08 (-0.08)	-0.04 (-0.02)	-0.08 (0.02)
O6	-0.06 (-0.05)	-0.11 (-0.22)	0.05 (0.04)	-0.07 (-0.04)	-0.09 (-0.22)	0.01 (0.02)
$\text{Fe}_B^{\text{H}_2\text{O}}$	-0.00 (-0.03)	0.01 (0.03)	0.04 (0.07)	0.01 (-0.01)	0.01 (0.01)	-0.05 (0.01)
$\text{Fe}_B(\text{S})$	0.00 (0.03)	-0.01 (-0.03)	0.11 (0.13)	0.00 (0.02)	-0.02 (-0.03)	0.08 (0.14)
$\text{O}^{\text{H}_2\text{O}}$	0.00 (0.00)	0.00 (0.00)	-0.10 (-0.08)	-0.09 (-0.10)	0.09 (0.10)	-0.26(-0.24)

positive indicating a weak binding which is consistent with the adsorption energies. The O^w in both the cases (1U and 1F) relaxes away from the surface but in 1F it is stronger by 0.14 Å. Unlike on top adsorption in 1U, we notice some lateral relaxation in 1F. The bond length $d_{\text{Fe}_B(\text{S})-\text{O}^w}$ is 2.16 Å in 1U and 2.22 Å in 1F. For comparison bulk $d_{\text{Fe}_B-\text{O}}$ is 2.06 Å. This shows that even though the H_2O molecule provides the missing coordination to the $\text{Fe}_B(\text{S})$ sites still it can only bind weakly. The other possible indicator to assess the bonding strength is the change occurring in the subsurface bond lengths. In the case of 1U the subsurface $d_{\text{Fe}_B-\text{O}}$ is unchanged while in 1F it is stretched by 0.06 Å, which coincides with the fact that E_{ads} of 1U is near zero and that of 1F is -0.40 eV. In the case of 1U, all the $\text{O}(\text{S})$ relax towards the subsurface layer which is consistent with the results obtained for the clean surface [26,27]. A slight deviation in the relaxation pattern occurs for 1F as evident from the Table 4.1 where some of the oxygen atoms relax outwards rather than inwards. Overall, the bond lengths ($d_{\text{Fe}_B-\text{O}}$) between the S and S-1 layer are contracted to 1.94-2.02 Å (except the adsorbed sites) while some of those between S-1 and S-2 expand to 2.07-2.14 Å when compared to the bulk distance of 2.06 Å. This trend is similar for 1F, 1U and the clean surface with variations in the magnitude. The $\text{Fe}_A(\text{S})$ layer relaxes outwards as seen from some bonds being elongated but without any lateral relaxation.

Within GGA, largely direction of relaxations are similar while the values might differ from those within GGA+ U . The GGA bond lengths of $d_{\text{Fe}_B(\text{S})-\text{O}^w}$ in the case of $\text{Fe}_2\text{O}_3(0001)$ [85] for 1U and 1F is 2.17 and 2.22 Å respectively. These values are quite close to our GGA results of 2.15 and 2.19 Å.

1D-1 (One H_2O molecule in dissociated configuration): The relaxations are listed in Table 4.2. Fig. 4.7 shows the top view of the surface layer together with lateral bond lengths. Additionally Fig. 4.9 right panel shows the side view with selected bond lengths. In this case Fe_B^{OH} and O^{OH} exhibit strong outward relaxations of 0.53 Å and 0.36 Å respectively. This is consistent with the strong electron density redistribution pattern (Fig. 4.6a,b). The magnitude of

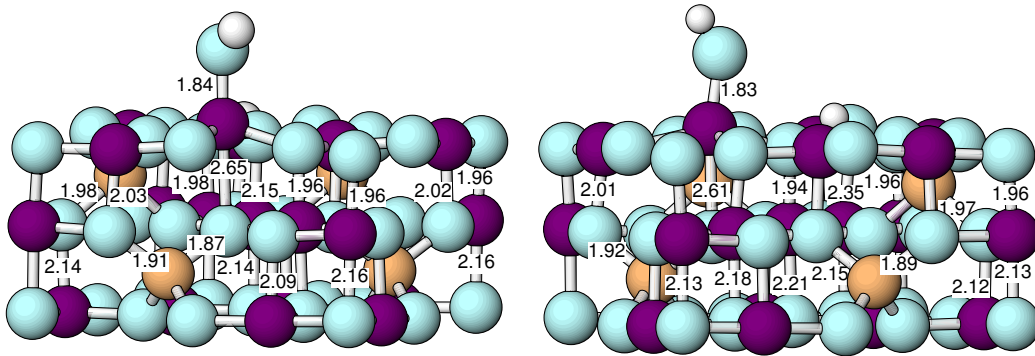


Figure 4.9: Side view of the relaxed 1D-1 (left panel) and 1D-2 (right panel) along with surface and sub-surface bond lengths. All bond lengths are given in Å and are obtained within GGA+ U .

Table 4.2: Atomic relaxations of the surface layer obtained within GGA+U in the case of 1D-1 is listed. The values in the parenthesis belong to the case of GGA. The Δz values typically represent relaxation along the surface normal, negative values indicate an outward while the positive means inward relaxation. The numbering of the atom corresponds to those shown in Fig. 10.1. All distances are in Å.

	1D-1		
	Δx	Δy	Δz
Fe _A (S)	0.03 (-0.02)	-0.00 (-0.01)	-0.19 (-0.10)
O1	-0.11 (-0.08)	-0.10 (-0.17)	0.02 (0.04)
O2	0.06 (-0.01)	0.09 (0.14)	-0.06 (0.07)
O3	0.19 (0.06)	0.19 (0.13)	-0.00 (0.10)
O4	0.07 (0.19)	0.06 (0.09)	0.01 (0.04)
O5	-0.06 (-0.16)	-0.04 (-0.06)	-0.02 (0.07)
O6	0.00 (-0.15)	0.01 (-0.07)	-0.16 (-0.06)
Fe _B ^{H₂O}	0.04 (-0.07)	-0.03 (-0.16)	-0.53 (-0.31)
Fe _B (S)	0.01 (-0.01)	-0.00 (0.01)	0.05 (0.12)
O ^{OH}	0.07 (-0.01)	-0.01 (0.31)	-0.36 (-0.08)

relaxation is very high when compared to Fe_B^{H₂O} of 1U and 1F by ~ 0.47 Å. The O^{OH} relaxes 0.1 Å more when compared to O^w in 1F forming a bond length of 1.84 Å for $d_{\text{Fe}_B(\text{S})-\text{O}^{\text{OH}}}$. The reason behind the large outward relaxation of Fe_B^{OH} is the electronegative nature of the OH group which attracts charge from the Fe_B(S) underneath thereby pulling it upwards. This huge upward shift of the Fe_B^{OH} elongates the sub-surface $d_{\text{Fe}_B-\text{O}}$ to 2.65 Å which is 0.5 Å longer than the bulk value of 2.06 Å. The lateral relaxation of Fe_B^{OH} and O^{OH} is negligible indicating an on-top adsorption. The H atom which sits on an adjacent O(S) tilts nearly parallel to the surface as shown in Fig. 4.7 and points towards an opposite O(S). The hydrogen bond between O(S)-H \cdots O(S) contributes to the stability of this termination. The O(S)-H actually induces a lateral elongation to the $d_{\text{Fe}_B-\text{O}}$ as shown in Fig. 4.7. It also elongates the subsurface bond with Fe_B(S-1) to 2.15 Å. Consistent with the observation in 1F and 1U, in 1D-1 also we find that the bonds between S and S-1 layer contract (except the adsorbed sites) and those between S-1 and S-2 layer expand. The relaxation of the other O(S) sites is small. We also see that the Fe_A(S) layer relaxes outwards.

The difference in surface relaxations between GGA and GGA+U is quite small in the case of O(S) except for the adsorbed sites. This difference is more visible in the case of Fe_B(S) and Fe_B^{OH} (Table 4.2). The $d_{\text{Fe}_B(\text{S})-\text{O}^{\text{OH}}}$ remains the same (1.84 Å), however, it is 0.05 Å higher than in the case of 1D-OH (Fig 4.10 right panel). Similar values are found in the case of Fe₃O₄(111) surface [86]

where the $d_{\text{Fe}_B(\text{S})-\text{O}^{\text{OH}}}$ is 1.83 Å within GGA+ U . The same value was obtained for $\text{Fe}_2\text{O}_3(0001)$ surface [85] within GGA.

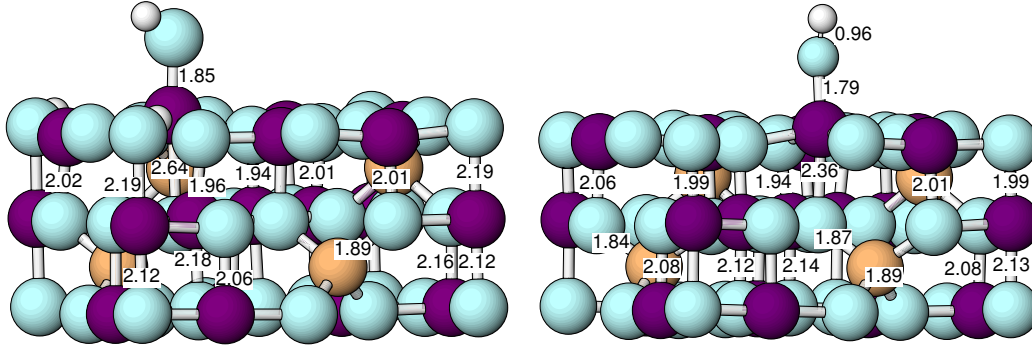


Figure 4.10: Side view of the relaxed 1D-3 (left panel) and 1D-OH (right panel) along with surface and sub-surface bond lengths. All bond lengths are given in Å. The 1D-3 shows results within GGA+ U while the 1D-OH shows from within GGA

Finally we discuss the changes induced with the adsorption of H atom at different sites (T2,T3). Fig 4.9 right panel shows the side view of 1D-2 and Fig 4.10 left panel shows that of 1D-3. The $d_{\text{Fe}_B(\text{S})-\text{O}^{\text{OH}}}$ remains within 0.02 Å compared to the corresponding distance in 1D-1. The difference is seen around the protonated O(S) site: In the case of 1D-2 the subsurface $d_{\text{Fe}_B-\text{O}}$ is 0.20 Å longer than in 1D-1 and 0.17 Å longer than in 1D-3. This means that O(S) at the T2 site is more reactive. We also notice a tilt of the $\text{Fe}_B(\text{S})-\text{O}^{\text{OH}}$ bond towards the surface and has an angle $\Theta_{\text{Fe}-\text{O}^{\text{OH}}-\text{H}}$ of 120.9°, 140.9° and 122.1° in the case of 1D-1, 1D-2 and 1D-3 respectively. This indicates that H of the O^{OH} group does not prefer to sit on top the $\text{Fe}_B(\text{S})$ and has some interaction with the substrate. In the case of 1D-OH we obtain an angle of 160.5°. This suggests that the extra H on the surface electrostatically attract the OH thereby decreasing $\Theta_{\text{Fe}-\text{O}^{\text{OH}}-\text{H}}$ as has been discussed in Section 4.1.

4.4 Summary

In this Chapter we have studied the adsorption of an isolated H_2O molecule on the $\text{Fe}_3\text{O}_4(001)$ surface. We have adsorbed the H_2O molecule in various adsorbate geometries. The dissociative mode of adsorption was the most favorable within GGA+ U . The heterolytic way of dissociation is preferred forming OH^- and H^+ wherein the OH adsorbs on top of $\text{Fe}_B(\text{S})$ while the H atom has an equal probability to adsorb at any adjacent or distant O(S) site. The hybridisation of the 3σ orbital of OH with the $\text{Fe}_B(\text{S})-3d$ band, along with a hydrogen bond formation between $\text{O}(\text{S})-\text{H}\cdots\text{O}(\text{S})$ contributes to the stability of the dissociated configuration. The bulk bond length $d_{\text{Fe}_B-\text{O}}$ has a value of 2.06 Å while the oxygen of molecular water (O^{w}) adsorbs at height of 2.15 Å

(1U) and at 2.22 Å (1F), and that of OH group (O^{OH}) adsorbs at a height of 1.84 Å. These differences in the bond lengths w.r.t to the Fe-O bulk bond length clearly indicates weak bonding in the case of O^w and strong ones in the case of O^{OH} . The nature of interaction between the adsorbed OH and $H^{O(S)-H}$ is attractive and influences the structural properties. The lifting up of the 1π orbital degeneracy is related to the tilt angle $\angle Fe_B(S)-O^{OH}-H$. We observe a general trend of bond contraction between S and S-1 layers whereas bond elongation occurs between S-1 and S-2 layers. We note that in this coverage regime we have discrepancy, GGA favors 1F while GGA+ U favors 1D-1. This discrepancy arises due to strong hybridisation within GGA between $1b_1$ MO of H_2O molecule and Fe- $3d$ band. Overall we find that different position and width of the Fe^{3+} - $3d$ band within GGA and GGA+ U leads to a hybridisation with different types of orbitals of the adsorbate species thus resulting in different binding strength.

Adsorption on a Defective Surface

In this Chapter we study the influence of defects on the surface and its electronic structure as well as on the adsorption of water molecules. Defects are often related to many important material properties [98]. The most common type are point defects. These can affect the chemical reactivity of the surface. The point defect which we are considering on the surface is an oxygen vacancy. Anion vacancy site acts as a Lewis acid [99], which lead to the formation of energetically favorable binding sites for adsorption of molecules like water [33]. Dissociation of a water molecule can occur at an ideal and on a defective surface but the latter has a more pronounced effect. For example, in the case of $\text{TiO}_2(110)$ [100], the initial dissociation of water molecules is attributed to oxygen vacancies. Atomistic level calculations are necessary to gain understanding for the description of a vacancy and its effects. In this Chapter we determine the vacancy formation energy in Section 5.1, before presenting the different adsorption models and their stability on the basis of E_{ads} in Section 5.2. In Section 5.3 we interpret the energetic trends based on the electronic structure change upon vacancy formation and subsequent water adsorption. These are also correlated to changes in the structural details as discussed in Section 5.4.

5.1 Formation of a F-center

We are considering only a F-center defect, i.e., a neutral oxygen vacancy (V_{O}) which is created by removing one of the surface oxygens in a lateral $(\sqrt{2} \times \sqrt{2})R45^\circ$ -unit cell. This results in a vacancy concentration of about $\sim 12.5\%$. As discussed in Chapter 3, we have two surfaces in the slab, which means two oxygen vacancies per $(\sqrt{2} \times \sqrt{2})R45^\circ$ -unit cell, ensuring that no artificial dipole is created. The defects are 8.41 \AA away from each other, thus vacancy-vacancy interaction is negligible. We will henceforth refer to this defective $\text{Fe}_3\text{O}_4(001)$ surface as $\text{B}+V_{\text{O}}$. The formation energy of one V_{O} per $(\sqrt{2} \times$

$\sqrt{2})R45^\circ$ -unit cell can be calculated w.r.t O atom as:

$$E_f^O = E_{\text{Fe}_3\text{O}_4(001)-\text{V}_O} + E_O - E_{\text{Fe}_3\text{O}_4(001)} \quad (5.1)$$

or to O_2 as:

$$E_f^{\frac{1}{2}\text{O}_2} = E_{\text{Fe}_3\text{O}_4(001)-\text{V}_O} + \frac{1}{2}E_{\text{O}_2} - E_{\text{Fe}_3\text{O}_4(001)}, \quad (5.2)$$

where $E_{\text{Fe}_3\text{O}_4(001)-\text{V}_O}$ and $E_{\text{Fe}_3\text{O}_4(001)}$ are the total energies of the $\text{Fe}_3\text{O}_4(001)$ surface with and without an oxygen vacancy. E_{O_2} and E_O are the energies of a gas-phase oxygen atom and molecule, respectively. A positive value for the vacancy formation energy means it is endothermic (i.e. it costs energy to create a vacancy). The E_{O_2} molecule energetics is described in appendix A.

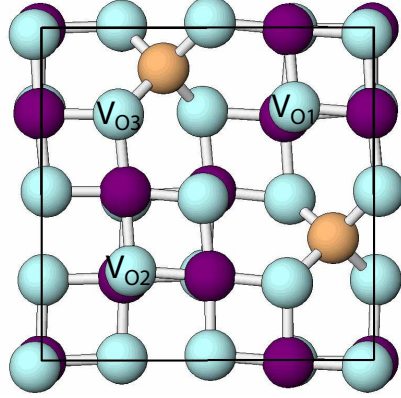


Figure 5.1: Top view of modified B-layer with three different surface oxygen sites considered for creating a vacancy. Positions of oxygen, Fe_B , Fe_A are marked by cyan, purple and orange respectively.

We consider three different oxygen surface sites (O(S)) to create a vacancy. The sites are named as V_{O1} , V_{O2} , V_{O3} and are shown in Fig. 5.1. The total energy of $\text{B}+\text{V}_{\text{O1}}$ and $\text{B}+\text{V}_{\text{O2}}$ are nearly degenerate while that of V_{O3} is significantly higher by 2.16 eV. V_{O3} site has high coordination number which implies more bonds need to be broken to create a vacancy hence higher formation energy. In $\text{B}+\text{V}_{\text{O1}}$, we find that the formation energy $E_f^{\frac{1}{2}\text{O}_2}$ is 0.8 eV higher within GGA+ U (2.47 eV) than within GGA (1.67 eV). If we calculate the same formation energy w.r.t an oxygen atom E_f^O we get 4.78 eV within GGA and 5.58 eV within GGA+ U . An even larger difference between the GGA and GGA+ U results was found for $\text{TiO}_2(110)$ ($\sim 1.5\text{eV}$) [101]. This variation in the formation energy is attributed to the overbinding effect of GGA [102, 103], to the different degree of localisation of the electronic charge around the V_O and to the difference in the structural relaxations. The formation energy in our case is comparable to other metal oxides surfaces [104, 105]. For example, the vacancy formation energy E_f^O (GGA : 4.78 eV) on $\text{Fe}_3\text{O}_4(001)$ is near to the

value obtained for $\text{Fe}_2\text{O}_3(0001)$ ($\sim 4.2\text{eV}$) [104]. E_f^{O} varies from 4 to 10 eV in the case of TiO_2 [105] and MgO [106].

5.2 Adsorption models and energetic stability

To determine the mode of adsorption we have considered a variety of adsorption models. Fig. 5.2 shows the top view of the adsorption models and their respective adsorption energies. The stability of each configuration is discussed based on the E_{ads} per molecule. Molecular adsorption was modeled by adsorbing a water molecule in a $1F_V$ configuration. In this configuration, the tilt angle α is 0° i.e. the molecule is parallel to the surface and the H atoms point towards O(S). The dissociated configuration $1D_V-1$ is modeled by adsorbing an OH group in the vacancy site V_{O} and a H atom on a nearby O(S). The possibility of the H atom to adsorb at a distant O(S) site is also taken into account by choosing three distinct O(S) sites, namely H1, H2, and H3 as shown in Fig. 5.2. This leads to three different dissociative configurations $1D_V-1$, $1D_V-2$ and $1D_V-3$, respectively.

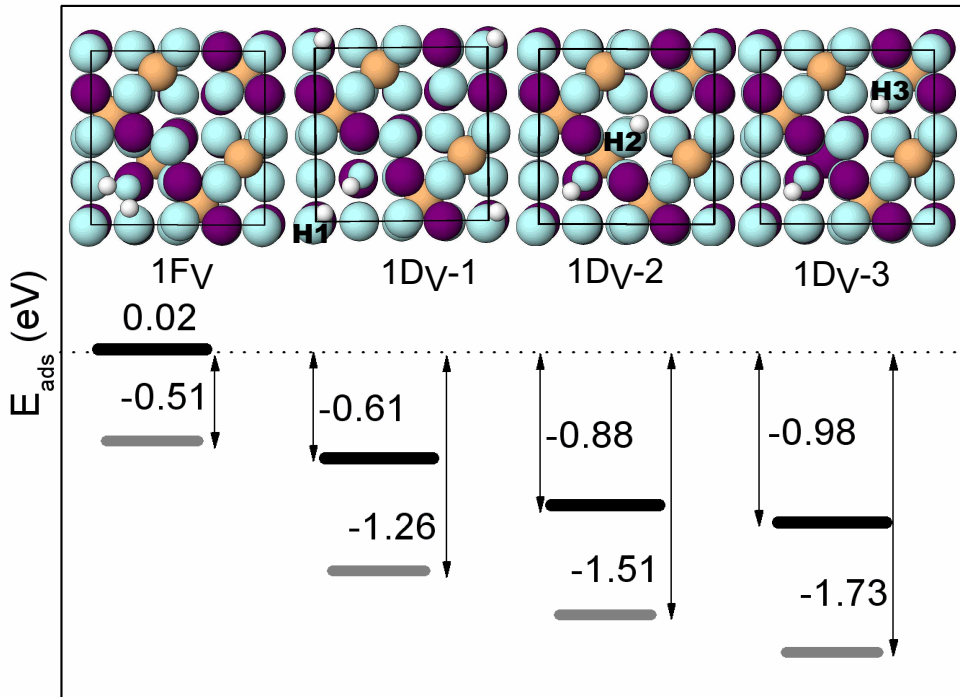


Figure 5.2: Top view of different adsorbate geometries considered for a single water molecule adsorbed in an oxygen vacancy on the $\text{Fe}_3\text{O}_4(001)$ surface. The GGA (GGA+U) adsorption energies (in eV per molecule) are given by a black (grey) line. In the case of dissociative adsorption, three different O(S) sites are indicated where diffusion of a H atom is considered: H1, H2 and H3

GGA: Within GGA the molecular adsorption $1F_V$ is unfavorable with a nearly vanishing E_{ads} . The dissociative mode of adsorption is the most favored. $1D_V-1$ is preferred over $1F_V$ by 0.59 eV. Interestingly, the adsorption of a H atom to a distant O(S) site is more favorable on a defective surface than on an ideal surface, as discussed in Section 4.1. The adsorption of H at H2 site ($1D_V-2$) is 0.27 eV more favorable than $1D_V-1$. The H3 site ($1D_V-3$ configuration) turns out to be the most stable one with an E_{ads} of -0.98 eV. This implies that the vacancy is a stronger binding site for the OH group and can promote dissociation of the H_2O molecule. E_{ads} for the dissociative adsorption is found to be 0.1 eV lower on defective $\text{Fe}_2\text{O}_3(0001)$ [104] surface than in the present case.

GGA+U: We also investigate the effect of an on-site Coulomb interaction term on this system and its stability. We notice that the dissociative mode of adsorption is also favorable within GGA+U. The molecular adsorption $1F_V$ is having an appreciable E_{ads} of -0.51 eV. At this point it is quite interesting to note that $1F_V$ has vanishing E_{ads} within GGA. We will discuss this variation in the next Section. The E_{ads} i.e. $1D_V - 3 < 1D_V - 2 < 1D_V - 1 < 1F_V$ retains its order in both approximations but the magnitude of E_{ads} varies between 0.49 and 0.75 eV when compared to GGA as shown in Fig. 5.2. In fact, the $1D_V-3$ configuration with an E_{ads} of -1.73 eV now shows much stronger binding and affinity to bind and dissociate the water molecule than within GGA. The comparison of adsorption energies of $1D_V-3$ and $1D-1$, within GGA+U, shows a variation of -1.0 eV. This is possibly the reason for the initial filling of all the vacancy sites during water adsorption as shown in the XPS studies [37].

5.3 Analysis of the electronic structure

In order to understand the variations and trends of the E_{ads} we analyze the electronic structure through the density of states (DOS) and the redistribution of electron density upon adsorption. We start the discussion with the vacancy induced changes in the electronic structure. The charge created by the vacancy tends to localize primarily at the surface or subsurface sites and in particular neighboring cation sites are preferred. This results in a change in the oxidation state of the transition metal oxide cations.

B+V_{O1} (B layer with an oxygen vacancy): We have analyzed the electronic structure before and after vacancy creation through DOS as shown in Fig.5.3c within GGA+U. A careful look at the bottom panel showing the total DOS reveals a narrow peak from -0.1 eV to E_F (will be referred as peak 2) and another peak at -0.75 eV (will be referred as peak 1) in the minority spin states. The peaks are separated by ~ 0.6 eV. The projected density of states (PDOS) shows that the former peak has $3d$ character originating from the bulk and the latter one has $3d$ states exclusively from $\text{Fe}_B(\text{S}-1)$ and $\text{Fe}_B^*(\text{S}-1)$ sites as shown in Fig. 5.3b,c. It is important to note that $\text{Fe}_B^*(\text{S}-1)$ is the

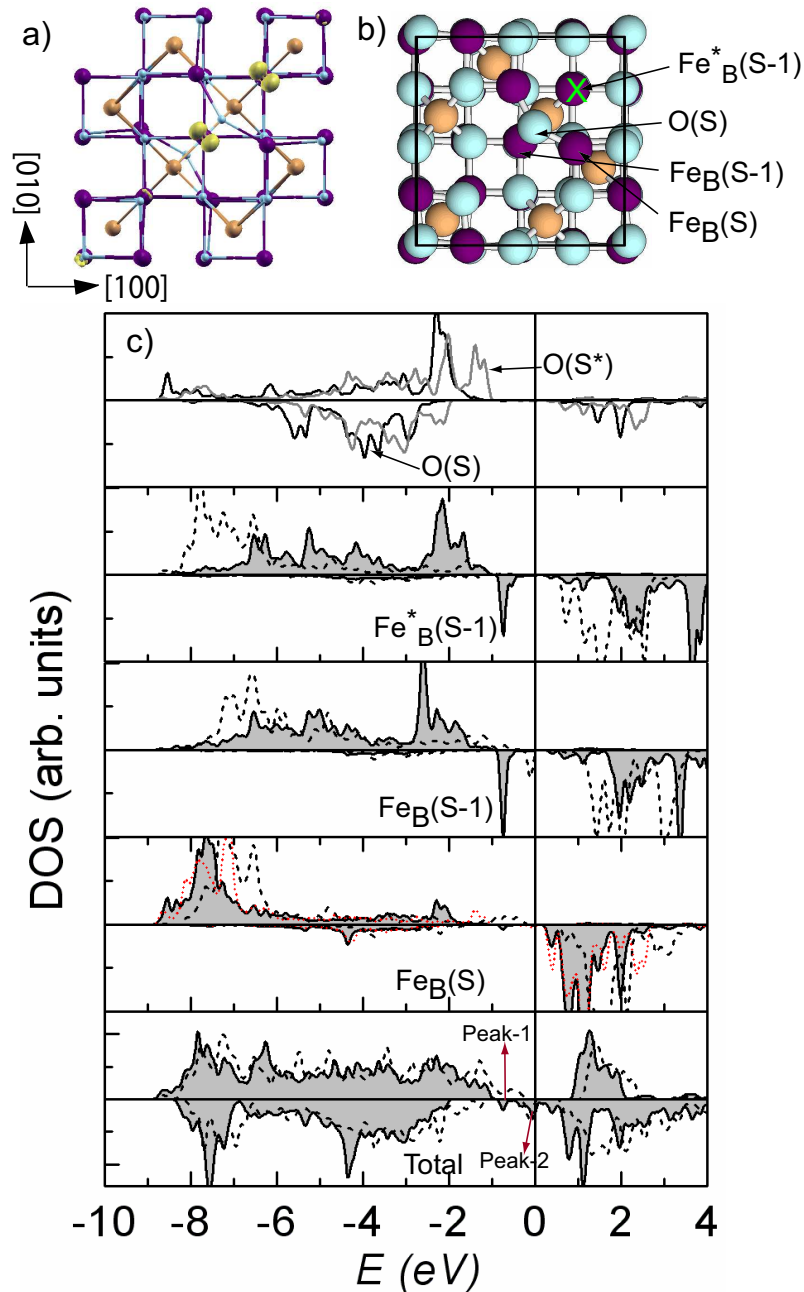


Figure 5.3: Top view of $B+V_\text{O}$ termination along with charge density and density of states within $GGA+U$. a) Charge density integrated from -1.2 eV to E_F for the sub-surface layer b) Top view indicating all the surface and sub-surface atom labels, the green cross marks the V_O site c) Density of states for $B+V_\text{O}$ (B-clean) in solid black line (black dashed line) : PDOS of $\text{O}(\text{S})$ (top panel), PDOS of $\text{Fe}_B(\text{S}-1)^*$ (top-1 panel), PDOS of $\text{Fe}_B(\text{S}-1)$ (top-2 panel), PDOS of $\text{Fe}_B(\text{S})$ (top-3 panel) where red dotted line are from the $\text{Fe}_B(\text{S})$ which are away from the V_O , total DOS is shown in bottom panel along with the peak-1 and peak-2 marked.

site beneath the oxygen vacancy and $\text{Fe}_B(\text{S-1})$ is the neighboring site. To get a qualitative picture we compare the DOS of the defective surface (solid line) with that of the clean surface (without defects: dashed lines) as shown in Fig. 5.3c. The PDOS of $\text{Fe}_B(\text{S-1})$ and $\text{Fe}_B^*(\text{S-1})$ shows a sharp localised feature in the minority spin states of the defective surface which is absent in the clean surface. This suggests a change in the oxidation state of both $\text{Fe}_B(\text{S-1})$ and $\text{Fe}_B^*(\text{S-1})$ from Fe^{3+} to Fe^{2+} upon vacancy creation. The peak 2 in the case of a clean surface contains Fe^{2+} $3d$ states from subsurface and bulk layers whereas in the case of defective surface it contains just the contribution from the bulk layer. The Fe^{2+} $3d$ states of the subsurface layer in the case of defective surface forms a peak 1 which is ~ 0.6 eV lower than peak 2. In order to get a better insight we integrated the charge density in the minority spin between -1.2 eV to E_F for the sub-surface layer as shown in Fig. 5.3a. We find charge localisation around $\text{Fe}_B(\text{S-1})$ and $\text{Fe}_B^*(\text{S-1})$ in the $d_{xz} \pm d_{yz}$ orbitals. The orbital orientation and charge ordering further will be discussed in Chapter 9. The exclusive contribution to the peak 1 comes from $\text{Fe}_B(\text{S-1})$ and $\text{Fe}_B^*(\text{S-1})$ which are near to the vacancy. In addition the top two B layers in both clean and defective surface were fully relaxed, confirming the charge localisation as discussed. However, we note that structural relaxations can also lead to peak splitting.

The other interesting feature is the relaxation of the O(S), as shown in the Fig. 5.3b. O(S) opposite to the vacancy relaxes towards the Fe_B row to compensate the under-coordination created by oxygen vacancy by $\sim 0.80 \text{ \AA}$. This is reflected in the shifting of the O- $2p$ band to a lower energy when compared to other surface oxygens. The $\text{Fe}_B(\text{S})$ are always in Fe^{3+} state and shift towards lower energy with the creation of oxygen vacancy.

1F_V (Single H₂O molecule adsorbed in the oxygen vacancy site in a flat orientation): Next we address the variation observed in the E_{ads} of 1F_V within GGA and GGA+ U . Additionally to get a better understanding, comparison is made between 1F_V and 1F from Section 4.2. Since both 1F and 1F_V are molecular adsorption, we base our discussion on the MOs of the H₂O molecule. Fig. 5.4a,b shows the total DOS and PDOS for the case of 1F_V and 1F within GGA and GGA+ U , respectively. In 1F_V, within GGA, the majority of $\text{Fe}_B(\text{S-1})$ - $3d$ states lie in the range of -4 eV to E_F . This minimises the degree of hybridisation between Fe_B - $3d$ states and the $1b_1$ and $3a_1$ MOs thus leading to a zero E_{ads} . In the case of GGA+ U the $\text{Fe}_B(\text{S-1})$ being a Fe^{2+} has a broad distribution of DOS unlike $\text{Fe}_B(\text{S})$. This enables a greater extent of hybridisation and hence a non-zero E_{ads} . The projected DOS of O^w in 1F_V and 1F within GGA+ U shows energy shifts in the MOs of water (the reference levels are as shown in Fig.4.5). The $1b_1$, which remains almost like a MO in 1F, now shows bonding/antibonding splitting for 1F_V with the antibonding states moving towards the Fermi level. This interaction is definitely preferred. However, the $3a_1$ level almost remains the same with a small shift towards the lower energy. The $1b_2$ level slightly shifts towards higher energy but essentially

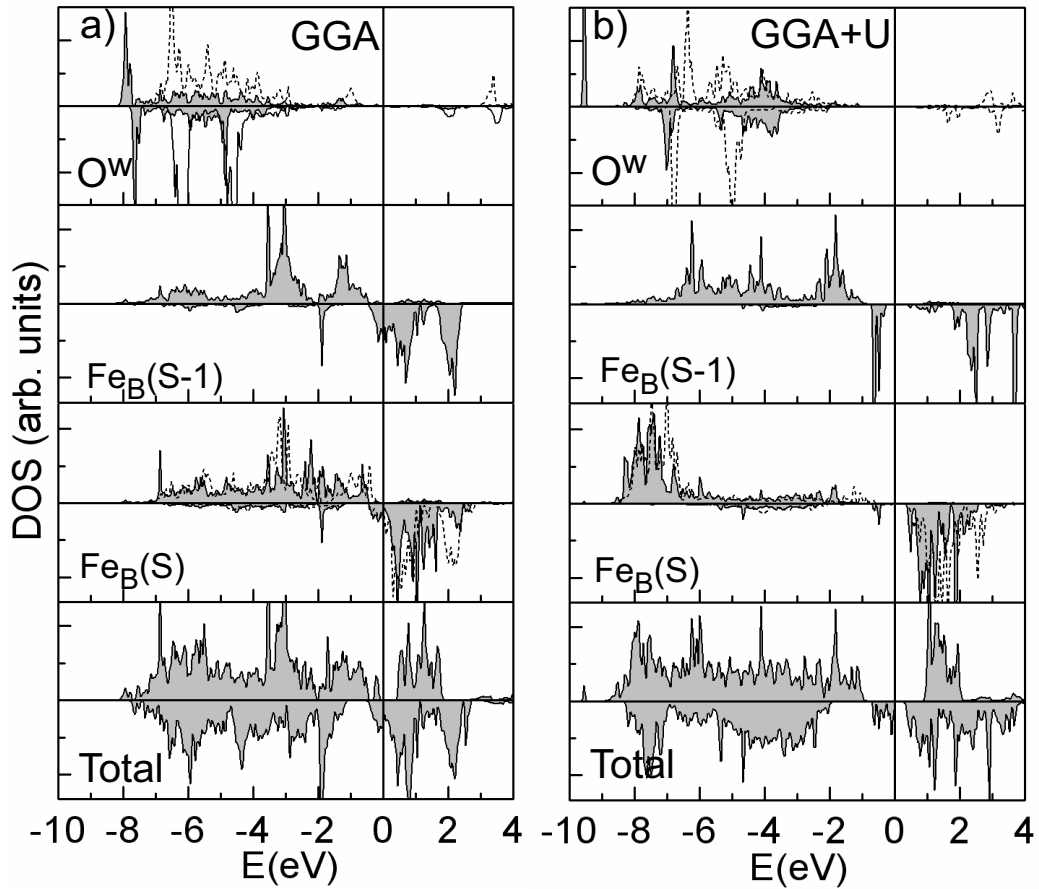


Figure 5.4: Density of states in the case of $1F_V$ ($1F$) shown with black line (black dashed lines) within GGA (a) and GGA+U (b). Top panel: PDOS of O^w , Top panel-1: PDOS of $Fe_B(S-1)$, Top panel-2: PDOS of $Fe_B(S)$, Bottom panel: total DOS

remains as a molecular level. These factors lead $d_{Fe_B(S-1)-O^w}$ to 2.63 \AA which is 0.57 \AA higher than the bulk distance and subsequently the E_{ads} for $1F_V$ is 0.12 eV/Mol higher than that in $1F$. A weak interaction of O^w with $Fe_B(S)$ results in a $d_{Fe_B(S)-O^w}$ of 2.75 \AA laterally. The elongated bond lengths are also due to the coordination number of O^w which is higher in $1F_V$ than in $1F$.

1D_V-3 (One H_2O molecule dissociated in an oxygen vacancy and H adsorbs at H3 O(S) site): Since the dissociation of H_2O molecules is more favored at defect sites, we will discuss the electronic structure of $1D_V-3$ within GGA+U. A strong charge density redistribution is observed upon adsorption in the case of $1D_V-3$ as shown in Fig. 5.5a,b. The hydroxyl group in the vacancy ($V_O + OH$) shows an accumulation in the 1π orbital and depletion in the 3σ orbital, whereas in the case of protonated surface oxygen (O(S)-H) the 3σ orbital shows charge accumulation. A similar pattern of accumulation/depletion of OH MOs is observed in the case of $1D-1$ (Section 4.2). We also notice that both the OH

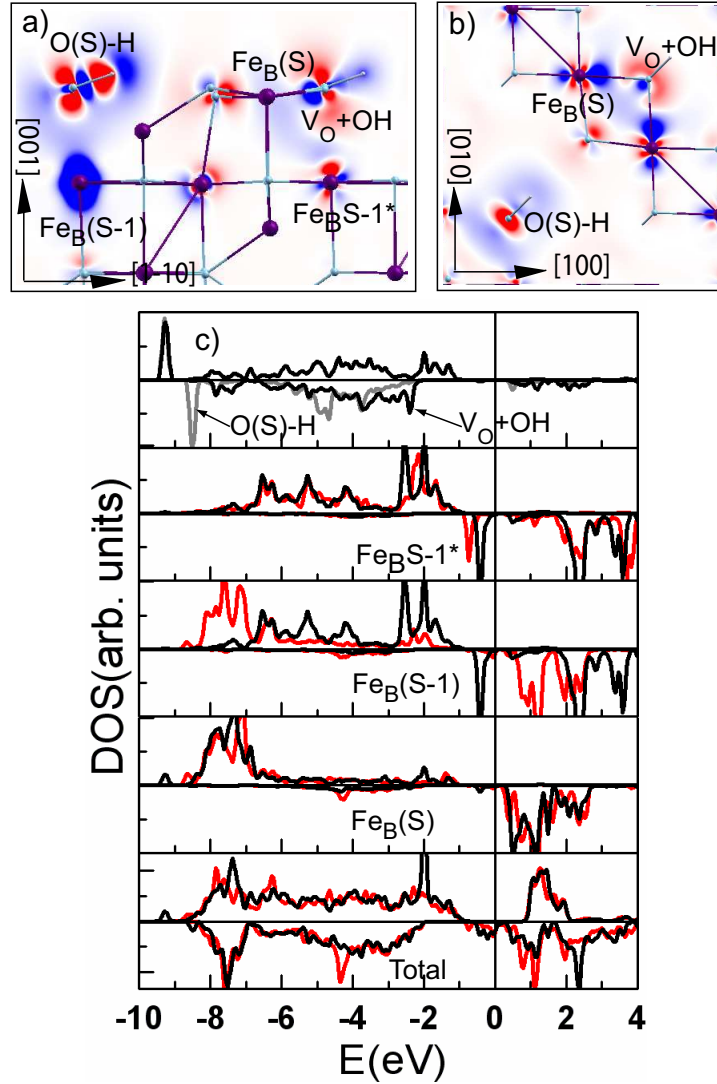


Figure 5.5: *Electron density redistribution plots and density of states (DOS) obtained within GGA+U for a single water molecule adsorbed in an oxygen vacancy on the $\text{Fe}_3\text{O}_4(001)$ surface ($1D_V-3$). a) and b) show a cross section and a top view of $\Delta\rho$, respectively; c) contains the total DOS and projected DOS on the oxygen of the OH group in the vacancy. Furthermore, the PDOS of the 3d states of a surface Fe_B next to the vacancy ($\text{Fe}_B(S)$), as well as the Fe_B -ions below the vacancy ($\text{Fe}_B^*(S-1)$) and the $\text{Fe}_B S-1$ (below $\text{O}(S)-\text{H}$) are shown. Black and red lines indicate the DOS before and after adsorption of the molecule, showing also a change in valence state at $\text{Fe}_B S-1$.*

groups are nearly parallel to the surface enabling the formation of hydrogen bonds with the opposite $\text{O}(S)$. This explains moderate accumulation of charge around the $\text{O}(S)$ opposite the OH group. We predict two determining factors for the relative stability among $1D_V-1$ to $1D_V-3$: One is the extent of hydrogen bond formation on the surface and second is the repulsive interaction between

the surface OH groups. In the case of $1D_V-3$ both these factors are highly satisfied when compared to the rest of the configurations. In fact the distance between the two surface OH group in $1D_V-3$ is larger (5.95 \AA) when compared to $1D_V-1$ (3.32 \AA) and in $1D_V-2$ (2.50 \AA). The E_{ads} vs OH-OH distance also indicates a repulsive interaction between the surface OH group which affects the lowest energy configuration. Fig. 5.5b shows charge donation from the $\text{Fe}_B(\text{S})-d_{yz}$ orbital to 1π orbital of OH and back donation from 3σ to $\text{Fe}_B(\text{S})-d_{xy}$ orbital due to the hybridisation between $\text{Fe}_B(\text{S})$ and $V_O+\text{OH}$. The interaction of O(S)-H with the $\text{Fe}_B(\text{S}-1)$ can be seen from the PDOS ($\text{Fe}_B(\text{S}-1)-3d$) shown in Fig. 5.5c wherein, a sharp localised peak (black line) in the minority spin appears which was absent before adsorption (red line). This means a change in the oxidation state from Fe^{3+} to Fe^{2+} occurs. The DOS of $\text{Fe}_B^*(\text{S}-1)$ shows a slight shift of the Fe^{2+} peak, the other changes before and after reduction of the surface being negligible. Interestingly, we find that the half metallic character of the defective surface remains even after the adsorption of H_2O molecules.

In this Section we observe that the electronic structure of the defective surface and the changes after H_2O adsorption is well described within $\text{GGA}+U$. We could also explain satisfactorily all the energetic trends obtained within GGA and $\text{GGA}+U$ through the analysis of the respective electronic structures and the discrepancies thereby.

5.4 Structural properties

In this Section we will study the effect of a vacancy and the adsorption of an H_2O molecule on the structural properties of the $\text{Fe}_3\text{O}_4(001)$ surface. The

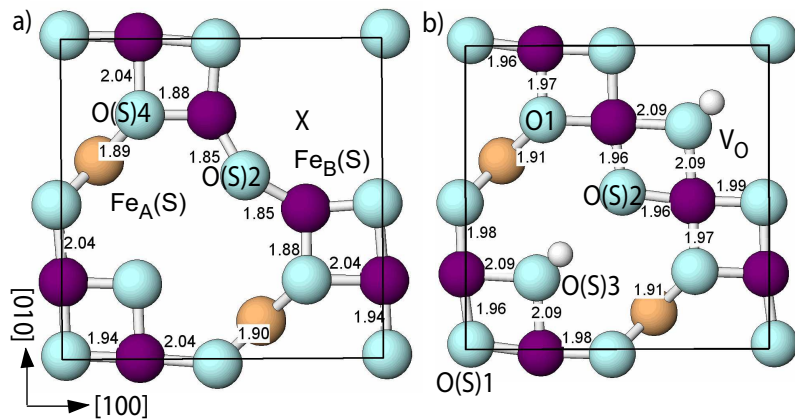


Figure 5.6: The relaxed top B-layer of $B+V_O$ (a) and of $1D_V-3$ (b) is shown indicating all the surface atoms used in the description of surface relaxations. The bond lengths $d_{\text{Fe}_B(\text{S})-\text{O}(\text{S})}$ are also shown. The bond lengths are given in \AA .

structural relaxations discussed in this Section are obtained within GGA+ U . The GGA results are explicitly mentioned for comparison.

B+V_O (B-layer with an oxygen vacancy): First we will discuss the structural changes induced with the creation of an oxygen vacancy. The relaxations for the surface atoms within GGA and GGA+ U are listed in Table 5.1. A schematic top view of the B layer with lateral bond lengths is shown in Fig 5.6a. The left panel of Fig. 5.7 also provides a side view of the B+V_O including characteristic bond lengths. The major change is in the lateral relaxation. In order to compensate the under-coordination created by the V_O, the O(S)2 relaxes laterally towards the Fe_B row by 0.57 Å and Fe_B(S) by 0.26 Å. This results in the subsequent reduction of the $d_{\text{Fe}_B(\text{S})-\text{O}(\text{S})}$ to 1.85 Å from the bulk value of 2.06 Å. The $\angle \text{Fe}_B(\text{S})-\text{O}(\text{S})2-\text{Fe}_B(\text{S})$ changes from 90° to 140° after full structural optimisation. The direction of relaxation (Δz) is inwards in the case of Fe_B(S) but outwards for O(S)2. Within GGA the magnitude of the lateral relaxation is quite similar (0.54 Å for O(S) and 0.29 Å for Fe_B(S)) and the $\angle \text{Fe}_B(\text{S})-\text{O}(\text{S})2-\text{Fe}_B(\text{S})$ is 143.56°. The lateral relaxations in turn affect the Fe_B(S)-O(S)(4) bond length which is 0.18 Å shorter. From Table 5.1, we notice that the O(S) show a stronger lateral relaxation within GGA than in GGA+ U . Nevertheless, we do observe reduction of $d_{(\text{Fe}_B(\text{S})-\text{O})}$ on the surface in both approximations. The change in the lateral bond lengths of the surface layer also affect the subsurface layer (S-1 and S-2) bond lengths. The outward relaxation of O(S)2 by 0.28 Å elongates the $d_{(\text{Fe}_B(\text{S}-1)-\text{O}(\text{S})2)}$ to 2.36 Å and the bond in the S-2 layer to 2.22 Å. We predict that the elongation of the bond length between O and Fe in the layers S and S-1 reduces the coordination of Fe_B(S-1) and perhaps is the reason for the change in oxidation state from Fe³⁺ to Fe²⁺. Surprisingly, the Fe_B beneath the vacancy site, which becomes Fe²⁺ from Fe³⁺ after reduction, does not alter the lateral $d_{(\text{Fe}_B-\text{O})}$ in the S-1 layer which remains close to the bulk value. On a clean surface, all the Fe_B(S) and O(S) relax inwards [26, 27], leading to bond contraction but with the creation of an oxygen vacancy on the surface, we see that the Fe_B(S) follows the trend while only O(S)2 and O(S)4 relax outwards. This outward movement is due to greater hybridisation with Fe_B(S) as shown in Fig. 5.3c. The relaxations in

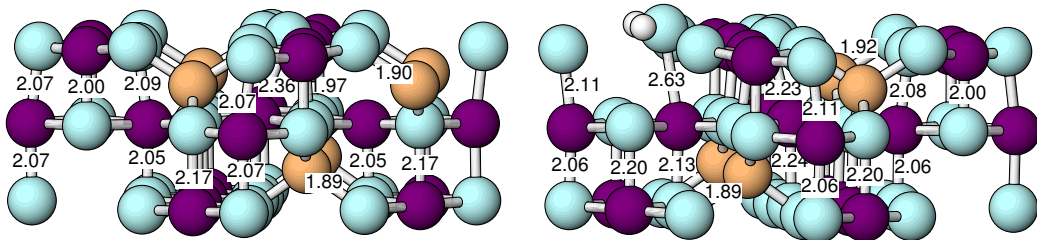


Figure 5.7: Side view of the relaxed B+V_O (left panel) and 1F_V (right panel) along with surface and sub-surface bond lengths. All bond lengths are given in Å and are obtained within GGA+ U .

Table 5.1: Atomic relaxations of the surface layer obtained within GGA and GGA+ U in the case of $B+V_O$. The Δz values represent relaxation along the surface normal, negative/positive values indicate an outward/inward relaxation. The numbering of the atom corresponds to those shown in Fig. 5.6. All distances are in \AA .

	GGA				GGA+ U			
	Δx	Δy	Δz	Δxy	Δx	Δy	Δz	Δxy
Fe _A (S)	0.03	0.05	-0.11	0.07	0.03	0.06	-0.15	0.07
O(S)2	-0.54	-0.54	-0.14	0.77	-0.57	-0.57	-0.28	0.81
O(S)3	0.18	0.18	0.03	0.26	0.09	0.09	0.01	0.13
O(S)4	0.12	-0.13	0.03	0.18	0.07	-0.07	-0.04	0.10
Fe _B (S)	-0.12	0.29	0.12	0.32	-0.09	0.26	0.09	0.28

the sub-surface layers are however small compared to the surface layer. The Fe_A(S) layer relaxes outward leading to some expansion in the bond lengths.

1F_V (Single H₂O molecule adsorbed in the oxygen vacancy site in a flat orientation): Structural relaxations after adsorption of a H₂O molecule at the vacancy site (1F_V) are given in Table 5.2. The atoms of the surface B-layer are shown schematically in Fig. 5.6b, and a side view of 1F_V along with some of the inter-layer bond lengths is shown in Fig. 5.7 right panel. The lateral relaxation of O(S)2 diminishes by 0.22 \AA with the adsorption of a water molecule but the $d_{(\text{Fe}_B(\text{S})-\text{O}(\text{S})2)}$ nearly remains the same (1.87 \AA). The O^w shows a lateral shift of 0.36 \AA moving the molecule away from the Fe_B row with the nearest $d_{(\text{Fe}_B(\text{S})-\text{O}^w)}$ of 2.75 \AA (2.57 \AA in GGA). However, outward relaxation of H₂O molecule is strong (0.60 \AA) elongating the $d_{(\text{Fe}_B(\text{S}-1)-\text{O}^w)}$ to 2.63 \AA (2.28 \AA in GGA). This affects also the sub-surface bond lengths. The bond lengths of O^w with the neighboring octahedral irons (Fe_B) are elongated due to high coordination number. All the O(S) relax inwards in the case of clean surface [26, 27] whereas in the present case the trend is opposite. It can be seen from the Fig. 5.7 right panel that, in general, bond lengths between S and S-1 layer contract and those between S-1 and S-2 elongate. The Fe_A(S) layer relaxes outwards. We also notice that within GGA the magnitude of relaxation is smaller compared to the values within GGA+ U .

1D_V-1 (One H₂O molecule dissociated in an oxygen vacancy and H adsorbs on O(S)1 site): The dissociation of the adsorbed H₂O changes the structural details further. We discuss the structural changes induced in 1D_V-1 as listed in Table 5.2. A side view depicting some of the characteristic bond lengths is shown in Fig. 5.8 left panel. The lateral relaxation of O(S)2 is further reduced by 0.10 \AA compared to 1F_V resulting in reduction of $d_{(\text{Fe}_B(\text{S})-\text{O}(\text{S})2)}$ to 1.91 \AA . Outward relaxation also gets diminished and the $d_{(\text{Fe}_B(\text{S}-1)-\text{O}(\text{S})2)}$ is 2.11 \AA . The O^{OH} reduces the lateral relaxation by 0.30 \AA when compared to O^w in the

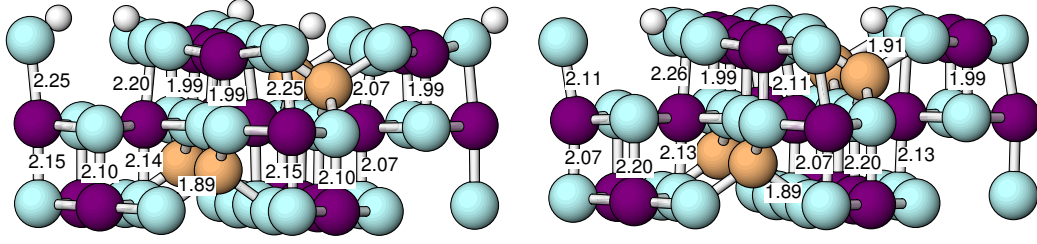


Figure 5.8: Side view of the relaxed $1D_V-1$ (left panel) and $1D_V-3$ (right panel) along with surface and sub-surface bond lengths. All bond lengths are given in \AA and are obtained within $GGA+U$.

Table 5.2: Atomic relaxations of the surface layer obtained within $GGA+U$ in the case of $1F_V$ and $1D_V-1$. The values in the parenthesis belong to the case of GGA . The numbering of the atom corresponds to those shown in Fig. 5.6. All distances are in \AA .

	$1F_V$			$1D_V-1$		
	Δx	Δy	Δz	Δx	Δy	Δz
$Fe_A(S)$	0.06 (0.06)	0.04 (0.05)	-0.18 (-0.10)	0.01 (-0.01)	0.00 (0.01)	-0.17 (-0.11)
$O(S)1$	-0.07 (-0.08)	-0.07 (-0.08)	-0.02 (0.01)	-0.10 (-0.10)	-0.10 (-0.10)	-0.26 (-0.11)
$O(S)2$	-0.35 (-0.23)	-0.35 (-0.23)	-0.27 (-0.05)	-0.15 (-0.12)	-0.15 (-0.12)	-0.17 (0.00)
$O(S)3$	0.10 (0.09)	0.10 (0.09)	0.00 (0.02)	0.12 (0.13)	0.12 (0.13)	0.02 (0.00)
V_O	-0.36 (-0.18)	-0.36 (-0.18)	-0.59 (-0.10)	0.06 (0.10)	0.06 (0.10)	-0.21 (-0.11)
$O(S)4$	0.07 (0.10)	-0.05 (-0.05)	-0.10 (0.03)	0.00 (-0.03)	-0.11 (-0.10)	-0.08 (0.03)
$Fe_B(S)$	-0.02 (0.04)	0.25 (0.30)	0.03 (0.13)	0.03 (0.04)	0.12 (0.14)	0.04 (0.11)

case of $1F_V$. O^{OH} relaxes outwards elongating the $d_{(Fe_B(S-1)-O^{OH})}$ to 2.20 \AA but when compared to $1F_V$, it actually has reduced the bond length. The other $O(S)$ where the H adsorbs, $O(S)1$, also shows an outward relaxation (0.26 \AA) apart from a moderate lateral relaxation. In this case the $d_{(Fe_B(S-1)-O(S)1)}$ is 2.26 \AA . In this configuration the two OH groups face each other leading to a repulsive interaction between them and forcing a tilt angle as shown in the Fig. 5.8 left panel. Most of the $O(S)$ relax inwards. The $Fe_A(S)$ layer also relaxes outwards as seen in the case of $1F_V$.

$1D_V-3$ (One H_2O molecule dissociated in an oxygen vacancy and H adsorbs at $O(S)3$ site): The most stable adsorption model $1D_V-3$ is shown in Fig. 5.8 right panel with some of the characteristic bond lengths. The structural relaxations are listed in Table 5.2 and a schematic view of the top B layer with lateral bond lengths is shown in Fig. 5.6. The lateral and vertical relaxations of $O(S)2$ have been further reduced to 0.11 and 0.03 \AA , respectively which is lower when compared to $1F_V$ and $1D_V-1$. This results in $d_{(Fe_B(S)-O(S)2)}$ of 2.09 \AA which is quite close to the bulk value. The lateral relaxation of O^{OH} and $O(S)3$ are of the order of 0.09 \AA stretching the $d_{(Fe_B(S)-O(S))}$ to 2.09 \AA .

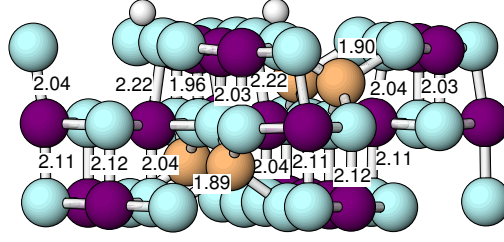


Figure 5.9: The left panel shows the side view of $1D_V-2$ along with bond lengths. All bond lengths are given in Å. The results are obtained within GGA

Table 5.3: Atomic relaxations of the surface layer obtained within GGA+U in the case of $1D_V-3$ is listed. The values in the parenthesis belong to the case of GGA. The numbering of the atom corresponds to those shown in Fig. 5.6. All distances are in Å.

	$1D_V-3$		
	Δx	Δy	Δz
Fe _A (S)	0.03 (0.06)	0.03 (0.06)	-0.20 (-0.12)
O(S)1	-0.11 (-0.10)	-0.11 (-0.10)	-0.03 (0.01)
O(S)2	-0.11 (-0.10)	-0.11 (-0.10)	-0.03 (0.01)
O(S)3	0.09 (0.11)	0.09 (0.11)	-0.25 (-0.14)
V _O	0.09 (0.11)	0.09 (0.11)	-0.25 (0.14)
O(S)4	-0.01 (0.00)	-0.01 (0.00)	-0.14 (0.04)
Fe _B (S)	0.02 (0.03)	0.10 (0.13)	0.04 (0.12)

In fact in all the configurations $1D_V-1,2,3$, wherever the surface OH group is formed, it actually elongates the bond length with the neighboring Fe_B(S). This has also been observed in $1D-1$. Apart from the surface interaction another factor which contributes to the bond elongation is the formation of hydrogen bonds (to a certain degree) between O(S)-H and the opposite O(S). In the case of O(S)-H, where an additional H adsorbs on the O(S), the hydrogen atom provides extra charge to the O(S) thereby weakening the bonds with the neighboring Fe_B(S), and thus leading to the just stated bond elongation. This can be further explained with the $\angle(\text{Fe}_B(\text{S}-1)-\text{O}^{\text{OH}}-\text{H})$. In the case of $1D_V-3$ this angle has a value of $\sim 105.4^\circ$ which increases to $\sim 109.95^\circ/111.9^\circ$ for $1D_V-2$ and further to $\sim 122.97^\circ/127.3^\circ$ for $1D_V-1$. This clearly shows that in the case of $1D_V-3$, the degree of hydrogen bond formation is higher and provides more stability. The tilting of the OH group influences the sub-surface $d_{(\text{Fe}_B(\text{S}-1)-\text{O}(\text{S}))}$ and in general elongates it, which is true once again for all the $1D_V-1,2,3$ and also for $1D-1$. The outward relaxation of O^{OH} and O(S)3 by

0.25 Å results in $d_{(\text{Fe}_B(\text{S}-1)-\text{O}^{\text{OH}}/\text{O}(\text{S})_3)}$ of 2.26 Å. All the O(S) and Fe_A(S) relax inwards. The general trend of bond elongation and contraction between S, S-1 and S-2 is seen here too with a variation in magnitude.

5.5 Summary

In the case of a defective surface we find consistency between the two approximations for the exchange-correlation potential (GGA and GGA+ U) which was lacking in the case of a monomer adsorption on an ideal Fe₃O₄(001) surface. The mode of adsorption is dissociative with preference for the H atom to adsorb at a distant O(S) site. The charge localisation from the vacancy occurs on the neighboring Fe_B(S-1) as shown in Fig. 5.3a,b. From our calculations we find the 1D_V-3 configuration to be the most stable geometry. The dissociative mode of adsorption was found also for 1D-1 within GGA+ U . A high E_{ads} of -1.73 eV shows the strong affinity of the vacancy for the water molecule to promote dissociation. This is perhaps the reason for filling up of all vacancy sites in the initial stages of adsorption such as observed by Kendelewicz *et al.* [37]. We identify two interactions between the surface OH groups (O(S)-H) on the surface which determine the lowest possible geometry: (i) the distance between the OH groups and (ii) the extent of hydrogen bonding with the opposite O(S). A strong hybridisation of V_O with the surface is seen in the density of states (DOS) and in the electron density redistribution patterns which coincides with the fact that anionic vacancies are Lewis acid in nature and provide a strong binding site. We also find change in oxidation state of sub-surface Fe_B from Fe³⁺ to Fe²⁺ with the creation of a vacancy and also with adsorption of OH. Interestingly, we also find that defective surface has a half metallic character which remains the same with the adsorption of water.

Dimer Adsorption

In the previous Chapters (4 and 5) we have investigated various adsorption mechanisms involving an isolated single H₂O molecule on a Fe₃O₄(001) surface. Here we include an additional water molecule on the surface making it a water dimer. With the inclusion of a second water molecule, intermolecular forces such as adsorbate-adsorbate interactions come into play which modifies the surface chemistry. In any adsorption related study, two main interactions have to be considered i.e. adsorbate-substrate and adsorbate-adsorbate. If the latter one dominates, we see clustering of water molecules on the surface [34, 80]. It was shown in the case of hydrated TiO₂(110) [107] that due to the low diffusion barrier for H₂O molecules, a water dimer is observed on the surface. In this Chapter apart from considering general adsorption configurations, we have also investigated models which facilitate the formation of inter-molecular hydrogen bond. In Section 6.1, we first discuss the various adsorption models and their relative stability in terms of E_{ads} . This includes a discussion on adsorption trends both within GGA and GGA+ U . In order to further understand the energetic trends and discrepancies between the GGA and GGA+ U results, we analyze the electronic structure in Section 6.2. In Section 6.3, we discuss various structural details and correlate them to the observed E_{ads} and electronic structure changes.

6.1 Adsorption models and energetic stability

In the coverage regime of two H₂O molecules we have considered more than 14 adsorption models representing all modes of adsorption. The top views of all these configurations can be seen in Fig. 6.1 and in Fig. 6.2. The most prominent among them are shown in Fig. 6.1. This figure shows also the relative stability of each case in terms of E_{ads} within GGA and GGA+ U . The noticeable feature is the trend in the adsorption energies, which is similar with and without a U parameter.

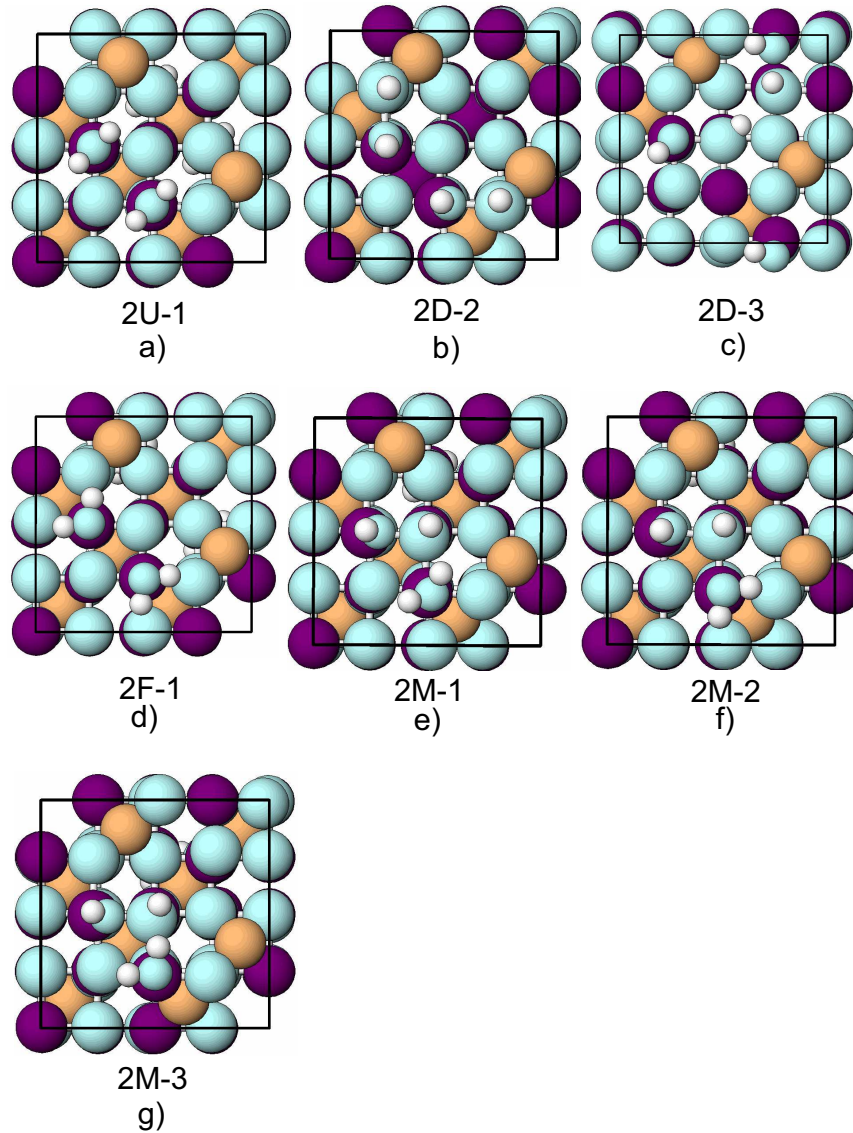


Figure 6.2: Top views of some more adsorbate geometries of two water molecules per $(\sqrt{2} \times \sqrt{2})R45^\circ$ -unit cell. Positions of O, Fe_B, and H are marked by cyan, purple and white circles.

hydrogen bond between the two H₂O molecules. One of the O^w is a hydrogen bond donor and other one is the acceptor. The E_{ads} reduces to -0.45 eV and the O^w-O^w distance reduces from 3.04 Å to 2.95 Å due to the hydrogen bond which is attractive in nature. In 2F-2 one of the molecules, denoted as H₂O-I, which is in a flat geometry acts as a hydrogen-bond donor to the second H₂O-II and to the neighboring O(S), while H₂O-II is strongly tilted with one hydrogen oriented towards a neighboring surface oxygen and the second pointing away from the surface. The different adsorbate orientation with respect to the surface results in a difference of 0.12 Å in $d_{(\text{Fe}_B(\text{S})-\text{O}^w)}$. The water dimer distance is 1.86 Å which is quite close to that observed for a gas-phase dimer (1.88 Å).

The formation of a hydrogen bond to O(S) and between the two molecules leads to weakening of the OH bonds (reflected in the longer bond lengths of 0.97-0.99Å) and finally to dissociation of H₂O-II. The E_{ads} for 2F-2 is degenerate with that of 2F-3. The importance of the 2F-2 will be described later in terms of a probable precursor for the partial dissociation.

Now if we focus on the simultaneous existence of an intact H₂O molecule and a dissociated molecule we enter a new regime of mixed adsorption. The energetic stability of mixed adsorption is highly dependent on the orientation of the intact molecule with that of the dissociated one. If we assume that the intact water molecule is nearly upright (2M-1) as shown in Fig. 6.2 then the total energy is even less than that of 2F-2/3. The reason for reduction is the inter-molecular interaction. In the next step we consider an intact H₂O molecule lying parallel to the surface. We end up with two different geometries 2M-2 and 2M-3. 2M-2 completely avoids any possibility for the formation of hydrogen bonds and hence the total energy is even less than 2M-1. But if the H₂O molecule is facing the OH group as shown in 2M-3 the E_{ads} gets favorable by 0.11 eV compared to 2M-1 and by 0.07 eV compared to 2F-3. This is attributed to higher contribution of adsorbate-adsorbate interaction. One can notice from the top views of 2M-1/2/3 that the OH group is not adsorbed on top of Fe_B(S) but slightly tilts towards the O(S)-H group due to the attractive interaction between OH and O(S)-H as described in Section 4.1. Further structural optimisation of 2M-3 leads to the most stable configuration among all considered models i.e. 2M-4 as shown in Fig. 6.1. The E_{ads} gets lower to -0.80 eV. Two hydrogen bonds, one between O^w-H...O^{OH} and another between O(S)-H...O(S), provide the additional stability. The OH group does not adsorb on top Fe_B(S) but drifts more towards the H₂O molecule than to the O(S)-H, as shown in 2M-3. This results in $d_{(\text{O}^{\text{OH}}-\text{O}^{\text{w}})}$ of 2.51 Å. This mixed mode of adsorption is also found for MgO(100) [108] and TiO₂(110) [109].

Finally, the dissociative mode of adsorption has been investigated as it has been proposed experimentally [37]. 2D-1 is the configuration where we adsorb hydroxyl groups on adjacent Fe_B(S) and the corresponding hydrogens on the nearby O(S). This gives a E_{ads} of -0.34 eV which is 0.04 eV lower than 2T-1. A similar trend was observed between 1D-1 and 1U where the E_{ads} differ by 0.04 eV. We also considered another configuration 2D-2 where we chose two other O(S) sites having Fe_A as neighbors to hold the hydrogen atoms. This configuration is energetically unfavorable compared to 2D-1. The only difference between 2D-1 and 2D-2 is the choice of O(S) for hydrogen adsorption site. This indicates that the O(S) with Fe_A(S) as neighbor is unfavorable for adsorption of H atoms.

GGA+U: Now we check the stable configurations by including an onsite Coulomb repulsion term and assess their stability. The E_{ads} and top views are shown in Fig. 6.1. The difference in the E_{ads} between GGA and GGA+U varies from 0.14 to 0.18 eV but the trends largely remain similar. The molecular adsorption in an upright configuration 2T-1 is the least favorable among other

adsorption models. However, the E_{ads} of -0.30 eV is a significant enhancement over the vanishing E_{ads} observed for 1U. This change is attributed to the intermolecular interactions. The next are the flat adsorption models i.e. 2F-2/3. The E_{ads} of 2F-2 is -0.45 eV similar to the one within GGA and is 0.15 eV more favorable than 2T-1. The E_{ads} of 2F-2/3 which were degenerate in the case of GGA, now differ by 0.16 eV, 2F-3 being lower.

The mixed adsorption 2M-4 is the most stable configuration with the lowest E_{ads} (-0.94 eV). The full dissociation of the water dimer in 2D-2 is unfavorable even though the E_{ads} of -0.34 eV is same as in GGA. If we adsorb the two dissociated H_2O molecules far apart as shown in 2D-3 of Fig. 6.1, we get a more stable configuration, next to 2M-4 with an E_{ads} of -0.58 eV. This configuration is even more stable than 2F-2/2F-3 by 0.11/0.29 eV and 2D-1 by 0.24 eV. This leads to an alternative reaction mechanism than the one suggested with 2F-2 above. In the mechanism involving 2D-3 the two H_2O molecules dissociate on top of $\text{Fe}_B(\text{S})$ which are far apart ($d_{(\text{Fe}_B(\text{S})-\text{Fe}_B(\text{S}))}$ 6.83 Å). In the subsequent step, the intact H_2O molecule adsorbs at an adjacent $\text{Fe}_B(\text{S})$ site provides high stability through a hydrogen bond while maintaining the mixed mode of adsorption. However, this results in a higher coverage, and hence, this mechanism will be discussed in the next Chapter with more details. The other adsorption models considered within GGA were not tested as they were either unfavorable or degenerate with the most stable configurations.

At this point we would like to mention that in the adsorption models considered above, we always adsorbed the water dimer in a molecular form on top of the adjacent $\text{Fe}_B(\text{S})$ and not on $\text{Fe}_B(\text{S})$ that were far apart. A low diffusion barrier is observed for H_2O molecules on the surface for e.g. on many metal surfaces [34, 80] and on metal oxides like $\text{TiO}_2(110)$ [107]. This ultimately results in the formation of cluster on nearby $\text{Fe}_B(\text{S})$. On the whole the most stable configuration 2M-4 requires hydrogen bonding for stability which can only be achieved well in the present chosen configuration.

6.2 Analysis of the electronic structure

In order to understand the energetic trends and stability of the surface terminations, we analyze the electronic structure through the density of states (DOS), projected density of states (PDOS), electron density redistribution plots and molecular orbital (MO) analysis.

2U-1 and 2T-1 (2 H_2O molecules in upright and tilted adsorption model): The change in the electronic structure within GGA from 2U-1 to 2T-1 can be understood from the DOS as shown in Fig. 6.3a. To get a better insight we also show the DOS and PDOS of 1U. The $\text{O}^{\text{w}}-2p$ band of 2U-1 and 1U span a similar energy range from -2 to -8 eV. The position of the $3a_1$ orbital and the extent of hybridisation with the $\text{Fe}_B(\text{S})-3d$ states also remain the same. This essentially means that the H_2O molecules in a dimer configuration of 2U-1

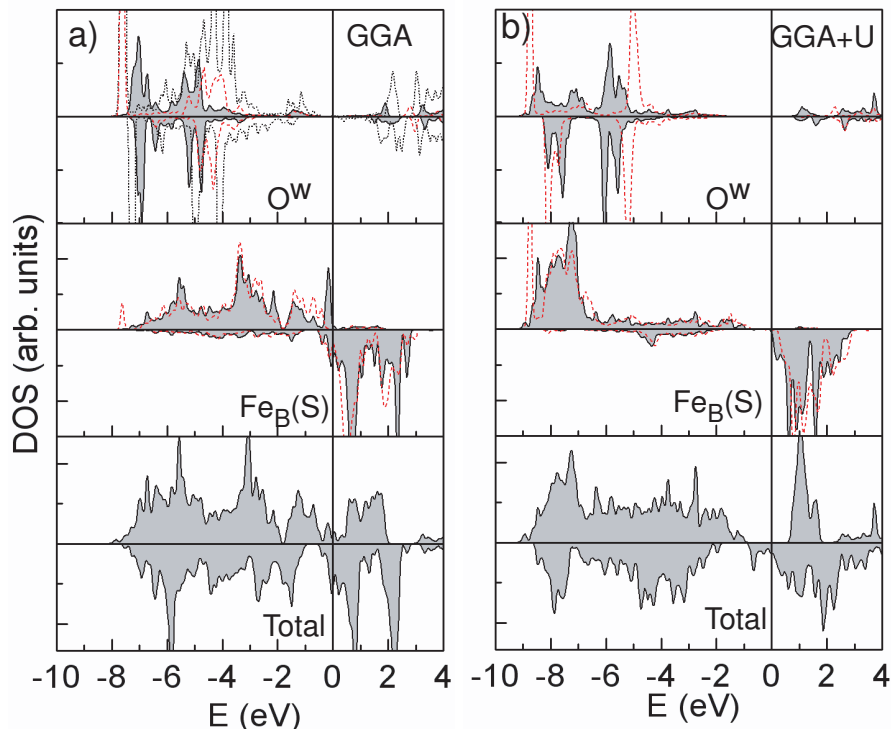


Figure 6.3: Density of states (DOS) of 2T-1 is shown in a) and b) obtained within GGA and GGA+U respectively. Top panel: PDOS of O^w in 2T-1 (black solid line), 2U-1 (black dotted line) and in 1U (red dashed line), Middle panel: PDOS of $Fe_B(S)$ in 2T-1 (black solid line) and in 1U (red dashed line), Bottom panel: total DOS. Please refer Fig. 4.5 for the MOs reference energies of H_2O .

behave independent of each other. This is due to the repulsive intermolecular interaction which results in the increase of E_{ads} . In the case of 2T-1, wherein the H_2O molecules tilt towards each other, the $1b_1$ MO moves towards lower energy compared to 2U-1 and 1U which explains the decrease in E_{ads} . The $3a_1$ MO remains localized as is in 1U and 2U-1.

Next we consider the changes within GGA+U between 2T-1 and 1U as shown in Fig. 6.3b. In the case of 2T-1, the $1b_1$ MO moves towards lower energy and the hybridisation of $1b_1$, $3a_1$ with $Fe_B(S)$ -3d states occurs to a larger extent (leading to bonding/antibonding splitting) when compared to 1U. This explains the lowering of E_{ads} to -0.30 eV. Fig. 6.3a and b shows the energy range spanned by O^w -2p band within GGA+U is -2 to -9 eV whereas within GGA it is -2 to -8 eV. This means a shift of 1 eV towards lower energy but interestingly the E_{ads} remains almost the same. The PDOS of $Fe_B(S)$ remains similar in 2T-1 and 1U. The total DOS reveals a metallic character for 2T-1 within GGA whereas it shows a half-metallic character within GGA+U.

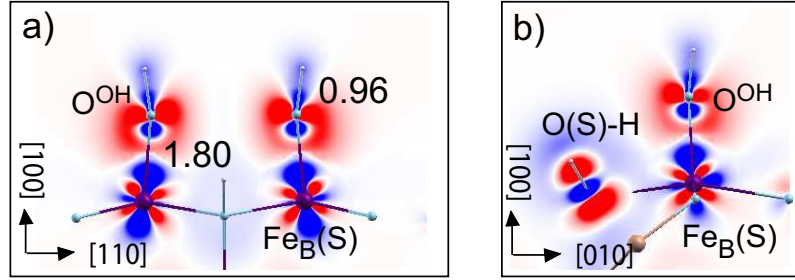


Figure 6.4: Electron density redistribution, obtained within GGA+U upon adsorption of a water dimer in 2D-1 configuration, is shown in a) and b) in different directions. Electron accumulation (depletion) is shown in red (blue). Positions of O, Fe_B, and H are marked by cyan, purple and white circles.

2D-1 (two H₂O molecules in dissociated configuration): In the case of fully dissociated dimer, a strong charge redistribution is observed within GGA+U as shown in Fig. 6.4a,b. The electron redistribution pattern within GGA and GGA+U is similar except for the Fe_B(S) orbital whose participation in the hybridisation process differs (t_{2g} vs. d_{z^2}) as explained in Section 4.2. The charge donation and back donation mechanism of the OH group explained in Section 4.2 is also seen here. The interaction of the OH MOs with the Fe_B(S)-3d states lead to the depletion of charge in the d_{z^2} orbital and an accumulation of charge in the 1π orbital. We also see a back donation of charge from the 3σ orbital of OH to the Fe_B(S)- d_{t2g} orbitals. The build up of charge is more towards the O^{OH} implying a net transfer of charge and thus ionic character in the bonding is predicted. In contrast the formation of the O(S)-H bond is associated with accumulation of charge in the 3σ orbital which was not the case with O^{OH}. The charge redistribution pattern in 2D-1 and 1D-1 are similar except that the O^{OH}-2p orbital shows accumulation of charge in the former case while it is absent in the latter case. We relate this to the tilt angle of the OH group ($\angle\text{Fe}_B(\text{S})\text{-O}^{\text{OH}}\text{-H}$) which is 120.9° for 1D-1 and 166.9° for 2D-1.

Within GGA+U the E_{ads} of 2D-1 is less favorable by 0.37 eV from 1D-1 which suggests a strong intermolecular repulsive interaction and is evident from the Fig. 6.4a where the charge redistribution, accumulation/depletion in between the OH groups is negligible. This can be further substantiated by the negligible change in $d_{(\text{OH}-\text{OH})}$ (0.04 Å) after structural relaxation and the $d_{(\text{Fe}_B(\text{S})-\text{O}^{\text{OH}})}$ of 1.80 Å. Fig. 6.5b shows the DOS and PDOS within GGA+U. The red dotted line shows the DOS of 1D-1 for comparison. The PDOS of O-2p in O^{OH} shows an appreciable change compared to that in O^w (Fig. 6.3). In fact the majority of states seem to have moved towards the E_F level represented by the 1π orbital. Another interesting aspect to be looked at is the splitting of the 1π peak in both 1D-1 and 2D-1. As expected, the origin of this splitting is not from bonding/antibonding, but rather comes from the degenerate nature of the 1π orbital. When the degeneracy is partially lifted up it causes the peak to split. On the other hand due to surface interactions both the 1π orbitals

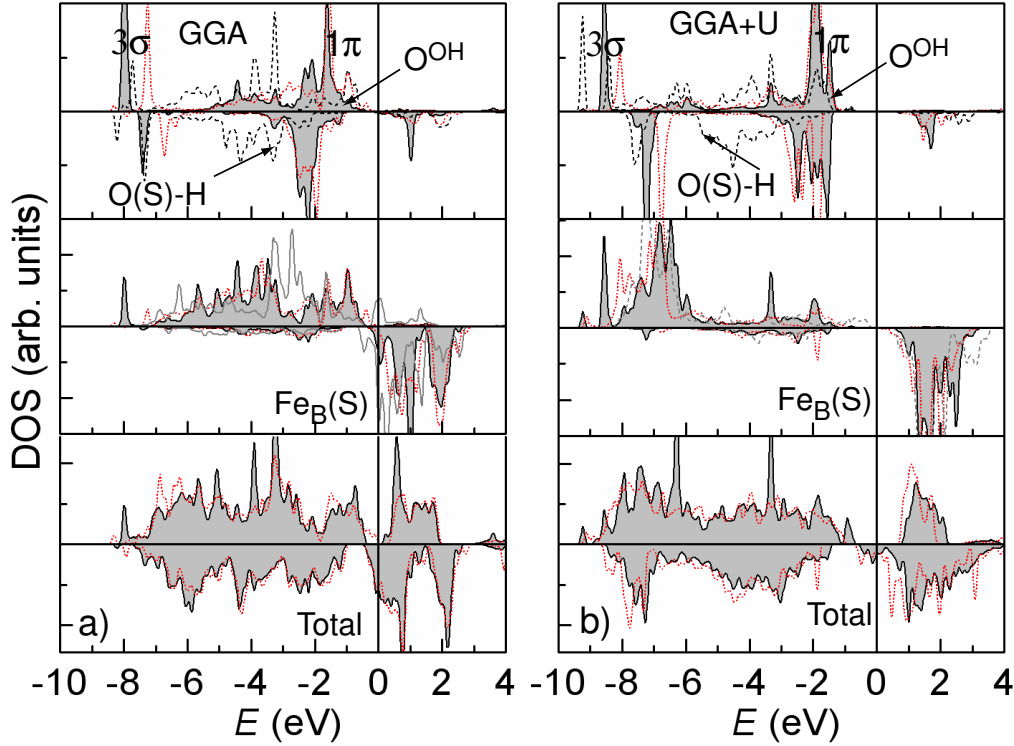


Figure 6.5: The panels show the total and projected DOS for 2D-1 (solid black lines) and for 1D-1 (red dotted lines) configuration within a) GGA and b) GGA+U. In the middle panel $Fe_B(S)$ of modified B-layer is shown by a grey dashed line. The MO of OH group 3σ and 1π are also marked for reference. Positions of O, Fe_B , and H are marked by cyan, purple and white circles.

$(1\pi_x, 1\pi_y)$ exhibit bonding/antibonding splitting. The lifting up of degeneracy in the 1π orbital [32] is also seen in the case of 1D-1 (Section 4.2) and is related to tilt of the OH group ($\angle Fe_B(S)-O^{OH}-H$).

We observe a correlation between the tilt angle and the intermolecular interaction to the extent of hybridisation with the surface. For example in 2D-1 the tilt angle ($\angle Fe_B(S)-O^{OH}-H$) is quite low when compared to 1D-1. Still due to intermolecular repulsion we see a lifting up of degeneracy and hence the 1π peak splits. This indicates that not only tilt angle ($\angle Fe_B(S)-O^{OH}-H$) but also intermolecular interaction is responsible for lifting up of degeneracy. The d_{z^2} orbital is quite significant in the hybridisation process as it interacts not only with 3σ orbital but also with 1π orbital. This happens due to strong bonding/antibonding splitting of d_{z^2} orbital as shown in Fig. 6.5b. The bonding peak interacts with 3σ and the antibonding peak moves towards higher energy and hybridizes with 1π orbital and in fact with both $1\pi_x$ and $1\pi_y$. Since the 1π orbital is the HOMO, any interaction which shifts it more towards E_F will result in energy gain and hence more stable. In 1D-1, we see two small peaks from $Fe_B(S)-3d$ band near the E_F which hybridizes with 1π states whereas in the case of 2D-1 the d_{z^2} antibonding peak is at lower energy than in 1D-1.

This shift in the position of hybridisation w.r.t E_F is partly responsible for the decrease in E_{ads} from 1D-1 to 2D-1. A further reason is the extent of interaction with 3σ orbital. From Fig. 6.5b, we notice that the 3σ peak in 2D-1 is lower in energy than in 1D-1 which means interaction in the latter case is enhanced.

In the case of GGA (Fig. 6.5a) the 1π orbital shows higher degree of broadening and silting of states (bonding/antibonding) than in GGA+ U . On the other hand the 3σ orbital of O^{OH} shifts slightly to lower energy in GGA+ U than in GGA. Different position and width of Fe_B - $3d$ band within GGA and GGA+ U leads to different degree of hybridisation with OH MOs. At this point we are unable to ascertain exactly the reason for similar E_{ads} in both approximations.

2M-4 (two H_2O molecules in mixed configuration): Finally we consider the mixed adsorption 2M-4 configuration. The charge density redistribution upon adsorption plots are obtained from Eq. 3.2 and the DOS are shown in Fig. 6.6. The charge redistribution patterns within GGA and GGA+ U are similar except for the $\text{Fe}_B(\text{S})$ - $3d$ orbital which participates in the hybridisation process. In the former case an accumulation/depletion of $\text{Fe}_B(\text{S})$ - d_{t2g} orbitals occur, while in the latter case a more clear picture evolves with the depletion of d_{z^2} orbital and accumulation in d_{t2g} orbital as shown in Fig. 6.6a. If we focus on the intact H_2O molecule, we see the electron density redistribution from $1b_1$ orbital to the surrounding in order to reduce Pauli repulsion. Strong accumulation of electron density in the $\text{Fe}_B(\text{S})$ - d_{z^2} orbital signifies its important role. The comparison of charge density redistribution upon adsorption with an isolated H_2O or OH group shows that the pattern essentially remains the same in 2M-4. However a difference is seen in the magnitude of electron density redistribution between the adsorbate and substrate, which points towards stronger binding and hence a lower E_{ads} -0.94 eV within GGA+ U . The other visible aspect is the strong polarisation of the H atom between the O^{OH} and O^{w} . This indicates a strong hydrogen bond as the $d_{(O^{\text{w}}-H^{\text{OH}})}$ is 1.4 Å. It also suggests the weakening of the OH bond of the H_2O molecule which leads to the increase of $d_{(\text{OH})}$ from 0.956 Å for a gas phase molecule to 1.10 Å on the surface.

This analysis can be further confirmed by the DOS and PDOS as shown in Fig. 6.6b,c within GGA and GGA+ U , respectively. Now we mainly focus on the DOS obtained within GGA+ U . The PDOS of O^{w} shows that the MOs of the H_2O molecule $1b_1$ and $3a_1$ hybridize strongly with $\text{Fe}_B(\text{S})$ - $3d$ band resulting in broadening and bonding/antibonding states. In the case of 1U/1F we see a peak related to the $1b_2$ orbital but in the present case it is absent which indicates its negligible interaction with the surface. On the other hand MOs of OH also interact strongly as visualized in charge density redistribution and can now be seen from the PDOS of O^{OH} . The general interaction of 1π and 3σ orbitals with $\text{Fe}_B(\text{S})$ - $3d$ states within GGA and GGA+ U follows the same bonding pattern as discussed in the case of 2D-1. Here we will

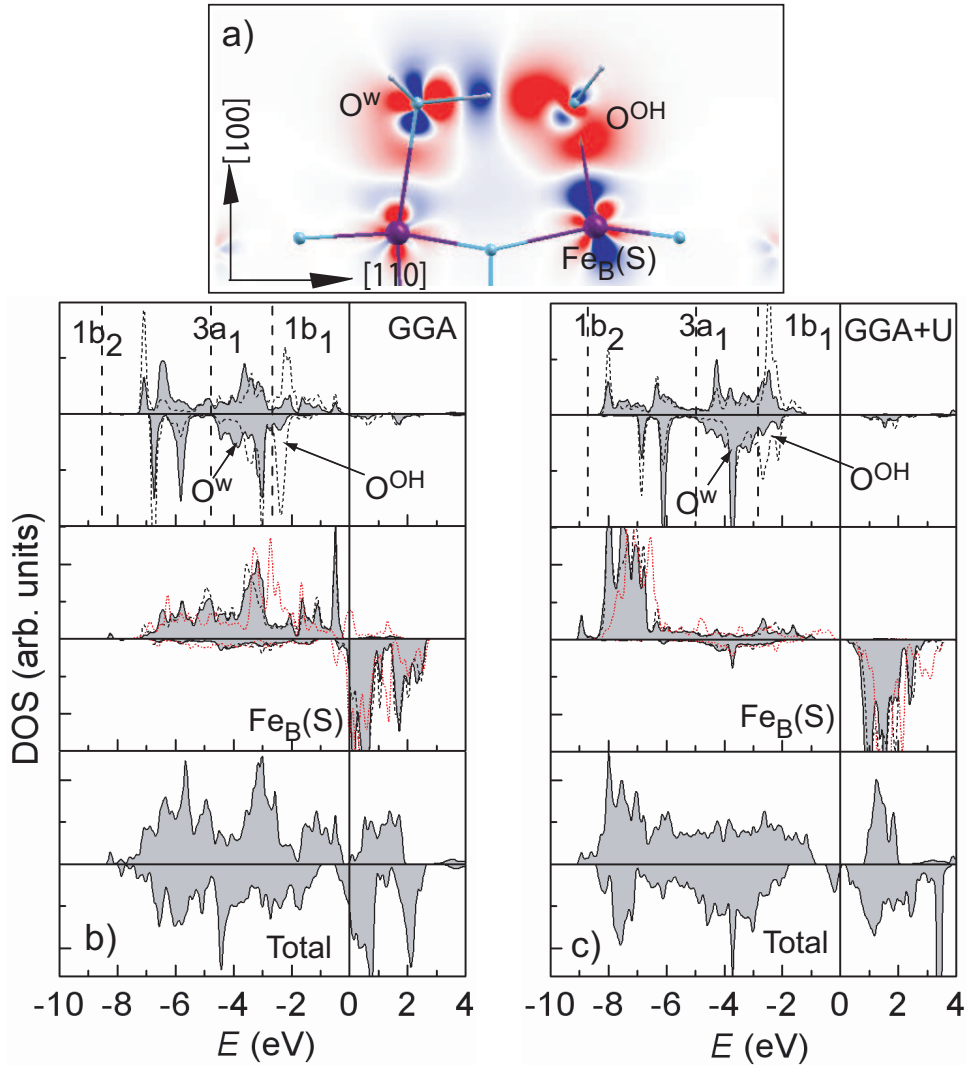


Figure 6.6: Electron density redistribution obtained within GGA+U upon adsorption of a water dimer in 2M-4 configuration is shown in a). Electron accumulation (depletion) is shown in red (blue). The DOS and PDOS within GGA and GGA+U are shown in b) and c) respectively. Top panel shows the PDOS of O^w in black and of O^{OH} in grey, Middle panel shows the PDOS of $Fe_B(S)$ in black and in red the $Fe_B(S)$ of modified B-layer, Bottom panel shows total DOS of the unit cell. We have also shown the relative position of the MOs of gas phase H_2O ($1b_1$, $3a_1$, $1b_2$) with vertical lines. Positions of O, Fe_B , and H are marked by cyan, purple and white circles.

explore additional features which appear due to the presence of a H_2O molecule and also other features which are responsible for providing higher stability to 2M-4. We notice that the degeneracy in the 1π orbital is completely lifted compared to the case of 2D-1 and 1D-1 and the individual $1\pi_x$ and $1\pi_y$ now show bonding/antibonding states along with broadening of the peaks. The first two peaks in the PDOS of O^{OH} represent these non-degenerate 1π orbitals

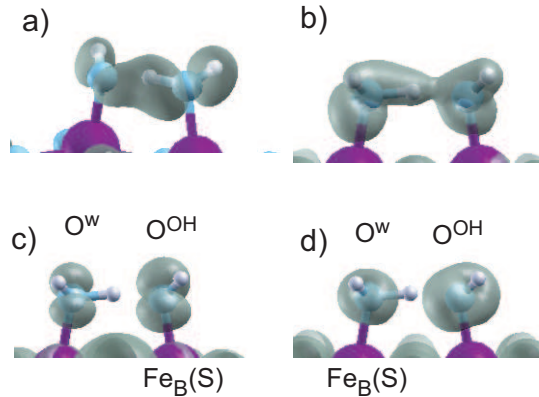


Figure 6.7: Charge density integrated in different energy ranges and the features of the MOs are shown. a) The $1b_2$ MO of H_2O interacts with 3σ of OH b) $3a_1$ of H_2O interacts with 3σ of OH, this feature is visible in DOS and is the reason for the $3a_1$ and 3σ to exactly span the same energy range, c) and d) shows two different orientations of 1π orbital in different energy range near E_F and both of them are non-degenerate as stated in the text.

and we can see their character after integrating charge around this region as shown in Fig. 6.7c,d. The hybridisation of 3σ with d_{xz}, d_{yz} is also more pronounced than in 1D-1 and 2D-1. A more careful look at the PDOS of O^w and O^{OH} shows that $3a_1$ and 3σ orbitals are strongly hybridized and in fact the peaks are spanning the same energy range. We further integrated the charge density in this energy range and found that $3a_1$ and 3σ orbitals are sharing the electron density as shown in Fig 6.7b. We also found that $1b_2$ and 3σ orbitals also interact as shown in Fig. 6.7a. The interaction of these MOs create bonding/antibonding states and those states which get hybridized with the surface are seen in the DOS.

At this point we will highlight the contribution of the hydrogen bond in the E_{ads} . The intermolecular interaction can be calculated in the following way. The total energy of the free standing adsorbate system ($E_{adsorbate}$) and then taking the frozen position of the adsorbates separately and converging them as: $1OH+H$ (E_{1OH+H}) and $1H_2O$ (E_{H_2O}). Now the intermolecular interaction energy is defined as: $E_{adsorbate}-E_{1OH+H}-E_{H_2O}$ which is 0.37 eV for the case of 2M-4 within GGA+ U . From E_{ads} of -0.94 eV, 0.37 eV comes from the intermolecular hydrogen bonds. This means that 0.57 eV is the contribution of the substrate-adsorbate bonding and this value is relatively close to the E_{ads} of 2F-3 or 2D-3. Within GGA the hydrogen bonding contribution is 0.22 eV. It is now quite clear that the intermolecular interaction is a prominent factor among others.

We find overall description of the electronic structure within GGA+ U is better. On the other hand we could also explain the main factors stabilising the mixed termination.

6.3 Structural properties

The structural changes in the surface layer due to adsorption of water molecule is an important aspect. The structural relaxations and electronic structure changes are interrelated. Additionally these structural details are helpful for comparison with experiments. The $d_{(\text{O}^{\text{OH}}-\text{Fe}_{\text{B}}(\text{S}))}$ and $d_{(\text{O}^{\text{w}}-\text{Fe}_{\text{B}}(\text{S}))}$ bond lengths generally differ due to chemisorption in the former case and physisorption in the latter case. In this Section we present results obtained within GGA+ U and wherever required GGA results are explicitly mentioned and used for comparison. The Table 6.2 and 6.1 lists all the relaxations of individual atoms in the surface layer. A schematic view of the top B layer is shown in Fig. 10.1.

2T-1 and 2F-2 (2 H_2O molecules in upright and flat/tilted adsorption model): First we consider the structural changes due to molecular adsorption in 2T-1 and 2F-2 configurations. The relaxations are listed in Table 6.1 and a side view with selected bond lengths are shown in Fig. 7.13. In the case of 2T-1 and 2F-2 the $\text{Fe}_{\text{B}}^{\text{H}_2\text{O}}$ relaxes away from the surface and the other $\text{Fe}_{\text{B}}(\text{S})$

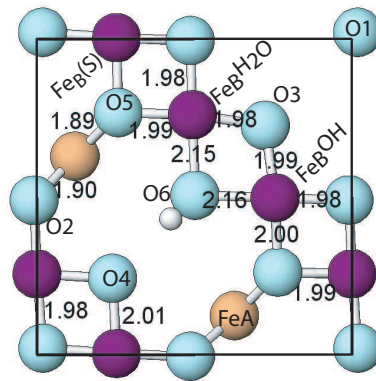


Figure 6.8: Top view of $2M-4$, also represents a schematic view of the surface B layer with all the lateral bond lengths. All the lengths are give in Å. Positions of O, Fe_{B} , and H are marked by cyan, purple and white circles.

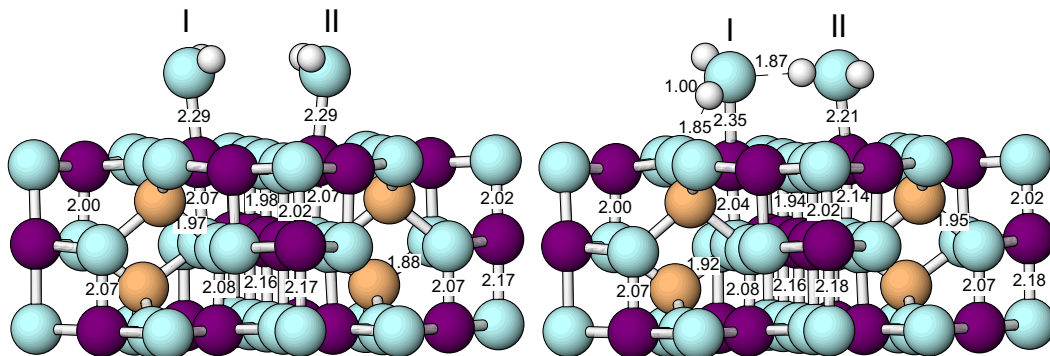


Figure 6.9: Side view of the relaxed 2T-1 (left panel) and 2F-2 (right panel) along with surface and sub-surface bond lengths. All bond lengths are given in Å and are obtained within GGA+ U . For color coding see Fig.10.1.

Table 6.1: Atomic relaxations of the surface layer obtained within GGA+U in the case of 2T-1 and 2F-2 are listed. The values in the parenthesis belong to the case of GGA. The Δz values typically represent relaxation along the surface normal, negative values indicate an outward or relaxation away from the surface while the positive means the opposite way. The numbering of the atom corresponds to those shown in Fig. 10.1. All distances are in Å.

	2T-1			2F-2		
	Δx	Δy	Δz	Δx	Δy	Δz
Fe _A (S)	0.02	-0.01	-0.15	0.00 (-0.00)	0.02 (0.02)	-0.16 (-0.14)
O1	-0.10	-0.10	-0.05	-0.10 (-0.15)	-0.09 (-0.11)	-0.05 (-0.02)
O2	0.07	0.03	-0.03	0.07 (0.10)	0.04 (0.05)	-0.03 (-0.01)
O3	0.08	0.08	-0.02	0.08 (0.09)	0.07 (0.08)	-0.02 (-0.01)
O4	0.08	0.08	0.03	0.08 (0.11)	0.09 (0.16)	0.00 (0.00)
O5	-0.04	-0.05	-0.00	-0.04 (-0.06)	-0.03 (-0.03)	-0.10 (-0.06)
O6	-0.09	-0.09	-0.01	-0.10 (-0.11)	-0.07 (-0.08)	0.04 (0.05)
Fe _B ^{H₂OI}	-0.03	0.02	-0.02	-0.03 (-0.04)	-0.03(-0.03)	0.02 (0.04)
Fe _B ^{H₂OII}				0.00 (0.00)	-0.02 (-0.03)	-0.10 (-0.07)
Fe _B (S)	-0.00	0.01	0.07	0.00 (-0.01)	0.03 (0.02)	0.06 (0.07)
O ^{H₂OI}	-0.17	0.18	-0.28	0.35 (0.35)	0.47 (0.46)	-0.24 (-0.24)
O ^{H₂OII}	-0.17	0.18	-0.28	0.14 (0.13)	0.45 (0.45)	-0.24 (-0.23)

sites without adsorbates on top relax towards the sub-surface layer, consistent with the observations made in Chapter 4 and 5. The magnitude of relaxation is very small (0.02-0.07 Å) when compared to other cases of 2D-1 and 2M-3 (Table 6.2). Stronger relaxation is observed in the case of O^w which relaxes away from the surface and also shows an appreciable lateral relaxation. O^w-I,II in the case of 2T-1 has an outward relaxation of 0.28 Å resulting in a bond length of 2.29 Å with the Fe_B(S). In fact this does not affect the sub-surface $d_{\text{Fe}_B(\text{S}-1)-\text{O}}$ compared to the bulk distance (2.06 Å). As discussed in Section 4.3, the change in the sub surface bond lengths reflects the extent of hybridisation. This means that 2T-1 shows physisorption and this is confirmed by the E_{ads} of -0.30 eV. In the case of flat adsorption 2F-3 (not shown here) and 2F-2 (Fig. 7.13 right panel), we see two different bond lengths for $d_{\text{O}^w-\text{Fe}_B(\text{S})}$. The possible reason for adsorbing at different heights is the hydrogen bond formation. As a consequence O^w participating in the acceptance of hydrogen bond has a longer bond length to the surface. In the case of 2F-3 there is only one hydrogen bond $d_{(\text{O}^w-\text{O}^w)}$ of 2.94 Å but in the case of 2F-2 two hydrogen bonds exist with 2.83 Å for $d_{(\text{O}^w-\text{O}^w)}$ and 2.66 Å for $d_{(\text{O}^w-\text{O}(\text{s}))}$. The two hydrogen bonds along with the tilting of the O^w-I make the 2F-2 termination

more interesting. The difference in the $d_{(\text{O}^{\text{w}}-\text{Fe}_{\text{B}}(\text{S}))}$ is 0.15 Å. The hydrogen atom which faces the O(S) is 1.0 Å away from the O^{w} which can be considered as a precursor for a possible dissociation of this molecule subsequently, leading to a mixed adsorption mode (Fig. 6.10 left panel). In both the systems, surface atoms without adsorbates on top tend to relax towards the sub-surface (S-1) layer while the atoms in the S-1 layer move away from the S-2 layer which is frozen.

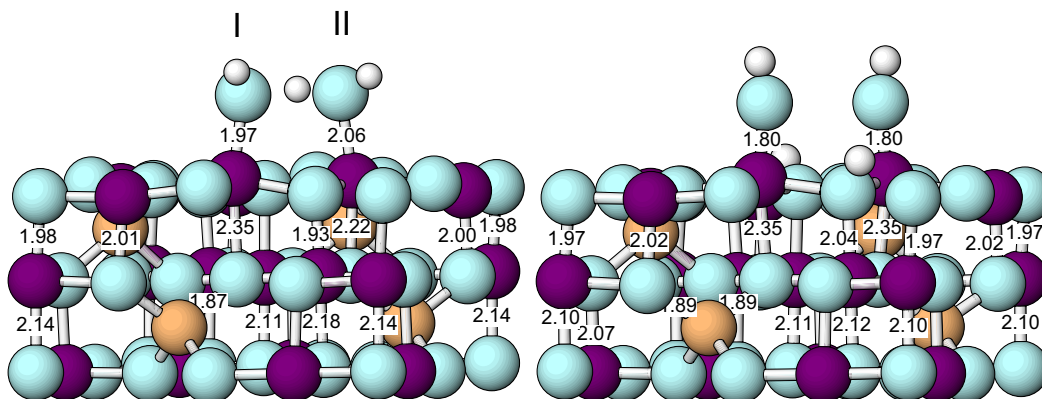


Figure 6.10: Side view of the relaxed 2M-4 (left panel) and 2D-1 (right panel) along with surface and sub-surface bond lengths. All bond lengths are given in Å and are obtained within GGA+U. For color coding see Fig.10.1.

2D-1 (two H_2O molecules in dissociated configuration): Now we look at the structural features of the 2D-1. Some of the characteristic bond lengths are shown in Fig. 6.10 right panel and the surface relaxations are listed in Table 6.2. The OH group being highly electronegative, forces the $\text{Fe}_{\text{B}}^{\text{OH}}$ to relax outwards by 0.28 Å resulting in $d_{(\text{Fe}_{\text{B}}(\text{S})-\text{O}^{\text{OH}})}$ of 1.80 Å and stretching the sub-surface $d_{(\text{Fe}_{\text{B}}(\text{S}-1)-\text{O})}$ bond by 0.29 Å compared to the bulk bond length (2.06 Å). If we compare 2D-1 with 1D-1, we find that $d_{(\text{Fe}_{\text{B}}(\text{S})-\text{O}^{\text{OH}})}$ has decreased by 0.03 Å and $d_{(\text{Fe}_{\text{B}}(\text{S}-1)-\text{O})}$ by 0.26 Å. An interesting observation comes from the $d_{(\text{Fe}_{\text{B}}(\text{S}-1)-\text{O})}$ under the O(S)-H site, which remains close to the bulk value. This is the reason for the 3σ peak of O(S)-H in 1D-1 to lie at lower energy than in 2D-1, and possibly contributes towards greater stabilisation. The lateral relaxations of O^{OH} and $\text{Fe}_{\text{B}}^{\text{OH}}$ is negligible indicating an on top adsorption. The $\text{Fe}_{\text{B}}(\text{S})$ sites which are not covered with adsorbates relax towards the surface while the adsorbed site relaxes outwards by 0.15 Å which is 0.10 Å less than in the case of 1D-1. The surface relaxations of O(S) are moreover comparable with 1D-1. The general trend in structural relaxation: the surface layer S relax towards the S-1 (except $\text{Fe}_{\text{B}}^{\text{OH}}$) layer and the S-1 layer moves away from the layer S-2 which is a frozen layer. The surface atom relaxations within GGA follow the same trends as in GGA+U even though in some cases the magnitude differs.

2M-4 (two H_2O molecules in mixed configuration): We now consider the most stable surface termination i.e. 2M-4. Fig. 6.10 left panel shows the side view with some of the selected bond lengths. The relaxation of the surface

Table 6.2: Atomic relaxations of the surface layer obtained within GGA+U in the case of 2M-3 and 2D-1 are listed. The values in the parenthesis belong to the case of GGA. The Δz values typically represent relaxation along the surface normal, negative values indicate an outward or relaxation away from the surface while the positive means the opposite way. The numbering of the atom corresponds to those shown in Fig. 10.1. All distances are in \AA .

	2M-4			2D-1		
	Δx	Δy	Δz	Δx	Δy	Δz
Fe _A (S)	0.01 (-0.01)	-0.02 (-0.03)	-0.16 (-0.07)	0.00 (-0.00)	0.00 (0.00)	-0.09 (-0.05)
O1	-0.13 (-0.18)	-0.12 (-0.18)	0.02 (0.06)	-0.07 (-0.15)	-0.07 (-0.15)	0.07 (0.06)
O2	0.05 (0.13)	0.03 (-0.03)	-0.07 (0.07)	0.11 (0.18)	-0.02 (-0.06)	0.08 (0.12)
O3	0.16 (0.16)	0.16 (0.15)	0.03 (0.12)	0.09 (0.09)	0.09 (0.09)	-0.03 (-0.01)
O4	0.03 (0.12)	0.04 (0.13)	0.02 (0.06)	0.08 (0.16)	0.08 (0.16)	0.07 (0.06)
O5	-0.10 (-0.17)	-0.03 (-0.01)	-0.00 (0.10)	0.02 (0.06)	-0.12 (-0.18)	0.08 (0.11)
O6	0.00 (-0.01)	0.02 (-0.01)	-0.06 (0.03)	-0.10 (-0.10)	-0.10 (-0.10)	-0.02 (-0.02)
Fe _B ^{H₂O}	-0.08 (-0.12)	0.04 (0.04)	-0.19 (-0.07)			
Fe _B ^{OH}	0.03 (0.04)	-0.05 (-0.13)	-0.29 (-0.22)	-0.12 (-0.15)	0.12 (0.15)	-0.28 (-0.25)
Fe _B (S)	-0.04 (-0.00)	-0.01 (-0.01)	0.08 (0.16)	0.01 (0.02)	-0.02 (-0.02)	0.15 (0.17)
O ^{H₂O}	0.12 (0.09)	-0.19 (-0.22)	-0.22 (-0.13)			
O ^{OH}	-0.15 (-0.14)	0.23 (0.20)	-0.23 (-0.12)	-0.01 (-0.01)	0.02 (0.02)	-0.06 (-0.03)

atoms are listed in Table 6.2 and a schematic top view of the B layer with lateral bond lengths is shown in Fig. 10.1. The fingerprint of this termination is the difference in the bond lengths of $d_{(\text{Fe}_B(\text{S})-\text{O}^{\text{OH}})}$ 1.97 \AA and $d_{(\text{Fe}_B(\text{S})-\text{O}^{\text{w}})}$ 2.06 \AA . The $d_{(\text{Fe}_B(\text{S})-\text{O}^{\text{w}})}$ bond length is similar to the bulk value of 2.06 \AA and the value within GGA is nearly the same. On the other hand an isolated H₂O molecule in 1F adsorbs 0.16 \AA higher. This points toward a stronger bonding in the present case. In fact, we do not find in any of the considered models where an intact H₂O molecule gets adsorbed at a distance comparable to the bulk bond length ($d_{(\text{Fe}_B-\text{O})}$). The H₂O molecule and the Fe_B^{H₂O} relax away from the surface by 0.22 \AA and 0.19 \AA , respectively, which results in stretching of sub-surface $d_{(\text{Fe}_B(\text{S}-1)-\text{O})}$ to 2.22 \AA . The O^{OH} and Fe_B^{OH} show similar relaxation pattern but the magnitudes are higher. The strong interaction of O^{OH} makes the Fe_B^{OH} move outwards by 0.29 \AA which results in $d_{(\text{Fe}_B(\text{S})-\text{O}^{\text{OH}})}$ of 1.97 \AA and an elongation of the subsurface $d_{(\text{Fe}_B(\text{S}-1)-\text{O})}$ to 2.35 \AA . In the case of 1D-1 the $d_{(\text{Fe}_B(\text{S})-\text{O}^{\text{OH}})}$ is 0.14 \AA and in 2D-1 it is 0.17 \AA lower than that in 2M-4. This indicates that OH in a mixed mode is less strongly bound than in the case of dissociated configurations (1D-1 or 2D-1).

The Fe_B(S) which are not covered by any adsorbates show a positive Δz of 0.08 \AA which means they relax opposite to the covered ones. The H₂O and OH do not prefer to sit on top of the Fe_B(S) but rather relax towards each other by ~ 0.5 \AA , which is also due to the hydrogen bond formation between them. The O^w donates the proton and the O^{OH} accepts the hydrogen bond with a distance

of $1.37 \text{ \AA} \text{ O} \cdots \text{H-O}$. The bond lengths shown in Fig. 6.10 left panel indicate that all the bond lengths between the S and S-1 layers actually contract by $\sim \pm 0.8 \text{ \AA}$ except the sites where adsorption took place, while the bond lengths between S-1 and S-2 layers tend to expand by $\sim \pm 0.5$ to 0.12 \AA . Another aspect to be noticed is the lateral bond elongation as shown in Fig. 10.1. We notice a general contraction in $d_{(\text{Fe}_B(\text{S})-\text{O}(\text{s}))}$ when compared to the bulk bond length except in the case where the H atom adsorbs. The site O(S)-H stretches the lateral bond length by 0.9 \AA and the H points to the opposite O(S) making a hydrogen bond with $d_{\text{O}(\text{S})\cdots\text{H}-\text{O}(\text{S})}$ of 3.13 \AA . The relaxation of O(S) in the z-direction is less when compared to the lateral relaxation. The surface Fe_A layer also relaxes away from the surface by 0.15 \AA thereby expanding the bond lengths. If we compare the surface atom relaxations within GGA and GGA+ U as listed in Table 6.2, we notice that in general the relaxation directions are similar.

6.4 Summary

We have studied more than 14 adsorption models for water dimer adsorption. The adsorption mode remains similar within GGA and GGA+ U unlike the case of a single H_2O molecule adsorption on a non-defective surface. The U parameter forces the lower Hubbard band of $\text{Fe}_B(\text{S})$ to move to lower energies thus populating different bonding/antibonding MOs of H_2O and OH and thereby creating a difference in E_{ads} . We find a crossover from dissociative mode of adsorption at single water molecule coverage to a mixed adsorption mode. In the mixed adsorption one of the H_2O molecules dissociates while the other molecule remains intact. The intermolecular interactions and hydrogen bond formation is the key reason for the stabilisation of this geometry and it is of the order of 0.37 eV from the E_{ads} of -0.94 eV . A complete lifting up of 1π degeneracy is also observed. We also predict two reaction mechanisms to arrive at a mixed mode configuration: In the first mechanism, the precursor is 2F-2 with two hydrogen bonds and along with the substrate interaction it is probable that most tilted H_2O molecule gets dissociated and we obtain the mixed configuration (2M-3). In the second mechanism: the substrate is already shown to dissociate H_2O molecule as shown in 1D-1 within GGA+ U . In the second step, intact H_2O molecules adsorb at the adjacent $\text{Fe}_B(\text{S})$ sites providing further stability with hydrogen bonding. A fingerprint of the mixed mode termination which makes it distinguishable from other terminations and is helpful in experimental identification are the two distinct bond lengths of $d_{(\text{Fe}_B(\text{S})-\text{O}^{\text{OH}})}$ (1.98 \AA) and $d_{(\text{Fe}_B(\text{S})-\text{O}^{\text{w}})}$ (2.09 \AA). These two vary because of the chemisorption in the former case and physisorption in the latter case.

Saturation Coverage

The mode of adsorption of H₂O molecules can change with coverage as shown in the case of Al₂O₃(0001) [87]. In turn coverage can be influenced by temperature and pressure of the atmosphere as well as by the exposure time to adsorbates [110]. In order to gain insight of the adsorption mechanism at higher coverages we have increased the number of H₂O molecules on the Fe₃O₄(001) surface so as to cover all surface cations, Fe_B(S). This leads to a coverage with four H₂O molecules per ($\sqrt{2} \times \sqrt{2}$)R45° surface unit cell. The mode of adsorption is investigated by adsorbing H₂O molecules in various geometries. In this case also, as in the case of a water dimer, we have considered possibility of including hydrogen bonds. The adsorption models are chosen based on their stability in the monomer and dimer cases. We have also investigated a full hydroxylated surface in which all the Fe_B(S) are covered with OH groups and all the O(S) are covered with H atom. Next, we have also checked hydrogenated model wherein all the O(S) atoms were adsorbed with H atoms. The energetic stability of each model is discussed in terms of its adsorption energies (E_{ads}) in Section 7.1. The E_{ads} energies are given in eV/molecule. To understand the energetic trends we have analyzed the electronic properties in Section 7.2. The effect of adsorption on the structural details and bond lengths are discussed in Section 7.3. We also investigated 0.5 ML A-layer termination which is discussed in Section 7.6.

7.1 Adsorption models and energetic stability

We have considered different adsorption models for the four water molecules coverage. The top view of the most stable and prominent models in this coverage regime are shown in Fig. 7.1 along with their respective E_{ads} . The adsorption energies within GGA and GGA+ U show a similar trend as in the case of water dimer adsorption. In the following, we first discuss the stability of each model within GGA and then within GGA+ U .

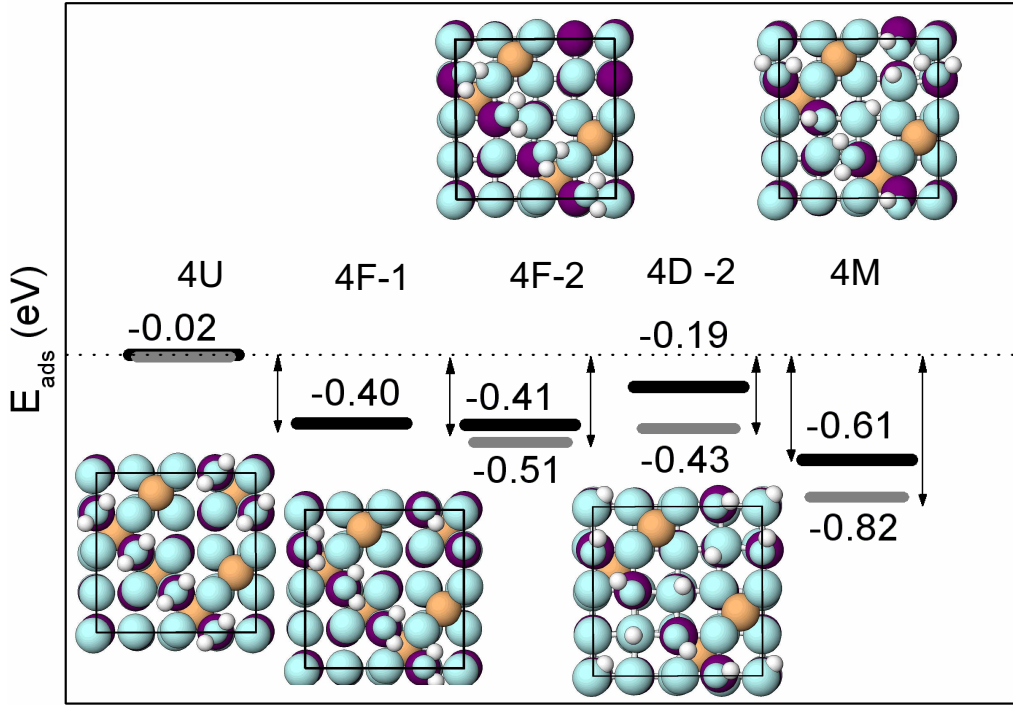


Figure 7.1: Top views of some selected adsorbate geometries from the four water molecule per $(\sqrt{2} \times \sqrt{2})R45^\circ$ -unit cell coverage. The figure above shows their corresponding adsorption energies (in eV per molecule). GGA (GGA+U) results are given by a solid black (grey) line. Positions of O, Fe_B, Fe_A, H are marked by cyan, purple, orange and white circles. The oxygens of the adsorbate are marked by smaller circles.

GGA: The adsorption of four H₂O molecules in an upright configuration (4U) gives a vanishing E_{ads} unlike the relatively high values obtained in the case of 1U and 2U-1 (0.39-0.62 eV). A further structural optimisation of this model with the pseudopotential code VASP [76] results in configuration 4T-1 as shown in Fig. 7.2. The E_{ads} of 4T-1 is 0.30 eV more favorable than that of 4U. This lowering of energy is because of the change in orientation of H₂O molecules. In 4T-1, two of the four H₂O molecules make an angle $\angle\text{Fe}_B(\text{S})\text{-O}^w\text{-H}$ of 105.4° , while the other two tilt further down with an angle of 65.4° , leading to the formation of hydrogen bond with the surface oxygens. In this configuration there are no intermolecular hydrogen bonds.

In the next model we consider the most preferable orientation of water molecules on the Fe₃O₄(001) surface, i.e., parallel to the surface (flat orientation) as has already been discussed in the case of 1F-1 (Section 4.1) and 2F-2 (Section 6.1). In Chapter 6, we came across two models 2F-2 and 2F-3 which not only have a flat/tilted adsorption of H₂O molecules but also allow intermolecular hydrogen bond formation. Following similar adsorbate configurations, here we have considered the 4F-1 and 4F-2 configurations as shown in Fig. 7.2. In 4F-1, each H₂O molecule accepts and donates a hydrogen bond

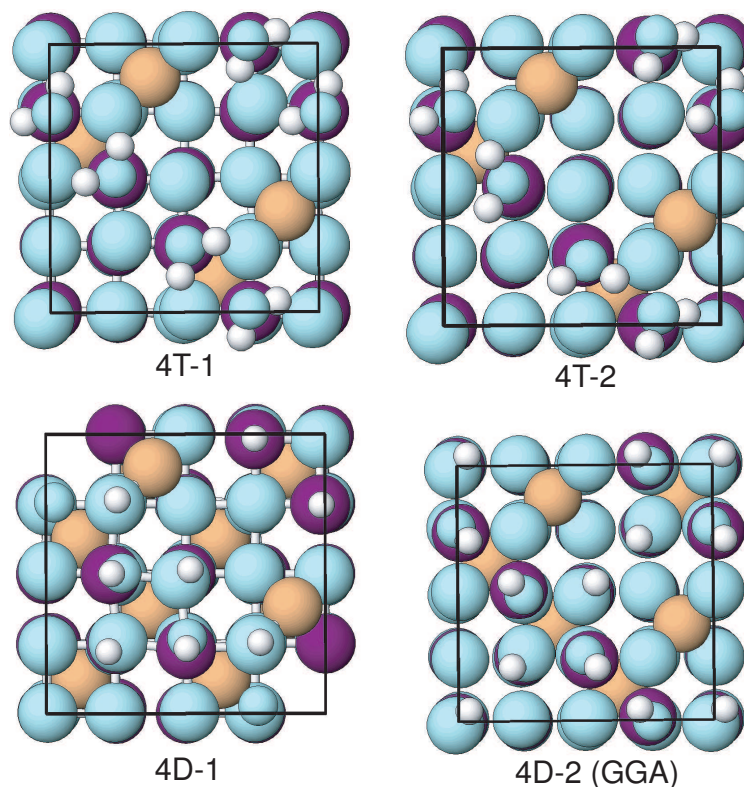


Figure 7.2: Top views of some selected configurations with four water molecule per $(\sqrt{2} \times \sqrt{2})R45^\circ$ -unit cell which are energetically less favorable than those shown in Fig. 7.1. They are shown here in order to assess the structural changes and other stabilising factors. O, Fe_B , Fe_A , H are marked by cyan, purple, orange and white circles. The oxygens of the adsorbate are marked by smaller circles.

with the neighboring H_2O molecules, thus forming a linear chain on top of the $Fe_B(S)$ row while in the case of 2F-2 alternating H_2O molecules either accept or donate a hydrogen bond. The $O^w-H \cdots O^w$ bond length of 2.97 Å is similar in 4F-1 and in 2F-3. Now we discuss the 4F-2 configuration wherein the H_2O molecules form pairs rather than a continuous chain as in 4F-1. However, the E_{ads} is nearly identical to that of 4F-1. A similar trend is observed between 2F-2 and 2F-3. In 4F-2, within a pair of H_2O molecules, one of H_2O molecule donates a hydrogen bond to another H_2O molecule and to a neighboring $O(S)$, while the other H_2O molecule, which accepts the hydrogen bond is highly tilted pointing with one of its H atom towards the $O(S)$ giving rise to a hydrogen bond, while the other H points away from the surface. In this way we have two hydrogen bonds per pair of H_2O molecules. This difference in orientation of H_2O molecules leads to a difference in $d_{Fe_B(S)-O^w}$ by 0.08 Å while in the case of 2F-2 it is 0.14 Å. The addition of a pair of H_2O molecules to 2F-2 will lead to 4F-2 configuration with a 0.03 eV increase in the E_{ads} . This clearly conveys a negligible interaction between the pairs of water molecules and therefore in

this adsorption model the effect of coverage is negligible.

In the next adsorption configuration we partially dissociate the adsorbate overlayer leading to a mixed mode of adsorption (4M) as shown in Fig. 7.2. This is the most stable mode of adsorption with an E_{ads} of -0.61 eV. In this configuration two of the H_2O molecules are intact while the rest are dissociated and thus forming two pairs of OH- H_2O . The lowest E_{ads} is attributed to the formation of four hydrogen bonds: two $\text{O}^{\text{w}} \cdots \text{O}^{\text{OH}}$, one between $\text{O}(\text{S})\text{-H} \cdots \text{O}(\text{S})$ and one between $\text{H}(\text{O}(\text{S})) \cdots \text{O}^{\text{OH}}$. The 4M configuration can also be achieved by adding a pair of OH- H_2O to 2M-4 which decreases the E_{ads} by 0.20 eV for the latter case. This decrease in E_{ads} is attributed to the intermolecular repulsion with increase in coverage.

The last adsorption model is the fully dissociated configuration. In this mode of adsorption we have considered two different geometries i.e. 4D-1 and 4D-2. In 4D-1, as shown in Fig. 7.2, we adsorb four OH groups on top of $\text{Fe}_B(\text{S})$ sites and H atoms are adsorbed on adjacent $\text{O}(\text{S})$ sites. In 4D-1 some of the $\text{O}(\text{S})$ sites chosen have $\text{Fe}_A(\text{S})$ as neighbor. In the case of 4D-2, none of the $\text{O}(\text{S})$ sites have an $\text{Fe}_A(\text{S})$ neighbour. As already mentioned in Section 6.1, the $\text{O}(\text{S})$ neighboring $\text{Fe}_A(\text{S})$ are less reactive than those without. In fact, in the present case we find that 4D-2 is 1.71 eV higher in total energy than 4D-1 in magnitude. The E_{ads} of 4D-2 is 0.16 eV lower than 4D-1 and interestingly the E_{ads} of the latter case is nearly zero (0.02 eV).

GGA+U: We now discuss the stability of the above described adsorption models within GGA+U. The E_{ads} of the upright adsorption 4U is nearly zero (-0.02 eV). Further structural optimisation of 4U using the pseudopotential code VASP [76] results in a configuration 4T-2 as shown in Fig. 7.2. Here all four H_2O molecules are flat adsorbed similar to 4F-2 except that the H_2O molecules which are not highly tilted now face each other. The E_{ads} of 4T-2 is 0.51 eV lower than that of 4U. The E_{ads} of 4U is nearly degenerate within GGA and GGA+U while this is not true for the case of 1U and 2U-1.

Among the flat adsorption models, only 4F-2 is considered within GGA+U as 4F-1 was already found less favorable within GGA. The E_{ads} of 4F-2 is -0.51 eV which is 0.07 eV lower than in 2F-3. The most stable termination, i.e., mixed adsorption mode 4M has an E_{ads} of -0.82 eV which is ~ 0.20 eV higher than that within GGA. It is 0.30 eV more favorable than 4F-2 and 0.40 eV more favorable than 4D-2. Interestingly the E_{ads} decreases from 2M-4 to 4M by 0.12 eV which is attributed to intermolecular repulsion. In terms of surface energy, the 4M termination has the lowest and is the most stable phase in the surface phase diagram.

Finally we look at the possibility of a fully dissociated configuration. The 4D-1 within GGA is less favorable and hence is not considered within GGA+U. The E_{ads} of 4D-2 is -0.43 eV, which is 0.24 eV lower from that within GGA. We would like to mention some differences in the final optimized structure of 4D-2 obtained within GGA and GGA+U. The respective top views are

shown in Fig. 7.1 and in Fig. 7.2. The main difference is that within GGA+ U the OH groups are tilted making an $\angle\text{Fe}_B(\text{S})\text{-O}^{\text{OH}}\text{-H}$ of $123.35^\circ/109.9^\circ$ along with a hydrogen bond in between, while in GGA the angle is 133.19° and the OH groups point away from each other. Interestingly the comparison of E_{ads} between 4D-2 and 2D-3 reveals, that 2D-3 is more stable than 4D-2 as the E_{ads} of 2D-3 is 0.17 eV higher. A careful look at the top view of 2D-3 (Fig. 6.1), 4D-2 and 4M gives us a rough picture of the surface reaction. The addition of two dissociated H_2O molecules to 2D-3 leads to the 4D-2 configuration which results in an increase of E_{ads} by 0.17 eV. On the other hand, if we add two intact H_2O molecules we realize 4M configuration which lowers the E_{ads} by 0.25 eV. This comparison actually reaffirms that 2D-3 is an alternate route for reaching 4M compared to the partial dissociation from the case of 4F-2 or 2F-3.

7.2 Analysis of the electronic structure

In this Section we will discuss the changes induced in the electronic structure with the adsorption of four H_2O molecules and compare the changes with that of single H_2O and two H_2O molecule coverage.

4U within GGA (Four H_2O molecules in upright configuration): Fig. 7.3 shows density of states (DOS) and projected density of states (PDOS) in the case of 4U within **GGA**. The DOS within GGA+ U is not analyzed in the present case as the E_{ads} is nearly zero and does not show any coverage dependence. However, the DOS for low coverages (1U and 2U-1) are discussed in detail in the previous Chapters and can be extended to the present case as well. The variation of E_{ads} within GGA from significant values in 1U and 2U-1 to nearly zero in the case of 4U is analyzed with the help of DOS. The majority of $\text{Fe}_B(\text{S})\text{-}3d$ states span the energy range from -6 eV to E_{F} which results in a stronger hybridisation with $1b_1$ orbital leading to broadening and bonding/antibonding splitting. By comparing the PDOS of O^{w} in 1U, 2U-1 and 4U, we notice the following : 1) The energy range spanned by the $1b_1$ orbital is the same i.e. from -6 to -3 eV; 2) The $1b_1$ peaks in the case of 1U and 2U-1 are similar except in 4U where it shows further splitting that can be attributed to an adsorbate-adsorbate interaction. In all the three cases (1U, 2U-1, 4U) the $3a_1$ orbital is localised, however, in 4U it shows an additional peak splitting. In a similar way the $1b_2$ peak is also highly localised at -10 eV (absent in the case of 1U). Thus the decrease in E_{ads} with the increase in coverage and finally to nearly zero in the case of 4U is attributed to the strong repulsive interaction between the upright H_2O molecules and to a weaker hybridisation with the $\text{Fe}_B(\text{S})\text{-}3d$ states.

In 4U $d_{\text{Fe}_B(\text{S})\text{-O}^{\text{w}}}$ increases by 0.10/0.07 Å compared to 1U/2U-1, respectively, which reaffirms the weak hybridisation. The PDOS of O(S) show more states near the Fermi level while those of O^{w} are shifted towards lower ener-

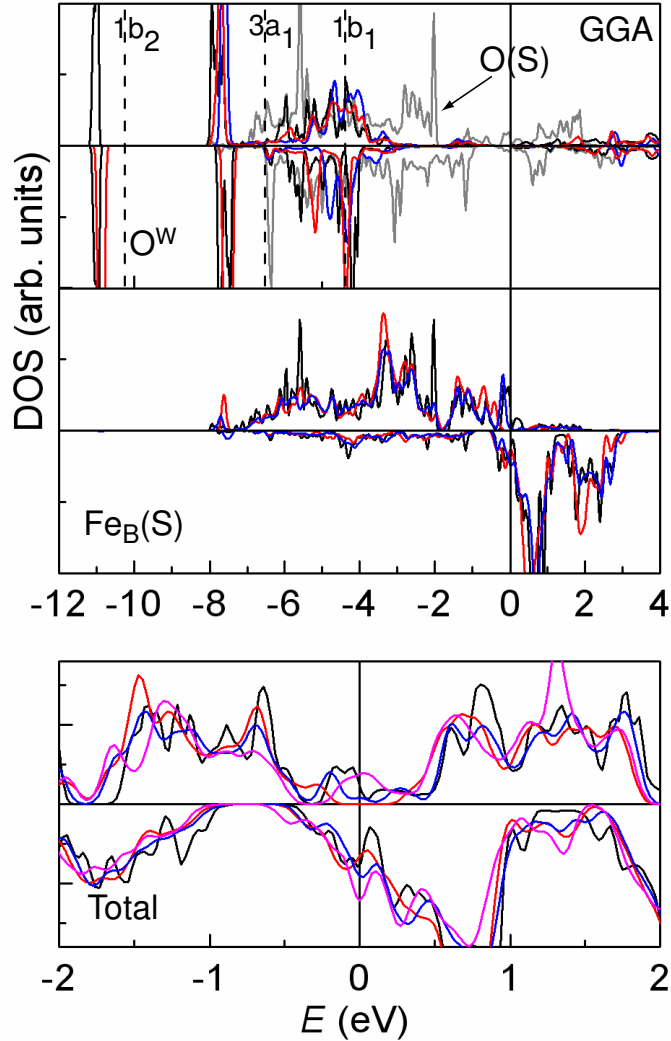


Figure 7.3: Density of states (DOS) and projected density of states (PDOS) of 4U within GGA. Top panel: PDOS of O^w in 4U (black solid line), 2U-1 (blue line), 1U (red line), and of O(S) (light grey line), Middle panel: PDOS of $Fe_B(S)$ in 4U (black solid line), 2U-1 (blue line) and 1U (red line), Bottom panel: total DOS of 4U, 2U-1, 1U and modified B-layer (magenta curve). The vertical dashed lines represent the molecular levels of the isolated gas phase H_2O molecule.

gies. Another interesting aspect can be seen from the bottom panel of Fig. 7.3, which shows the total DOS for 1U, 2U-1, 4U and the clean surface. The states around the E_F in the case of modified B-layer (clean surface) which points towards a metallic behavior within GGA [25] now gets completely depleted with the adsorption of a single H_2O molecule in 1U configuration. This makes the system with adsorbates half metallic. As we increase the coverage to two and four H_2O molecules, the states near the E_F start increasing and metallic character is regained.

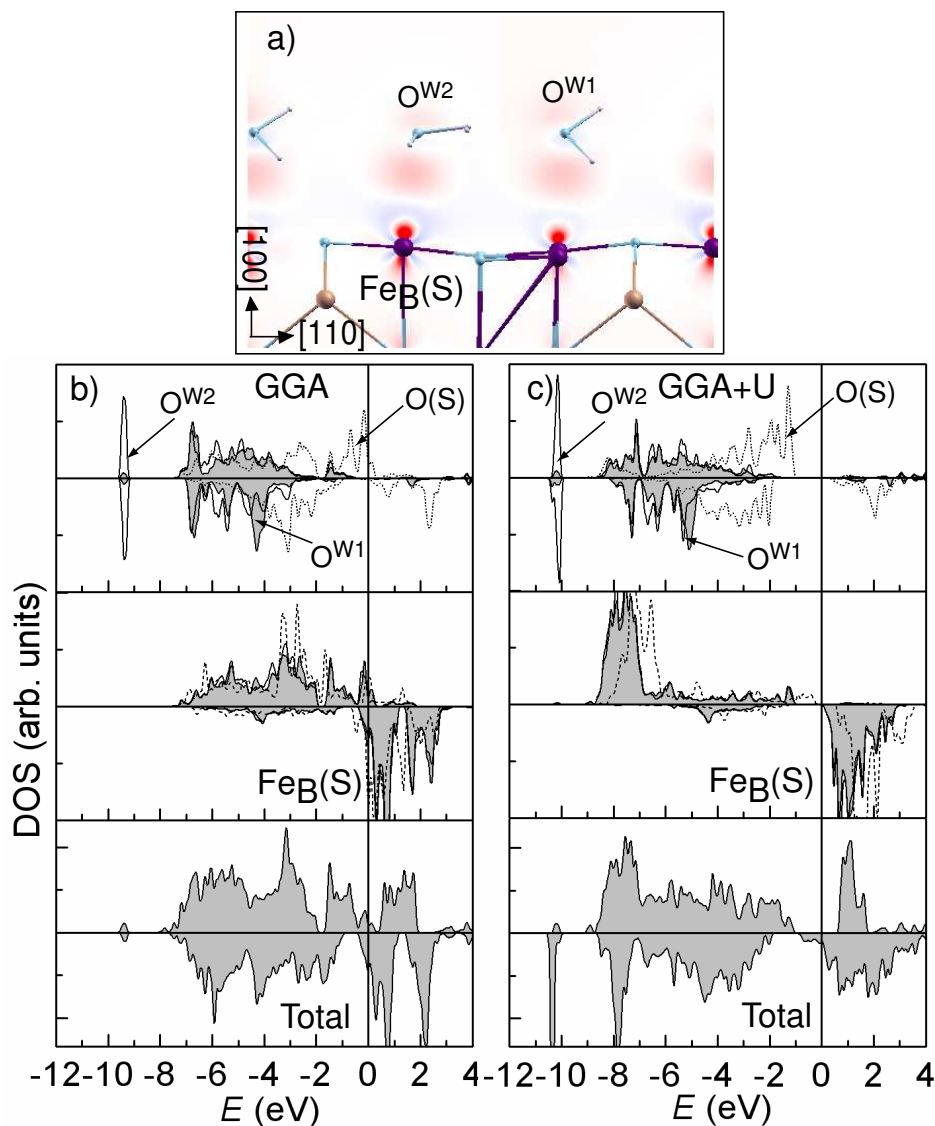


Figure 7.4: a) Electron density redistribution ($\Delta(\rho)$) with the adsorption of four H_2O molecules in 4F-2 configuration obtained within GGA+U. The accumulation/depletion of charge is shown in red/blue colour, respectively. The DOS and PDOS are shown in b) and c) within GGA and GGA+U, respectively. Top panel shows the PDOS of O^{W1} (grey filled curve) and O^{W2} (black solid line), as labeled in (a), along with that of $O(S)$ (black dotted line), Middle panel: shows PDOS of $Fe_B(S)$ in 4F-2 (black solid line) and in modified B-layer (black dashed line), Bottom panel: shows the total DOS of the system.

4F-2 (Four H_2O molecules in flat/tilted configuration): Next we discuss the case of 4F-2 which is the second most stable configuration. Fig. 7.4a shows the electron density redistribution upon adsorption of four H_2O molecules within GGA+U. The electron density redistribution within GGA is similar and therefore is not shown here. We see an accumulation of charge in the d_{z^2} orbital of

the $\text{Fe}_B(\text{S})$ which confirms the electron redistribution in the surface cations. The linear chain of H_2O molecules shifts laterally by $\sim 0.5\text{-}0.6$ Å parallel to (110) direction from the atop site on $\text{Fe}_B(\text{S})$ row. As a result Fig. 7.4a shows a plane perpendicular to the $\text{Fe}_B(\text{S})$ site and does not contain the H_2O row. However, we do notice some partial charge redistribution between $\text{Fe}_B(\text{S})$ and O^w . This is further confirmed by the DOS and PDOS as shown in Fig. 7.4b and c within GGA and GGA+ U respectively. The top panels show the PDOS of $\text{O}^{\text{W}1}$, $\text{O}^{\text{W}2}$ and $\text{O}(\text{S})$. The schematic representation of these O atoms can be seen in Fig. 7.4a. As stated earlier the difference in the tilting of $\text{O}^{\text{W}1}$ ($\angle\text{Fe}_B(\text{S})\text{-O}^{\text{W}1}\text{-H} = 72.51^\circ$) and $\text{O}^{\text{W}2}$ ($\angle\text{Fe}_B(\text{S})\text{-O}^{\text{W}2}\text{-H} = 103.02^\circ$) creates a difference in the $d_{\text{Fe}_B(\text{S})\text{-O}^w}$ by 0.10 Å within GGA+ U . If we compare the PDOS of $\text{O}^{\text{W}1}$ and $\text{O}^{\text{W}2}$, we do not see any appreciable change except some minor ones which are more visible within GGA.

A weak interaction is suggested between the $\text{Fe}_B(\text{S})\text{-}3d$ states and the MOs of the H_2O because the tilt angle and difference in heights do not produce any substantial change in the PDOS. This clearly indicates that only a large intermolecular interaction can be responsible for the appreciable E_{ads} in this configuration. In fact, as mentioned earlier, in some cases the adsorbate-adsorbate interaction can be larger than the adsorbate-substrate interaction [32]. The hybridisation mechanism between the $\text{Fe}_B(\text{S})\text{-}3d$ states and the MOs of H_2O follow the same trend as given for 1F within GGA and GGA+ U . However, we observe additionally $1b_2$ orbital which is strongly localised at -9.2 eV within GGA and at -10.0 eV within GGA+ U . The $1b_2$ peak of $\text{O}^{\text{W}1}$ is more pronounced than that of the $\text{O}^{\text{W}2}$ which is attributed to the different tilt angles. Other features which we observe from the DOS are: the PDOS of $\text{O}(\text{S})$ is higher in energy than that of $\text{O}^{\text{W}1}$ and $\text{O}^{\text{W}2}$, indicating relatively strong hybridisation in the latter case. We also notice that the $\text{Fe}_B(\text{S})\text{-}3d$ states shift to lower energy compared to the modified B-layer (clean surface). In the total DOS, within GGA we observe states in the majority spin channel near the Fermi level pointing towards a metallic character, while within GGA+ U the states are shifted to a lower energy and the band gap in the majority spin channel suggests half metallic character.

4D-2 (Four H_2O molecules in dissociated configuration): Next we look at the electronic structure of the dissociated configuration 4D-2. The electron density redistribution upon adsorption within GGA+ U is shown in Fig. 7.5a. A strong charge redistribution pattern is observed with the accumulation of charge in the 1π orbital of the OH group along with a depletion in the d_{z^2} orbital of the $\text{Fe}_B(\text{S})$. According to the charge donation and back donation mechanism explained for the OH group in Section 4.2, here we see a depletion of charge in the 3σ orbital and an accumulation of charge in the $d_{xz,yz}$ orbital. In this configuration, the OH groups are tilted leading to the formation of a hydrogen bond. It is important to note that an OH group is not only a good hydrogen bond acceptor but also a hydrogen bond donor, even though it is

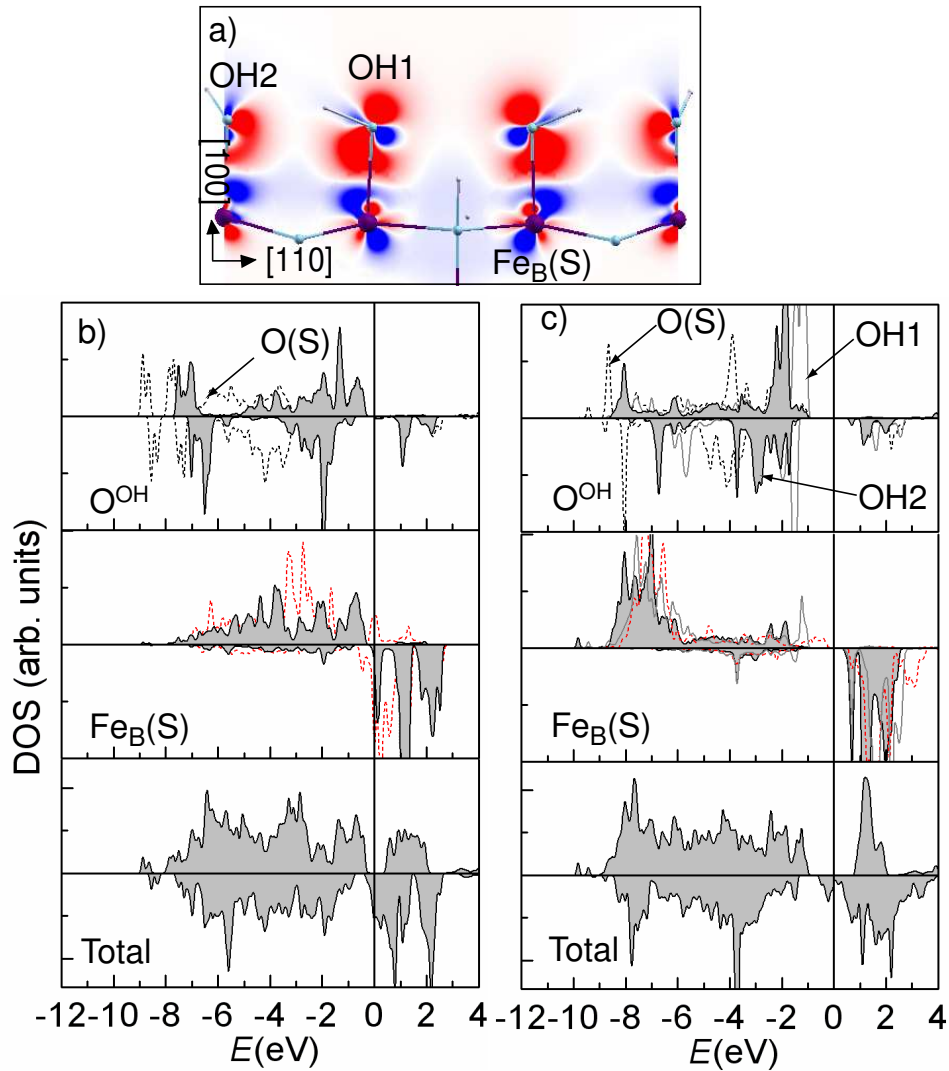


Figure 7.5: Electron density redistribution ($\Delta(\rho)$) with the adsorption of four dissociated H_2O molecules in 4D-2 configuration obtained within GGA+U is shown in a), the accumulation/depletion of charge is shown in red/blue colour respectively. The DOS and PDOS are shown in b and c within GGA and GGA+U respectively. Top panel shows the PDOS of OH1 and OH2, as labeled in (a), along with that of O(S) is shown, Middle panel shown PDOS of Fe_B(S) of 4D-2 in black solid line and that of modified B-layer in red dotted line, Bottom panel shows the total DOS of the unit cell.

weaker in this respect when compared to a H_2O molecule [111]. Unlike the case of 2D-1, where the 1π orbital was not tilted, in this case we see a large tilt angle, also for the d_{z^2} orbital. As shown in Fig. 7.5a OH1 is the hydrogen bond donor and OH2 is the hydrogen bond acceptor, due to which we see the tail of charge accumulation near the OH2. The type of bonding is nearly ionic as the charge transfer between orbitals is complete.

We can further analyze 4D-2 with the help of DOS and PDOS as shown in Fig. 7.5b and c within GGA and GGA+ U respectively. The PDOS of OH1 and OH2 within GGA does not show any difference since the $\angle\text{Fe}_B(\text{S})\text{-O}^{\text{OH}}\text{-H}$ is the same, whereas in the case of GGA+ U due to the difference in the tilt angles by $\sim 13.6^\circ$, we see a shift of OH2 states to lower energy. The hybridisation mechanism of the MOs of the OH group with that of the $\text{Fe}_B(\text{S})\text{-}3d$ states, described in the previous Chapters for 1D and 2D-1, applies equally to the present case both within GGA and GGA+ U . To avoid repetition we look at some additional features. Within GGA+ U the 1π orbital in the case of OH2 shows stronger peak splitting than in OH1 along with slight lifting up of degeneracy in the 1π orbital. On the other hand, the 3σ states show bonding/antibonding splitting within GGA+ U but within GGA the magnitude of splitting decreases due to fewer $\text{Fe}_B(\text{S})\text{-}3d$ states present in that energy range which implies weaker hybridisation. The $\text{Fe}_B(\text{S})\text{-}3d$ band with OH1 and OH2 on top within GGA shows no difference while within GGA+ U they vary due to the different tilt angles. The $3d$ band of the $\text{Fe}_B(\text{S})$ with OH2 on top shifts strongly towards the E_F compared to the $\text{Fe}_B(\text{S})$ with OH1 on top. The states around E_F in case of GGA are depleted when compared to modified B-layer due to adsorption of H_2O , while in the case of GGA+ U the states shift further towards lower energy. The total DOS shows that both within GGA and GGA+ U , we observe half metallic character. The only difference lies in the minority spin states where different atoms contribute to the DOS at E_F . Within GGA these states come from surface and sub-surface $\text{Fe}_B(\text{S})$ atoms while within GGA+ U only sub surface layers contribute to these states.

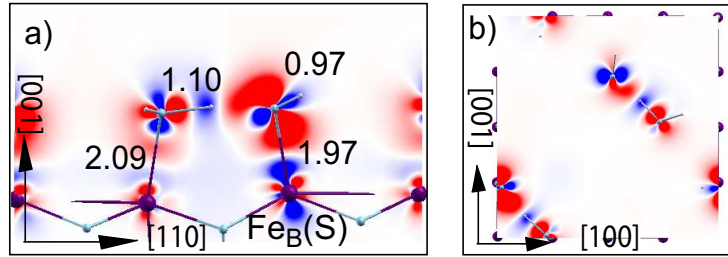


Figure 7.6: *Electron density redistribution upon adsorption of four H_2O molecules in 4M configuration is shown in a) and b). The pattern is obtained within GGA+ U . The red/blue colors represent charge accumulation/depletion.*

4M (Four H_2O molecules in mixed mode configuration): Finally, we discuss the electronic structure of the most stable termination 4M. The electron density redistribution upon adsorption is similar both within GGA and GGA+ U and therefore only the GGA+ U result is shown in Fig. 7.6a and b. However, GGA and GGA+ U differ in the $\text{Fe}_B(\text{S})\text{-}3d$ orbital involved in the hybridisation process as was also seen in the case of 2M-4. Fig. 7.6a shows that the electron density in the $1b_1$ orbital of H_2O molecule is partly localized into the surroundings to reduce Pauli repulsion while accumulation of electron density

at $\text{Fe}_B(\text{S})-d_{z^2}$ orbital shows its prime importance in bonding. The $\text{Fe}_B(\text{S})$ with OH group on top donates charge via the d_{z^2} orbital to the 1π orbital of the OH group. We also notice the depletion of charge from the 3σ orbital and accumulation in the $d_{xz,yz}$ orbitals. This pattern of electron density redistribution is similar to the one observed for 2M-4, which indicates an increase in coverage does not alter the charge donation and back donation mechanism within the mixed mode of adsorption. The E_{ads} energy decreases by 0.12 eV from 2M-4 to 4M. This is attributed to the intermolecular repulsive interaction. We have divided H_2O -OH pairs into two groups: W1-OH1 and W2-OH2 as shown in Fig. 7.7a. This is done because each pair acts almost independently, which can be correlated to the distance between consecutive oxygens: $d_{(\text{O}^{\text{W1}}-\text{O}^{\text{OH1}})}$ is 2.51 Å and $d_{(\text{O}^{\text{W1}}-\text{O}^{\text{OH2}})}$ is 3.21 Å.

The density of states (DOS) and projected density of states (PDOS) of 4M is shown in Fig. 7.7 and in Fig. 7.9 within GGA and GGA+ U respectively. The interaction of the MOs of a H_2O molecule or a OH group with that of the $\text{Fe}_B(\text{S})-3d$ states was already discussed in the case of 2M-4 (Section 6.2) and can be fully extended to the present case. In order to avoid the same discussion we highlight some major changes with the increase in coverage.

GGA: We will start by discussing the changes within GGA. The top panel in Fig. 7.7 d and e, shows the PDOS of the O atom of various adsorbates (W1,W2,OH1 and OH2). We notice two additional peaks in the case of W2-OH2 at -7.97 eV and at -9.24 eV that are absent in the case of W1-OH1. The former is attributed to the $3a_1$ peak and the latter to the $1b_2$ peak. The possible reason for the absence of these additional peaks in W1-OH1 is due to the structural differences between the pairs (W1-OH1 and W2-OH2). We notice that in the present case (4M) the $3a_1$ orbital not only shows bonding/antibonding states but also further splits, giving rise to an additional peak namely the $3a_1-1$. This type of splitting is not observed in 4F-2 or 4U but is seen in 2M-4. Thus we can conclude that it is a characteristic feature of the mixed adsorption mode. The hydrogen bond between the $\text{O}^{\text{W}} \cdots \text{O}^{\text{OH}}$ is responsible for the $3a_1-1$ peak. The splitting of $3a_1$ is more prominent in the case of W2-OH2 than in W1-OH1. The $3a_1-1$ peak is concurrent with the 3σ peak of OH. To ascertain the character of this peak we integrated the charge density from -7.25 to -6.75 eV and from -6.5 to -6.0 eV as shown in Fig. 7.7 c and d respectively. In Fig. 7.7c, the $3a_1$ orbital can be recognized from its shape around the H_2O molecule while in Fig. 7.7b the orbital has similarities with 3σ . It is known that $3a_1$ results from the linear combination of the $\text{O}(2s \text{ and } 2p_z)$ orbitals and the $\text{H}(1s)$ orbital, but if we remove the contribution of one of the H atoms, we end up with an orbital as shown in Fig. 7.7 b i.e. $3a_1-1$. The $3a_1-1$ peak individually shows bonding/antibonding splitting and is also responsible for the additional peak at -7.97 eV.

We also partly attribute additional stability of the 4M configuration to the formation of the $3a_1-1$ orbital. In order to compare the change in electronic structure with coverage, Fig. 7.8a top panel shows the PDOS of O^{W1} , O^{W2}

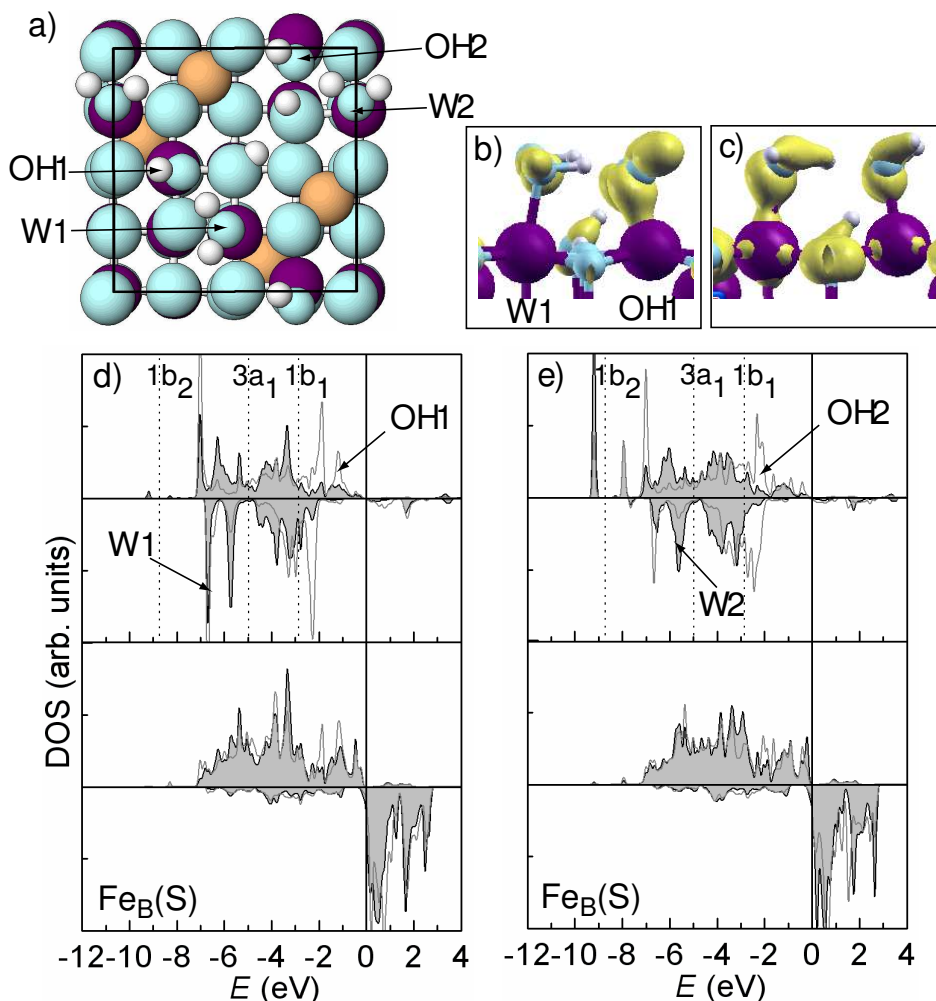


Figure 7.7: DOS, PDOS and electron density redistribution upon adsorption of 4M within GGA. a) schematic top view of 4M along with labeling of adsorbate atoms (W1, W2, OH1 and OH2) b) charge density integrated in the energy range -6.75 to -7.25 eV. c) charge density integrated in the energy range -6.0 -6.5 eV. d) and e) Top panel: PDOS of O^{W1} , O^{W2} (grey filled curves) and O^{OH1} , O^{OH2} (light grey line). Bottom panel: PDOS of $Fe_B(S)$ -3d with intact water molecule on top (grey filled curve) and OH on top (light grey curve). The MOs of the isolated H_2O molecule are shown with vertical dotted lines. Positions of O, Fe_B , and H are marked by cyan, purple and white circles.

in 4M, O^w in 2M-4 and O^w in 1F. In 1F we observe only $3a_1$ states whereas in 2M-4 and 4M we see $3a_1$ and $3a_1-1$ states. The PDOS of O^w in 2M-4 is similar to that of $O^{W1/W2}$ in 4M, the only difference is due to the additional peaks observed for the case of O^{W2} as discussed above. The PDOS of OH1 and OH2 are shown in Fig. 7.7d and e. We notice splitting of the 1π orbital in the energy range of -1 to -3 eV which points to the lifting up of degeneracy unlike in the case of 4D-2 where it was not complete. Since 1π is the highest

occupied molecular orbital (HOMO), any shift of the peak towards the Fermi level is more desirable and in the present case this is achieved due to peak splitting. The difference between PDOS of OH1 and OH2 lies again in the two additional peaks as was found and discussed in the case of O^{W2} . This also implies that the 3σ orbital shows an additional splitting and hybridizes with $3a_1$ and $1b_2$ orbitals of $W2$.

A comparative PDOS of the OH groups is shown in the middle panel of the Fig. 7.8a. The 1π states between 0 to -3 eV show stronger splitting in

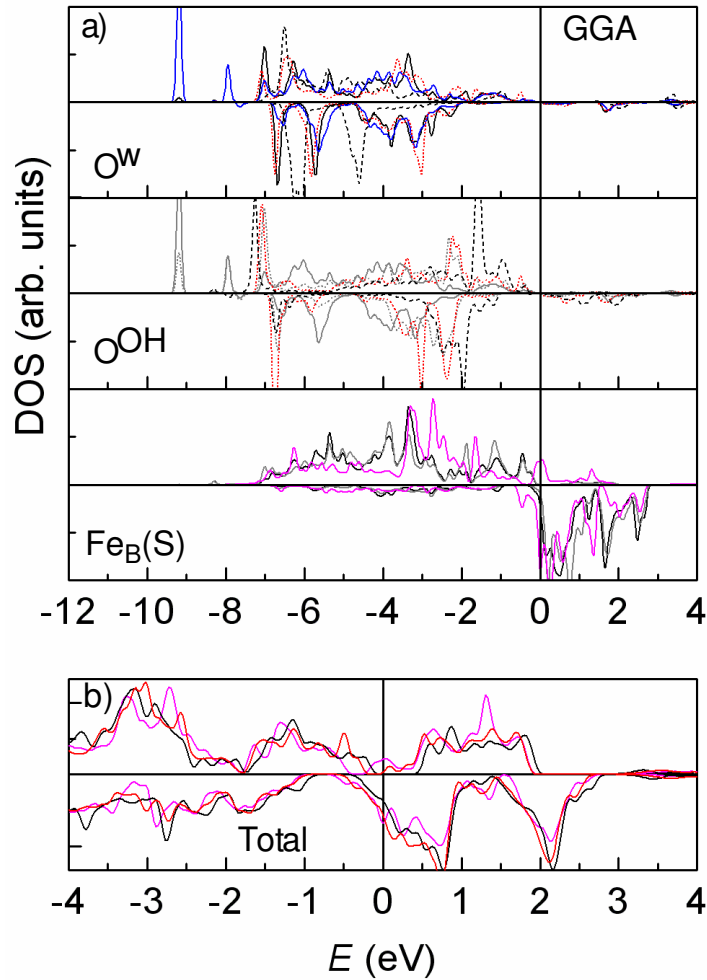


Figure 7.8: DOS and PDOS of 4M is compared to 2M-4, 1F, 1D-1 and modified B layer, within GGA. a) Top panel: PDOS of O^{W1} (black line), O^{W2} (blue line) in 4M and in 1F (black dotted line), in 2M-4 (red dotted line), Middle panel: PDOS of O^{OH1} (grey line), O^{OH2} (dotted grey line) in 4M, in 2M-4 (red dotted line) and in 1D-1 (black dotted line), Bottom panel: PDOS of $Fe_B(S)$ in 4M with H_2O on top (black line), with OH on top (grey line) and $Fe_B(S)$ in modified B layer (magenta curve). b) The total DOS of 4M (black line), 2M-4 (red line) and modified B layer (magenta curve).

the case of 2M-4 and 4M than in 1D-1. The 3σ peak slightly shifts to higher energies with increase in coverage from 1D-1 \rightarrow 2M-4 \rightarrow 4M and only in the case of 4M we see the presence of additional peaks at -7.97 eV and -9.24 eV. The bottom panel of Fig. 7.7d and e shows the PDOS of $\text{Fe}_B(\text{S})$ with OH and H_2O on top. Apart from some minor changes we do not find much difference between them. The bottom panel of Fig. 7.8a shows the PDOS of $\text{Fe}_B(\text{S})$ in 4M and modified B-layer. The important feature is the depletion of states near E_F in both the minority and majority spin channels which were otherwise present in the case of modified B-layer. The total DOS is shown in Fig. 7.8b. The modified B-layer shows states in the majority band gap and hence the system is metallic [25]. As we adsorb H_2O molecules in the 2M-4 configuration, we see depletion of states around the E_F in the majority spin channel and the system is half metallic. We also notice that the top of the valence band moves towards the E_F . Increasing the coverage to 4M, we see further depletion in states near the E_F and the top of the valence band moves toward the E_F , retaining the half metallicity.

GGA+ U : We analyze next the changes in the electronic structure with the inclusion of an U parameter. The PDOS of all the adsorbates (W1, W2, OH1, OH2) and of $\text{Fe}_B(\text{S})$ are shown in Fig. 7.9c,d. The PDOS of $\text{O}^{\text{W}1}$ and $\text{O}^{\text{W}2}$ shows that an additional peak at -8.9 eV is present only in the latter case which can be attributed to the $3a_1-1$ orbital. The peak at -9.5 eV is related to the $1b_2$ orbital and is present for both W1 and W2 whereas within GGA it was absent for W1. The splitting of $3a_1$ orbital into $3a_1$ and $3a_1-1$ remains consistent and, therefore, is independent of the U parameter. However, the peaks are much broadened when compared to their counterparts within GGA. The reason for the broadening is the shift of lower Hubbard band of $\text{Fe}_B(\text{S})$ to lower energies implying greater hybridisation with the $3a_1$ orbital. Fig. 7.10a shows the comparison of the PDOS of O- $2p$ band. In the top panel we notice that $1b_1$ states in the case of 4M or 2M-4 are shifted more towards the Fermi level than in the case of 1F and hence hybridisation is stronger in the former cases. The $3a_1$ states in the majority spin channel also show broadening but we observe a slight shift towards higher energy in the case of 1F than in 4M or 2M-4. The $1b_2$ peak is absent in the case of 2M-4 whereas in the case of 4M and 1F we notice its presence. The PDOS of OH1 and OH2 is shown in Fig. 7.9c,d which reveals that the extent of hybridisation of 1π with $\text{Fe}_B(\text{S})$ - $3d$ states is low but still we notice peak splitting near -2 eV indicating a partial lifting up of 1π orbital degeneracy as is observed within GGA.

The 3σ states also show peak splitting and occupy the same energy range as $3a_1$, $3a_1-1$ and $1b_2$ peaks. In order to understand further the character of these peaks, we integrated the charge density around the corresponding energy range as shown in Fig. 7.9a,b. We see the hybridisation between 3σ , $3a_1$ and $1b_2$ orbitals. Fig. 7.10 middle panel shows a comparative PDOS of various O^{OH} . We notice that 1π peaks in the case of 1D-1 are more shifted towards the E_F than in the case of 2M-4 and 4M. This indicates that due to hydrogen

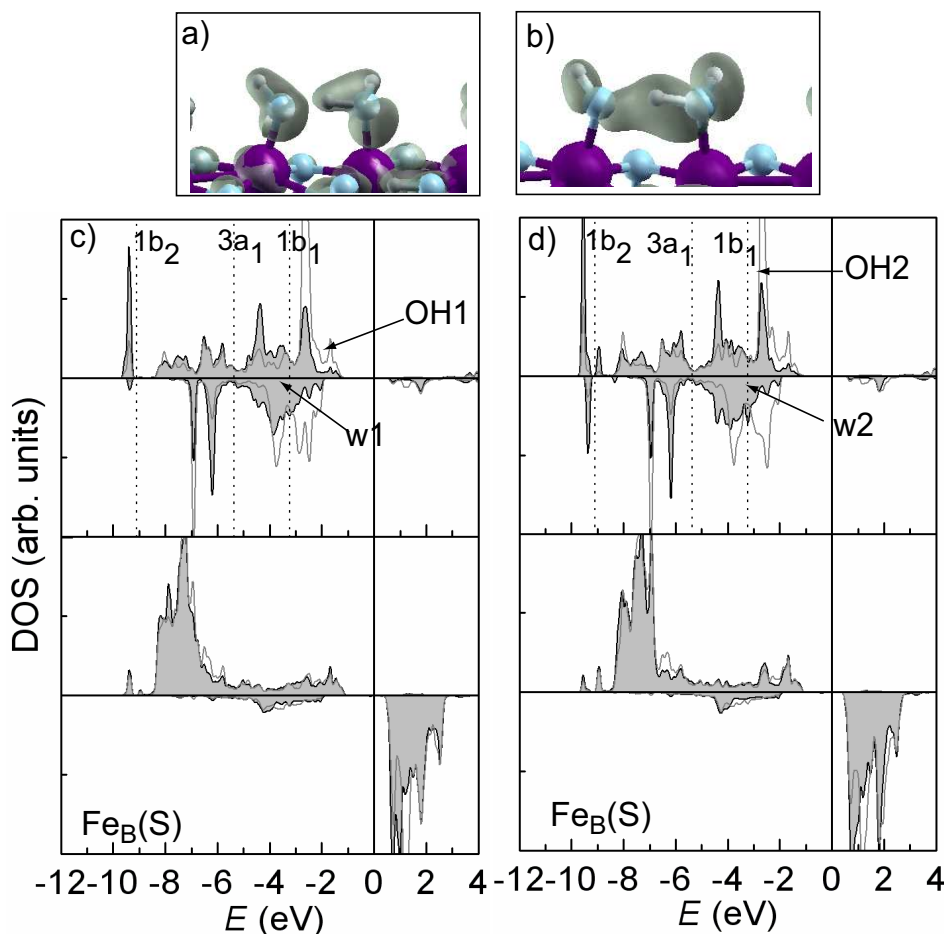


Figure 7.9: The charge density was integrated in the energy range spanning the MO of the H₂O molecule within GGA+U and is shown in a) and b). The figures show some interesting aspects of the interaction of various MOs of H₂O and OH. c) and d) Top panel: PDOS of O^{W1}, O^{OH1} (grey filled curves) and O^{OH2} (light grey curve). Bottom panel: PDOS of Fe_B(S)-3d with intact water molecule on top (grey filled curve) and OH on top (light grey curve). The MOs of the isolated H₂O molecule are shown with vertical dotted lines.

bond in the mixed configuration, the OH group is less bound than in 1D-1. On the other hand 3 σ orbital which splits in the mixed mode of adsorption remains localized in the case of 1D-1. The PDOS of Fe_B(S) in Fig. 7.9c,d shows no appreciable difference between the Fe_B(S) with H₂O or OH on top. The comparison of PDOS of Fe_B(S) in different models is shown in Fig. 7.10a bottom panel. It shows that by adsorption of H₂O in 4M configuration the states have shifted to lower energies than in the case of modified B-layer. The total DOS is shown in Fig. 7.10b. In the case of modified B-layer, there are no electronic states around E_F indicating an insulating character [26]. In the majority spin states the top of the valence band is determined by the Fe_B(S)-3d and O-2p states whereas in the case of minority spin states the

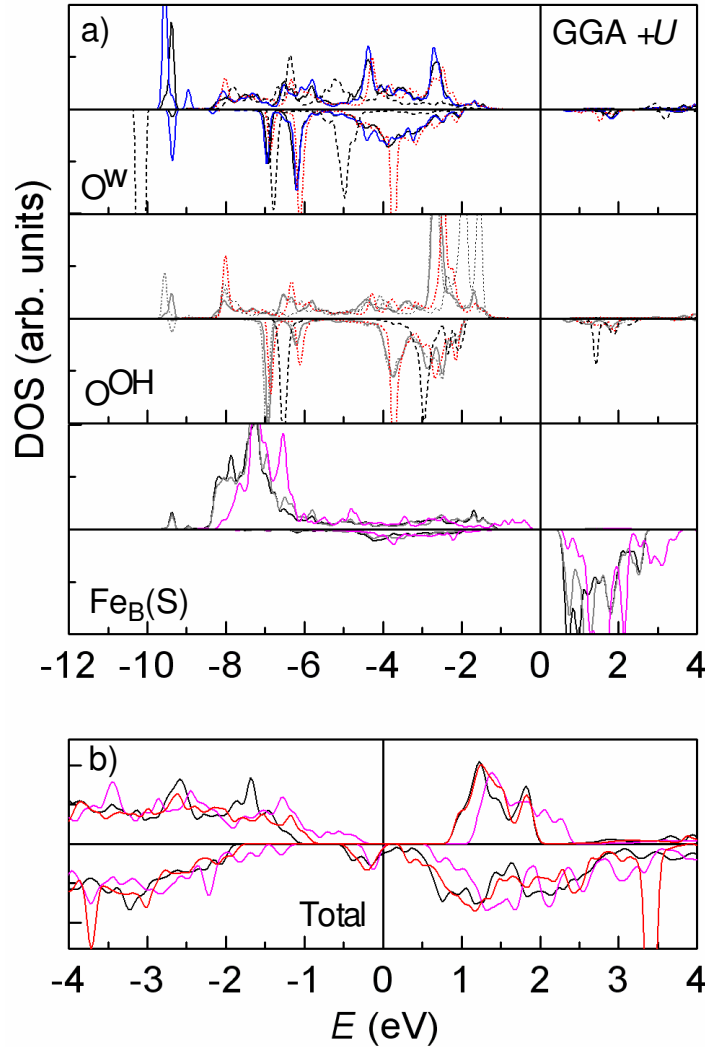


Figure 7.10: DOS and PDOS of 4M is compared to 2M-4, 1F, 1D-1 and modified B layer, within GGA+U. a) Top panel: PDOS of O^{W1} (black line), O^{W2} (blue line) in 4M and in 1F (black dotted line), in 2M-4 (red dotted line), Middle panel: PDOS of O^{OH1} (grey line), O^{OH2} (dotted grey line) in 4M, in 2M-4 (red dotted line) and in 1D-1 (black dotted line), Bottom panel: PDOS of $Fe_B(S)$ in 4M with H_2O on top (black line), with OH on top (grey line) and $Fe_B(S)$ in modified B layer (magenta curve). b) The total DOS of 4M (black line), 2M-4 (red line) and modified B layer (magenta curve).

top of the valence band is determined from the sub-surface and the central layer Fe_B -3d states. We notice that with increasing coverage in the mixed mode of adsorption the top of valence band in the spin majority channel shifts towards lower energy. In the minority spin, with no states around the E_F for the modified B-layer, we see an increase in DOS. This finally leads to a half metallic character for 4M from an insulating modified B-layer.

Overall we find that the electronic structure is well described within GGA+ U and is consistent with the energetic trends. In this Section we explained not only the variation of energetic trend but also described various changes in the electronic structure with coverage successfully.

7.3 Structural details

In this Section we discuss the structural changes upon adsorption of H_2O molecules. Tables 7.1, 7.2, 7.3 list the relaxation of the surface atoms. Tables 7.5, 7.4 list bond lengths and other structural features in different coverage regimes providing a comparative view. The results shown in this Section are obtained within GGA+ U while wherever needed GGA values are explicitly mentioned and compared.

4F-2 (Four H_2O molecules in flat/tilted configuration): The surface atoms relaxations are shown in Table 7.1 and a schematic view of the top B layer is shown in Fig. 7.11. A side view is also shown in Fig. 7.12 left panel with some of the characteristic bond lengths. In this configuration there are two groups of H_2O molecules namely W1,W3 and W2,W4. In the first pair (W1,W3) $\angle\text{Fe}_B(\text{S})\text{-O}^w\text{-H}$ is 72.51° and in the second pair (W2,W4) it is 103.2° . Due to this difference in the tilt angle, bond lengths $d_{(\text{Fe}_B(\text{S})\text{-O}^{w1}/\text{O}^{w2})}$ also differ by 0.10 \AA . The row of H_2O molecules (W1-W4) laterally shifts from the on top position by $\sim(0.55\text{-}0.62) \text{ \AA}$ away from the Fe_B row along (110). The shift is due to tilting of the H_2O molecules which favors formation of intermolecular hydrogen bonds. The vertical relaxation of all the H_2O molecules is outwards and the magnitude is similar ($\sim 0.25\text{-}0.27 \text{ \AA}$). On the other hand, the vertical relaxation of the $\text{Fe}_B(\text{S})$ with on top W1 and W3 is outwards while those with

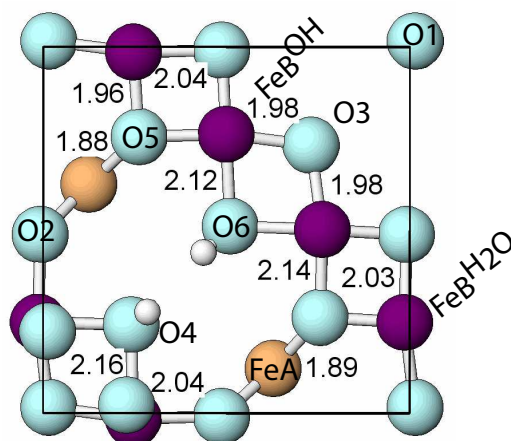


Figure 7.11: Top view of $4M$, also represents a schematic view of the surface B-layer with all the lateral bond lengths. All the lengths are give in \AA . Positions of O , Fe_B , and H are marked by cyan, purple and white circles.

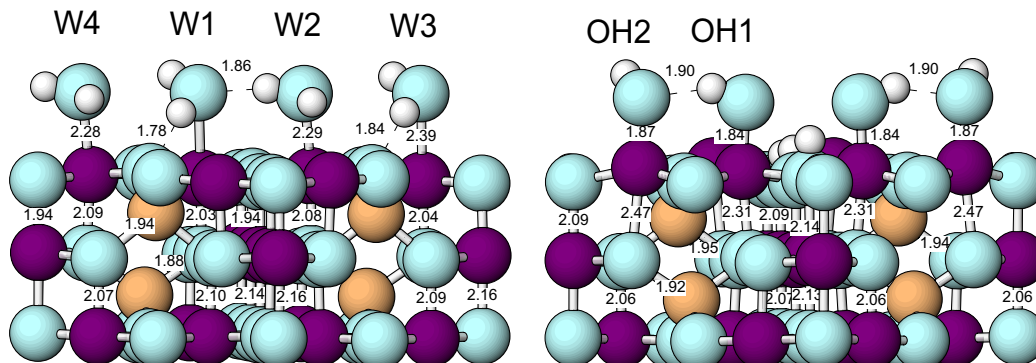


Figure 7.12: Side view of the relaxed 4F-2 (left panel) and 4D-2 (right panel) along with surface and sub-surface bond lengths. All bond lengths are given in Å and are obtained within GGA+U. For color coding see Fig. 7.11.

W2 and W4 is inwards. We have seen in the previous Chapters that $\text{Fe}_B(\text{S})$ without any adsorbate on top relaxes inwards as is observed in the case of a clean surface (modified B-layer). The outward relaxation of $\text{Fe}_B(\text{S})$ with on top W2 and W4 indicates a weak hybridisation compared to W1 and W3 and much of the stabilisation comes from hydrogen bonds. The lateral relaxation is also quite low for $\text{Fe}_B(\text{S})$ atoms. The bond lengths between S (surface) and S-1 (sub-surface) layer is reduced except for those beneath the adsorbate row. This shortening of bond lengths ($d_{(\text{Fe}_B(\text{S})-\text{O})}$) between S and S-1 layers and elongation between S-1 and S-2 is consistent with the behavior observed for lower coverages. The change in the bond lengths $d_{(\text{Fe}_B(\text{S})-\text{O}^w)}$ ($w=\text{W1/W2}$) with coverage can be seen in Table 7.5: the increase of 0.07 Å is seen from configuration 1F to 4F-2. Moreover the O(S) (O1-O6) show low surface relaxations both laterally and vertically with some exceptions. The direction of relaxation is outwards for half of them and inwards for the other half as is also observed for lower coverages. The Fe_A layer shows no lateral relaxation while it has vertical relaxation which moves it outwards.

The qualitative trend of surface layer relaxations in the case of GGA is similar to that in GGA+U except for some atoms and also the magnitudes may vary. In fact Table 7.5 shows that for the present configuration (4F-2), the structural features like bond lengths and angles are nearly identical within GGA and GGA+U. The lowering of E_{ads} within GGA+U by 0.10 eV is attributed to the extent of hydrogen bonding and to the electronic structure as discussed in Section 7.2.

4D-2 (Four H_2O molecules in dissociated configuration): The surface layer relaxations are listed in Table 7.2 and a schematic view of the top B-layer is shown in Fig. 7.11. A side view is also shown in Fig. 7.12 right panel along with some selected bond lengths. As mentioned in Section 7.1 this configuration has two types of OH, i.e. OH1 and OH2, shown in Fig. 7.12

Table 7.1: Atomic relaxations of the surface layer obtained within GGA+U in the case of 4F-2 is listed. GGA values are given in parenthesis. The Δz values represent relaxation along the surface normal, negative values indicate an outward while the positive means inward relaxation. The numbering of the atoms corresponds those shown in Fig. 7.11. All distances are in Å.

	4F-2		
	Δx	Δy	Δz
Fe _A (S)	0.00 (-0.01)	0.01 (0.02)	-0.15 (-0.15)
O1	-0.08 (-0.12)	-0.05 (-0.06)	0.04 (0.05)
O2	0.04 (0.07)	0.07 (0.08)	-0.02 (-0.00)
O3	0.09 (0.10)	0.08 (0.09)	-0.04 (-0.02)
O4	0.09 (0.11)	0.08 (0.12)	0.01 (0.00)
O5	0.00 (-0.03)	-0.01 (-0.03)	-0.12 (-0.09)
O6	-0.09 (-0.12)	-0.05 (-0.07)	0.05 (0.05)
Fe _B ^{W1}	-0.04 (-0.05)	-0.04 (-0.04)	0.02 (0.04)
Fe _B ^{W2}	0.00 (0.00)	0.00 (-0.01)	-0.05 (-0.04)
Fe _B ^{W3}	-0.02 (0.06)	0.00 (-0.01)	0.04 (0.06)
Fe _B ^{W4}	0.01 (0.02)	0.01 (0.00)	-0.04 (-0.02)
O ^{W1}	0.32 (0.20)	0.50 (0.58)	-0.25 (-0.25)
O ^{W2}	0.20 (0.20)	0.59 (0.59)	-0.25 (-0.25)
O ^{W3}	0.29 (0.30)	0.46 (0.46)	-0.27 (-0.27)
O ^{W4}	0.17 (0.17)	0.56 (0.55)	-0.25 (-0.25)

right panel. The formation of a weak hydrogen bond between OH1...OH2 makes this configuration more interesting to investigate. The strong electron density redistribution seen in Fig. 7.4 is well reflected in the greater surface atom relaxation compared to 4F-2. We notice appreciable lateral relaxation for both the OH groups especially in [100] direction. This favors the formation of hydrogen bond between O^{OH1} ... O^{OH2} of 2.79 Å. The OH group relaxes outwards as is observed in the case of 1D-1 and 2D-1 but the O^{OH2} relaxes stronger by 0.13 Å than O^{OH1}. This leads to two different $d_{\text{Fe}_B(\text{S})-\text{O}^{\text{OH1/OH2}}}$ of 1.84 and 1.87 Å respectively. The bond length of 1.84 Å is similar to that observed in 1D-1 and 2D-3 as shown in Table 7.4. The OH2 has an $\angle \text{Fe}_B(\text{S})-\text{O}^{\text{OH}}-\text{H}$ of 123.35° which is also similar to that observed in the case of 1D-1 and 2D-3 (Table 7.4), while OH1 has an angle of 109.8°. As discussed already in Section 7.2 OH2 hybridizes more strongly with Fe_B(S) than OH1 which is

Table 7.2: Atomic relaxations of the surface layer obtained within GGA+ U in the case of 4D-2 is listed. GGA values are given in parenthesis. The Δz values represent relaxation along the surface normal, negative values indicate an outward while the positive means inward relaxation. The numbering of the atom corresponds to those shown in Fig. 7.11. All distances are in \AA .

	4D-2		
	Δx	Δy	Δz
Fe _A (S)	0.01 (0.00)	-0.02 (0.00)	-0.05 (-0.03)
O1	-0.04 (-0.09)	-0.04 (-0.09)	-0.02 (0.02)
O2	0.10 (0.02)	-0.01 (0.02)	0.13 (0.12)
O3	-0.03 (0.09)	-0.03 (0.09)	-0.14 (0.03)
O4	-0.12 (0.09)	-0.12 (0.09)	-0.02 (0.03)
O5	-0.01 (-0.02)	-0.03 (-0.02)	0.05 (0.12)
O6	-0.10 (-0.09)	-0.10 (-0.09)	-0.04 (0.03)
Fe _B ^{OH1}	-0.12 (-0.10)	0.05 (0.10)	-0.26 (-0.31)
Fe _B ^{OH2}	-0.05 (-0.10)	0.12 (0.10)	-0.36 (-0.31)
O ^{OH1}	-0.16 (0.06)	-0.08 (-0.06)	-0.08 (-0.11)
O ^{OH2}	-0.19 (0.06)	0.00 (-0.06)	-0.21 (-0.11)

clearly reflected in the tilting angle. We can see the strong binding of OH2 from the following structural changes as well: 1) The outward relaxation of Fe_B^{OH2} is 0.10 \AA stronger than Fe_B^{OH1} indicating greater amount of charge redistribution and hence strong binding 2) The change in the sub-surface bond lengths also indicates the binding strength: the $d_{(\text{Fe}_B^{\text{OH1}}-\text{O}(\text{S}-1))}$ is 0.16 \AA shorter than $d_{(\text{Fe}_B^{\text{OH2}}-\text{O}(\text{S}-1))}$ clearly shows a greater interaction in the latter case. Except for few atoms of the O(S) (O1-O6), the lateral and vertical relaxations are quite small. The outward relaxation of Fe_A layer is very negligible unlike 4F-2 wherein we saw appreciable outward relations. We see overall good agreement between the structural details and the change in electronic structure within GGA+ U .

Now within GGA, the magnitude of relaxation is different. One of the reason is the lack of hydrogen bond in between O^{OH1} ... O^{OH2} which was otherwise present within GGA+ U . As a consequence OH1 and OH2 behave the same and this is reflected in the bond lengths and relaxations. The outward relaxation of Fe_B(S) and OH1/2 remains the same but the O(S) (O1-O6) now show a difference by relaxing inwards with no exception.

4M (Four H₂O molecules in mixed mode configuration): All the surface layer relaxations are listed in Table 7.3 and a schematic view of the top B-layer with lateral bond lengths is shown in Fig. 7.11. A side view with some

Table 7.3: Atomic relaxations of the surface layer obtained within GGA+U in the case of 4M is listed. GGA values in the parenthesis. The Δz values represent relaxation along the surface normal, negative values indicate an outward while the positive means inward relaxation. The numbering of the atom corresponds to those shown in Fig. 7.11. All distances are in Å.

	4M		
	Δx	Δy	Δz
Fe _A ^S	0.02 (0.03)	-0.02 (0.01)	-0.13 (-0.05)
O1	-0.09 (-0.17)	-0.09 (-0.16)	0.07 (0.13)
O2	0.04 (0.08)	0.07 (0.06)	-0.00 (0.14)
O3	0.12 (0.18)	0.12 (0.14)	0.07 (0.14)
O4	0.03 (-0.30)	0.04 (0.01)	-0.15 (-0.02)
O5	0.00 (0.06)	-0.05 (-0.03)	-0.02 (0.10)
O6	-0.05 (-0.00)	-0.05 (0.03)	0.01 (0.07)
Fe _B ^{W1}	-0.10 (-0.06)	0.01 (0.01)	-0.11 (-0.03)
Fe _B ^{OH1}	-0.01 (0.06)	-0.09 (-0.03)	-0.25 (-0.21)
Fe _B ^{W2}	-0.02 (-0.06)	0.12 (0.08)	-0.11 (0.00)
Fe _B ^{OH2}	0.01 (0.24)	0.04 (0.02)	-0.22 (-0.04)
O ^{W1}	0.12 (0.04)	-0.20 (-0.29)	-0.17 (-0.12)
O ^{OH1}	-0.18 (-0.07)	0.19 (0.27)	-0.19 (-0.11)
O ^{W2}	0.22 (0.21)	-0.09 (-0.01)	-0.18 (-0.11)
O ^{OH2}	0.18 (-0.50)	0.19 (0.02)	-0.16 (0.12)

of the characteristic bond lengths is also shown in Fig. 7.13. All the adsorbates W1, OH1, W2 and OH2 relax outwards and moreover the magnitudes are quite similar (0.16-0.19 Å). We also notice lateral relaxation due to the formation of hydrogen bonds. The two hydrogen bonds on the surface are : O^{w1}...O^{OH1} and O^{w2}...O^{OH2} both being 2.49 Å which is quite close to 2M-4. The bond length $d_{(\text{Fe}_B(\text{S})-\text{O}^w)}$ with flat/tilted H₂O varies from 2.22 Å to 2.39 Å within configurations involving molecular adsorption like 1F, 2F-3 and 4F-2 while in the case of mixed adsorption it decreases to 2.09 Å for 4M and 2.06 Å for 2M-3. The latter is close to the bulk bond length of 2.06 Å. This suggests that H₂O adsorbs strongly on the surface if a OH group is adsorbed at a neighboring site. The angle $\Theta_{\text{H}-\text{O}^w-\text{H}}$ also expands by $\sim 4^\circ - 5^\circ$ from the gas phase value of 104.5°. The tilt angle $\Theta_{\text{Fe}_B(\text{S})-\text{O}^w-\text{H}}$ lies between 111° – 120°. The OH group: OH1 and OH2 interact more strongly with the Fe_B(S) than the H₂O molecule. This can be seen by the outward relaxation of Fe_B(S) with on top OH which is 0.12-0.14 Å lower than those with on top H₂O molecules. The

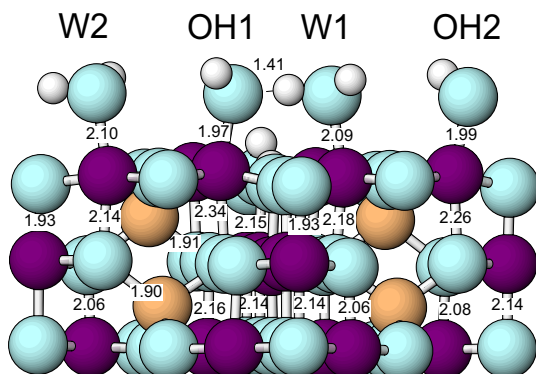


Figure 7.13: The side view of the fully optimized 4M structure along with surface and sub-surface bond lengths. All bond lengths are given in Å and are obtained within GGA+U. For color coding see Fig. 7.11.

$d_{(\text{Fe}_B(\text{S})-\text{O}^{\text{OH}})}$ varies from 1.84-1.90 Å in various dissociated models whereas in the mixed adsorption mode it elongates further to 1.97 Å and 1.99 Å. This is due to difference in the intermolecular interactions on the surface including the hydrogen bonds. The other factors which influence the relative bonding strength of the OH group are: 1) the change in the subsurface bond length, as also pointed out for 4D-2, can give a rough estimate of the extent of interaction: in the case of 1D-1 and 2D-3, the subsurface $d_{(\text{Fe}_B(\text{S})-\text{O}(\text{S}-1))}$ is ~ 2.65 Å which decreases to 2.47 Å in 4D-2 and further to 2.34/2.24 Å in 4M and 2M-3. This suggests that within the mixed mode of adsorption the extent of OH hybridisation with $\text{Fe}_B(\text{S})$ is less compared to the fully dissociated models. We can also say that at higher coverages the reactivity of the OH group is hindered due to intermolecular interactions and even more in the case of mixed mode of adsorption. (2) the tilt of OH, i.e. $\Theta_{\text{Fe}_B(\text{S})-\text{O}^{\text{OH}}-\text{H}}$: A careful look at Table 7.4 shows that the tilt angle of $120^\circ - 123^\circ$ appear for those OH which are reactive according to criterion (1) and those with $< 120^\circ$ are relatively less reactive. By considering the above discussion we believe that a fully hydroxylated surface is energetically unfavorable. The O(S) (O1-O6) moreover show small lateral or vertical relaxation except for few atoms. The direction of relaxation is not uniform as some relax outwards while the others relax inwards. The Fe_A shows no lateral but outwards relaxations.

At this point we would like to add some information about the GGA results as well. Even though the bond lengths and angles may vary as can be seen in Table 7.4 and Table 7.5, the conclusion stated above still holds true. The magnitude of surface relaxations are quite low when compared to GGA+U. The difference in the results is attributed to different molecular orbitals involved in the hybridisation mechanism.

Table 7.4: Adsorbate-substrate bond lengths in Å and angles in degrees in the case of 1D-1, 1D_V-3, 2D-2, 2D-3, 4D-2, 2M-3, 4M. The bond length $d_{\text{H}_{\text{Ow}} \cdots \text{Ow}}$ represents the hydrogen bonding in the system.

	$d_{\text{FeB(S)}-\text{OOH}}$		$d_{\text{O}-\text{H}}$		$d_{\text{O}^{\text{OH}}-\text{H}^{\text{O}^{\text{surf}}}}$		$d_{\text{Ow}-\text{HOH}} \setminus d_{\text{O}^{\text{OH}}-\text{HOH}}$		$\Theta_{\text{FeB(S)}-\text{OOH}-\text{H}}$	
	GGA	GGA+U	GGA	GGA+U	GGA	GGA+U	GGA	GGA+U	GGA	GGA+U
1D-1	1.83	1.84	0.97	0.97	3.23	3.36	126.4	120.8	114.8	111.5
1D _V -3	2.23	2.26	0.97	0.98			130.7	105.3	130.7	105.3
2D-2	1.80	1.80	0.96	0.96	2.70	2.43	168.7	167.4	141.7	136.6
2D-3		1.84,1.90		0.97-1.00		1.69		20.5,121.6		108.6,148.11
4D-2	1.83	1.87,1.84	0.97	0.99,0.97	2.84	2.34-2.89	133.2,133.3	123.3,109.8	132.2	107.9-170.9
2M-3	1.95	1.97	0.97	0.97	3.12	3.26	119.4	116	114.6	111.7
4M	1.94,1.99	1.97,1.99	0.97,1.07	0.97,1.10	1.79	2.50	116.9,118.9	114.5,115.3	116,118	112.5,147.3

Table 7.5: Adsorbate-substrate bond lengths in Å and angles in degrees in the case of 1F-1, 2F-3, 4F-2, 2M-3, 4M. The bond length $d_{\text{H}_{\text{Ow}} \cdots \text{Ow}}$ represents the hydrogen bonding in the system.

	$d_{\text{Fe}-\text{Ow}}$		$d_{\text{Ow}-\text{H}}$		$d_{\text{O(S)}-\text{Hw}}$		$d_{\text{Ow}-\text{HOH}} \setminus d_{\text{Ow}-\text{Hw}}$		$\Theta_{\text{H}-\text{Ow}-\text{H}}$		$\Theta_{\text{FeB(S)}-\text{Ow}-\text{H}}$	
	GGA	GGA+U	GGA	GGA+U	GGA	GGA+U	GGA	GGA+U	GGA	GGA+U	GGA	GGA+U
1F-1	2.28	2.22	0.98	0.98	2.61	2.54	105.3	106.5	101.8	101.6		
2F-3	2.24,2.39	2.21,2.35	0.97-0.99	0.97-1.00	1.90,2.59	1.85,2.55	1.87	1.87	105.3,107.1	105.8,107.7	76.25,102.9	76.3,103.1
4F-2	2.32,2.42	2.29,2.39	0.97,0.99	0.97,0.99	1.82,1.88,2.57	1.82,1.88,2.56	1.86,1.85	1.86,1.85	102.9,104.9	103.54,105.0	72.2,103.4	72.2,103.4
2M-3	2.09	2.06	0.97,1.08	0.97, 1.11	3.01,2.61	2.93	1.43	1.37	108.5	108.7	105.21,111.76	104.7,114.4
4M	2.14	2.09	0.97,1.07	0.97,1.10	2.89	2.90	1.44,1.49	1.40	105.3,107.9	109.2,110.4	100.7-105.9	104.9,110.5

7.4 Hydroxylation and hydrogenation

In this Section we will consider a complete saturation of the surface with H and OH groups: OH groups are adsorbed on all the $\text{Fe}_B(\text{S})$ sites and all the $\text{O}(\text{S})$ are covered with H atoms thereby forming surface OH groups. In the case of hydrogenation we cover all the $\text{O}(\text{S})$ with H atoms and the $\text{Fe}_B(\text{S})$ remain uncovered.

Hydroxylation: For the fully hydroxylated surface we performed calculations within GGA and GGA+ U and the top view of the resulting fully optimised structure within GGA+ U is shown in Fig. 7.14b. The final optimised structures in the case of GGA and GGA+ U vary due to hydrogen bond formation in the latter case similar to the 4D-2 configuration.

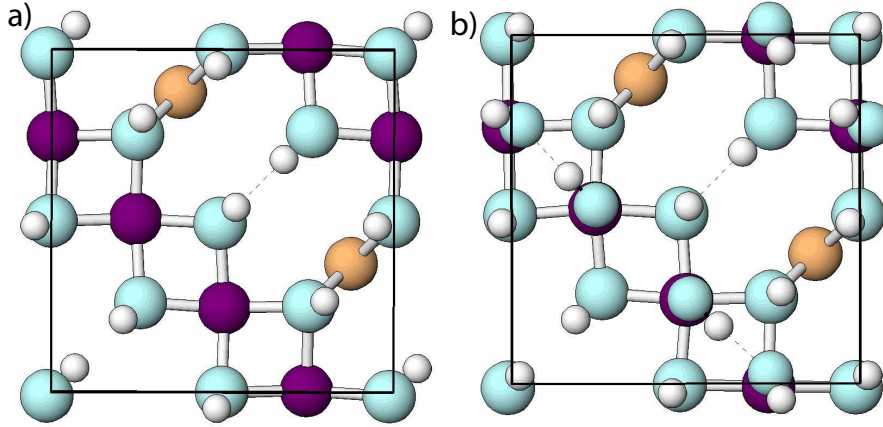


Figure 7.14: Top view of the surface B-layer of a) a hydroxylated surface along with hydrogen bond shown in dotted black lines, b) hydrogenated surface along with hydrogen bond shown by dotted black lines. The top views are obtained from the optimized structure within GGA+ U .

Hydrogenation: For the hydrogenated surface we performed the calculation within GGA and GGA+ U . A top view of the optimized structure within GGA+ U is shown in Fig. 7.14a. The E_{ads} in this case is defined w.r.t molecular hydrogen:

$$E_{\text{eads}} = \frac{E_{\text{Fe}_3\text{O}_4(001)/n\text{H}} - E_{\text{Fe}_3\text{O}_4(001)} - n/2E_{\text{H}_2}}{n}. \quad (7.1)$$

where n is the no. of hydrogen atoms adsorbed. The E_{ads} in the case of hydrogenation is -1.85 eV which is lower than in hydroxylation.

7.5 0.5 ML A layer termination

Until now we have discussed all the adsorption models using the B-layer terminated surface but in this Section we will briefly look at the 0.5 A-layer

terminated surface. We did calculations within GGA for a complete hydroxylation of the surface wherein all the $\text{Fe}_B(\text{S})$ and $\text{Fe}_A(\text{S})$ are covered with OH groups while all the $\text{O}(\text{S})$ are covered with H atoms. The surface phase diagram within GGA [25] shows that surface models with A-layer termination including 0.5 ML A-layer are not stable within accessible partial pressures of oxygen (p_{O_2}). A theoretical study using GGA+ U [26] approximation finds one of the A-layer models as the stable termination at low p_{O_2} . The surface phase diagram prepared within our work predict no stability for the 0.5 A-layer termination. Further work is needed to explore and confirm the stability of different A layers models.

7.6 Coverage vs. E_{ads} and $\Delta\Phi$

In order to get a better understanding of the water adsorption process on the $\text{Fe}_3\text{O}_4(001)$ surface, we will discuss the change in adsorption energy (E_{ads}) and work function with coverage as shown in Fig. 7.15 and Fig. 7.16, respectively.

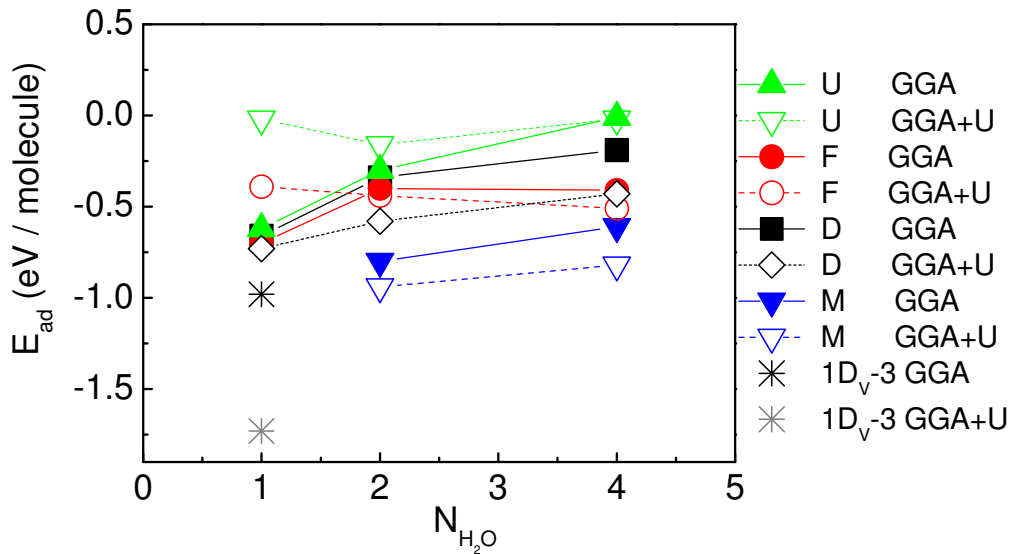


Figure 7.15: E_{ads} as a function of coverage. Types of adsorption geometry included are upright (U), flat (F), dissociated (D) and mixed (M). The GGA values are shown by filled symbols connected with a solid line and those of GGA+ U with empty symbols connected with a dashed line.

GGA: Fig. 7.15 shows the E_{ads} varying with the number of water molecules adsorbed. The mode of adsorption at very low coverages i.e. a single water molecule adsorption per $(\sqrt{2} \times \sqrt{2})R45^\circ$ unit cell is molecular on an ideal

surface and dissociative on a defective surface. The E_{ads} between the flat adsorption (1F) and dissociative adsorption (1D-1) differ by only 0.04 eV which also indicates competition between both the modes. When we increase the coverage to two H_2O molecules we see a crossover from molecular adsorption to a mixed type of adsorption. A further increase in coverage to four H_2O molecules maintains the mixed mode of adsorption as the most preferred.

The E_{ads} increases with increase in coverage due to intermolecular repulsive interaction. The repulsive interaction weakens the adsorbate-substrate bonding. The increase in E_{ads} from a single H_2O molecule to a dimer is higher than that from dimer to a further coverage of four H_2O molecules. In many configurations of $4\text{H}_2\text{O}$ molecules, the water molecule acts in a pair as in 4F-2 and 4M thereby behaving like in the case of water dimer adsorption. This is the reason for a small increase in E_{ads} with higher coverages.

GGA+U: Unlike in the case of GGA, we observe dissociative adsorption at low coverage on an ideal surface and on a defective surface. The E_{ads} on a defective surface is lowest as shown in Fig. 7.15. The value indicates strong affinity of the V_O towards H_2O molecules. When we increase the coverage to two water molecules, the mode of adsorption shows a crossover as in the case of GGA, to a mixed mode of adsorption and retains it as the preferred mode at higher coverages. The mode of adsorption at higher coverages is same both in GGA and GGA+U. The E_{ads} increases with increase in coverage as in GGA. The dissociative configurations show a steep increase while the flat adsorption shows an opposite behavior where the E_{ads} decreases. This is due to the presence of hydrogen bonding between the H_2O molecules.

Fig. 7.16 shows the change in work function with coverage. There are two factors which cause in the change of work function ($\Delta\Phi$): the dipole moment of the adsorbates (induced or permanent) and the charge transfer between the adsorbate and substrate. The work function decreases if charge is donated to the surface as in the case of adsorption of intact H_2O molecule. On the other hand it increases if charge is taken away from the surface [32, 113] e.g. in the case of an OH group. The adsorption of an oxygen and a H atom on the surface can contribute to the opposite signs of $\Delta\Phi$. Therefore it is difficult to distinguish OH and H_2O from $\Delta\Phi$ alone. The water molecule has a positive dipole moment of 1.83×10^{-18} esu cm [32], and if it is oriented upright (U configuration), the work function shows the strongest decrease as shown in Fig. 7.16. $\Delta\Phi$ becomes more negative with increase of coverage, from 1U to 4U and the trend is consistent with the trend observed for other oxide surfaces [32]. If the H_2O molecule is adsorbed parallel to the surface (F configuration), the change in $\Delta\Phi$ is smaller but remains negative. At higher coverage, $\Delta\Phi$ saturates. In the case of dissociative adsorption we expect an increase in $\Delta\Phi$, and this in fact is observed. Nevertheless due to the subsequent adsorption of a H atom, the change w.r.t the clean surface is small. This is because OH group accepts charge while H atom donates charge, two opposing effects for $\Delta\Phi$ which leads to cancelation of effects and hence small $\Delta\Phi$ w.r.t the

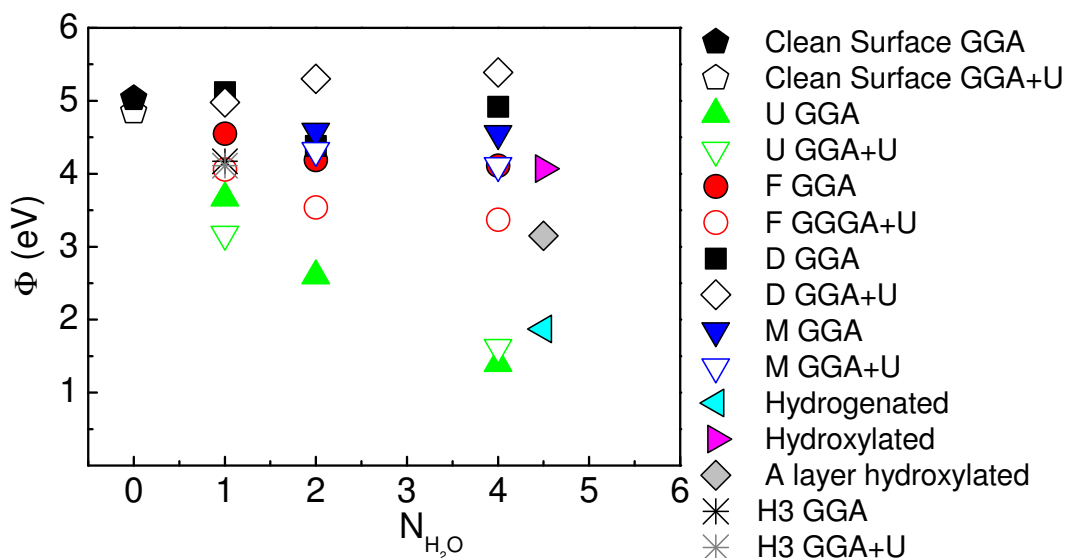


Figure 7.16: Work function Φ (eV) as a function of coverage. Types of adsorption geometry included are upright (U), flat (F), dissociated (D) and mixed (M). The GGA values are shown by filled symbols and those of GGA+U with empty symbols.

clean surface. Increasing the coverage from 1D-1 to 4D-2 leads to an increase in $\Delta\Phi$. In the case of mixed adsorption, it is difficult to apply the criteria discussed above as the OH and H_2O have opposing trends and nearly cancel. We see a negative change in $\Delta\Phi$ which is relatively small compared to the upright configuration. In the case of mixed termination, the change in $\Delta\Phi$ with coverage is small. Interestingly, full hydrogenation and hydroxylation leads to a decrease in the work function. This can be attributed to the reduction in polarity of the surface with water adsorption. Finally, it is also important to note that the trend in $\Delta\Phi$ is similar within GGA and GGA+U.

7.7 Summary

We have studied the adsorption of four H_2O molecules on the surface saturating all the surface $\text{Fe}_B(\text{S})$. In this coverage regime, we have considered more than 10 configurations. The mixed mode of adsorption, where every second H_2O molecule dissociates, remains the most stable configuration. The stability is provided by the hydrogen bond formation between $\text{O}^w \cdots \text{O}^{\text{OH}}$. This results in the splitting of the $3a_1$ orbital into $3a_1$ and $3a_1-1$ and is unique to the mixed mode termination 4M. The H_2O molecule physisorbs on the surface while the OH group chemisorbs leading to two different bond lengths, $d_{(\text{Fe}_B(\text{S})-\text{O}^w)}$ of 2.09 Å and $d_{(\text{Fe}_B(\text{S})-\text{O}^{\text{OH}})}$ of 1.97/1.99 Å. This also acts as a fingerprint to

identify the mixed adsorbed termination in experiments (LEED results see Chapter 11). The coverage dependent adsorption trend is also analyzed. At low coverages dissociative mode of adsorption of H_2O molecules is observed on the ideal surface and specifically on defect sites which have more affinity to H_2O molecules. With the increase in coverage we observe a crossover from dissociative to partial dissociation of H_2O molecules. The hydrogen bond contribution is around 0.37 eV which is quite appreciable. We also present two different reaction mechanisms for attaining the 4M configuration. In 4F-2 the different tilt angles of the H_2O molecules along with the formation of hydrogen bond weakens the OH bond. Subsequently due to interaction with $\text{Fe}_B(\text{S})$ sites dissociation is induced in every second molecule. In the second mechanism, the H_2O are dissociated on the surface at far apart $\text{Fe}_B(\text{S})$ sites. In the next step, intact H_2O molecules adsorb on the neighboring $\text{Fe}_B(\text{S})$ sites resulting in 4M. Further, complete hydroxylation of the surface is difficult due to the less reactive surface oxygens neighboring the Fe_A sites.

Surface Phase Diagram

Metal oxides are used in a wide range of technical applications, among which one of the most important use is in catalysis. The complex atomic surface structure of these materials is highly dependent on the environmental conditions for e.g. temperature (T), pressure (p) in the gas phase [67, 114]. In fact, the presence of oxygen and hydrogen in the atmosphere led to some common guess based on simple arguments about the surface termination e.g. the stability of the oxygen termination in most of the experimental conditions. The reason for this was the lack of atomistic knowledge regarding the surface at various temperatures and pressures and a thermodynamic framework to deal with them simultaneously. *ab-initio* thermodynamics [45, 46] allows to combine atomic level understanding with thermodynamics thereby enabling us to deal with situations like describing the stability of a metal oxide surface surrounded by gaseous atmosphere [46, 67, 114]. However, one should keep in mind that these surface phase diagrams from *ab-initio* thermodynamics serve as a guidance and may not exactly coincide with the experimental phase diagrams. *ab-initio* thermodynamics has been applied to many metal oxide surfaces like $\text{Fe}_3\text{O}_4(001)$ [25, 26], $\text{Al}_2\text{O}_3(0001)$ [46], $\text{RuO}_2(110)$ [66, 67] and $\text{Fe}_2\text{O}_3(0001)$ [115].

In the previous chapters we have discussed the mode of adsorption of H_2O molecules on the $\text{Fe}_3\text{O}_4(001)$ surface and its dependence on coverage. In this chapter we will extend these results to finite temperatures (T) and pressures (p) from the calculated values using *ab-initio* thermodynamics. By doing so we extend the surface phase diagram of $\text{Fe}_3\text{O}_4(001)$ [25, 26] to account for the presence of water vapour in the atmosphere. This surface phase diagram will be helpful in predicting the most stable termination of the surface at a given partial pressure of oxygen (p_{O_2}) and of water vapour ($p_{\text{H}_2\text{O}}$) with temperature.

8.1 Compilation of the surface phase diagram

In this Section we briefly describe some of the assumptions which are made for the surface phase diagram. Using Eq. 2.45 and Eq. 2.46 we calculate the surface energy, γ , of a particular termination within the framework of *ab-initio* thermodynamics as discussed in Section 2.4. Since we have two components in the system i.e. $\mu_{\text{H}_2\text{O}}$ and μ_{O} the resulting surface phase diagram is 3-dimensional as shown in Fig. 8.1. The negative surface energy is obtained because the elements in gas phase have no counterparts in the bulk or surface [116]. In order to identify and investigate the stable phases in the phase diagram we have to look at the bottom view as shown in Fig. 8.2 and in Fig. 8.3 within GGA and GGA+ U respectively. These figures also show temperature and pressure corresponding to the chemical potential chosen for $\mu_{\text{H}_2\text{O}}$ and μ_{O} using Eq. 2.47. The range of $\mu_{\text{H}_2\text{O}}$ and μ_{O} corresponds to two different temperatures, i.e. 300K and 800K, latter corresponds to a typical annealing temperature.

Vibrational contribution: The vibrational energy contribution to the surface gets largely canceled due to the calculated difference in surface energy. However the vibration contribution from the adsorbates which do not have any counterpart in the bulk do contribute to the surface energy ($\gamma^{\text{vib}}(T)$). A rough estimate was made in Ref. [67] wherein for the temperature range <700-800 K

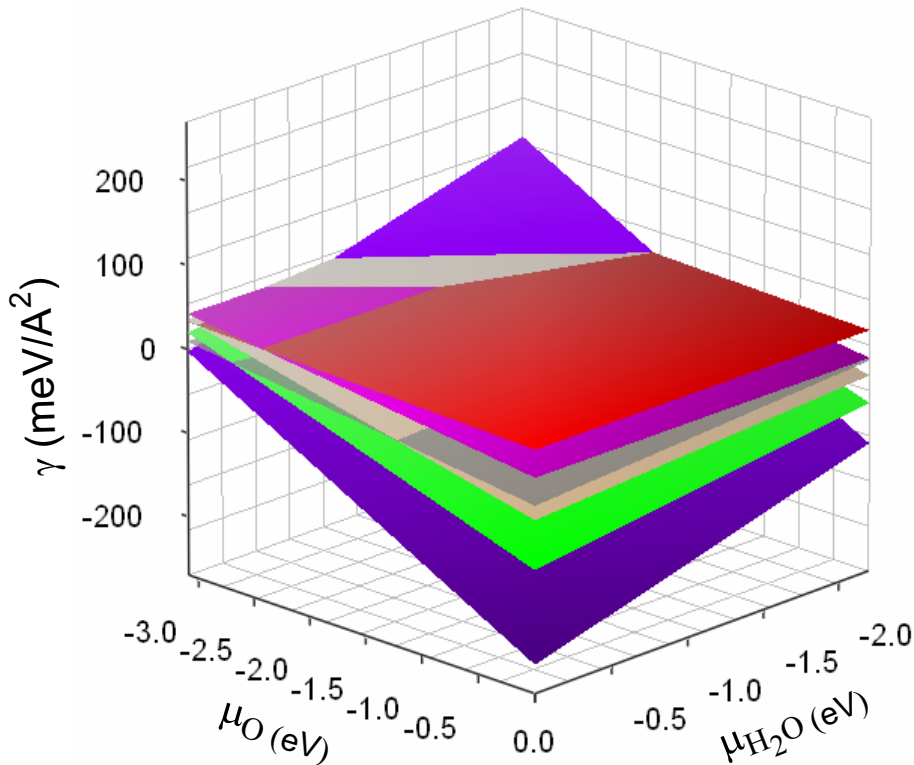


Figure 8.1: A 3-dimensional view of the surface phase diagram calculated using Eq. 2.45 and Eq. 2.46 within GGA+ U

the vibrational contribution to the surface energy ($\gamma(T)$) from a hydroxyl group was estimated to be $\sim 15 \text{ meV}/\text{\AA}^2$ and that from a water species to be $\sim 30 \text{ meV}/\text{\AA}^2$. We have verified that such contributions will not qualitatively change our picture.

Water vapor formation: We assume that oxygen and hydrogen surrounding the $\text{Fe}_3\text{O}_4(001)$ surface are in thermodynamic equilibrium. Given such an equilibrium the formation of water is dominant [46,67] and therefore we study the phase diagram also with respect to $\mu_{\text{H}_2\text{O}}$. The range of T and p chosen for the surface phase diagram of $\text{H}_2\text{O} + \text{Fe}_3\text{O}_4(001)$ (Fig. 8.2, Fig. 8.3) corresponds to the vapour phase of water in the experimental phase diagram of water.

Rich and poor limit of μ_{O} , $\mu_{\text{H}_2\text{O}}$, μ_{H} : In the rich limit, gas component starts condensing on the surface, while in the poor limit bulk oxide starts decomposing. For e.g. in the μ_{O} poor limit, oxygen starts leaving the metal oxide surface resulting in a metallic sample while in the rich limit the oxygen has the chemical potential of the gas phase molecule.

8.2 Discussion

GGA: Fig. 8.2 shows the most stable terminations of $\text{H}_2\text{O} + \text{Fe}_3\text{O}_4(001)$ system calculated within GGA. The left bottom corner is the poor limit of $\mu_{\text{H}_2\text{O}}$ and μ_{O} while the right top corner is the rich limit. The vacancy termination $\text{B} + \text{V}_{\text{O}}$ (B-layer with an oxygen vacancy) is stabilized at very low chemical potential of μ_{O} and $\mu_{\text{H}_2\text{O}}$ which is expected due to the lack of oxygen and hydrogen in the surroundings. With increasing oxygen pressure, the vacancies get filled with additional oxygen available and the modified B-layer termination is recovered. The modified B-layer (clean surface) termination is the most stable clean surface termination predicted previously [27]. It is stable within broad range of μ_{O} . Now with the introduction of water in the system i.e. with increasing $\mu_{\text{H}_2\text{O}}$, hydroxylation of the $\text{B} + \text{V}_{\text{O}}$ occurs which is represented by model $1D_{\text{V}} - 3$ (B-layer with an oxygen vacancy + one dissociated H_2O molecule). Adsorbing additional H_2O molecules on $1D_{\text{V}} - 3$ leads to $2\text{M}-3$ (B-layer + 2 H_2O molecules partially dissociated) termination and further adsorption of H_2O molecules may lead to the 4M . Alternatively, H_2O molecules can also adsorb on modified B-layer leading to $2\text{M}-3$ and subsequently to the 4M termination. An interesting point to note here is that the surface terminations with one H_2O molecule does not appear in the phase diagram which means that these terminations are not stable. The major part of the phase diagram has 4M termination which is the most stable termination and is stable across wide range of accessible μ_{O} and $\mu_{\text{H}_2\text{O}}$. The T and p range shown in the Fig. 8.2 allows to compare the phase diagram with experimental conditions. The LEED measurements correspond to 10^{-12} mbar which is described in Chapter 11 coincides with the 4M termination at room temperature from

Fig. 8.2 [124].

Fig. 8.5a shows a 2-dimensional projection of the surface phase diagram in $\mu_{\text{H}_2\text{O}}$ poor limit in which μ_{O} is varied in its entire range. In the absence of hydrogen in the system, modified B-layer termination is completely recovered as the most stable termination for a broad range of μ_{O} . In the oxygen poor limit B+V_O is stabilized.

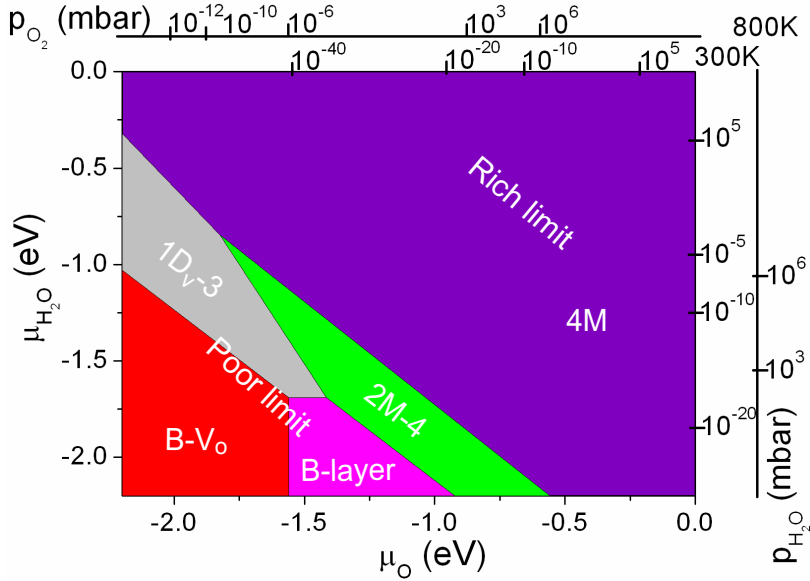


Figure 8.2: Bottom view of the surface phase diagram of $\text{H}_2\text{O}+\text{Fe}_3\text{O}_4(001)$ showing the most stable terminations for a given $(\mu_{\text{O}}, \mu_{\text{H}_2\text{O}})$: B+V_O (red), B-layer (magenta), dissociated molecule in an oxygen vacancy $1D_V - 3$ (grey area), mixed adsorption of two (green) and four water molecules on a B-layer (purple). The ranges of μ_{O} and $\mu_{\text{H}_2\text{O}}$ correspond to the vapor phase of H_2O . μ_{O} and $\mu_{\text{H}_2\text{O}}$ have been converted into pressures for 300 and 800 K.

GGA+U: Fig. 8.3 shows the bottom view of the 3-dimensional surface phase diagram shown in Fig. 8.1 which is compiled within GGA+U. Unlike the phase diagram within GGA which shows five different stable terminations, here we have only four. At a very low μ_{O} and $\mu_{\text{H}_2\text{O}}$ (poor limit), B+V_O is stabilised. With a slight increase in μ_{O} and $\mu_{\text{H}_2\text{O}}$, isolated water molecules get dissociated and fill up all the vacancy sites first as shown by the model $1D_V - 3$. Since this mechanism occurs at very low partial pressures, it is expected that even a small trace of H_2O will react with vacancy and defective surface will be difficult to observe. The termination $1D_V - 3$ is shown in a transparent hatched area so as to see the underlying competitive terminations. A 2-dimensional phase diagram enables us to clearly see different competing surface terminations at low $\mu_{\text{H}_2\text{O}}$ is shown in Fig. 8.5b. It shows that in the absence of H_2O , modified B-layer gets stabilized and is consistent with the clean surface phase diagram [26]. With a further increase of μ_{O} and $\mu_{\text{H}_2\text{O}}$ a crossover to a mixed mode of adsorption takes place. At a low and intermediate $\mu_{\text{H}_2\text{O}}$

we see that in a narrow range 2M-3 (two H_2O in a mixed mode of adsorption) exists while 4M is stable across a broad range of $\mu_{\text{H}_2\text{O}}$. The phase diagram is therefore largely dominated by two terminations: $1D_V - 3$ and 4M. The T and p scale shown in the Fig. 8.3 gives an estimate of the range of accessible T and p and rough estimate in order to compare with experimental conditions.

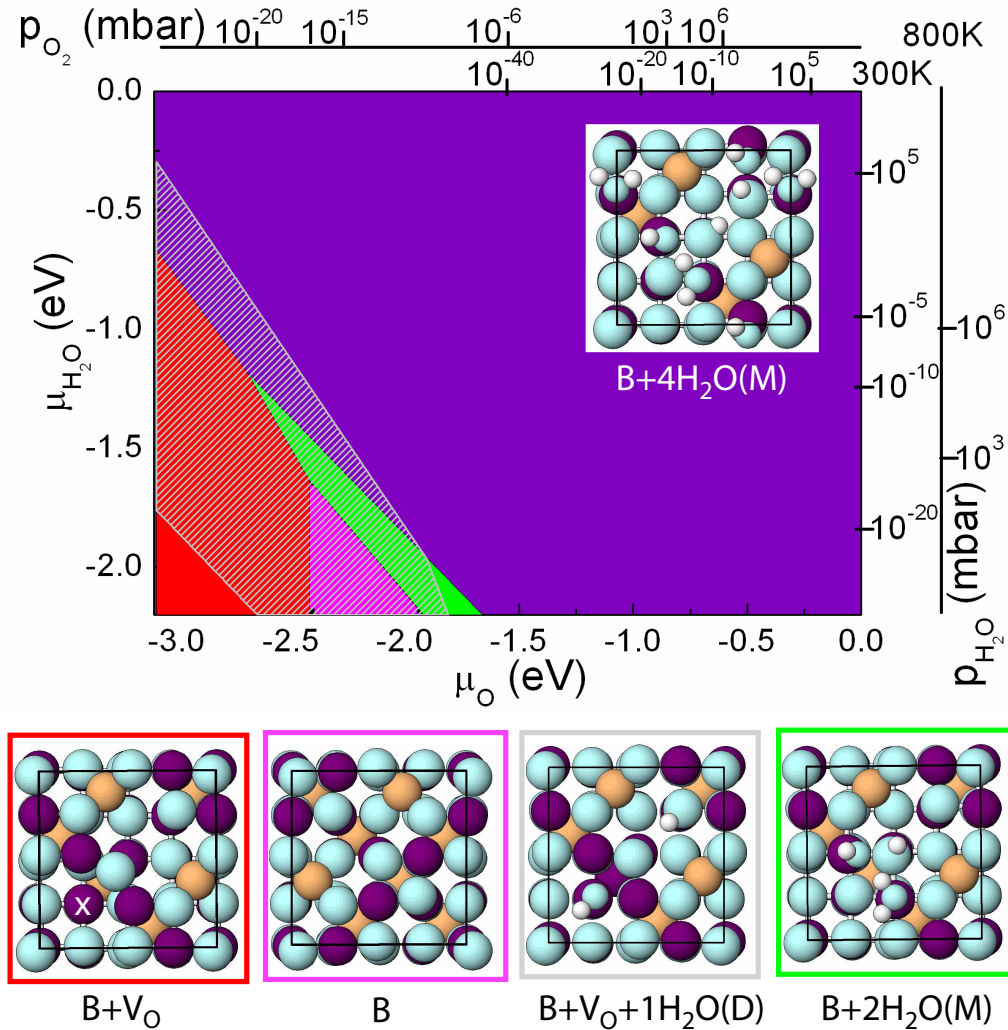


Figure 8.3: Bottom view of the surface phase diagram of $\text{Fe}_3\text{O}_4(001)$ showing the most stable configurations for given $(\mu_{\text{O}}, \mu_{\text{H}_2\text{O}})$: $B+V_{\text{O}}$ (red), B -layer (magenta), dissociated molecule in an oxygen vacancy $1D_V - 3$ (grey hatched semitransparent area), mixed adsorption of two (green) and four water molecules on a B -layer (purple). The ranges of μ_{O} and $\mu_{\text{H}_2\text{O}}$ correspond to the vapor phase of H_2O . μ_{O} and $\mu_{\text{H}_2\text{O}}$ have been converted into pressures for 300 and 800 K. Additionally, the top views of the most stable configurations are displayed with positions of O, Fe_B , Fe_A and H marked by cyan, purple, orange and white circles, respectively. In $B+V_{\text{O}}$ a white cross marks the position of the vacancy.

In principle the phase diagram within GGA and GGA+ U is largely the same except that the range of μ_{O} and $\mu_{\text{H}_2\text{O}}$ creates the difference. There is a good agreement between the results within GGA and GGA+ U .

So far we have considered the dependence on μ_{O} and $\mu_{\text{H}_2\text{O}}$ surface phase diagram. Now, we replace $\mu_{\text{H}_2\text{O}}$ by μ_{H} (chemical potential of H atom) in order to see the changes occurring in the surface phase diagram. This allows us to see some surface terminations which are stable in the absence of a thermodynamic equilibrium between μ_{O} and μ_{H} i.e. when water is not formed. The surface phase diagram compiled within GGA and GGA+ U is shown in Fig. 8.4 left and right panel respectively.

GGA: The surface phase diagram within GGA using μ_{H} remains almost similar to that with $\mu_{\text{H}_2\text{O}}$. The difference is that in the present case, the major portion of the phase diagram is occupied by the clean surface termination (modified B-layer). At very low μ_{O} and μ_{H} , the vacancy termination is stabilized ($\text{B}+\text{V}_{\text{O}}$). The $1D_{\text{V}}-3$ which can be looked as a B-layer with 2 hydrogen atoms adsorbed gets stabilized at very low μ_{O} and moderate μ_{H} . It is also the only stable hydrogen terminated surface model seen in the phase diagram. At higher values of μ_{O} and μ_{H} , the formation of water cannot be ruled out due to which partially dissociated terminations like 2M-3 and 4M get stabilized. In order to explicitly search for hydrogen terminated surface models, we have plotted a 2-dimensional cut through the 3D phase diagram side of the hydrogen rich limit as shown in Fig. 8.6 left panel. We note that $1D_{\text{V}}-3$ is more stable than $\text{B}+8\text{H}$ (B layer + 8 hydrogen atoms adsorbed) and $\text{B}+1\text{H}$ (B layer + 1 hydrogen atoms adsorbed) in the entire range of μ_{O} . Interestingly, the

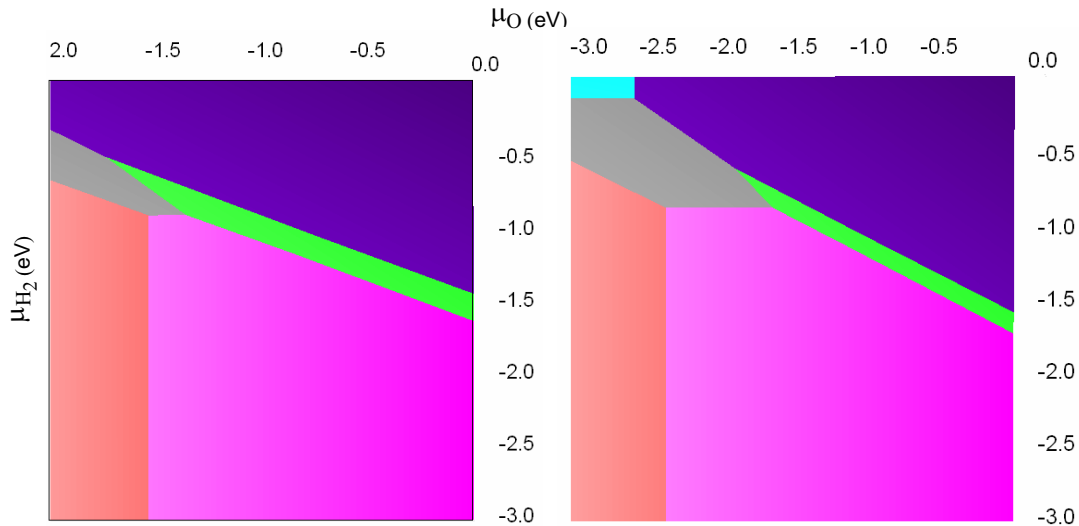


Figure 8.4: Bottom view of the surface phase diagram of $\text{Fe}_3\text{O}_4(001)$ showing the most stable configurations for given $(\mu_{\text{O}}, \mu_{\text{H}})$: $\text{B}+\text{V}_{\text{O}}$ (red), B-layer (magenta), dissociated molecule in an oxygen vacancy $\text{B}+\text{V}_{\text{O}}+1\text{H}_2\text{O}(\text{D})$ (grey area), mixed adsorption of two (green) and four water molecules on a B-layer (purple).

stability of B+8H is almost the same as B+1H.

GGA+U: The surface phase diagram within GGA+U shows six stable phases whereas within GGA it shows five different phases. The difference is that in addition to the five terminations within GGA, B+8H gets stabilized at very high μ_{H} . The rest of the surface phase diagram and stability range are similar as in the case of GGA. A 2-dimensional side cut at the hydrogen rich limit is shown in Fig. 8.6 right panel. In this case the B+8H is stabilized in the μ_{O} poor limit than the $1D_{\text{V}} - 3$ and B+1H unlike in the case of GGA.

8.3 Summary

The surface phase diagram compiled here allows to determine the most stable configurations for a given μ_{O} , $\mu_{\text{H}_2\text{O}}$ and μ_{H} . The surface phase diagram compiled within GGA+U shows four stable surface terminations. At very low partial pressures of p_{O_2} and $p_{\text{H}_2\text{O}}$, vacancy termination B+V_O is stabilized. In the absence of water vapor from the atmosphere the clean surface (modified B-layer) is stabilized at an intermediate p_{O_2} . With increase in p_{O_2} and $p_{\text{H}_2\text{O}}$, H₂O molecules start dissociating at vacancy site forming $1D_{\text{V}} - 3$ termination (B-layer with an oxygen vacancy + one dissociated H₂O molecule). With further increase in water and oxygen pressures the 2M-3 (B-layer + 2 H₂O molecules partially dissociated) gets stabilized in a narrow region of the surface phase diagram. This is followed by 4M (B-layer + 4 H₂O molecules partially dissociated) which is the most stable termination across a wide range of p_{O_2} and $p_{\text{H}_2\text{O}}$. The major features of the phase diagram within GGA and GGA+U are similar. The surface phase diagram clearly suggest that after dissociative adsorption at vacancy sites, a crossover to mixed adsorption mode follows. As previously discussed the high stability of mixed adsorption is mainly attributed to the intermolecular hydrogen bond. This picture of the phase diagram does not change when considering μ_{O} and μ_{H} . In fact it confirms the formation of water on surface within the considered range of chemical potential and shown in terms of the stable 4M termination. At room temperature the surface is quite reactive to any small trace of hydrogen or oxygen in the system and this is confirmed in the work of *kendelwicz et.al* [37] wherein beyond a threshold partial pressure of $10^{-3} - 10^{-4}$ mbar already water reacts with the surface.

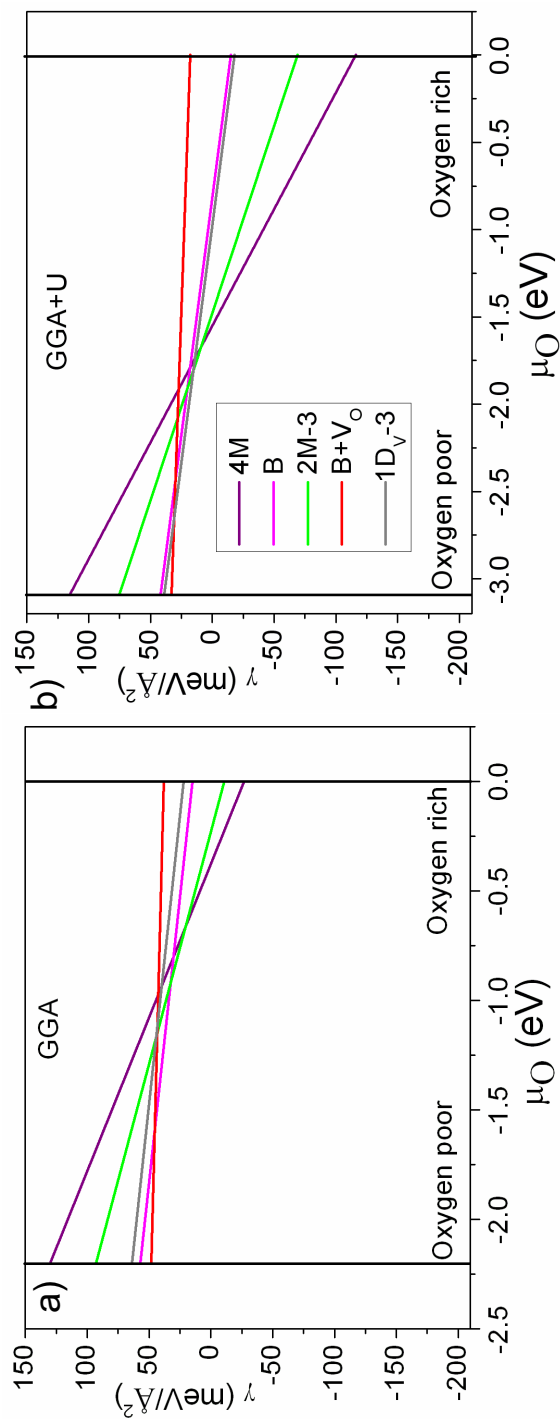


Figure 8.5: A two-dimensional surface phase diagram within poor limit of $\mu_{\text{H}_2\text{O}}$. a) Surface phase diagram calculated within GGA b) Surface phase diagram calculated within GGA+U. The μ_{O} rich and poor limit are marked.

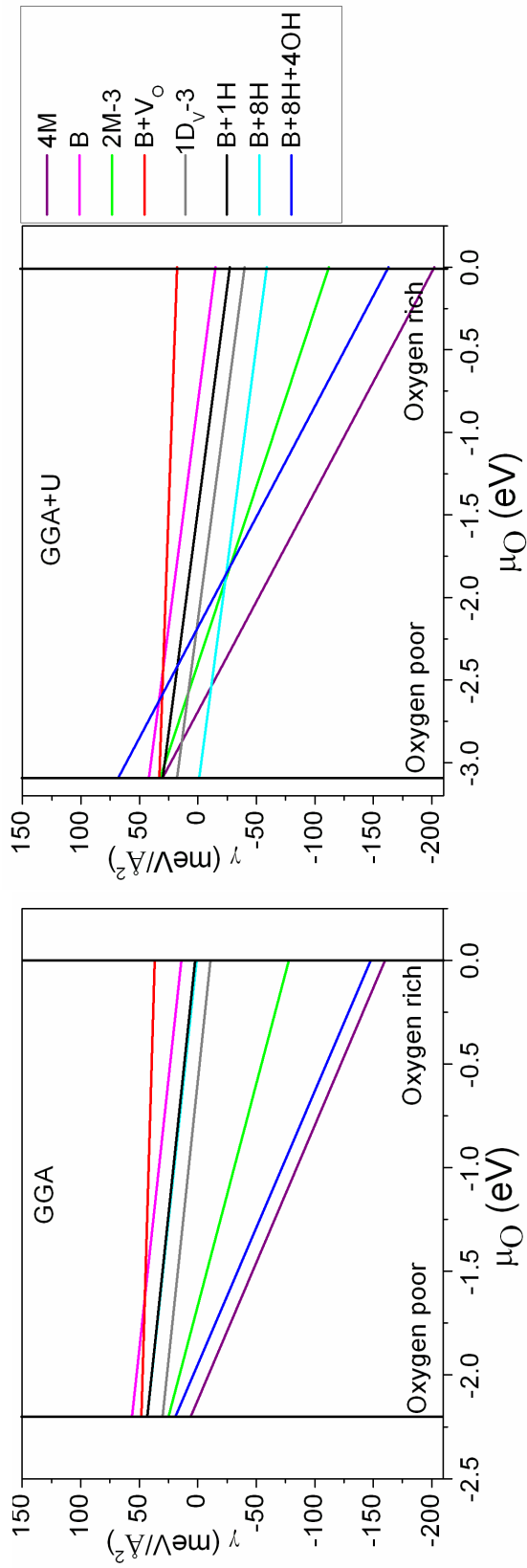


Figure 8.6: A two-dimensional surface phase diagram in the rich limit of μ_H . a) Surface phase diagram calculated within GGA b) Surface phase diagram calculated within GGA+U. The μ_O rich and poor limit are marked.

Magnetic Properties and Charge/Orbital Ordering

Magnetite has many applications originating from its magnetic properties. In this Chapter we focus on the change in magnetic properties with water adsorption. A further aspect which will be addressed is the charge and orbital order. Transition metal ions like Fe(Iron)/V(vanadium) exhibit different oxidation states for e.g. 2+/3+ and also 5+ in the case of Fe. The electron localisation at a particular atomic site results in the long range order and is referred to as charge order. Similarly, if the transition metal ions show different occupied orbitals (for e.g different d orbitals) then the arrangement is referred to as orbital order. In the case of magnetite a charge ordered state was first proposed by Verwey [5] to explain the unusual metal to insulator transition, the so called Verwey transition at a temperature of ~ 120 K. The high temperature phase is predicted to be a half-metallic ferrimagnet [12] with a high magnetic ordering temperature of $T_C=850$ K. Both the type of transitions (metal-to-insulator vs. semiconductor-to-semiconductor [7, 8]) and the type of charge (CO) and orbital ordering (OO) at the octahedral iron sites in the low temperature phase are subject of an ongoing debate [6, 9–11]. In this chapter we argue that the creation of surface and adsorption of molecules leads to a unique charge and orbital ordering in $\text{Fe}_3\text{O}_4(001)$ surface. Thus, surface and adsorbates like H_2O and OH provides a novel way to tailor catalytic properties of a material. In Section 9.1, the change of the magnetic moment after adsorption of H_2O is described and the related charge and orbital ordering (CO/OO) is discussed in Section 9.2. Finally conclusions are given in Section 9.3.

9.1 Change in magnetic properties

In this Section the change of the magnetic moment after the adsorption of H_2O molecules is discussed. Table 9.1 lists all the magnetic moments in the top two surface layers.

GGA: The magnetic moment (M) of the two surface Fe_B atoms ($\text{Fe}_B(\text{S}1)$, $\text{Fe}_B(\text{S}3)$) in the vacancy termination ($\text{B}+\text{V}_\text{O}$: B layer with an oxygen vacancy) differ by $0.91 \mu_B$. The decrease of M in one of the $\text{Fe}_B(\text{S})$ is due to the undercoordination created by the oxygen vacancy. When the undercoordination is eliminated in the clean surface (modified B-layer) the magnetic moments are nearly equal. With the addition of adsorbates on the surface (H , OH , H_2O), the M of the $\text{Fe}_B(\text{S})$ increases w.r.t that in the modified B-layer and depends on the adsorption model considered. In $1\text{D}_V\text{-3}$ (one water molecule dissociated), an increase is noticed in the M by $\sim 0.50/0.45 \mu_B$ while in $2\text{M}\text{-3}$ (two water molecules in mixed adsorption) only those $\text{Fe}_B(\text{S})$ covered with adsorbates show $\sim 0.73/0.78 \mu_B$ increase. On the other hand in the case of 4M (four water molecules in mixed adsorption) where all the $\text{Fe}_B(\text{S})$ are covered, an increase in M of $\sim 0.70 \mu_B$ is observed on average compared to the clean surface $\text{Fe}_B(\text{S})$. The subsurface Fe ($\text{Fe}_B(\text{S}\text{-}1)\text{1-}4$) atoms show no noticeable differences before and after adsorption. Another interesting aspect to note is the gain in M of the oxygen atoms in the surface layer. Usually the free oxygen atom has zero magnetic moment and also in the bulk Fe_3O_4 . In the models considered, we notice a gain in the M of surface oxygen ($\text{O}(\text{S}1/2)$) by $\sim 0.10/0.20 \mu_B$. The oxygen atom of adsorbates like OH and H_2O shows an increase of $\sim 0.10 \mu_B$ and $\sim 0.05 \mu_B$ respectively. The M of subsurface layer oxygen atoms ($\text{O}(\text{S}\text{-}1)\text{1-}2$) are small and show no differences with adsorption.

GGA+U: Within $\text{GGA}+U$, in the case of Fe^{3+} the lower Hubbard band in the majority spin channel is fully occupied while the upper Hubbard band in minority spin channel is unoccupied. On the other hand in the case of Fe^{2+} some t_{2g} orbital in the minority spin channel are occupied enabling us to distinguish between the Fe^{3+} and Fe^{2+} . The oxidation state of $2+$ and $3+$ of the Fe atoms can be easily identified from the magnetic moments (M). The typical range of M for Fe^{2+} is $3.54\text{-}3.75 \mu_B$ while that of Fe^{3+} is $3.90\text{-}4.10 \mu_B$. The M of $\text{Fe}_B(\text{S})$ atoms in the vacancy termination differ by only $0.08 \mu_B$. In the case of a clean surface both $\text{Fe}_B(\text{S})$ ($\text{Fe}_B(\text{S}1)$, $\text{Fe}_B(\text{S}3)$) show the same M ($4.04 \mu_B$). Now with the adsorption of H_2O , OH no appreciable change in M of $\text{Fe}_B(\text{S})$ is noticed. In fact, in most of the cases we observe that all the surface irons are in $3+$ oxidation state except in a few cases involving an oxygen vacancy. An interesting aspect is noticed in the subsurface layer where we see a difference in the M of $\text{Fe}_B(\text{S}\text{-}1)$. The M in the subsurface layer change by $\sim 0.40\text{-}0.50 \mu_B$ compared to the one in modified B-layer. We observe the existence of two different oxidation states of $\text{Fe}(2+/3+)$. This charge ordered state is elaborated in the next Section 9.2. The M of the oxygen atom in the surface and sub surface layer as well those of adsorbates also show some

Table 9.1: Magnetic moments (μ_B) of the surface (S) and sub surface layer (S-1) are listed. The most stable surface terminations are chosen as shown in Fig. 8.3. All the magnetic moments are given in μ_B

	B+V _o		modified B-layer		1D _v -3		2M-3		4M	
	GGA	GGA+U	GGA	GGA+U	GGA	GGA+U	GGA	GGA+U	GGA	GGA+U
Fe _B (S1)	2.55	4.01	3.00	4.04	3.51	4.02	2.80	4.03	3.69	4.10
Fe _B (S2)							2.80	4.04	3.70	4.10
Fe _B (S3)	3.44	3.92	3.06	4.04	3.51	4.02	3.78	4.10	3.76	4.10
Fe _B (S4)							3.73	4.11	3.71	4.10
O(S2)	0.02	0.06	0.01	0.04	0.03	0.05	0.04	0.06	0.07	0.06
O(S1)	0.08	0.27	0.12	0.27	0.25	0.23	0.09	0.27	0.28	0.27
Fe _A (S1)	-3.46	-3.94	-3.44	-3.95	-3.39	-3.95	-3.44	-3.95	-3.34	-3.94
Fe _B (S-1)1	3.51	3.99	3.42	3.67	3.51	3.59	3.50	4.00	3.63	3.54
Fe _B (S-1)2	3.51	3.59	3.44	3.92	3.57	3.99	3.58	3.60	3.60	4.02
Fe _B (S-1)3	3.38	3.47	3.54	4.06	3.51	3.60	3.58	4.04	3.62	4.07
Fe _B (S-1)4	3.49	4.00	3.45	4.06	3.57	3.99	3.51	4.06	3.63	4.05
O(S-1)1	0.08	0.09	0.08	0.07	0.08	0.08	0.10	0.10	0.07	0.04
O(S-1)2	0.08	0.03	0.05	0.10	0.08	0.03	0.06	0.07	0.09	0.09
O _{H₂O}							0.05	0.05	0.05	0.05
O _{OH}							0.10	0.08	0.10	0.08

increase in M similar to that observed in the case of GGA. A similar observation was also made in the case of H_2O adsorption on $\text{NiO}(001)$ [84].

9.2 Adsorbate induced CO/OO

In this Section we will discuss the effect of surface and adsorbate induced electronic effects on $\text{Fe}_3\text{O}_4(001)$. The electron density is integrated in the minority spin channel from -1.2 eV to E_F and plotted to display the t_{2g} occupancies at the Fe_B -sites as shown in Fig. 9.1. This allows a clearer distinction between sites with predominant Fe^{2+} or Fe^{3+} -character. We have also explored the influence of U parameter used on the charge (CO) and orbital order (OO). We varied U parameter from 0-8 eV and found that charge disproportionation at the Fe_B -sites is found beyond $U = 2$ eV as shown in Fig. 9.2. The notation Fe^{2+} and Fe^{3+} is used here for simplicity, but the difference in total $3d$ occupation within the muffin-tin sphere is typically much smaller (0.2 - $0.4e$) as shown in Fig. 9.2 and is consistent with XRD- [6] and LDA+ U studies for the low temperature bulk phase [9, 10]. For most of the stable systems we find that the surface layer contains exclusively Fe^{3+} while a unique charge and orbitally ordered state emerges in the deeper layers depending on the type of termination.

In the case of $\text{B}+\text{V}_{\text{O}1}$ (Fig. 9.1a) the two subsurface Fe_B next to $\text{V}_{\text{O}1}$ are Fe^{2+} ($d_{xz} \pm d_{yz}$). On the other hand, a vacancy created at $\text{V}_{\text{O}2}$ (Fig. 5.1) induces $\text{Fe}^{2+} \setminus \text{Fe}^{3+}$ on the surface while all the subsurface Fe_B are in Fe^{3+} state as shown in Fig. 9.1c). The charge ordered state of the latter case is more favorable due to the availability of different oxidation states of Fe_B on the surface and hence is more reactive. Now coming back again to the former case ($\text{B}+\text{V}_\text{O}$) and continuing with water adsorption, we observe the distribution of the Fe^{2+} changes in $\text{B}+\text{V}_\text{O}+1\text{H}_2\text{O}(\text{D})$. The two Fe_B below the surface OH groups are Fe^{2+} , resulting in alternating Fe^{2+} , Fe^{3+} -sites as shown in Fig. 9.1e. In the mixed adsorption case ($\text{B}+4\text{H}_2\text{O}(\text{M})$) the charge ordering in the subsurface layer is not significantly altered compared to B-layer, where one out of four $\text{Fe}_B(\text{S}-1)$ is Fe^{2+} and a second is in an intermediate valence state. However, the slight tilting of the t_{2g} orbital at Fe^{2+} induces a completely different OO in S-2: from $d_{xz} \pm d_{yz}$ to alternating d_{xy} and d_{xz} -orbitals. Recent GGA+ U calculations have shown that in bulk magnetite a variety of CO/OO states can be realized by symmetry lowering [117]. Here the presence of a surface and adsorbates imposes a unique CO/OO state for each termination reaching several layers below the surface. Moreover, most of them violate the Anderson criterion: Fe_4O_4 cubes in the surface and subsurface layer are predominantly electron poor ($3\text{Fe}^{3+}+1\text{Fe}^{2+}$), while those in S-1 and S-2-layer are electron rich ($1\text{Fe}^{3+}+3\text{Fe}^{2+}$). Evidence for orbital ordering in thin magnetite films was reported recently from resonant soft x-ray diffraction [11].

The charge ordered state in the modified B-layer (clean surface) leads to the

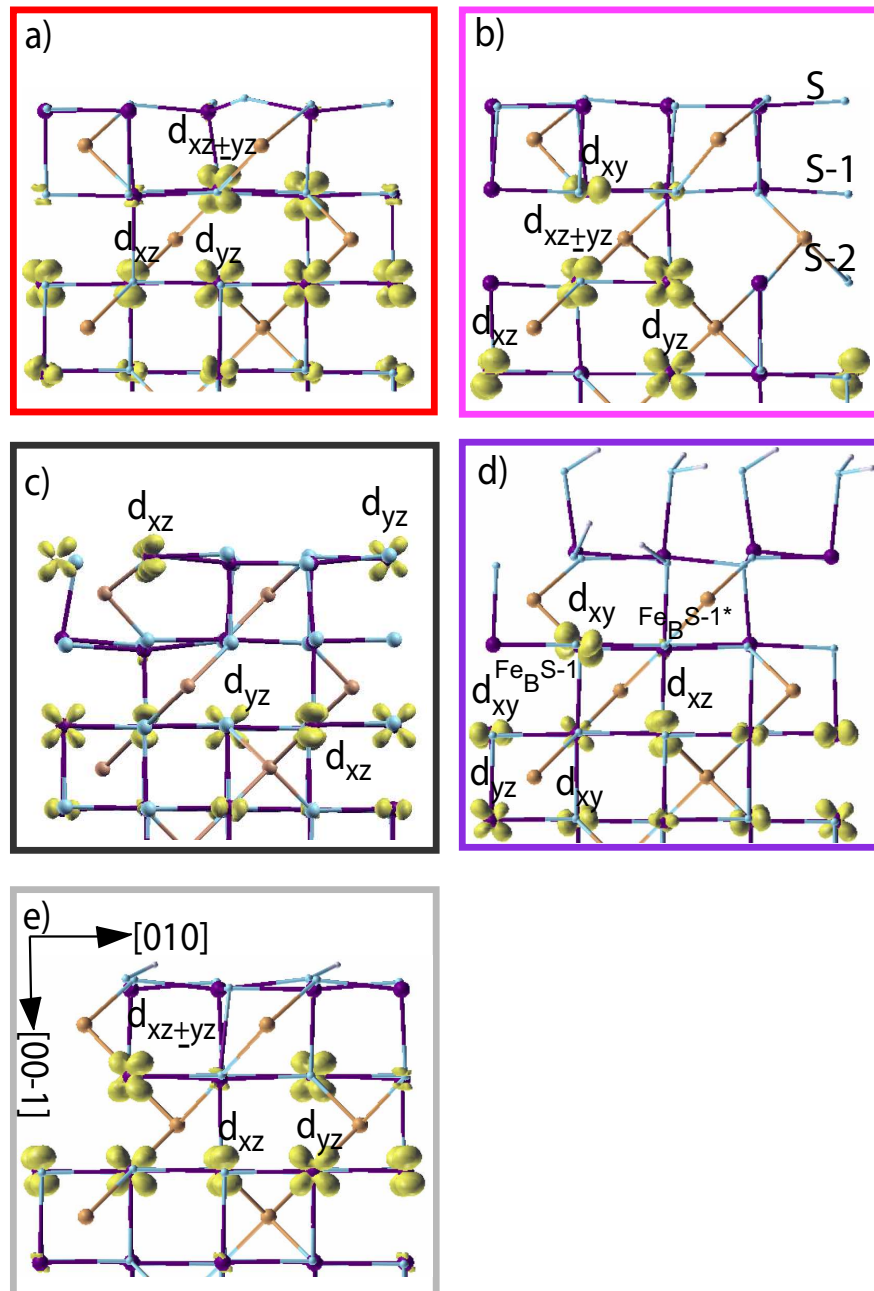


Figure 9.1: The electron density plots integrated from -1.2 eV to E_F is shown for various stable terminations. a) $B+V_{O1}$ b) Modified B-layer c) $B+V_{O2}$ with vacancy created by another oxygen d) $B+4H_2O(M)$ e) $B+V_O + 1H_2O(D)$. Since the minority spin channel is occupied in the energy range chosen for some $Fe_B(S)$ therefore the orbitals represent Fe^{2+} .

opening of a band gap of 0.3 eV as shown in Fig. 7.10b, consistent with previous calculations [26] and scanning tunneling spectroscopy measurements [118]. However the adsorption of water on the surface and the formation of surface hydroxyl groups leads to a half-metallic behavior.

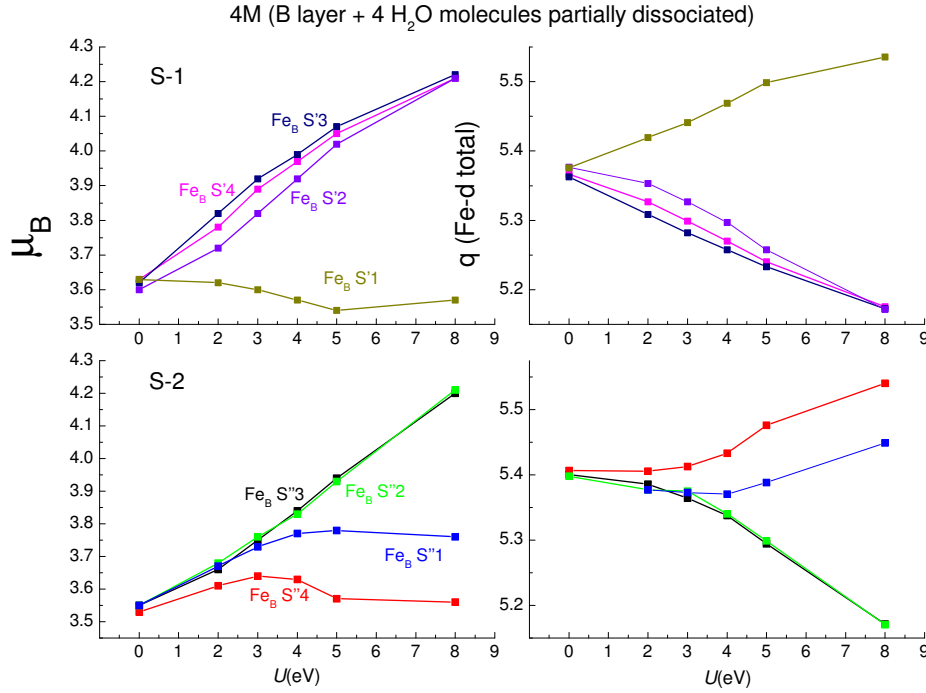


Figure 9.2: The change in magnetic moment and charge inside the muffin-tin sphere for the d -orbital vs. the U parameter. The top row shows the values for the sub surface layer (S-1) and the bottom row shows that for the S-2 layer.

9.3 Summary

The magnetic moments in the case of GGA+ U can help to distinguish the Fe^{2+} and Fe^{3+} oxidation state. The typical range of MM for Fe^{2+} is 3.54-3.75 μ_{B} while that of Fe^{3+} is 3.90-4.10 μ_{B} . The magnetic moment of the surface Fe_{B} does not show any significant change with the adsorption of H_2O molecule. On the other hand the sub-surface Fe_{B} changes the oxidation state after adsorption. The localisation of charge at a particular atomic site which result in different oxidation states ($\text{Fe}^{2+}/\text{Fe}^{3+}$) is referred to as charge ordering. In fact we find different charge and mainly orbitally ordered states after the adsorption of H_2O molecules in a mixed adsorbed termination. This provides a novel way to tailor the properties of a catalyst. The surface and adsorbate oxygen's gain magnetic moment from zero in a free atom to $\sim 0.05 - 0.20 \mu_{\text{B}}$. The adsorption of water leads to a transition from insulator to half-metallic character.

Surface Core Level Shifts

The binding energy of the core electrons is extremely sensitive to its chemical environment [69, 70]. The change of the binding energy w.r.t a free atom is called core level shift (CLS). The difference between the core level of a surface atom and a bulk atom is the surface core level shift (SCLS). CLS and SCLS are being used as tools for 1) atom specific structural determination 2) detects the changes in the electrostatic potential around the atom 3) determination of the composition of substitutional random alloys [69, 71]. Experimentally the binding energy of the core electron of a bulk or a surface atom can be determined by highly sensitive XPS (X-ray photoemission spectroscopy) [69]. The surface core level spectroscopy is a useful tool to study chemisorption as it provides information about the adsorption site, charge transfer and change in adsorption strength which may be related to the substrate band filling [69]. In core level spectroscopy, the excitation of core electron to the Fermi level and subsequent relaxation effects contribute to the total shifts.

The total SCLS (Δ^{SCLS}) consists of two effects: *initial state effect* which reflects the electronic charge distribution in the normal surface i.e. before excitation of the core hole, and a *final state effect* which is due to different screening effects of the core-ionized system (in the bulk and at the surface) [69]. Experimentally these two contributions cannot be distinguished. The advantage of DFT calculations is that one can distinguish between the initial and final state effects which makes it complementary to the experimental results. However, an extra calculation is needed to calculate the final state effects. Theoretical calculations are also needed to verify the structural and electronic models proposed by experimental shifts [69]. Core level shifts can be related to various material properties like cohesive energy, heat of mixing, segregation energy and charge transfer.

In this Chapter we will determine the surface core level shifts due to the adsorption of water on the $\text{Fe}_3\text{O}_4(001)$ surface. The FP-LAPW (full potential linear augmented plane wave) method used here, has as an all electron method the advantage over the pseudopotential related methods as it treats the core electrons explicitly and thus the core level binding energy can be directly

accessed. The theory and computational details are described in Section 2.5.

10.1 Origin and factors contributing to SCLS

Compared to the bulk atom, a surface atom is undercoordinated. This change in chemical environment influences the local potential. This typically results in narrowing of the valence band. The change in the local potential ultimately influences the binding energy of the core electron. Other factors which affect the SCLS are the 1) interatomic charge transfer; 2) changes due to screening of core hole; 3) changes in the Fermi level relative to the center of gravity of bands, and, finally 4) redistribution of charge due to bonding and hybridisation in the case of adsorption.

10.2 SCLS of H₂O on Fe₃O₄(001)

The surface core level shifts (Δ^{SCLS}) are calculated within GGA+ U for the most stable surface terminations as shown in Fig. 8.3 namely, B+V_O, 1D_V-3, 2M-3 and 4M. As stated earlier the total shift consists of an initial state contribution calculated using Eq. 2.53 while the final state contribution was calculated using the Slater-Janak transition state method as discussed in Section 2.4 (Eq.2.54). Tables 10.1, 10.2 and 10.3 list the calculated Δ^{SCLS} . A schematic top view of each termination is shown in Fig. 10.1 along with the labeling of atoms used. The sign convention adopted from our calculation is: positive Δ^{SCLS} refer to stronger binding energies and positive screening means that the core hole is less screened on the surface than in the bulk. In the following, we first discuss the O1s Δ^{SCLS} and then Fe 2p surface core level shifts.

Δ^{SCLS} O1s:

modified B-layer, 1F and 1D-1 (B-layer clean surface, B-layer with one H₂O molecule flat adsorbed and B-layer with one H₂O molecule dissociated): The Δ^{SCLS} for each termination is listed in Table 10.1. The negative initial and total shifts of the surface oxygens O^{S2-S5} of the modified B-layer can be attributed to the undercoordination of the O(S) compared to the bulk oxygen. As stated earlier the initial state effect is related to the electron charge redistribution in the system before core excitation. In the XPS measurements [20,119] on clean Fe₃O₄(001) surface, O1s Δ^{SCLS} of 1.0-1.1 eV is observed. The origin of which was not exactly known but was attributed to final state effects. In fact the total shift of ~ 1.0 eV of O^{S3-S4} coincides well with experiments and indeed confirms that these additional peaks arise from the final state effects. With the adsorption of a H₂O molecule (1F), we do not notice much change in

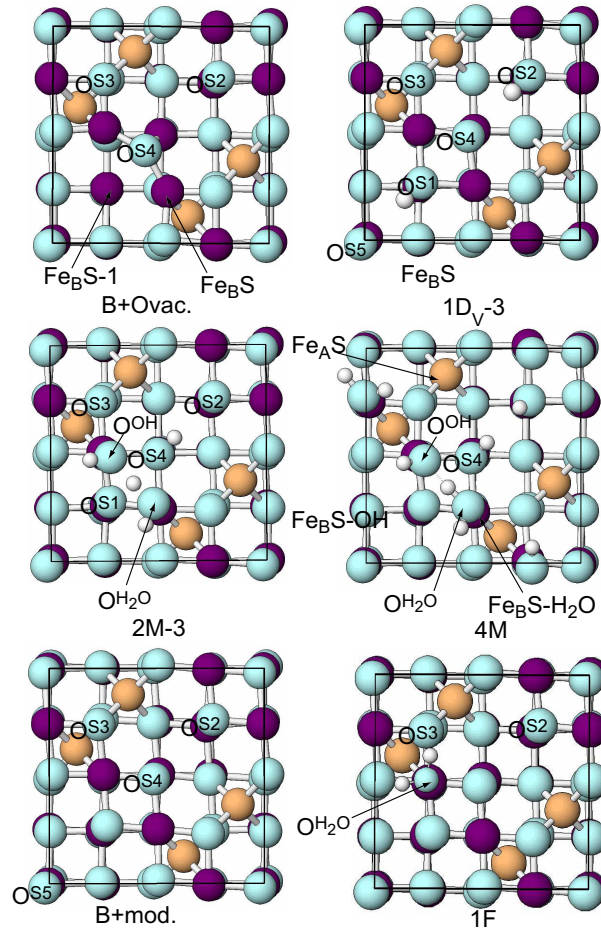


Figure 10.1: Top view of the most stable surface terminations (see Fig. 8.3) a) $B+V_O$ b) $1D_V-3$ c) $2M-3$ and d) $4M$ with schematic labeling of atoms for which Δ^{SCLS} are calculated and listed in Table 10.2 and 10.3. Positions of oxygen, Fe_B , and hydrogen are marked by cyan, purple and white circles.

the initial and total shifts of $O(S)$. However the positive initial shift of O^{H_2O} confirms a weak charge transfer from the H_2O molecule to the surface resulting in less repulsion and hence higher binding energy of $O1s$ level. The final state shift of 5 eV corresponds to the gas phase molecule shift observed in XPS measurements [37]. This well confirms the physisorption of water molecule. The dissociation of the water molecule reverses the direction of SCLS shift. In this case we find negative initial shift due to charge transfer from the surface to the OH group resulting in strong electronic repulsion and hence low binding energy. Final state effect is low due to screening effects.

$B+V_O$ (B-layer termination with an oxygen vacancy (V_O)): Table 10.2 shows negative values in the initial and total shifts as observed for modified B-layer. The initial state shift in the case of O^{S1} is higher than in O^{S3} due to reduced coordination in the latter case. In contrast, the screening contribution is positive for all the surface oxygen ($O(S)$) atoms. The screening effect in the

Table 10.1: *O*1s and Fe 2p_{1/2} and 2p_{3/2} surface core level shifts Δ^{SCLS} for B-layer modified, 1F and 1D-1 with initial, screening and final state contributions are listed. $\Delta_{total}^{SCLS} = \Delta^{screen} + \Delta^{initial}$.

	modified B-layer			1F			1D-1		
	Initial	Screening	Total	Initial	Screening	Total	Initial	Screening	Total
O ^{S1}	-1.61	+0.58	-1.03				-1.51	+0.76	-0.75
O ^{S2}							-1.35	+0.43	-0.92
O ^{S3}	-1.13	+0.99	-0.14	-1.14	+1.18	+0.04			
O ^{S4}	-1.76	+0.99	-0.77	-1.73	+0.97	-0.76	-0.49	+1.89	+1.40
O ^{S5}	-1.67	+0.75	-0.92						
O ^{H₂O}				+1.04	+4.02	+5.06			
O ^{OH}							-1.81	+2.30	+0.49
Fe _B S 2p _{1/2} and 2p _{3/2}									
Fe _B S 2p _{1/2}	-0.61	+1.42	+0.81	+0.53	-0.67	-0.14	+0.33	-1.01	-0.68
Fe _B S 2p _{3/2}	-0.61	+1.42	+0.81	+0.53	-0.67	-0.14	+0.33	-1.01	-0.68
Fe _A S 2p _{1/2}	-0.80	+1.31	+0.51	-0.70	+2.78	+2.08	-0.47	+2.62	+2.15
Fe _A S 2p _{3/2}	-0.80	+1.31	+0.51	-0.70	+2.78	+2.08	-0.47	+2.62	+2.15

case of O^{S3} is stronger than in O^{S1} due to the following reason: The O^{S3} compensates the undercoordination created by the oxygen vacancy for the surface iron (Fe_B(S)) by reducing $d_{\text{Fe}_B(\text{S})-\text{O}(\text{S})}$ from 2.06 Å in bulk to 1.85 Å. This increased proximity to Fe_B(S) and the shift of the O 2p band to lower energy provides poor screening to the core hole as shown in Fig. 10.2a. The more positive the screening contribution is, the less is the core hole screened on the surface compared to the bulk atom. The O^{S2} is having an Fe_A neighbor which makes it less active as already stated in previous chapters. The initial state and screening contribution are similar in magnitude but differ in signs resulting in a weak total Δ^{SCLS} .

1D_V-3 (B-layer with oxygen vacancy + 1H₂O molecule dissociated): The initial state shift is again negative and that for screening remains positive for all the O(S). The Δ^{SCLS} for O^{S3}, O^{S5} are similar as in O^{S1} of B+V_O. To get a comparative view, each row in Table 10.2 lists the equivalent site in both the terminations. The difference is observed for those oxygens (O^{S1}, O^{S4}) which have now hydrogen on top. Even though the initial state shift is very small, there is a significant screening contribution which results in a significant total shift. While the total shift for all uncovered O(S) is negative, the one for O^{S1} and O^{S4} is positive. The reason is the shift of the O2p band for the latter cases to lower energy which provides poor screening compared to other uncovered surface oxygens (O(S)).

2M-3 and 4M (two H₂O molecules in mixed mode adsorption and four H₂O molecules in mixed mode of adsorption): Δ^{SCLS} is given in Table 10.3. The initial state shift largely remains negative with positive screening contribution

Table 10.2: $O1s$ and $Fe\ 2p_{\frac{1}{2}}$ and $2p_{\frac{3}{2}}$ surface core level shifts Δ^{SCLS} for $B+V_O$ and $1D_V-3$ with initial, screening and final state contributions are listed. $\Delta_{total}^{SCLS} = \Delta^{screen} + \Delta^{initial}$.

	B+V _O			1D _V -3		
	Initial	Screening	Total	Initial	Screening	Total
O ^{S1}				-0.07	+1.27	+1.19
O ^{S2}	-1.37	+0.21	-1.16	-0.07	+1.27	+1.20
O ^{S3}	-0.55	+0.46	-0.09	-0.64	+0.34	-0.30
O ^{S4}	-0.82	+0.48	-0.34	-1.27	+0.28	-0.99
O ^{S5}						
Fe _B S 2p _{1/2} and 2p _{3/2}						
Fe _B S 2p _{1/2}	+0.57	-0.57	0.00	+0.79	-0.86	-0.07
Fe _B S 2p _{3/2}	+0.57	-0.57	0.00	+0.79	-0.86	-0.07
Fe _B S-1 2p _{1/2}	+0.17	-0.74	-0.57	-	-	-
Fe _B S-1 2p _{3/2}	+0.17	-0.74	-0.57	-	-	-
Fe _A S 2p _{1/2}	-0.53	+2.96	+2.43	-	-	-
Fe _A S 2p _{3/2}	-0.53	+2.96	+2.43	-	-	-

Table 10.3: $O1s$ and $Fe\ 2p_{\frac{1}{2}}$ and $2p_{\frac{3}{2}}$ surface core level shifts Δ^{SCLS} for $2M-3$ and $4M$ with initial, screening and final state contributions are listed. $\Delta_{total}^{SCLS} = \Delta^{screen} + \Delta^{initial}$

	2M-3			4M		
	Initial	Screening	Total	Initial	Screening	Total
O ^{S1}	-1.60	+1.04	-0.56	-1.60	+1.18	-0.42
O ^{S2}	-1.39	+0.66	-0.73			
O ^{S3}	-0.94	+0.84	-0.09			
O ^{S4}	-0.43	+2.07	+1.64	-0.19	+2.12	+1.93
O ^{H₂O}	-0.27	+2.87	+2.60	-0.17	+3.10	+2.93
O ^{OH}	-1.04	+2.48	+1.44	-1.04	+2.48	+1.44
Fe _B S 2p _{1/2} and 2p _{3/2}						
Fe _B S-H ₂ O 2p _{1/2}	+0.84	-1.09	-0.25	+0.72	-1.04	-0.32
Fe _B S-H ₂ O 2p _{3/2}	+0.84	-1.09	-0.25	+0.72	-1.04	-0.32
Fe _B S-OH 2p _{1/2}	+0.73	-1.16	-0.41	+0.66	-1.04	-0.38
Fe _B S-OH 2p _{3/2}	+0.73	-1.16	-0.41	+0.67	-1.04	-0.38
Fe _A S 2p _{1/2}	-0.50	+2.55	+2.05	-0.67	+2.66	+1.99
Fe _A S 2p _{3/2}	-0.50	+2.55	+2.05	-0.67	+2.66	+1.99

as discussed above for the uncovered oxygens. On the other hand O(S) which have a hydrogen atom on top or O^{H₂O} or O^{OH} show high screening effects and hence positive total shifts. The O^{S4} in the mixed termination behaves similar to the O^{S4} of 1D_V-3. The initial state effect of O^{H₂O} is small compared

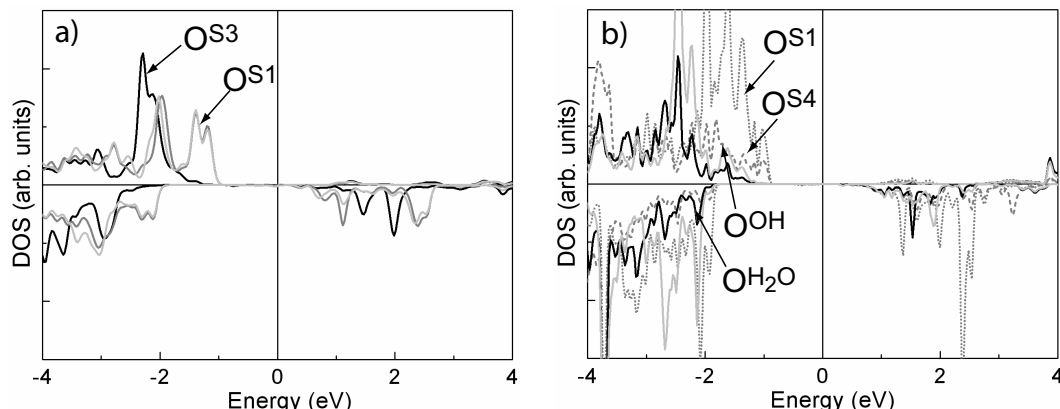


Figure 10.2: Partial density of states (PDOS) of oxygen 2p band a) PDOS of O^{S1} (light grey line), O^{S2} (dark grey line) and O^{S3} (black solid line) in $B+V_O$ b) PDOS of O^{S1} (dotted line), O^{S4} (dashed line), O^{OH} (light grey line) and O^{H_2O} (black solid line).

to that of O^{OH} . This correlates with weaker bond with the substrate in the former case and a stronger bond in the latter case. On the other hand if we compare the initial state shifts of O^{H_2O} and O^{OH} with that in 1F and 1D-1, we notice a substantial decrease in 2M-3 and 4M due to hydrogen bond formation. Due to similar reason we notice lowering in the screening effects. However the screening contributions are very high (2.48-3.10 eV) compared to other surface oxygens. The oxygen 2p band of O^{OH} is more pronounced near the Fermi level compared to O^{H_2O} leading to a lower screening contribution in the former case as shown in Fig. 10.2. On the other hand O 2p band of both are lower in energy when compared to O(S) as shown in Fig. 10.2. This explains the poor screening for O^{OH} and O^{H_2O} . We note that the final states obtained here play a dominant role.

The inclusion of final state is necessary in order to compare with experiments [120,121]. In some of the transition metals (Ru [72],Rh) and metal oxides (RuO₂ [121]), final state effects although important are not as pronounced as in our case.

The oxygen of the hydroxyl group (O^{OH} and $O(S)+H$) shows a Δ^{SCLS} of 1.19-1.93 eV which is consistent with the XPS measurement done by Kendelwicz *et.al* [37] (1-2.5 eV). The Δ^{SCLS} of a hydrogen bonded O^{H_2O} is 2.60-2.93 eV which is close to the experimental values [122, 123].

$\Delta^{SCLS} \text{ Fe}_B 2p_{\frac{1}{2}}$ and $2p_{\frac{3}{2}}$: In the case of iron the initial state effect is positive while screening is negative. This is opposite to that of oxygen as discussed above. The final state effect is mainly due to the intra atomic *d*-electron screening [72]. The core excitation will lead to the filling of the core hole by a valence electron in order to maintain charge neutrality which in turn will shift the unoccupied states to lower energies and this leads to greater screening (negative shifts). The $\text{Fe}_B(S)$ with H₂O or OH on top does not show any significant difference in 2M-3 and 4M while in 1D-1 and 1F we do see

a change in the direction of shifts. We notice that hydrogen bond between OH and H₂O significantly influences the Δ^{SCLS} . The total shifts of Fe_B(S) 2*p* are much lower compared to O 1*s* shifts, similar results were obtained by the XPS measurements done on the clean surface [20] and on water dosed Fe₃O₄(001) surface [37]. However we notice a large total shift in the case of Fe_AS of the magnitude of 1.99-2.43 eV. This is possibly due to poor screening when compared to Fe_B(S).

10.3 Summary

The surface core level shifts (Δ^{SCLS}) were calculated using the Slater-Janak transition state method [73]. The surface oxygen shows a negative total shift i.e. the core level moves towards lower binding energy. On the other hand oxygens with H on top or of H₂O and OH show a positive total shift indicating higher binding energies. We find that the main contribution comes from the screening effect which can be related to the relative positions of the O-2*p* band near the Fermi level. The shifting of the O-2*p* band to lower energy is the likely reason for poor screening. The Δ^{SCLS} of O^{H₂O} (2.60-2.90 eV) or O^{OH} (1.14-1.93 eV) is in good agreement with experimentally observed shifts. The Δ^{SCLS} of Fe_B(S) are very low and therefore can not be measured due to constraints in the experimental resolution.

Low Energy Electron Diffraction

Low energy electron diffraction (LEED) is a surface sensitive technique which primarily is able to determine the surface structure. The electrons in the energy range (20-500 eV) have mean free path of $\sim 5-10 \text{ \AA}$ [129] i.e. effective attenuation occurs after the first few atomic layers, which means that the diffracted intensity stems typically from the first few surface layers only. The diffraction pattern obtained in this technique gives information about size, symmetry and orientation of the surface unit cell. The intensity of the beams is usually recorded by a video camera as a function of the electron energy, so called $I(V)$ curves, which can be compared to theoretical curves whereby the information about the surface structure can be obtained. In this Chapter we will discuss the LEED investigation of water adsorption on the $\text{Fe}_3\text{O}_4(001)$ surface¹. We have focused mainly on: 1) The type of surface termination after the adsorption of the H_2O molecules, and 2) The influence of water adsorption on the $(\sqrt{2} \times \sqrt{2})R45^\circ$ reconstruction. The results are compared to the DFT calculations.

11.1 Experimental set up

In a typical LEED setup as shown in Fig. 11.1 left panel, the electron gun is normal to the sample surface. In order to avoid contamination from residual gas, LEED experiments are performed in an ultra high vacuum chamber (UHV) with a typical pressure of 10^{-10} to 10^{-11} mbar (Fig. 11.1 right panel). Normal incidence is not always necessary but usually chosen when the symmetry of the diffraction pattern can be used to control the incidence angle. The elastically back scattered electrons are made visible on a fluorescent screen, while the inelastically scattered electrons are filtered out by retarding grids. The wavelength of the electrons is of the same order as the interatomic distances and

¹The LEED measurements at low temperature were done by Maria Wieland as part of the project. The calculations have been supported by Prof. Moritz.

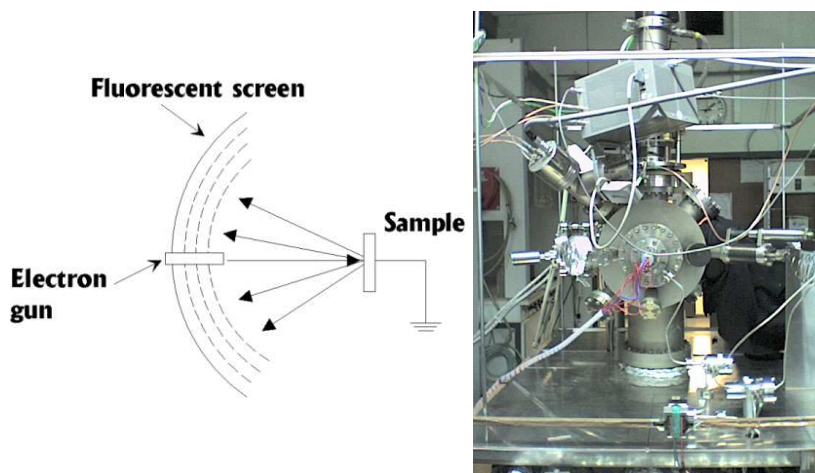


Figure 11.1: A schematic diagram of LEED setup is shown in the left panel. The experimental setup is shown in the right panel displaying a typical the UHV-vacuum chamber.

therefore well suited for the structure determination. The diffraction pattern observed on the screen gives an overview of the 2-D reciprocal lattice of the surface structure. This diffraction pattern is the so called LEED pattern and contains directly information about the symmetry of the surface unit cell and the step density and domain sizes at the surface. Narrow diffraction peaks indicate a well ordered surface. The measurement of the intensity of the diffracted spots as a function of the electron energy gives the LEED $I(V)$ curves which are used for the structure determination.

11.2 Experimental procedure

LEED measurements were performed on a synthetic magnetite sample. The clean surface was prepared by Ar^+ -ion sputtering and subsequent annealing at 900-1000 K at $p_{\text{O}_2} = 5 \times 10^{-7}$ mbar for 2-3 h. This preparation exhibited the well known $(\sqrt{2} \times \sqrt{2})R45^\circ$ -LEED pattern [27, 126] with sharp superstructure reflections and low background (Fig. 11.2 a). A quartz-glass tube containing double distilled water connected through a gas inlet valve to the main chamber was used as water source. The sample was exposed to water vapour through a stainless steel tube mounted in front of the sample. Water was adsorbed at different temperatures with varying exposure time. The water vapor pressure in all the experiments was maintained at 2×10^{-6} mbar. In order to understand the adsorption behavior of H_2O molecules on the $\text{Fe}_3\text{O}_4(001)$ surface and on $(\sqrt{2} \times \sqrt{2})R45^\circ$ surface reconstruction, we performed experiments at a wide range of temperatures. This is important as water adsorption is an activated process. We divide our experiments into two different sets: high temperature and low temperature. The superstructure spots in the LEED pattern of

a clean $\text{Fe}_3\text{O}_4(001)$ surface as shown in Fig. 11.2a confirms the presence the $(\sqrt{2} \times \sqrt{2})R45^\circ$ surface reconstruction. The visibility of these superstructure spots in each experiment is analyzed to understand the effect of water adsorption on the surface.

Experiments:

On the high temperature side, we measured at room temperature (300 K), 318 K and at 347 K. We refer to these experiments as Exp_1 , Exp_2 and Exp_3 , respectively. In Exp_1 , we expose the sample for 25 minutes in three cycles, while observing the LEED pattern after each cycle. We notice that the superstructure spots were still clearly visible as shown in Fig. 11.2d which indicates the presence of surface reconstruction. In Exp_2 , we exposed the sample once again for 25 minutes in multiple steps. However, it should be noted that each experiment is performed on a well prepared clean surface and not continued from any of the previous experiments. The LEED pattern of Exp_2 shows faint super structure spot (Fig. 11.2 c) which means the adsorption process is not similar to that of Exp_1 . The faint superstructure spots also indicate partial suppression of the surface reconstruction in some of the domains. In Exp_3 , after 15 minutes of water vapor exposure, we notice the absence of superstructure spots in the LEED pattern. This well means surface reconstruction is lifted up. One can not rule the influence of thermal vibrations on the adsorption process with higher temperatures and in order to minimize them we performed some low temperature measurements as well.

In the low temperature experiment we adsorb water at 273 K and then subsequently cool the sample to 100 K, in order to make LEED measurements. We will refer this experiment as Exp_4 . We also tried adsorption at 100 K but as expected an insulating ice layer was observed on top of the surface. In Exp_4 [124,125], we expose the sample for 2 minutes and interestingly, the LEED pattern shows the absence of superstructure spots (Fig. 11.2 b). Comparatively, in this experiment the exposure time is way less than in the high temperature measurements. Further, after adsorption, we anneal the sample to two different temperatures (773 and 937 K), to access the stability of the termination. This experiment will be referred as Exp_5 [124,125].

11.3 Results and discussion

In this Section, we will analyse the results obtained from Section 11.2 and discuss the adsorption process involved.

Firstly, it should be noted that H_2O adsorption energy lies in between physisorption and chemisorption. Water adsorption is an activated process, meaning certain amount of energy is required for the adsorption process to begin. In Exp_1 , the superstructure spots are relatively brighter, which indi-

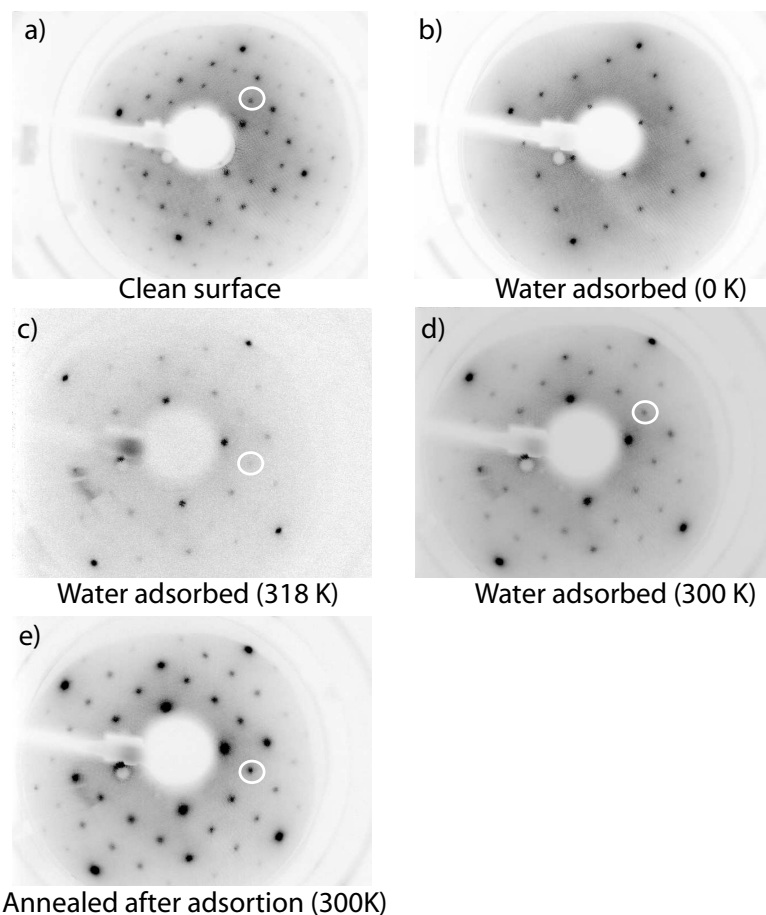


Figure 11.2: *LEED pattern obtained in different experiments. a) Clean surface b) water adsorbed at 0 K c) water adsorbed at 318 K d) water adsorbed at room temperature 300 K e) The same was annealed for 15 minutes after water was adsorbed at 300 K. The super structure spot is indicated within a small white circle.*

icates that water molecules are already desorbing from the surface due to its low adsorption energy (E_{ads}). However, we can not completely rule out adsorption of small amounts of water. Now with the increase in temperature to 318 K i.e. Exp₂, we notice faint superstructure spots. We predict that due to surface interactions and temperature effects, the water molecules either partially dissociate or form a hydrogen bonded network of species (OH, H, H₂O), which essentially has higher E_{ads} , thus adsorbing on the surface. In fact, this can be substantiated from our DFT calculation where a hydrogen bonded network of H₂O \cdots OH stabilizes the Fe₃O₄(001) surface. However, the distribution of adsorbate groups is not even on all over the surface therefore we see faint superstructure spots. Further, increasing the temperature to 347 K, as in Exp₂, we see complete suppression of the $(\sqrt{2} \times \sqrt{2})R45^\circ$ surface reconstruction. In this case due to high temperature, we expect either dissociated water molecules or a hydrogen bonded network of adsorbate species saturating the surface. A high coverage of adsorbates is also predicted based on the complete

disappearance of $(\sqrt{2} \times \sqrt{2})R45^\circ$ surface reconstruction. This can be explained using the kinetic energy of adsorbates, which at high temperature have more probability to diffusion and spread on the surface hence high adsorbate coverage is predictable. Annealing to high temperature after adsorption shows bright superstructure spots (Fig. 11.2 e).

In order to get a complete picture of the adsorption process, we compared the Exp₁ and Exp₂ with the low temperature adsorption Exp₄. Adsorption at 273 K shows a complete disappearance of superstructure spot with a small exposure time (2 minutes), contrary to the high temperature measurements. This immediately suggest a complete reaction of water molecules with the surface as well as lifting of the $(\sqrt{2} \times \sqrt{2})R45^\circ$ surface reconstruction. The low E_{ads} of water molecules supports the prediction. The low vibrational and thermal effect makes the H₂O molecule to stick on the surface with out prior desorption as observed at high temperatures. The low temperature measurements are also useful in predicting the adsorbate-substrate interaction separately due to negligible thermal effects. Annealing to high temperatures at 573 K and 973 K exhibit the superstructure spots. In all the above three experiments enhanced background intensity is observed. This increase of the background current during the measurement is attributed to uncorrelated defects induced by the electron beam, but no changes were observed in the LEED $I(V)$ curves during repeated measurements over periods of several hours. For a filament current of 50 -100 nA a rough estimate of the electron dose is 1-2 (electrons/unit cell) per 10 seconds. Seven LEED $I(V)$ curves of the (1×1) -surface were measured in the energy range 50 - 300 eV in all the experiments.

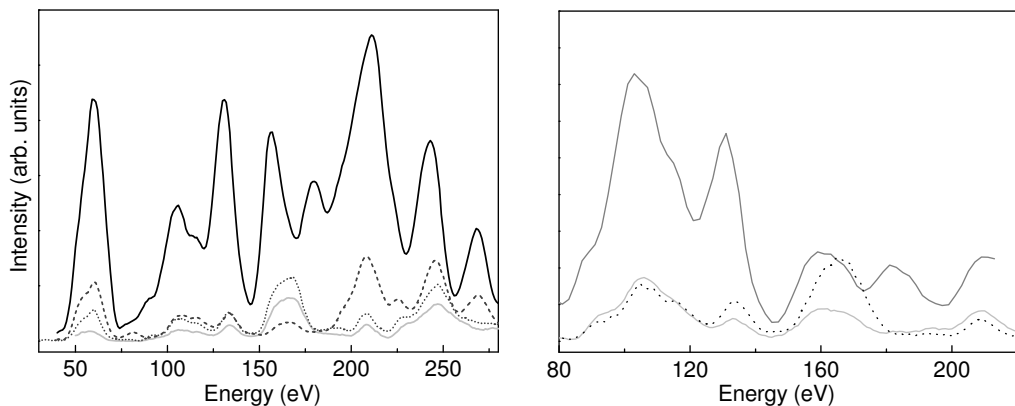


Figure 11.3: LEED $I(V)$ curves at different temperatures. Left panel: The LEED $I(V)$ curves of spot $(0,2)$ of clean surface (solid black line), water adsorption at 273 K (light grey line), annealing at 573 K after water adsorption (black dotted line) and at 773 K (black dashed line). Right Panel: The LEED $I(V)$ curves of spot $(0,2)$ at room temperature (dark grey), water adsorption at 273 K (light grey) and annealed curve (black dotted line) .

In Fig. 11.3, the LEED $I(V)$ curves after annealing upto 573 K and 773 K are not the same as that of the clean surface even though superstructure spots in the LEED pattern are visible. This indicates that some residual hydroxylation of the surface remains, in agreement with observations by Kendelewicz *et al.* [37]. The comparison of the LEED $I(V)$ curves from low temperature and room temperature measurements are shown in Fig. 11.3 right panel. We notice similarity in the peak positions of the curves but difference exists in the intensities, which can be attributed to prolonged exposure in the case of room temperature adsorption. This similarity in the curve brings an interesting aspect i.e. even at room and elevated temperatures, adsorption (Exp₁ and Exp₂) of water molecules did take place.

LEED calculations were performed for Exp₄ with the layer doubling method and a least squares optimisation [127] using constraints for bond lengths. The crystal potential was calculated from a superposition of atomic potentials using optimized muffin-tin radii [128] which led to reliable structural determination of the clean $\text{Fe}_3\text{O}_4(001)$ -surface [27]. 10 phase shifts were used. All atomic positions and occupation numbers within the adsorbate and top B-A-B substrate layers were optimized in a $(\sqrt{2} \times \sqrt{2})R45^\circ$ -unit cell, while thermal parameters were kept fixed. The best fit ($R_P = 0.27$) was obtained for a model where all

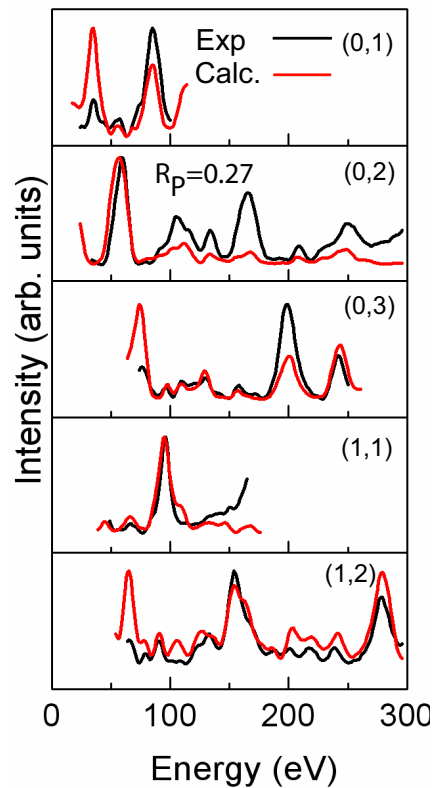


Figure 11.4: LEED $I(V)$ curves of the water adsorption at 273 K is shown with black solid line while the theoretically calculated $I(V)$ curves are shown with red solid line. The pendry factor R_P is 0.27.

Fe_BS sites have adsorbed oxygen on top as shown in Fig. 11.4. Both the surface Fe_B - and adsorbate sites are occupied by $\sim 80\%$ possibly due to defect creation during the preparation procedure. The adsorbed O shows strong lateral shifts by $\sim 0.4 \text{ \AA}$ off the Fe_B sites in agreement with the DFT results (0.23-0.28 \AA). The main feature are the two different bond lengths $\text{Fe}_B\text{-O}^w/\text{O}^{\text{OH}}$: 2.12 \AA and 1.93 \AA , confirming the simultaneous occurrence of hydroxyl groups and molecular adsorption.

Further analysis of the structural data obtained from LEED calculations confirms the contraction of bond length $d_{\text{Fe}_B\text{-O}}$ from 2.06 \AA to 1.97 \AA between surface and sub-surface layer as observed in DFT calculations.

11.4 Summary

LEED pattern obtained after water adsorption at various temperatures shows the suppression of the superstructure spots. The LEED experiments done at low and room temperature also show similar LEED $I(V)$ curves suggesting the validity of the results in both the temperature ranges. However at low temperatures, due to reduced vibrational contribution, the adsorption process is more favorable. Annealing after water adsorption to high temperature always show appearance of superstructure spots even though the LEED $I(V)$ curves are not exactly the same. The LEED calculations done [124] confirms the mixed mode of adsorption as suggested by the DFT results and also additionally shows the suppression of the $(\sqrt{2} \times \sqrt{2})R45^\circ$ surface reconstruction.

Conclusions and Outlook

The interaction of water with a mineral oxide surface is a fundamental process in nature. An in-depth understanding of these reactions is essential in the field of heterogeneous catalysis and geochemistry. This study is the first systematic investigation of the reaction between H_2O and the $\text{Fe}_3\text{O}_4(001)$ surface. An atomistic level understanding is achieved by theoretical description based on Density Functional Theory (DFT). These are complemented by low energy electron diffraction (LEED) measurements and analysis.

The calculations were performed using the full potential linear augmented plane wave method (FP-LAPW) within the generalized gradient approximation (GGA) for the exchange-correlation potential. The FP-LAPW method as implemented in Wien2k, along with the supercell approach, assures a high level of accuracy of the extracted energetics. To improve the description of electronic correlation of the highly localized $3d$ orbitals of the iron cation, an on-site Coulomb repulsion term U is included within the GGA+ U approximation. Thorough analysis indicates that GGA+ U gives a more reliable description of the surface and adsorption properties of $\text{Fe}_3\text{O}_4(001)$. In order to probe the energetics as a function of coverage, we have varied the concentration, geometric configuration of H_2O and OH groups on the surface. This is followed by full structural optimisation to reach the global minima or lowest energy configuration. The results are extended to account for finite pressures of the molecules in the gas phase (e.g. H_2O , O_2 , H_2) and at high temperatures (T) within the framework of *ab-initio* atomistic thermodynamics.

Isolated H_2O molecules are found to dissociate on the defect-free surface. Here the OH group adsorbs on top of a octahedrally coordinated surface iron $\text{Fe}_B(\text{S})$ and the H atom prefers adsorption on a surface oxygen $\text{O}(\text{S})$ site. The OH group tilts from its on top position which leads to the lifting up of the 1π orbital degeneracy [33]. In addition, the formation of hydrogen bonds between $\text{O}(\text{S})\text{-H}\cdots\text{O}(\text{S})$ stabilizes the system.

Increasing the coverage to two H_2O molecules on the surface per $(\sqrt{2} \times$

$\sqrt{2}R45^\circ$ unit cell brings the adsorbate-adsorbate interactions in to play. As a result, a crossover from dissociative to partial dissociation of H_2O molecules takes place. In this mixed mode of adsorption one of the H_2O molecules is dissociated while the second one remains intact. The OH and H_2O adsorb on top of the $\text{Fe}_B(\text{S})$ while the ejected proton (H atom) adsorbs on a nearby surface oxygen site. The hydrogen bond formed between $\text{O}^{\text{H}_2\text{O}} \dots \text{O}^{\text{OH}}$ stabilizes the system.

Increasing the coverage to four H_2O molecules on the surface per $(\sqrt{2} \times \sqrt{2})R45^\circ$ unit cell saturates all the available surface iron sites. In this coverage also the mixed mode of adsorption remains favorable. A fingerprint of the mixed termination are the two distinct bond lengths of $d_{\text{Fe}_B(\text{S})-\text{OH}}$ (1.98 Å) and $d_{\text{Fe}_B(\text{S})-\text{O}^{\text{H}_2\text{O}}}$ (2.09 Å). These two characteristic distances are identified in the quantitative LEED analysis as discussed in Chapter 11. Thus, the LEED results support the predicted mixed adsorption from the DFT calculations. Furthermore, the LEED pattern also shows the suppression of $(\sqrt{2} \times \sqrt{2})R45^\circ$ surface reconstruction. The variation in bond lengths is attributed to chemi- and physisorption in the case of OH and H_2O , respectively. Even after annealing up to 700 K, the hydroxyl groups remain on the surface [37]. This can be explained with the high adsorption energy E_{ads} (-0.8/-0.9 eV) of the mixed adsorption which corresponds to a desorption temperature of 900-1050 K. The stability of the mixed termination is displayed by the surface phase diagram compiled within the framework of *ab-initio* thermodynamics. Here the mixed termination dominates over a wide range of accessible partial pressures of oxygen (p_{O}) and water ($p_{\text{H}_2\text{O}}$) and especially at high pressures. This work is the first investigation to find a mixed adsorption of H_2O molecules on the $\text{Fe}_3\text{O}_4(001)$ surface, whereas on $\text{Fe}_3\text{O}_4(111)$ a dissociative adsorption was determined by experiments [37, 131]. In fact, the mixed adsorption is not observed for any other iron oxide surface like $\text{Fe}_2\text{O}_3(0001)$ [115] and $\text{FeO}(111)$ [130]. On the other hand, a mixed adsorption mode has been reported for other metal oxide surfaces like $\text{MgO}(100)$ [108] and $\text{TiO}_2(110)$ [109].

Additionally, the role of defects on the adsorption of H_2O molecules has been explored. The results show that a H_2O molecule strongly favors dissociation at an oxygen vacancy site. The resulting termination is stable at low to intermediate p_{O} and $p_{\text{H}_2\text{O}}$, whereas the oxygen vacancy termination is stable only at oxygen and water poor conditions as seen from the surface phase diagram. The strong E_{ads} of water in defect surfaces (-1.78 eV) is possibly the reason for the initial filling of all the vacancy sites during water adsorption as suggested by XPS-studies [37]. In order to interpret X-ray photoemission spectroscopic data, surface core level shifts (SCLS) have also been calculated. In fact, there is a good agreement between XPS [37] and the calculated SCLS results. Furthermore, our SCLS results reveal high contribution of the screening effects in the total shifts.

Another very interesting outcome of this work is the manipulation of charge states of the surface and subsurface iron ions with surface defects and adsorbates. All $\text{Fe}_B(\text{S})$ of the clean surface are in Fe^{3+} state, consistent with Ref. [26]. An oxygen vacancy on the surface can induce Fe^{2+} either in the surface or in the subsurface layer. Adsorbates like H_2O , OH and H can also induce unique charge and orbital ordered states in the surface and deeper layers. This provides a novel way to alter the surface reactivity and tailor catalytic properties of the $\text{Fe}_3\text{O}_4(001)$ surface.

Concerning the electronic properties, bulk Fe_3O_4 is predicted to be half metallic at room temperature. Charge and orbital order in the sub-surface layers induce an insulating character at the clean surface [26, 118]. We identified an insulator-to-half-metal transition upon adsorption of water on the $\text{Fe}_3\text{O}_4(001)$ surface.

The partially dissociated overlayer provides three functional groups i.e. OH , H_2O and H which can influence the adsorption of further species like toxic heavy metal ions (As(V) , Cr(IV)), hydrocarbons and organic molecules. The heavy metal adsorption can have important applications in waste water treatment. Presently magnetite nanoparticles are also studied for the same purpose [133]. Extension or comparison of the present knowledge of the Fe_3O_4 surface to Fe_3O_4 nanoparticles is an interesting aspect and could give more insight about the adsorption process. The availability of different charge and orbital ordered states on the surface and subsurface layers facilitates electron transfer processes in adsorption/desorption reactions. Further study of electron transfer processes is desirable. While this work has concentrated on the stability of different adsorbate geometries, further studies are necessary to determine activation energies and dissociation barriers. The observed insulating-to-half-metal transition can be explored for applications in spintronics. On the theoretical side, further improvement of the description of exchange-correlation through, e.g., dynamic mean field theory (DMFT), should be explored.

Reference energies

The total and cohesive energies of the reference systems: H_2O , O_2 , H_2 are calculated using DFT as listed in Table A.1. All the technical parameters used are similar to the one for slab calculations (Section 3.4). The calculations are done within GGA. From the Table A.1 we observe that the calculated bond lengths and angles of all the molecules considered are in good agreement with experiments. However, the atomization energies of most molecules are well described within GGA, a larger error is observed for O_2 [134]. As in our study we are interested in energy differences between various adsorbate configurations, where the uncertainty in description of these reference energies largely cancels out. Moreover, the energy of the oxygen molecule is used only for calculating the formation energy of oxygen vacancies on the defective $\text{Fe}_3\text{O}_4(001)$ surface.

Table A.1: *The cohesive energies of H_2O , O_2 and H_2 molecules are listed. The values from our work as well as from other references are also presented. a points to Ref [44], b points to Ref [67] and c to Ref [134]. The bond lengths are in Å and angles are in degrees.*

	Cohesive energy (eV)			
	Experimental ^{a,b}	Calculated-This work	Calculated ^c	Calculated ^b
H_2O	10.06 ^a ,9.60 ^b	11.26	10.15	9.81
O_2	5.2 ^a ,5.16 ^b	6.21	6.20	5.86
H_2	4.75 ^a ,4.52 ^b	5.65	4.50	4.50
d_{OH}	0.96 Å	0.97 Å		
d_{O_2}	1.20 Å	1.22 Å		
d_{H_2}	0.74 Å	0.75 Å		
$\Theta_{\text{H-O}^{\text{w}}-\text{H}}$	104.5	104.3		

Bibliography

- [1] R. M Cornell and U. Schwertmann, *The Iron Oxides*, Wiley-Vch (2003).
- [2] J. L. Kirschvink, *J. Exp. Biol.* **92**, 333 (1980).
- [3] P. Majewski and B. Thierry, *Crit. Rev. Solid State Mat. Sci.* **32**, 203 (2007).
- [4] V.E. Henrich, *Metal oxide surface and interfaces. In: The chemical physics of solid surfaces*, Vol. 9: Oxide surfaces, Eds. D. P. Woodruff (Elsevier, 2001).
- [5] E. W. J. Verwey, *Nature* **144**, 327 (1939.)
- [6] J.P. Wright, J.P. Attfield, and P.G. Radaelli, *Phys. Rev. Lett.* **87**, 266401 (2001).
- [7] J.-H. Park, L. H. Tjeng, J. W. Allen, P. Metcalf, and C. T. Chen, *Phys. Rev. B* **55**, 12813 (1997).
- [8] D. Schrupp, M. Sing, M. Tsunekawa, H. Fujiwara, S. Kasai, A. Sekiyama, S. Suga, T. Muro, V. A. M. Brabers, and R. Claessen, *Europhys. Lett.* **70**, 789 (2005).
- [9] I. Leonov, A. N. Yaresko, V. N. Antonov, M. A. Korotin, and V. I. Anisimov, *Phys. Rev. Lett.* **93**, 146404 (2004).
- [10] H.-T. Jeng, G.Y. Guo, and D. J. Huang, *Phys. Rev. Lett.* **93**, 156403 (2004).
- [11] J. Schlappa, C. Schler-Langeheine, C. F. Chang, H. Ott, A. Tanaka, Z. Hu, M. W. Haverkort, E. Schierle, E. Weschke, G. Kaindl, and L. H. Tjeng, *Phys. Rev. Lett.* **100**, 026406 (2008).

-
- [12] Z. Zhang and S. Satpathy, *Phys. Rev. B* **44**, 13319 (1991).
- [13] P. W. Tasker, *J. Phys. C* **12**, 4977 (1979).
- [14] C. Noguera, *J. Phys.: Condens. Matter* **12**, R367R410 (2000).
- [15] G. Tarrach, D. Brgler, T. Schaub, R. Wiesendanger, and H. Gntherodt, *Surf. Sci.* **285**, 1 (1993).
- [16] Y. J. Kim, Y. Gao, and S. A. Chambers, *Surf. Sci.* **371**, 358 (1997).
- [17] J. M. Gaines, P. J. H. Bloemen, J. T. Kohlhepp, C. W. T. Bulle-Lieuwma, R. M. Wolf, R. M. Reinders, R. M. Jungblut, P. A. A. van der Heijden, J. T. W. M. van Eemeren, J. aan de Stegge, and W. J. M. de Jonge, *Surf. Sci.* **373**, 85 (1997).
- [18] J. F. Anderson, M. Kuhn, U. Diebold, K. Shaw, P. Stoyanov, and D. Lind, *Phys. Rev. B* **56**, 9902 (1997).
- [19] F. C. Voogt, T. Fujii, P. J. M. Smulders, L. Niesen, M. A. James, and T. Hibma, *Phys. Rev. B* **60**, 11193 (1999).
- [20] S. A. Chambers, S. Thevuthasan, and S. A. Joyce, *Surf. Sci.* **450**, L273 (2000).
- [21] B. Stanka, W. Hebenstreit, U. Diebold, and S. A. Chambers, *Surf. Sci.* **448**, 49 (2000).
- [22] G. Mariotto, S. Murphy, and I. V. Shvets, *Phys. Rev. B* **66**, 245426 (2002).
- [23] I. V. Shvets, G. Mariotto, K. Jordan, N. Berdunov, R. Kantor, and S. Murphy, *Phys. Rev. B* **70**, 155406 (2004).
- [24] C. H. F. Peden, G. S. Herman, I. Z. Ismagilov, B. D. Kay, M. A. Henderson, Yong-Joo Kim and S. A. Chambers, *Catal. Today* **51**, 513 (1999).
- [25] R. Pentcheva, F. Wendler, H. L. Meyerheim, W. Moritz, N. Jedrecy, and M. Scheffler, *Phys. Rev. Lett.* **94**, 126101 (2005).
- [26] Z. Lodziana, *Phys. Rev. Lett.* **99**, 206402 (2007).
- [27] R. Pentcheva, W. Moritz, J. Rundgren, S. Frank, D. Schrupp, and M. Scheffler, *Surf. Sci.* **602**, 1299 (2008).
- [28] M. Fonin, R. Pentcheva, Yu. S. Dedkov, M. Sperlich, D. V. Vyalikh, M. Scheffler, U. Rüdiger, and G. Güntherodt, *Phys. Rev. B* **72**, 104436 (2005).
- [29] K. Ohe, Y. Tagai, S. Nakamura, T. Oshima, and Y. Baba, *J. Chem. Eng. Jpn.* **38**, 671 (2005).

- [30] H. Katsumata, S. Kaneco, K. Inomata, K. Itoh, K. Funasaka, K. Masuyama, T. Suzuki, and K. Ohta, *J. Environ. Manage.* **69**, 187 (2003).
- [31] C. Martos C. Martos, J. Dufour, and A. Ruiz, *Int. J. Hydrogen Energy* **34**, 4475 (2009).
- [32] P. A. Thiel and T. E. Madey, *Surf. Sci. Rep.* **7**, 211 (1987).
- [33] M. A. Henderson, *Surf. Sci. Rep.* **46**, 1 (2002).
- [34] A. Verdaguer, G. M. Sacha, H. Bluhm, and M. Salmeron, *Chem. Rev.* **106**, 1478 (2006)
- [35] N. S. Clarke and P. G. Hall, *Langmuir* **8**, 642 (1992).
- [36] N. S. Clarke and P. G. Hall, *Langmuir* **7**, 678 (1991).
- [37] T. Kendelewicz, P. Liu, C. S. Doyle, G. E. Brown Jr., E. J. Nelson, and S. A. Chambers, *Surf. Sci.* **453**, 32 (2000).
- [38] P. Liu, T. Kendelewicz, G.E. Brown Jr., G.A. Parks, and P. Pianetta, *Surf. Sci.* **416**, 326 (1998).
- [39] J.R. Rustad, A.R. Felmy, and E.J. Bylaska, *Geochim. Cosmochim. Acta* **67**, 1001 (2003).
- [40] T.K. Kundu, K. Hanumantha Rao, and S.C. Parker, *J. Colloid Interface Sci.* **295**, 364 (2006).
- [41] S. Cottenier, *Density Functional Theory and the family of (L)APW-methods: a step-by-step introduction* (Instituut voor Kern- en Stralingsfysica, K.U.Leuven, Belgium), 2002, ISBN 90-807215-1-4 (to be found at http://www.wien2k.at/reg_user/textbooks).
- [42] P. Blaha, K. Schwarz, and J. Luitz, *WIEN2k, An Augmented Plane Wave + Local Orbitals Program for Calculating Crystal Properties*, (Karlheinz Schwarz, Techn. Univ. Wien, Austria), 2001. ISBN 3-9501031-1-2
- [43] V. I. Anisimov, I. V. Solovyev, M. A. Korotin, M. T. Czyzyk, and G. A. Sawatzky, *Phys. Rev. B* **48**, 16929 (1993).
- [44] J.P. Perdew, K. Burke, and M. Ernzerhof, *Phys. Rev. Lett.* **77**, 3865 (1996).
- [45] C. Stampfl, M. V. Ganduglia-Pirovano, K. Reuter, and M. Scheffler, *Surf. Sci.* **500**, 368 (2002).
- [46] Xiao-Gang Wang, Anne Chaka, and M. Scheffler, *Phys. Rev. Lett.* **84**, 3650 (2000).

-
- [47] M. Born and J. R. Oppenheimer, *Ann. Physik* **84**, 457 (1927).
- [48] E. Schrödinger, *Ann. Phys.*, **79**, 361, 486; **80**, 437; **81**, 109 (1926).
- [49] D. R. Hartree, *Proc. Cambridge. Philos. Soc* **24**, 328 (1928).
- [50] V. A. Fock, *Z. Phys.* **15**, 126 (1930).
- [51] P. Hohenberg and W. Kohn, *Phys. Rev. B* **76**, 6062 (1964).
- [52] W. Kohn and L. J. Sham, *Phys. Rev.* **140**, A1133 (1965).
- [53] D. M. Ceperley and B. J. Alder, *Ground state of the electron gas by stochastic method*, *Phys. Rev. Lett.* **45**, 566 (1980).
- [54] A. Gro, *Theoretical surface science: A microscopic perspective*, Springer Verlag, Berlin, Heidelberg (2003).
- [55] A. D. Becke, *Phys. Rev. A* **38**, 3098 (1988).
- [56] C. Lee, W. Yang and R. Parr, *Phys. Rev. B* **37**, 785 (1988).
- [57] J.P. Perdew, J. A. Chevary, S. H. Vosko, K. A. Jackson, M. R. Pederson, D. J. Singh, and C. Fiolhais, *Phys. Rev. B* **46**, 6671 (1992).
- [58] J.P. Perdew and Y. Wang, *Phys. Rev. B* **45**, 132445 (1992).
- [59] B. Hammer, L. B. Hansen, and J. k. Norksov, *Phys. Rev. B* **59**, 7413 (1999).
- [60] J. C. Slater, *Phys. Rev.* **51**, 846 (1937).
- [61] O. K. Andersen, *Phys. Rev.* **12**, 3060 (1975).
- [62] C.M. Weinert and M. Scheffler, in *Defects in Semiconductors*, edited by H. J. von Bardeleben, *Mater. Sci. Forum Vols. 1012* (Trans Tech, Aedermannsdorf, Switzerland, 1986), p. 25.
- [63] M. Scheffler, in *Physics of Solid Surfaces* 1987, edited by J. Koukal (Elsevier, Amsterdam, 1988).
- [64] E. Kaxiras, Y. Bar-Yam, and J. D. Joannopoulos, *Phys. Rev. B* **35**, 9625 (1987).
- [65] G.-X. Qian, R. Martin, and D. J. Chadi, *Phys. Rev. B* **38**, 7649 (1988).
- [66] K. Reuter and M. Scheffler, *Phys. Rev. B* **65**, 035406 (2002).
- [67] Q. Sun, K. Reuter, and M. Scheffler, *Phys. Rev. B* **67**, 205424 (2003).
- [68] D.R. Stull and H. Prophet, *JANAF Thermochemical Tables*, 2nd ed.(U.S. National Bureau of Standards), Washington, DC, 1971).

- [69] D. Spanjaard, C. Guillot, M. C. Desjonqueres, G. Treglia, and J. Lecante, *Surf. Sci. Rep.* **5**, 1 (1985)
- [70] B. Johansson and N. Mårtensson, *Phys. Rev. B* **21**, 4427 (1980).
- [71] W. Olovsson, C. Göransson, T. Marten, and I. A. Abrikosov, *phys. stat. sol. (b)* **243**, 2447 (2006)
- [72] S. Lizzit, A. Baraldi, A. Groso, K. Reuter, M. V. Ganduglia-Pirovano, C. Stampfl, M. Scheffler, M. Stichler, C. Keller, W. Wurth, and D. Menzel, *Phys. Rev. B* **63**, 205419 (2001).
- [73] J. F. Janak, *Phys. Rev. B* **18**, 7165 (1978); J. P. Perdew and M. Levy, *ibid.* **56**, 16021 (1997).
- [74] J. P. LaFemina, *Crit. Rev. Surf. Chem.* **3**, 297 (1994).
- [75] M. Scheffler and C. Stampfl, *Theory of Adsorption on Metal Substrates. In: Handbook of Surface Science*, Vol. 2: Electronic Structure, Eds. K. Horn and M. Scheffler (Elsevier, Amsterdam, 2000).
- [76] G. Kresse, J. Hafner, *Phys. Rev. B* **47**, 558 (1993); G. Kresse, J. Hafner, *Phys. Rev. B* **48**, 13115 (1993); G. Kresse, J. Hafner, *Phys. Rev. B* **49**, 14251 (1994).
- [77] B. Santra, A. Michaelides, and M. Scheffler, *J. Chem. Phys.* **127**, 184104 (2007).
- [78] B. Santra, A. Michaelides, M. Fuchs, A. Tkatchenko, C. Filippi, and M. Scheffler, *J. Chem. Phys.* **129**, 194111 (2008).
- [79] P. Thissen, G. Grundmeier, S. Wippermann, W. G. Schmidt, *Phys. Rev. B* **80**, 245403 (2009).
- [80] A. Michaelides, V. A. Ranea, P. L. de Andres, and D. A. King, *Phys. Rev. Lett.* **90**, 216102 (2003).
- [81] K. Morgenstern and K.-H. Rieder, *J. Chem. Phys.* **116**, 5746 (2002).
- [82] K. Morgenstern and K.-H. Rieder, *Chem. Phys. Lett.* **358**, 250 (2002).
- [83] T. Mitsui, M. K. Rose, E. Formin, D. F. Ogletree, and M. Salmeron, *Science* **297**, 1850 (2002).
- [84] N. Yu, Wei-Bing Zhang, N. Wang, Yu-Fei Wang, and Bi-Yu Tang, *J. Phys. Chem. C* **112**, 452 (2008).
- [85] S. Yin, X. Ma, and D.E. Ellis, *Surf. Sci.* **601**, 2426 (2007).

- [86] M. E. Grillo, M. W. Finnis, and W. Ranke, *Phys. Rev. B* **77**, 075497 (2008).
- [87] V. A. Ranea, W. F. Schneider, and I. Carmichael, *Surf. Sci.* **602**, 268 (2008).
- [88] H.-J. Shin *et al.*, *Nature Mat.* DOI:10.1038/NMAT2740 (2010).
- [89] A. Nilsson, L. G. M. Pettersson and J. K. Norksov, *Chemical Bonding at Surface and Interfaces*, (Elsevier, Amsterdam, 2008).
- [90] T. Schiros, K. J. Andersson, L. G. M. Pettersson, A. Nilsson, and H. Ogasawara, *J. Electron Spectrosc.* **177**, 85 (2010).
- [91] T. Schiros, O. Takahashi, K. J. Andersson, H. Öström, L. G. M. Pettersson, A. Nilsson, and H. Ogasawara, *J. Chem. Phys.* **132**, 094701 (2010).
- [92] N. D. Lang, *Solid State Commun.* **9**, 1015 (1971).
- [93] J. E. Muscat and D. M. Newns, *Surf. Sci.* **74**, 355 (1978).
- [94] Harry B. Gray, *Chemical Bonds: An Introduction of Atomic and Molecular Structure*, (University Science Books 1994).
- [95] A. Michaelides, *Appl. Phys. A* **85**, 415 (2006).
- [96] H. Tamura, N. Katayama, and R. Furuichi, *Environ. Sci. technol.* **30**, 1198 (1996).
- [97] J. Ren and S. Meng, *Phys. Rev. B* **77**, 054110 (2008).
- [98] *The chemical physics of oxide surface: Oxide surfaces*, Vol. 9, Edited by D. P. Woodruff, (Elsevier, Amsterdam 2001).
- [99] *Transition metal oxides: Surface chemistry and catalysis*, Edited by H. H. Kung, (Elsevier, Amsterdam 1989).
- [100] O. Bikondoa, C. L. Pang, R. Ithnin, C. A. Muryn, H. Onishi, and G. Thornton, *Nat. Mat.* **5**, 189 (2006).
- [101] B. J. Morgan and G. W. Watson, *Surf. Sci.* **601**, 5034 (2007).
- [102] Benjamin J. Morgan, and Graeme W. Watson, *Surf. Sci.* **601**, 5034 (2007).
- [103] C. Di Valentin, G. Pacchioni, and A. Selloni, *Phys. Rev. Lett.* **97** (2006) 166803.
- [104] S. Yin and D. E. Ellis, *Surf. Sci.* **602**, 2047 (2008).

-
- [105] M. Veronica Ganduglia-Pirovano, A. Hofmann, and J. Sauer, Surf. Sci. Rep. **67**, 219 (2007).
- [106] F. Finocchi and J. Goniakowski, Phys. Rev. B **64**, 125456 (2001).
- [107] J. Matthiesen, J. . Hansen, S. Wendt, E. Lira, R. Schaub, E. Lgsgaard, F. Besenbacher, and B. Hammer, Phys. Rev. Lett. **102**, 226101 (2006).
- [108] Michael Odelius, Phys. Rev. Lett. **18**, 3919 (1999).
- [109] P. J. D. Lindan, N. M. Harrison, and M. J. Gillan, Phys. Rev. Lett. **80**, 762 (1998).
- [110] R. S. Cutting, C.A. Muryn, D.J. Vaughan, and G. Thornton, Surf. Sci. **602**, 1155 (2008).
- [111] Chin-Hung Lai, and Pi-Tai Chou, J. Comput. Chem. **28**, 1357 (2007).
- [112] K. Reuter and M. Scheffler, Phys. Rev. B **65**, 035406 (2001).
- [113] M. -L. Bocquet, A. M. Rappe, and H. -L. DA, Mol. Phys. **103**, 883 (2005).
- [114] K. Reuter and M. Scheffler, Phys. Rev. Lett. **90**, 046103 (2003).
- [115] A. Rohrbach, J. Hafner, and G. Kresse, Phys. Rev. B **70**, 125426 (2004).
- [116] Z. Lodziana, N.-Y. Topse, and J. K. Nrskov, Nat. Mat. **3**, 289 (2004).
- [117] H.P. Pinto and S.D. Elliot, J. Phys.: Condens. Matter **18**, 10427 (2006).
- [118] K. Jordan, A. Cazacu, G. Manai, S. F. Ceballos, S. Murphy, and I. V. Shvets, Phys. Rev. B **74**, 085416 (2006).
- [119] S. A. Chamber and S. A. Joyce, Surf. Sci. **420**, 111 (1999).
- [120] A. Nilsson, A. Stenborg, H. Tillborg, K. Gunnelin, and N. Martensson, Phys. Rev. B **47**, 590 (1993).
- [121] K. Reuter and M. Scheffler, Surf. Sci. **490**, 20 (2001).
- [122] S Yamamoto, H Bluhm, K Andersson, G Ketteler, H Ogasawara, M Salmeron, and A Nilsson, J. Phys.: Condens. Matter **20**, 184025 (2008).
- [123] H. Perron, J. Vandenborre, C. Domain, R. Drot, J. Roques, E. Simoni, J-J. Ehrhardt, and H. Catalette, Surf. Sci. **601**, 518 (2007).
- [124] N. Mulakaluri, R. Pentcheva, M. Wieland, W. Moritz, and M. Scheffler, Phys. Rev. Lett **103**, 176102 (2009).
- [125] M. Wieland, *Bachelor Thesis*, LMU, 2008.

-
- [126] B. Stanka, W. Hebenstreit, U. Diebold, and S. A. Chambers, *Surf. Sci.* **448**, 49 (2000).
- [127] H. Over, U. Ketterl, W. Moritz, and G. Ertl, *Phys. Rev. B* **46**, 15438 (1992).
- [128] J. Rundgren, *Phys. Rev. B* **68**, 125405 (2003).
- [129] M. C. Desjonqueres and D. Spanjaard, *Springer series in surface science Vol. 30 Concepts in surface physics*, Springer Verlag (1993).
- [130] Y. Joseph, W. Renke, and W. Weiss, *J. Phys. Chem. B* **104**, 3224 (2000).
- [131] Y. Joseph, C. Kuhrs, W. Renke, M. Ritter, and W. Weiss, *Chem. Phys. Lett.* **314**, 195 (1999).
- [132] A. Subagyo and K. Sueoka, *Jap. J. App. Phys.* **45**, 2255 (2006).
- [133] Hu J, Lo IM, and G. Chen, *Water Sci. Technol.* **50**, 139 (2004).
- [134] S. Kurth, J. P. Perdew, P. Blaha, *Int. J. Quantum Chem.* **75**, 889 (1999).

A

Manuscript

Partial dissociation of H₂O on Fe₃O₄(001): Adsorbate
induced charge and orbital order

Phys. Rev. Lett. **103**, 176102, (2009)

Partial Dissociation of Water on $\text{Fe}_3\text{O}_4(001)$: Adsorbate Induced Charge and Orbital Order

Narasimham Mulakaluri,^{1,2} Rossitza Pentcheva,^{1,*} Maria Wieland,¹ Wolfgang Moritz,¹ and Matthias Scheffler²

¹*Department of Earth and Environmental Sciences, University of Munich, Theresienstr. 41, 80333 Munich, Germany*

²*Fritz-Haber-Institut der Max-Planck-Gesellschaft, Faradayweg 4-6, D-14195 Berlin, Germany*

(Received 7 July 2009; published 23 October 2009)

The interaction of water with $\text{Fe}_3\text{O}_4(001)$ is studied by density functional theory calculations including an on-site Coulomb term. For isolated molecules, dissociative adsorption is strongly promoted at surface defect sites, while at higher coverages a hydrogen-bonded network forms with alternating molecular and dissociated species. This mixed adsorption mode and a suppression of the $(\sqrt{2} \times \sqrt{2})R45^\circ$ reconstruction are confirmed by a quantitative low energy electron diffraction analysis. Adsorbate induced electron transfer processes add a new dimension towards understanding the catalytic activity of magnetite(001).

DOI: [10.1103/PhysRevLett.103.176102](https://doi.org/10.1103/PhysRevLett.103.176102)

PACS numbers: 68.43.Bc, 68.35.Md, 68.47.Gh, 73.20.-r

Magnetite has attracted continued interest in the past decades due to its fascinating properties: The high temperature phase is predicted to be a half-metallic ferrimagnet [1] with a high Curie temperature (858 K). At ~ 120 K it undergoes the so called Verwey transition [2]. Both the type of transition (metal-to-insulator vs semiconductor-to-semiconductor [3,4]) and the type of charge (CO) and orbital ordering (OO) at the octahedral iron sites in the low temperature phase are subject to an ongoing debate [5–8].

In addition to its applications in magnetic recording and as a prospective material for spintronics, magnetite acts as a catalyst, e.g., in environmental redox reactions [9,10], or in the water gas phase shift reaction [11]. Typically these reactions take place in an aqueous environment prompting the need to understand how water interacts with the Fe_3O_4 surface. Water can bind to a surface in different modes (e.g., molecular or dissociative) leading to a variety of functional groups that can affect significantly the surface properties and availability of reaction sites and result in a complex surface chemistry [12,13].

The catalytic activity of magnetite is typically related to the presence of both ferrous (Fe^{2+}) and ferric (Fe^{3+}) iron in its inverse spinel structure. In the [001] direction two types of layers alternate: *A* layers with tetrahedral iron (Fe_A^{3+}) and *B* layers containing oxygen and octahedral iron ($\text{Fe}_B^{2+,3+}$). Both bulk truncations of $\text{Fe}_3\text{O}_4(001)$, either with an *A* or a *B* layer are polar of type three according to the classification of Tasker [14]. To explain the origin of the $(\sqrt{2} \times \sqrt{2})R45^\circ$ reconstruction, previous surface models proposed an ordering of surface defects (e.g., [15,16]). Recently, density functional theory (DFT) calculations [17,18] have shown that the symmetry lowering at $\text{Fe}_3\text{O}_4(001)$ is achieved rather by a distorted *B* layer, supported also by surface x-ray diffraction [17], low energy electron diffraction (LEED) [19] and scanning tunneling microscopy (STM) [20].

Despite its importance, only a few studies have addressed the interaction of water with $\text{Fe}_3\text{O}_4(001)$. While initial adsorption was related to surface defect sites, an

extensive hydroxylation was reported from x-ray photoemission experiments (XPS) beyond a threshold pressure of 10^{-3} – 10^{-4} mbar [21]. Both this study and temperature programmed desorption (TPD) measurements [22] indicate multiple adsorbate sites on the surface. Molecular dynamics simulations with empirical potentials [23,24] point towards a dissociative adsorption. However, such studies cannot provide reliable information on the energetics and underlying electronic phenomena.

Here we address these fundamental questions within a combined DFT and LEED approach. By varying the coverage and adsorbate configuration of water molecules we compile a surface phase diagram in the framework of *ab initio* atomistic thermodynamics. The results show that isolated molecules dissociate on the clean $\text{Fe}_3\text{O}_4(001)$ surface. This process is strongly favored at oxygen vacancies. With increasing coverage a crossover to a mixed adsorption (both molecular and dissociative) takes place that is confirmed in a quantitative LEED analysis. LEED shows also a strong suppression of the $(\sqrt{2} \times \sqrt{2})R45^\circ$ surface reconstruction. Furthermore, we find that the adsorbed species invoke electron transfer processes in the subsurface layers resulting in a unique CO/OO that may have important implications on the catalytic activity of the surface.

DFT calculations were performed using the full potential linear augmented plane wave method in the WIEN2K [25] implementation. The generalized gradient approximation (GGA-PBE) [26] of the exchange-correlation potential, used here, tends to overestimate hydrogen bonding by up to 20 meV/bond [27] which does not affect our conclusions. Because magnetite is a strongly correlated material we have used an on-site Coulomb correction to the local density approximation (LDA/GGA + *U* method) [28] with $U = 5$ eV and $J = 1$ eV [29], similar to values used for bulk Fe_3O_4 [6,7,30]. The surfaces were modeled in the supercell geometry with slabs containing seven *B* layers and six *A* layers separated by a vacuum region of 10–12 Å [31]. The positions of adsorbates and the atoms in the outer two *BA* layers were relaxed.

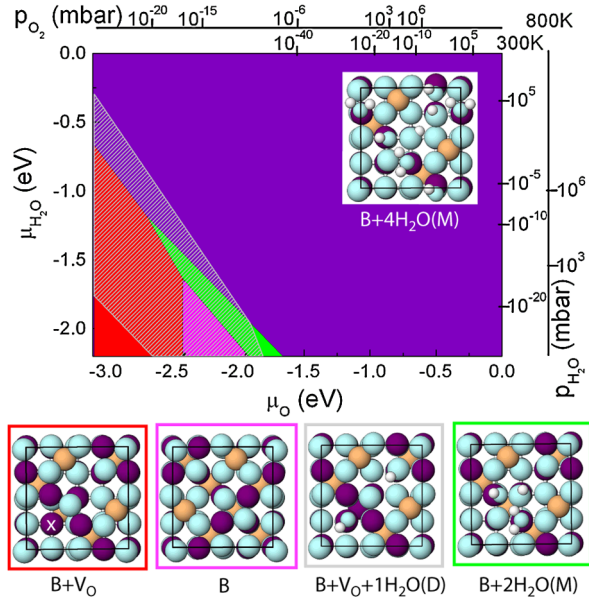


FIG. 1 (color online). Surface phase diagram of $\text{Fe}_3\text{O}_4(001)$ showing the most stable configurations as a function of μ_{O} , $\mu_{\text{H}_2\text{O}}$: $B + \text{V}_\text{O}$ [red (medium gray)], B layer [magenta (lighter medium gray)], dissociated molecule in an oxygen vacancy $B + \text{V}_\text{O} + 1\text{H}_2\text{O}(D)$ (gray hatched semitransparent area), mixed adsorption of two [green (light gray)] and four water molecules on a B layer [purple (dark gray)]. The ranges of μ_{O} and $\mu_{\text{H}_2\text{O}}$ correspond to the vapor phase of H_2O . μ_{O} and $\mu_{\text{H}_2\text{O}}$ have been converted into pressures for 300 and 800 K. Additionally, the top views of the most stable configurations are displayed with positions of O, Fe_B , Fe_A and H marked by cyan (light gray), purple (dark gray), orange (medium gray) and white circles, respectively. In $B + \text{V}_\text{O}$ a white cross marks the position of the vacancy.

We have compared the stability of more than 30 different configurations using *ab initio* atomistic thermodynamics [32]. The surface energy, $\gamma(T, p) = \frac{1}{2A}(G_{\text{Fe}_3\text{O}_4(001)}^{\text{slab}} - N_{\text{Fe}}\mu_{\text{Fe}} - N_{\text{O}}\mu_{\text{O}} - N_{\text{H}_2\text{O}}\mu_{\text{H}_2\text{O}})$ depends on the Gibbs free energy and the chemical potentials of the constituents. The Gibbs free energy can be expressed through the total energy from the DFT calculations [32]. Because there are two species in the gas phase, O_2 and H_2O , the surface phase diagram is three dimensional. Figure 1 displays a two-dimensional projection with the most stable configurations for given μ_{O} , $\mu_{\text{H}_2\text{O}}$. We first consider the termination of the clean surface as a function of oxygen pressure. As discussed previously, a modified B layer (denoted as B) showing lateral and vertical distortions in the surface layer with a *wavelike* pattern is favored over a broad range of oxygen pressures. However, at oxygen poor conditions a B layer with oxygen vacancies ($B + \text{V}_\text{O}$) is stabilized. This defective surface, previously proposed in a STM study [16], shows dramatic relaxations where the oxygen opposite the vacancy moves towards the Fe_B row by $\sim 0.8 \text{ \AA}$. Starting from these two terminations [33], we have adsorbed water molecules, varying their concentration and geometry. We find a strong tendency for isolated molecules

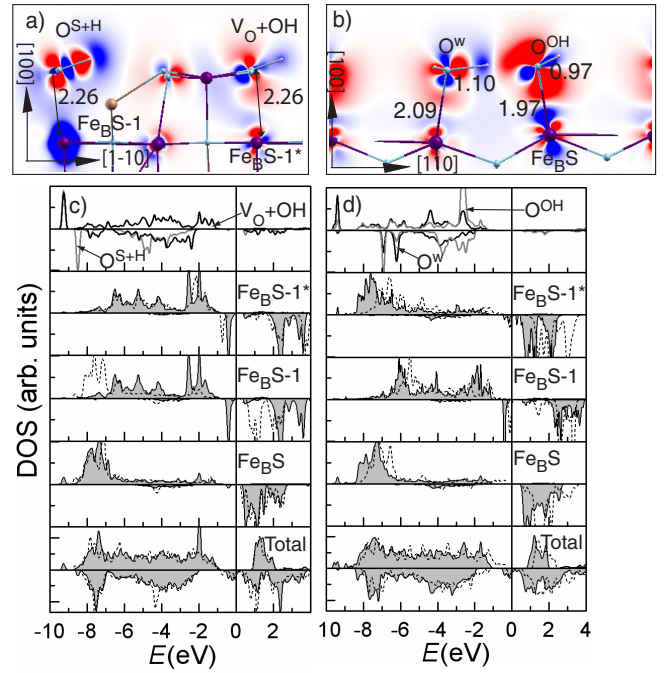


FIG. 2 (color online). Adsorbate induced electron density redistribution for (a) $B + \text{V}_\text{O} + 1\text{H}_2\text{O}(D)$ and (b) $B + 4\text{H}_2\text{O}(M)$. Red (medium gray)/blue (dark gray) corresponds to regions of charge accumulation/depletion. Relevant bond lengths are given in \AA . Total and projected density of states (DOS) before (dashed line) and after water adsorption (solid line, gray area) for (c) $B + \text{V}_\text{O} + 1\text{H}_2\text{O}(D)$ and (d) $B + 4\text{H}_2\text{O}(M)$. S ($S-1$) denote surface (subsurface) Fe_B sites.

to dissociate in surface oxygen vacancies ($\text{V}_\text{O} + \text{OH}$) whereby a proton diffuses to a surface oxygen (O^S) further away and forms a surface OH group ($\text{O}^S + \text{H}$). Thus, even at very low water vapor pressures, all surface defects are expected to be filled with OH groups, consistent with XPS results [21]. As shown in Figs. 2(a) and 2(c), the dissociation of water in the defect sites invokes significant changes in the electronic structure involving the 1π and 3σ molecular orbitals of the OH groups and a switching from Fe^{3+} to Fe^{2+} of $\text{Fe}_B S-1$ underneath $\text{O}^S + \text{H}$.

The adsorbate-adsorbate interaction that sets in, when a second molecule is adsorbed within the $(\sqrt{2} \times \sqrt{2})R45^\circ$ unit cell, leads to a mixed adsorption mode: One molecule dissociates protonating a surface oxygen, while the intact molecule forms a hydrogen bond with the OH group. The main part of the phase diagram is dominated by a mixed adsorption mode of four water molecules where all surface Fe_B sites ($\text{Fe}_B S$) are saturated ($B + 4\text{H}_2\text{O}(M)$). Full dissociation is $12 \text{ meV}/\text{\AA}^2$ less stable. Full hydroxylation of the surface is also not likely to occur as the formation of a surface OH group neighboring a subsurface Fe_A is extremely unfavorable.

The electron density redistribution with respect to the B layer in Fig. 2(b) indicates a weak charge accumulation between $\text{Fe}_B S$ and the oxygen of the water molecule (O^w). The strongest charge rearrangement takes place between

Fe_B and the OH group (O^{OH}) of the dissociated molecule, involving depletion of 3σ and accumulation in 1π molecular orbitals of OH along with depletion of the d_{z^2} orbital at Fe_BS . The main actuator of partial dissociation appears to be the formation of strong intermolecular hydrogen bonds. As a result both H_2O and OH tilt from the on-top position towards each other and $\text{O}^w\text{-H}$ elongates from 0.95 Å (gas phase) to 1.10 Å, resulting in an $\text{O}^w\text{-H}\cdots\text{O}^{\text{OH}}$ of 2.47 Å. The two distinct bond lengths between $\text{Fe}_B\text{-O}^w$ and $\text{Fe}_B\text{-O}^{\text{OH}}$ of 2.09 Å and 1.97 Å, respectively, are a fingerprint of the mixed adsorption. This feature is confirmed by the LEED analysis described below.

LEED measurements were performed on a synthetic magnetite sample. The clean surface, prepared by Ar^+ -ion sputtering and subsequent annealing at 900–1000 K at $p_{\text{O}_2} = 5 \times 10^{-7}$ mbar for 2–3 h, exhibited a $(\sqrt{2} \times \sqrt{2})R45^\circ$ -LEED pattern with sharp superstructure reflections and low background [Fig. 3(a)]. Water was adsorbed at 273 K for 2 min at a water vapor pressure of 2×10^{-6} mbar, resulting in a (1×1) -LEED pattern with an enhanced background [Fig. 3(b)]. The latter is attributed to uncorrelated defects possibly induced by the electron beam [34]. However, the LEED $I(V)$ curves remained unchanged during repeated measurements over periods of several hours. Annealing up to 770 K restores the superstructure spots but the shape of the LEED $I(V)$ curves cannot be recovered, indicating some residual hydroxylation of the surface, as observed by Kendelewicz *et al.* [21]. Seven LEED $I(V)$ curves of the (1×1) surface were measured in the energy range 50–300 eV at 100 K.

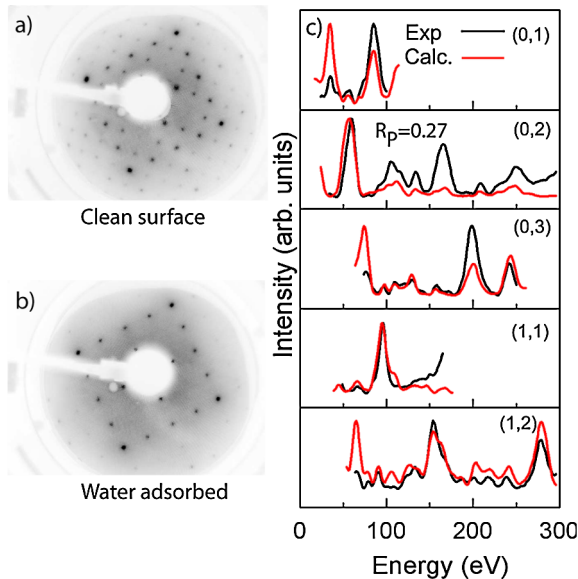


FIG. 3 (color online). LEED pattern (a) before and (b) after water adsorption. The superstructure spots in (a) indicative of the $(\sqrt{2} \times \sqrt{2})R45^\circ$ surface reconstruction are largely suppressed in (b). (c) Experimental (averaged over symmetrically equivalent beams - black) and calculated [red (medium gray)] LEED $I(V)$ curves of the water adsorbed surface.

LEED calculations were performed with the layer doubling method and a least squares optimization [35] using constraints for bond lengths. The crystal potential was calculated from a superposition of atomic potentials using optimized muffin-tin radii [36] which led to reliable structural determination of the clean $\text{Fe}_3\text{O}_4(001)$ surface [19]. Ten phase shifts were used. All positions and occupation numbers within the adsorbate and top B - A - B substrate layers were optimized in a $(\sqrt{2} \times \sqrt{2})R45^\circ$ -unit cell, while thermal parameters were kept fixed. The best fit ($R_p = 0.27$) was obtained for a model where all Fe_BS sites have adsorbed oxygen on top. Both the surface Fe_B and adsorbate sites are occupied by $\sim 80\%$ possibly due to defect creation during the preparation procedure. The adsorbed O shows strong lateral shifts by ~ 0.4 Å off the Fe_B sites in agreement with the DFT results (0.23–0.28 Å). The main features are the two different bond lengths 2.12 Å (Fe-O^w) and 1.93 Å (Fe-O^{OH}), confirming the simultaneous occurrence of hydroxyl groups and molecular adsorption. Further details on the structural analysis will be published elsewhere.

We turn next to the surface and adsorbate induced electronic effects on $\text{Fe}_3\text{O}_4(001)$. The electron density plot in Fig. 4 displays the minority t_{2g} occupancies at the Fe_B sites, thus allowing us to distinguish between sites with predominant Fe^{2+} or Fe^{3+} character [29]. The notation Fe^{2+} and Fe^{3+} is used here for simplicity, but the difference in total $3d$ occupation within the MT sphere is much smaller (0.2–0.4 e) consistent with x-ray diffraction [5] and LDA + U studies of the low temperature bulk phase [6,7]. The magnetic moments allow a clearer discrimination: $M_{\text{Fe}^{2+}} = 3.54\text{--}3.75\mu_B$, $M_{\text{Fe}^{3+}} = 3.90\text{--}4.10\mu_B$, respec-

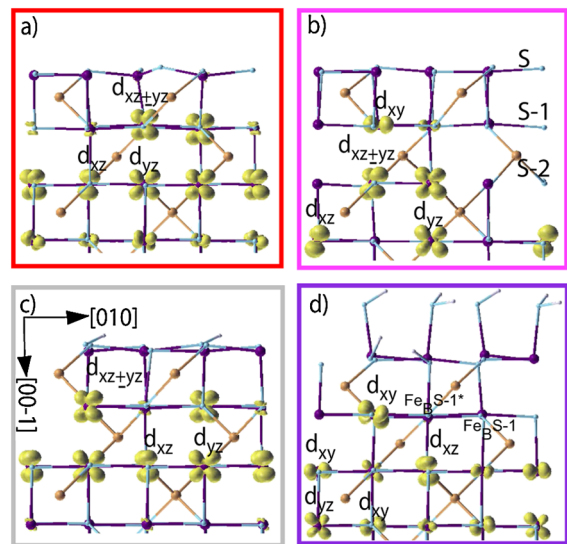


FIG. 4 (color online). Side view of the electron density integrated between -1.3 eV and E_F showing the occupation of the minority t_{2g} orbitals at the Fe_B sites. (a) $B + \text{V}_\text{O}$; (b) B layer; (c) $B + \text{V}_\text{O} + 1\text{H}_2\text{O}(\text{D})$; (d) $B + 4\text{H}_2\text{O}(\text{M})$. For the color code see Fig. 1.

tively. For most of the stable systems we find that the surface layer contains exclusively Fe^{3+} while a unique charge and orbitally ordered state emerges in the deeper layers depending on the type of termination [37]. In $B + V_O$ [Fig. 4(a)] the two subsurface Fe_B next to V_O are Fe^{2+} ($d_{xz} \pm d_{yz}$). Upon water adsorption the positions of Fe^{2+} switch in $B + V_O + 1\text{H}_2\text{O}(D)$: now the two Fe_B below the surface OH groups are Fe^{2+} , resulting in alternating Fe^{2+} , Fe^{3+} sites. In the mixed adsorption case ($B + 4\text{H}_2\text{O}(M)$) the charge ordering in the subsurface layer is not significantly altered compared to the B layer, where one out of four $\text{Fe}_B S-1$ is Fe^{2+} and a second is in an intermediate valence state. However, the slight tilting of the t_{2g} orbital at Fe_B^{2+} induces a completely different OO in $S-2$: from $d_{xz} \pm d_{yz}$ to alternating d_{xy} and d_{xz} -orbitals. Recent GGA + U calculations have shown that in bulk magnetite a variety of CO/OO states can be realized by symmetry lowering [30]. Here the presence of a surface and adsorbates imposes a unique CO/OO state for each termination reaching several layers below the surface. Moreover, most of them violate the Anderson criterion: Fe_4O_4 cubes in the surface and subsurface layer are predominantly electron poor ($3\text{Fe}^{3+} + 1\text{Fe}^{2+}$), while those in the $S-1$ and $S-2$ layers are electron rich ($1\text{Fe}^{3+} + 3\text{Fe}^{2+}$). Evidence for orbital ordering in thin magnetite films was reported recently from resonant soft x-ray diffraction [8].

The charge ordered state in the B layer leads to the opening of a band gap of 0.3 eV as shown in Fig. 2(d), consistent with previous calculations [18] and scanning tunneling spectroscopy measurements [38]. However, the adsorption of water on the surface and the formation of surface hydroxyl groups leads to half-metallic behavior.

We have shown that on $\text{Fe}_3\text{O}_4(001)$ water tends to dissociate in oxygen vacancies or partially dissociate on the nondefective surface in contrast to the full dissociation found on $\text{Fe}_3\text{O}_4(111)$ [21,39]. This adsorption mode is triggered by the presence of both Lewis acid and base sites on the surface and the intermolecular interaction as reported also on rutile(110) [40], anatase(001) [41], and $\text{MgO}(001)$ surfaces [42]. The hydrogen-bonded OH and H_2O can easily rearrange and thus provide adsorption sites for further species (e.g., heavy metal complexes). Our results indicate a pathway to manipulate, e.g., the catalytic properties of transition metal oxide surfaces by triggering electron transfer processes and inducing new charge and orbitally ordered states via adsorbates.

We acknowledge discussions with G.E. Brown and T. Kendelewicz and support by the German Science Foundation (PE883/1-2) and a grant for computational time at the Leibniz Rechenzentrum Garching.

*pentcheva@lrz.uni-muenchen.de

- [1] Z. Zhang and S. Satpathy, Phys. Rev. B **44**, 13 319 (1991).
[2] E.J.H. Verwey, Nature (London) **144**, 327 (1939).

- [3] J.H. Park *et al.*, Phys. Rev. B **55**, 12 813 (1997).
[4] D. Schrupp *et al.*, Europhys. Lett. **70**, 789 (2005).
[5] J.P. Wright, J.P. Attfield, and P.G. Radaelli, Phys. Rev. Lett. **87**, 266401 (2001).
[6] I. Leonov *et al.*, Phys. Rev. Lett. **93**, 146404 (2004).
[7] H.-T. Jeng, G.Y. Guo, and D.J. Huang, Phys. Rev. Lett. **93**, 156403 (2004).
[8] J. Schlappa *et al.*, Phys. Rev. Lett. **100**, 026406 (2008).
[9] K. Ohe *et al.*, J. Chem. Eng. Jpn. **38**, 671 (2005).
[10] H. Katsumata *et al.*, J. Environ. Manage. **69**, 187 (2003).
[11] C. Martos *et al.*, Int. J. Hydrogen Energy **34**, 4475 (2009).
[12] M.A. Henderson, Surf. Sci. Rep. **46**, 1 (2002).
[13] P.A. Thiel and T.E. Madey, Surf. Sci. Rep. **7**, 211 (1987).
[14] P.W. Tasker, J. Phys. C **12**, 4977 (1979).
[15] S.A. Chambers, S. Thevuthasan, and S.A. Joyce, Surf. Sci. **450**, L273 (2000).
[16] B. Stanka *et al.*, Surf. Sci. **448**, 49 (2000).
[17] R. Pentcheva *et al.*, Phys. Rev. Lett. **94**, 126101 (2005).
[18] Z. Lodziana, Phys. Rev. Lett. **99**, 206402 (2007).
[19] R. Pentcheva *et al.*, Surf. Sci. **602**, 1299 (2008).
[20] M. Fonin *et al.*, Phys. Rev. B **72**, 104436 (2005).
[21] T. Kendelewicz *et al.*, Surf. Sci. **453**, 32 (2000).
[22] C.H.F. Peden *et al.*, Catal. Today **51**, 513 (1999).
[23] J.R. Rustad, A.R. Felmy, and E.J. Bylaska, Geochim. Cosmochim. Acta **67**, 1001 (2003).
[24] T.K. Kundu *et al.*, J. Colloid Interface Sci. **295**, 364 (2006).
[25] P. Blaha *et al.*, WIEN2K, An Augmented Plane Wave + Local Orbitals Program for Calculating Crystal Properties (K. Schwarz, TU Wien, Austria, 2001).
[26] J.P. Perdew *et al.*, Phys. Rev. Lett. **77**, 3865 (1996).
[27] B. Santra *et al.*, J. Chem. Phys. **127**, 184104 (2007).
[28] V.I. Anisimov *et al.*, Phys. Rev. B **48**, 16 929 (1993).
[29] We have varied U between 0–8 eV: Charge disproportionation at the Fe_B sites is found beyond $U = 2$ eV.
[30] H.P. Pinto and S.D. Elliot, J. Phys. Condens. Matter **18**, 10427 (2006).
[31] We have used muffin-tin (MT) radii of $R_{\text{H}}^{\text{MT}} = 0.60$ Bohr, $R_{\text{Fe}}^{\text{MT}} = 1.90$, and $R_{\text{O}}^{\text{MT}} = 1.10$, an energy cutoff for the wave functions and potential of 25 Ry and 196 Ry, respectively, and 16 k_{\parallel} points for the integration in the Brillouin zone.
[32] K. Reuter and M. Scheffler, Phys. Rev. B **65**, 035406 (2001).
[33] A clean or water adsorbed half-occupied A layer was found to be less stable in the pressure ranges studied here.
[34] For a filament current of 50–100 nA a rough estimate of the electron dose is 1–2 (e/u.c.) per 10 s.
[35] H. Over *et al.*, Phys. Rev. B **46**, 15 438 (1992).
[36] J. Rundgren, Phys. Rev. B **68**, 125405 (2003).
[37] Only for $B + V_O$ a configuration with Fe^{2+} in the surface layer competes with the configuration in Fig. 4(a).
[38] K. Jordan *et al.*, Phys. Rev. B **74**, 085416 (2006).
[39] M.E. Grillo, M.W. Finnis, and W. Ranke, Phys. Rev. B **77**, 075407 (2008).
[40] P.J.D. Lindan, N.M. Harrison, and M.J. Gillan, Phys. Rev. Lett. **80**, 762 (1998).
[41] A. Vittadini *et al.*, Phys. Rev. Lett. **81**, 2954 (1998).
[42] L. Giordano, J. Goniakowski, and J. Suzanne, Phys. Rev. Lett. **81**, 1271 (1998); M. Odelius, Phys. Rev. Lett. **82**, 3919 (1999).

B

Manuscript

Coverage dependent adsorption mode of water on $\text{Fe}_3\text{O}_4(001)$:
Insights from First Principles calculations

J. Phy. Chem. C **114**, 11148 (2010)

Coverage-Dependent Adsorption Mode of Water on Fe₃O₄(001): Insights from First Principles Calculations

Narasimham Mulakaluri,^{†,‡} Rossitza Pentcheva,^{*,†} and Matthias Scheffler[‡]

Department of Earth and Environmental Sciences, University of Munich (LMU), Theresienstr. 41, 80333 Munich, Germany, and Fritz-Haber-Institut der Max-Planck-Gesellschaft (FHI), Faradayweg 4-6, D-14195 Berlin, Germany

Received: January 13, 2010; Revised Manuscript Received: May 4, 2010

Using density functional theory calculations together with an on-site Coulomb repulsion term (GGA+*U*), we investigate the adsorption of water on Fe₃O₄(001). Starting from a single water molecule per ($\sqrt{2} \times \sqrt{2}$)R45° unit cell, we vary the concentration and configuration of water and hydroxyl groups. Isolated water molecules on the clean surface tend to dissociate heterolytically with an OH group adsorbed on top of an octahedral iron and a proton donated to a surface oxygen. Furthermore, oxygen defects are found to promote strongly water dissociation. The released protons bind to distant surface oxygen to minimize the repulsive interaction between the surface OH groups. At higher coverages, the interplay between adsorbate–adsorbate and adsorbate–substrate interactions and the formation of hydrogen bonds between the surface species result in a crossover to a mixed adsorption mode where every second molecule is dissociated. The energetic trends are related to the underlying electronic mechanisms.

1. Introduction

Water plays a crucial role in many oxide-catalyzed reactions in the field of geochemistry, environmental sciences, and heterogeneous catalysis. Water adsorption can alter the catalytic reactivity, redox potential, and adsorption capacity of the surface¹ by influencing the electronic properties and availability of surface reaction sites. A fundamental understanding of how water molecules interact with metal oxide surfaces is essential^{1,2} in order to control the catalytic properties. Important questions include the mode of adsorption (e.g., molecular or dissociative), the interaction between adsorbates, and the formation of functional groups and hydrogen-bonded networks.

Magnetite (Fe₃O₄) has versatile technical applications in magnetic recording media, as a potential material for spintronics applications, and as a catalyst. Some examples for the catalytic activity are the binding and reduction of heavy metals in environmental processes^{3,4} or the high-temperature water gas phase shift reaction.⁵ Because these reactions take place in a humid environment or in aqueous solutions, it is important to understand how water interacts with the Fe₃O₄(001) surface.

Magnetite has an inverse spinel structure with a stacking of A layers and B layers in the [001] direction. The former contain tetrahedral iron (Fe_A) and the latter oxygen and octahedral iron (Fe_B). Although both bulk truncations of the crystal are polar of type three according to the classification of Tasker,⁶ density functional theory (DFT) calculations^{7,8} have recently shown that a distorted B layer is stabilized on the Fe₃O₄(001), which explains the experimentally observed ($\sqrt{2} \times \sqrt{2}$)R45° reconstruction. The presence of both cations and anions on an oxide surface is typically considered to promote water dissociation, because the cation sites act as strong Lewis acids, attracting the lone pairs of the water molecule, and the surface oxygen

acts a Brønsted base site, attracting the protons of the water molecule. However, NiO(001) is an example for a surface with both cations and anions exposed where only molecular adsorption has been reported so far.⁹

Despite intensive research on the clean Fe₃O₄(001) surface, there are only a few studies on its interaction with water. Kendelewicz et al.¹⁰ measured oxygen 1s core level shifts from X-ray photoemission spectroscopy (XPS). For low water vapor pressures, these were interpreted in terms of dissociative adsorption activated by surface defects. Beyond water vapor pressures of 10⁻³ to 10⁻⁴ mbar, an extensive hydroxylation was observed. The onset pressure is similar to values reported for the Fe₃O₄(111)¹⁰ and α -Fe₂O₃(0001)¹¹ surfaces. On the other hand, water-immersed surfaces showed smaller chemical shifts. A broad feature at 1.6 eV was attributed to hydroxyl groups at nonequivalent sites. Furthermore, no sign of formation of a surface oxyhydroxide was found in near-edge extended X-ray adsorption fine spectra (NEXAFS) of the Fe L edge. In thermal-programmed desorption (TPD) experiments¹² of epitaxially grown Fe₃O₄(001) films on a MgO(001) substrate, three desorption peaks were detected at 320, 280, and 225 K. These were associated with different chemisorbed states, but the exact adsorbate configurations and their relative stability cannot be directly accessed from experiment.

On the theoretical side, the water adsorption on Fe₃O₄(001) has been studied by molecular dynamics (MD)^{13,14} with empirical potentials. These studies point at a dissociative adsorption. However, in ref 14, the surface is modeled by a termination with a 0.5 ML (monolayer) of tetrahedral iron (0.5 A layer), which, according to DFT calculations,⁷ is energetically unfavorable. First-principles calculations have proven very useful to resolve the energetic stability and structural properties of different adsorbate geometries. In a combined density functional theory (DFT) and low-energy electron diffraction (LEED) study,¹⁵ we have recently presented a surface phase diagram obtained within the framework of ab initio atomistic thermodynamics.¹⁶ Although this investigation has focused exclusively

* To whom correspondence should be addressed. E-mail: Rossitza.Pentcheva@lrz.uni-muenchen.de.

[†] LMU.

[‡] FHI.

TABLE 1: Interatomic Distances^a in Å and Tilt Angles in Degrees between OH Group and the Surface, as well as the H-O-H Angle of the Adsorbed Water Molecule

	$d_{\text{Fe-O}^{\text{W}}}$	$d_{\text{Fe-O}^{\text{OH}}}$	$d_{\text{O-H}}$	$d_{\text{O}^{\text{OH}}\dots\text{H}^{\text{W}}}$	$d_{\text{O}^{\text{S}}\dots\text{H}^{\text{W}}}$	$\Theta_{\text{H-O}^{\text{W}}-\text{H}}$	$\Theta_{\text{Fe-O}^{\text{OH}}-\text{H}}$
1D _v -3		2.26	0.98				105.3
1F-1	2.22		0.97		2.54	106.5	
1D-1		1.84	0.97				120.3
2M	2.06	1.97	0.97/1.11	1.37	2.93	108.7	116.0
4M	2.09	1.98	0.97/1.10	1.40	2.90	109.5	114.5

^a $d_{\text{O}^{\text{OH}}\dots\text{H}^{\text{W}}}$ is the hydrogen bond between the adsorbed water and OH group in the mixed adsorption.

on the most stable configurations for given oxygen and water pressures, here, we present a detailed DFT study of the initial adsorption of water on Fe₃O₄(001). We have varied systematically the concentration of water molecules on the surface and identify different stable and metastable physi- and chemisorbed configurations (sections 3.1, 3.3, and 3.4). Furthermore, in section 3.2, we investigate the role of surface defects on the adsorption mode of water. To explain the energetic trends, we analyze the structural and electronic properties of the systems. Because Fe₃O₄ is a strongly correlated material, we have considered the influence of electronic correlations within the GGA+*U* approach and explore, in section 3.5, the origin of differences between the GGA and GGA+*U* results. Finally, in section 3.6, we discuss the overall trends of the adsorption energy as a function of coverage and compare the adsorption properties of Fe₃O₄(001) to other metal oxide surfaces. The results are summarized in section 4.

2. Computational Details

Density functional theory calculations were performed using the FP-LAPW (full potential linear augmented plane-wave) method in the WIEN2k¹⁷ implementation. The generalized gradient approximation (GGA)¹⁸ of the exchange-correlation potential is used. We have considered the influence of electronic correlations within the LDA/GGA+*U*¹⁹ method applying $U = 5$ eV and $J = 1$ eV, similar to values used for bulk Fe₃O₄.^{20,21} The muffin-tin (MT) radii are $R_{\text{Fe}}^{\text{MT}} = 1.90$ Bohr, $R_{\text{O}}^{\text{MT}} = 1.10$ Bohr, and $R_{\text{H}}^{\text{MT}} = 0.60$ Bohr. A mixed augmented plane-wave (APW+lo) and linear augmented plane-wave (LAPW) basis sets was used. Inside the MTs, the wave functions are expanded in spherical harmonics up to $l_{\text{max}}^{\text{wf}} = 10$. Nonspherical contributions to the electron density as well as potential are considered up to $l_{\text{max}}^{\text{pot}} = 6$. The energy cutoff for the plane-wave representation and potential are $E_{\text{max}}^{\text{wf}} = 25$ Ry and $E_{\text{max}}^{\text{pot}} = 196$ Ry, respectively. For the integration in the Brillouin zone, 16 k_{BZ} -points were used. Gas-phase O₂ and H₂O molecules are calculated in a box of $8 \times 8 \times 8$ Å using the same cutoff parameters as for the slab calculation.²³

The Fe₃O₄(001) surface is modeled in the supercell geometry with slabs containing seven B layers and six A layers. Laterally, a $(\sqrt{2} \times \sqrt{2})R45^\circ$ unit cell is used. Water is adsorbed on both sides of the inversion symmetric slab. The slab is separated in the z direction by a 12 Å vacuum from its periodic images to avoid spurious interaction. The lateral lattice constant of the supercell is set to the GGA bulk lattice constant of 8.41 Å, which is close to the experimental value of 8.39 Å. We have done full structural optimization of the various adsorbate configurations where the adsorbates along with the outer two AB layers are allowed to relax, whereas the central three AB layers are frozen to the bulk positions of the ions.

The systems contain typically 100–130 atoms, which results in a high numerical demand with matrix sizes for the diagonalization of up to $31\,000 \times 31\,000$. To reduce the computa-

tional cost and to search more efficiently for the most favorable adsorbate geometries, we have performed for some of the systems a structural optimization using the Vienna ab initio Simulation Package (VASP)²⁴ with a default cut-off energy for the plane-wave basis and a force relaxation up to 0.01 eV/Å. Using these geometries, several further relaxation steps were done subsequently with the WIEN2k code.

3. Results and Discussion

As mentioned above, DFT calculations predict that the clean Fe₃O₄(001) surface is terminated by a modified B layer.^{7,8} This result is supported by quantitative X-ray diffraction⁷ and LEED²⁵ analyses and scanning tunneling microscopy measurements.²⁶ Starting from this termination,²⁷ we adsorb water molecules in different configurations. As there are four cationic sites per $(\sqrt{2} \times \sqrt{2})R45^\circ$ unit cell, we have varied the coverage of water molecules from one to four (full saturation). Additionally, we have studied the adsorption of water molecules on a defective surface with one oxygen vacancy per $(\sqrt{2} \times \sqrt{2})R45^\circ$ unit cell, which is stabilized at low oxygen pressures.¹⁵

In the following, we describe the adsorbate geometries, structural details, and relative stabilities of different configurations beginning with a single water molecule and successively increasing the coverage. The adsorption energy E_{ads} of H₂O to the Fe₃O₄(001) surface in (eV/molecule) is described as

$$E_{\text{ads}} = \frac{1}{n}(E_{n\text{H}_2\text{O:Fe}_3\text{O}_4(001)} - E_{\text{Fe}_3\text{O}_4(001)} - nE_{\text{H}_2\text{O}}) \quad (1)$$

where n is the number of water molecules adsorbed. $E_{n\text{H}_2\text{O:Fe}_3\text{O}_4(001)}$ and $E_{\text{Fe}_3\text{O}_4(001)}$ are the total energies of the system with adsorbates and the clean surface, and $E_{\text{H}_2\text{O}}$ is the energy of a gas-phase molecule. Structural parameters and adsorption energies are listed in Tables 1 and 2. To analyze the underlying mechanisms, the bonding character is discussed based on the electron density redistribution ($\Delta\rho$), which is defined as

$$\Delta\rho = \rho_{n\text{H}_2\text{O:Fe}_3\text{O}_4(001)} - \rho_{\text{Fe}_3\text{O}_4(001)} - \rho_{n\text{H}_2\text{O}} \quad (2)$$

where $\rho_{n\text{H}_2\text{O:Fe}_3\text{O}_4(001)}$, $\rho_{\text{Fe}_3\text{O}_4(001)}$, and $\rho_{n\text{H}_2\text{O}}$ are the electron densities of the system with adsorbates, the clean Fe₃O₄(001) surface, and water molecules, respectively. In the reference systems, the positions of the atoms correspond to the ones in the adsorbate system.

3.1. Adsorption of an Isolated Water Molecule on the Nondefective Fe₃O₄(001) Surface. We start the discussion with a single H₂O molecule on Fe₃O₄(001) per $(\sqrt{2} \times \sqrt{2})R45^\circ$ unit cell. The adsorbate geometries are shown in Figure 1. These include a molecular adsorption in an upright (1U) and flat (1F) geometry on top of surface octahedral iron (Fe_BS) as well as

TABLE 2: Adsorption Energies (eV/molecule) of Water Molecules Adsorbed in Different Configurations on Fe₃O₄(001) Obtained within GGA and GGA+U

	molecular, upright		molecular, flat		dissociative		mixed	
	GGA	GGA+U	GGA	GGA+U	GGA	GGA+U	GGA	GGA+U
1 H ₂ O	-0.62	-0.02	-0.70	-0.39	-0.66	-0.76		
2 H ₂ O	-0.30	-0.16	-0.45	-0.47	-0.34	-0.58	-0.80	-0.94
4 H ₂ O	-0.01	-0.02	-0.41	-0.51	-0.19	-0.43	-0.61	-0.82

dissociative adsorption where an OH group forms on top of Fe_BS and a proton goes either to a neighboring (1D-1) or to a distant surface oxygen (1D-2/1D-3). We find that 1U, where the hydrogen atoms point away from the surface (Figure 2a), has a nearly vanishing binding energy to the surface. The most favorable molecular configuration is 1F (-0.39 eV), where the molecule is nearly parallel to the surface with hydrogen atoms oriented toward surface oxygens (O^S) (1F, side view Figure 2b). However, the dissociative adsorption with a proton adsorbed either at a neighboring O^S (1D-1) (-0.73 eV) or at a more distant surface oxygen (1D-3) (-0.76 eV) turns out to be the most favorable configuration. In fact, all dissociated configurations have a similar adsorption energy, which is ~0.3 eV lower than the value for molecular adsorption. Thus, the mode of adsorption for an isolated water molecule is dissociative, as reported also for Fe₃O₄(111).²⁸

To shed more light on the adsorbate mode, we have investigated the electron density redistribution upon adsorption for the different adsorbate configurations. The $\Delta\rho$ and density of states (DOS) plots for an upright and flat H₂O molecule are shown in Figure 2. Molecular water adsorbs with oxygen pointing toward a surface Fe_B, and the main charge rearrangement takes place along the O^W-Fe_B bond. Only in the case of flat adsorption, there is some contribution of the neighboring surface oxygen that is involved in the formation of a hydrogen bond. We find a stronger accumulation of electron density between the molecule and the surface for the flat geometry, consistent with the stronger binding energy. Charge accumulation in the d_{z2} orbital of Fe_BS on the side of the adsorbate indicates that it is the main orbital participating in the bonding. The pattern of electron rearrangement is consistent with the common understanding² that the adsorbate-surface interaction proceeds through a donation from the water lone pairs that act as a Lewis base into available Lewis acid surface orbitals of Fe_B.

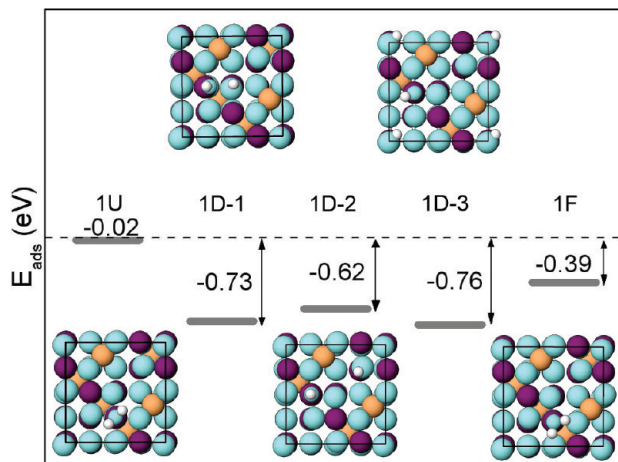


Figure 1. Top views of different adsorbate geometries of a single water molecule per $(\sqrt{2} \times \sqrt{2})R45^\circ$ unit cell. The diagram shows the corresponding adsorption energies (in eV per molecule) obtained within GGA+U. Positions of oxygen, Fe_B, Fe_A, and H are marked by cyan, purple, orange, and white circles. The oxygens of the adsorbate are marked by smaller circles.

The main effects expected due to the interaction with the substrate are a shift of position and change in width of the molecular levels of the adsorbate.^{29,30} Analysis of the partial DOS shows that, for the upright geometry, the 3a₁ and 1b₁ molecular levels (MO) of water remain very narrow. While 3a₁ shifts by 1.5 eV to lower energies, the 1b₁ state stays at the position of the gas-phase molecule. A narrow split-off d_{z2} orbital of the lower Hubbard Fe 3d band overlaps with the 3a₁ state. The weak interaction between occupied adsorbate orbitals and the substrate 3d band explains the vanishing E_{ads}.

For the flat/tilted adsorption, both the 3a₁ and the 1b₁ MO participate in the bonding to the surface. The stronger broadening/splitting observed here compared with the upright geometry indicates a stronger hybridization with the surface and a reduction of lifetime of the molecular states and is consistent with the higher E_{ads}. This electron redistribution serves to reduce Pauli's repulsion and to stabilize the system.³² The electron density accumulation between molecule and substrate goes hand in hand with a depletion at the hydrogen positions, indicating a

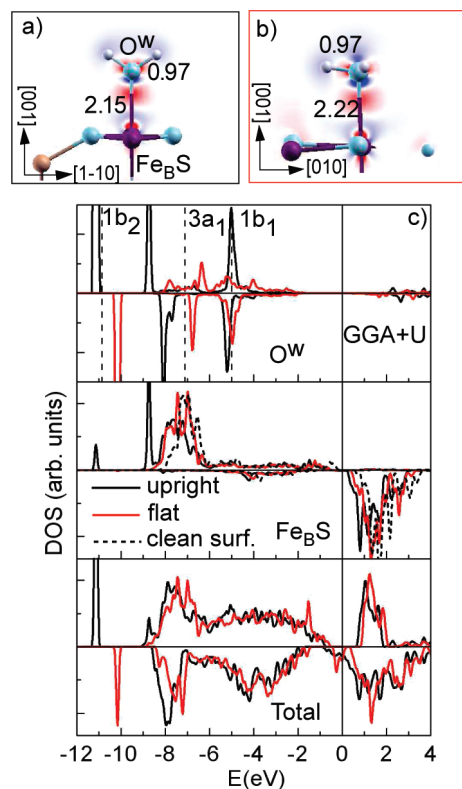


Figure 2. Electron density redistribution in a plane perpendicular to the surface obtained upon adsorption of a single water molecule in an (a) upright and (b) flat geometry. Electron density accumulation (depletion) is shown in red (blue). Positions of oxygen, Fe_B, and hydrogen are marked by cyan, purple, and white circles. (c) Total and projected density of states (DOS) at the oxygen and Fe_B sites for the two adsorbate geometries. The molecular orbitals of a gas-phase H₂O molecule are indicated by vertical dotted lines. These are obtained by aligning the 2a₁ core level of the gas-phase and adsorbed H₂O molecule. The Fe 3d band of the clean surface is also shown with a dashed line.

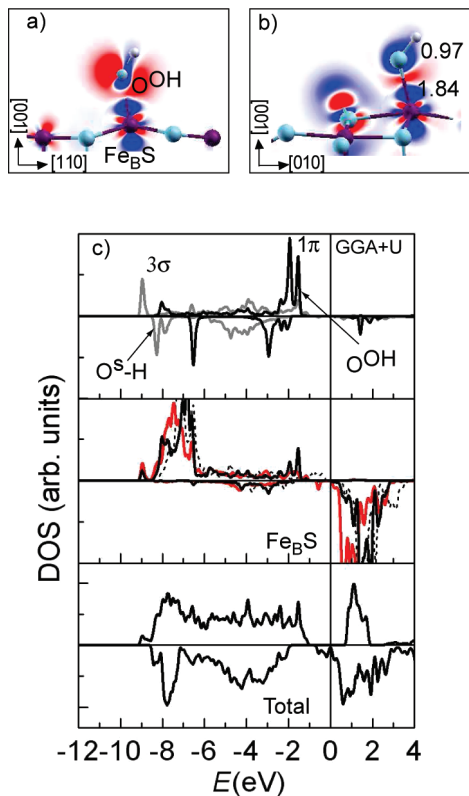


Figure 3. Electron density difference plots and DOS for the dissociative adsorption (1D-1) of an isolated H₂O molecule. $\Delta\rho$ is shown in a plane perpendicular to the surface along the (a) [110] and (b) [010] directions. The cut in (b) contains both the OH groups on top of a surface Fe_B and the protonated neighboring O^S. (c) Total and projected DOS (PDOS): (upper panel) PDOS of oxygen of the OH group on top of Fe_B (solid black line) as well as of the protonated neighboring surface oxygen (gray line); (central panel) PDOS of the 3d states of Fe_B with (solid black) and without (solid red line) an OH group on top. For comparison, the PDOS of Fe_B on the clean Fe₃O₄(001) surface is shown with a dashed line.

weakening of the OH bond. This is also expressed in a significant upward shift of the 1b₂ molecular level of water in the case of 1F. The polarization of the OH bond goes hand in hand with a slight elongation of the bond from 0.96 Å for the gas-phase molecule to 0.97/0.98 Å for the upright/flat adsorbed molecule. In 1F, the hydrogen of the water molecule forms a hydrogen bond to a surface oxygen with a bond length of 2.54 Å. As a result of the interaction with the surface, the angle $\Theta_{\text{H-O}^w\text{-H}}$ is enhanced (106.5°). We have also optimized the tilt angle of the molecule w.r.t. the surface $\Theta_{\text{Fe}_B\text{-O}^w\text{-H}}$ and obtain ~102°. The large distance of the molecule to the surface Fe_B (1U, 2.15 Å; 1F, 2.22 Å) suggests a relatively weak overall interaction with the substrate. We note, however, that the bond lengths are shorter than the ones reported for molecular adsorption on 4d metal surfaces (2.3–2.7 Å).³¹

The strongest electron density redistribution is found for the dissociative adsorption (Figure 3a,b). We notice a significant charge transfer from Fe_BS d_{z²} orbitals to the 1π MO of OH, which is now 1.5 eV below the Fermi level. Furthermore, there is a donation of charge from the 3σ lone pair of the OH ion to the t_{2g} states of the surface Lewis acid site. Conversely, charge is accumulated in the 3σ orbital of the OH group formed between a surface oxygen and the hydrogen of the dissociated H₂O (O^S-H). These features are further confirmed by the density of states in Figure 3c. The Fe_B 3d band is slightly broadened and shifted to lower energies w.r.t the one of the

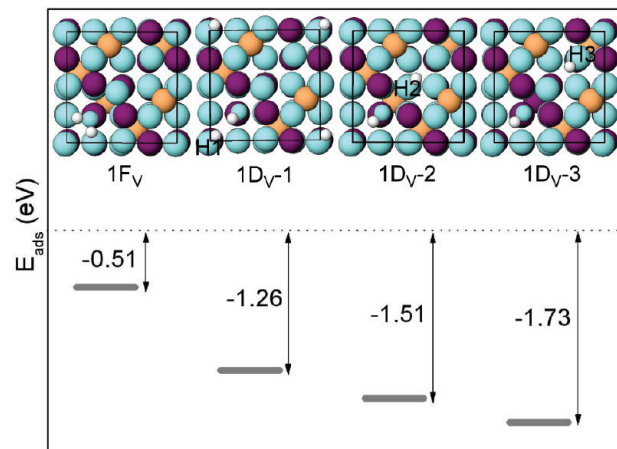


Figure 4. Schematic top views of different adsorbate geometries of a single water molecule adsorbed in an oxygen vacancy on the Fe₃O₄(001) surface. The solid gray lines show the adsorption energies (in eV per molecule) obtained within GGA+U.

clean surface (dashed line). The lower Hubbard band, extending mainly between -8.5 and -6 eV, hybridizes predominantly with the 3σ molecular orbital of OH and only weakly with 1π. The splitting (lifting up of degeneracy) of the 1π MO strongly depends on the tilt angle $\Theta_{\text{Fe}_B\text{-O}^{\text{OH-H}}}$, the optimum value of the latter being 120.3°. The strong electron redistribution for the dissociative adsorption invokes a pronounced outward relaxation of Fe_B and a shorter Fe_B-O^{OH} bond length of 1.84 Å compared with 2.15–2.22 Å for the molecular adsorption.

Besides the heterolytic adsorption where an OH group is adsorbed on a cation site and a surface oxygen is protonated, we have also investigated a homolytic dissociation (H₂O = H $\dot{\text{O}}$ + $\frac{1}{2}$ H₂), where $\frac{1}{2}$ H₂ is released and a neutral H $\dot{\text{O}}$ is adsorbed on a cation site. This type of dissociation mechanism is highly endothermic (0.51 eV per H₂O molecule within GGA).

3.2. Adsorption of an Isolated Water Molecule on a Defective Fe₃O₄(001) Surface. Defects play an important role on oxide surfaces and can significantly influence the interaction of water with the surface. The relevant type of defects, especially at low oxygen pressures, are oxygen vacancies.¹⁵ Here, we investigate the adsorption of water on a defective surface containing one oxygen vacancy (V_O) per ($\sqrt{2} \times \sqrt{2}$)R45° surface unit cell, which corresponds to a defect concentration of ~12.5%. The vacancies are separated by 8.41 Å from each other; thus, their interaction is negligible. The formation energy of one V_O per ($\sqrt{2} \times \sqrt{2}$)R45° unit cell is calculated as $E_f = E_{\text{Fe}_3\text{O}_4(001)\text{-V}_O} + \frac{1}{2}E_{\text{O}_2} - E_{\text{Fe}_3\text{O}_4(001)}$, where $E_{\text{Fe}_3\text{O}_4(001)\text{-V}_O}$ and $E_{\text{Fe}_3\text{O}_4(001)}$ are the total energies of the Fe₃O₄(001) surface with and without oxygen defects and E_{O_2} is the energy of a gas-phase oxygen molecule. We find that the formation energy is 1.08 eV higher for an oxygen vacancy with a neighboring Fe_A (3.51 eV) than without (2.47 eV). The latter type of oxygen vacancies is, therefore, expected to prevail and has been further considered for the adsorption of water.

Figure 4 shows the adsorption models studied on the defective surface along with the corresponding adsorption energies. Besides the molecular adsorption of H₂O in a vacancy, we have investigated a number of dissociative configurations where an OH group occupies the vacancy and a hydrogen is adsorbed at different surface oxygen sites (configurations 1D_V-1, 1D_V-2, and 1D_V-3). The bonds between oxygen of the flat/tilted molecule and the neighboring Fe_B ($d_{\text{O}^w\text{-Fe}_B} = 2.75$ Å, $d_{\text{O}^w\text{-Fe}_B(\text{S-1})} = 2.63$ Å) are much longer than the O^w-Fe_BS distance on the nondefective surface (2.22 Å). Still, the adsorption energy is

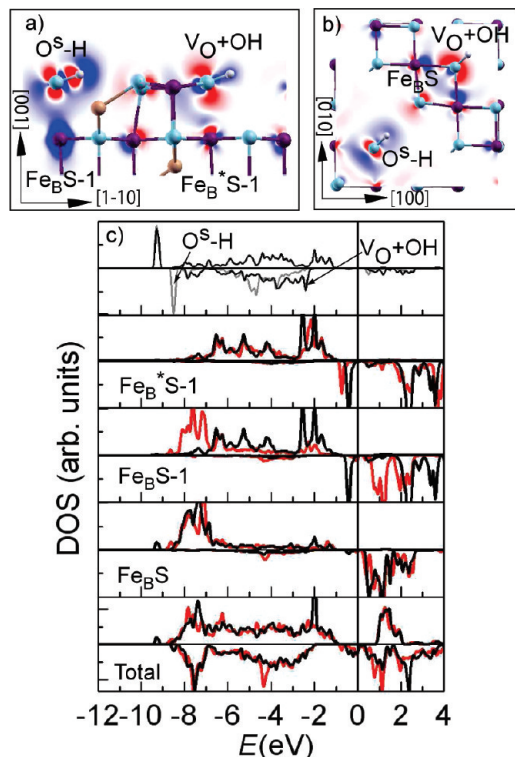


Figure 5. Electron density difference plots and DOS of a single water molecule dissociated in an oxygen vacancy on the $\text{Fe}_3\text{O}_4(001)$ surface (1D_V-3). (a, b) Cross sections of $\Delta\rho$ perpendicular and parallel to the surface, respectively. (c) (top panel) The projected DOS on the oxygen of the OH group in the vacancy and the protonated surface oxygen; (central panel) PDOS of the 3d states of a surface Fe_B next to the vacancy (Fe_BS), as well as the Fe_B ions beneath the vacancy ($\text{Fe}_B^*\text{S-1}$) and beneath $\text{O}^{\text{S-H}}$ ($\text{Fe}_B\text{S-1}$) are shown. Black and red lines indicate the DOS before and after adsorption of the molecule, showing also a change in valence state at $\text{Fe}_B\text{S-1}$.

significant (-0.51 eV). This is related to the higher coordination of the molecule in the V_O than on the nondefective surface. Also, the much broader majority spin band at Fe^{2+} in the subsurface layer (not shown here but similar to $\text{Fe}_B^*\text{S-1}$ in Figure 5c) allows a stronger hybridization with the molecular orbitals of H_2O .

On the defective surface, the dissociative adsorption is strongly favored (by 0.75 – 1.23 eV) over the molecular. While on the defect-free surface, several proton binding sites have similar energies, here, the proton prefers a distant O^{S} (configuration 1D_V-3). This indicates a repulsive interaction between the surface OH groups and results in a distribution of the OH groups at a distance of 5.95 Å. The $\text{O}^{\text{S-H}}$ and OH tilt strongly toward the opposite O^{S} in order to form a hydrogen bond, thereby aligning themselves nearly parallel to the surface.

The electron density difference plots for the dissociative adsorption in a defect (1D_V-3) are displayed in Figure 5a,b. The hydroxyl group in the vacancy shows an accumulation in the 1π orbital and depletion in the 3σ orbital, whereas the 3σ orbital is occupied upon formation of the $\text{O}^{\text{S-H}}$ group. We note that $\text{O}^{\text{S-H}}$ in 1D_V-3 (Figure 5c) has an even stronger splitting of the 1π orbital compared to that in 1D-1 (Figure 3c).

An interesting feature is that the OH group in the vacancy forms stronger bonds to the neighboring Fe_BS (stronger charge redistribution within the Fe_B 3d orbitals) than to the Fe_B underneath [$\text{Fe}_B(\text{S-1})$]. This is expressed in an elongated $\text{Fe}_B(\text{S-1})\text{-O}^{\text{OH}}$ bond length of 2.26 Å. The dissociative adsorption in a vacancy induces significant electronic/valence changes

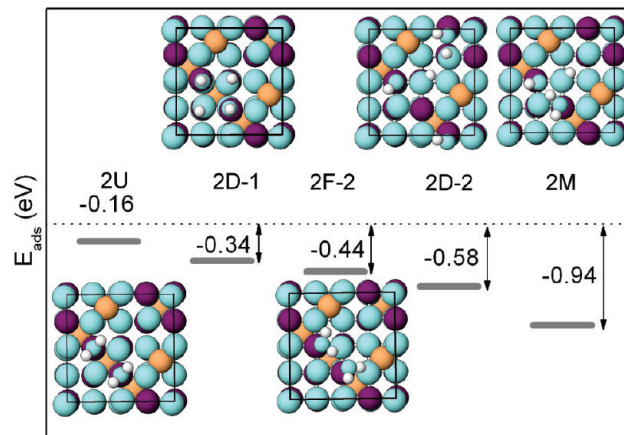


Figure 6. Top views of different adsorbate geometries of two water molecules per $(\sqrt{2} \times \sqrt{2})R45^\circ$ unit cell. The diagram above shows the adsorption energies (in eV per molecule) obtained within GGA+ U (solid gray lines). For the color coding, see Figure 1.

in the magnetite surface: At the defective surface, the two subsurface Fe_B around the vacancy are Fe^{2+} . Upon adsorption, both $\text{Fe}_B(\text{S-1})$ sites underneath the surface OH groups become Fe^{2+} . This effect of electron transfer may have important implications in understanding the catalytic activity of $\text{Fe}_3\text{O}_4(001)$. For a more detailed analysis of the charge ordering, the reader is referred to ref 15.

3.3. Adsorption of Two Water Molecules. With the inclusion of a second H_2O molecule, the adsorbate–adsorbate interaction sets in besides the adsorbate–substrate interaction. We have considered a variety of models of two adsorbed H_2O molecules and present in Figure 6 only the most stable ones. In the most favorable molecular configuration, 2F-2 (-0.44 eV), the two molecules are oriented parallel to the surface, one pointing with one of the OH bonds along the $[110]$ direction acting as a proton donor and the other one acting as a proton acceptor. Additionally, the latter forms a hydrogen bond with a surface oxygen.

Furthermore, two dissociated configurations are displayed in Figure 6. The one with OH groups adsorbed on adjacent Fe_BS sites (2D-1) is 0.24 eV less favorable than 2D-2 where Fe_BS sites with and without adsorbed OH groups alternate. The latter geometry is preferred because it decreases the repulsive interaction between the OH groups on top of Fe_BS and facilitates hydrogen bond formation between $\text{O}^{\text{S-H}}\cdots\text{O}^{\text{S-H}}$.

The most stable configuration turns out to be the one where partial dissociation of water takes place (2M) ($E_{\text{ads}} = -0.94$ eV). Here, one molecule dissociates and the hydrogen forms an OH group with a neighboring O^{S} . The intact molecule is oriented toward the OH group, forming a hydrogen bond. The proton at O^{S} shifts from the on-top position toward the opposite O^{S} , thereby also making a hydrogen bond.

Configuration 2F-2 can be considered as a precursor for the partial dissociation; therefore, we discuss in the following the structure of 2F-2 and 2M (shown in Figure 7a,b) in more detail. In 2F-2, one of the molecules, denoted $\text{H}_2\text{O-I}$, which is in a flat geometry, acts as a hydrogen-bond donor to the second H_2O and to the neighboring O^{S} , whereas $\text{H}_2\text{O-II}$ is strongly tilted with one hydrogen oriented toward a neighboring surface oxygen and the second pointing away from the surface. The different adsorbate orientations with respect to the surface results in a difference of 0.12 Å in the $\text{Fe}_B\text{-O}^{\text{W}}$ bond length. The water dimer distance is 1.86 Å, which is quite close to that observed for a gas-phase dimer (1.88 Å). The formation of a hydrogen

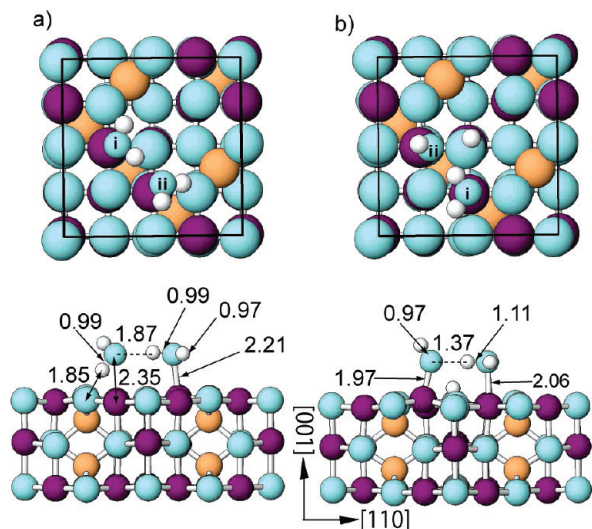


Figure 7. Top and side views of (a) two hydrogen-bonded water molecules (2F-2) and (b) a mixed molecular and dissociative adsorption (2M).

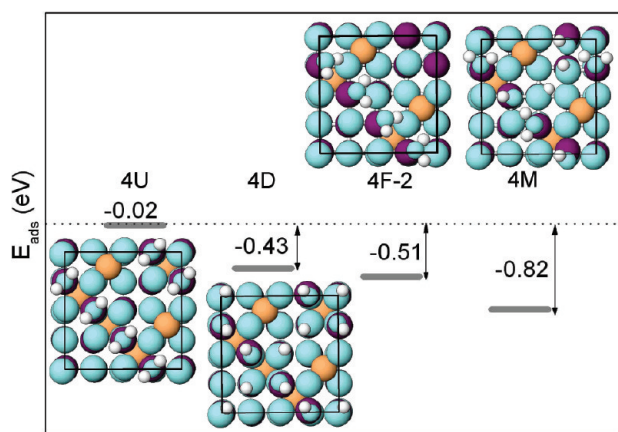


Figure 8. Top views of different adsorbate geometries of four water molecules adsorbed on Fe₃O₄(001). The diagram shows the adsorption energies (in eV per molecule) obtained within GGA+*U*. For the color coding, see Figure 1.

bond to O^S and between the two molecules leads to weakening of the OH bonds (bond length increased to 0.97–0.99 Å). This facilitates the dissociation of H₂O-II, resulting in configuration 2M.

Another possible scenario for the mixed adsorption is that, after an initial dissociation of isolated H₂O, further molecules arriving on the surface form hydrogen bonds with the present OH groups, resulting in the 2M configuration.

In the partially dissociated case (Figure 7b), the adsorbate–adsorbate (H₂O–OH) interaction results in a longer Fe_B–O^{OH} bond (1.97 Å) compared with the one of an isolated dissociated molecule (1.84 Å). On the other hand, the Fe_B–O^w bond length is 2.06 Å, significantly shorter than in the case of the isolated molecule (1F, 2.22 Å) and identical to the bulk Fe_B–O value. The stronger interaction between H₂O and OH in 2M is reflected in a 0.50 Å shorter O^{OH}···H^{H₂O} bond length (1.37 Å) in 2M compared with the O^w···H^{H₂O} distance in 2F-2 (1.87 Å).

3.4. Adsorption of Four Water Molecules. The adsorption of four H₂O molecules completely saturates the surface cationic sites. The different configurations are shown in Figure 8. The most favorable adsorption mode is again the mixed adsorption (4M) with an adsorption energy of –0.82 eV. Similar to the two-molecule case, this is followed in stability by a hydrogen-

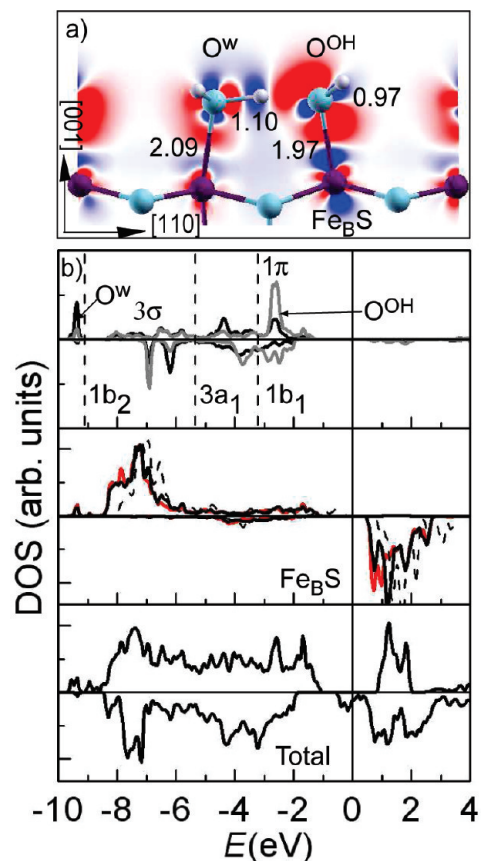


Figure 9. Four H₂O in a mixed adsorption mode (4M): (a) Difference density plot showing a cut perpendicular to the surface along the [110] direction and (b) (upper panel) PDOS of the O^w (black) and O^{OH} (gray). The molecular orbitals of a gas-phase H₂O molecule are indicated by vertical dotted lines. The central panel shows the 3d bands of Fe_B with an adsorbed H₂O molecule (black) and an OH group [red (gray)]. For comparison, the PDOS of Fe_B on the clean surface is displayed (black dashed line). The third panel shows the total DOS.

bonded chain (4F-2) (0.3 eV less favorable) of flat molecules where every second H₂O provides a hydrogen bond both to the neighbor (which itself is tilted) and to a surface oxygen. The dissociative adsorption is 0.4 eV less stable.

The electron density redistribution upon adsorption shown in Figure 9 bears some similarities to $\Delta\rho$ of the isolated flat (Figure 2) and dissociated (Figure 3) molecules. For example, the d₂₂ orbital of Fe_B hybridizes with the MO of water. For the dissociated molecule, an accumulation of the 1 π and depletion in the 3 σ orbital of the OH group is observed, similar to the case of an isolated dissociated molecule (1D-1). We find also a pronounced outward relaxation of Fe_B toward the OH group, leading to an Fe_B–O^{OH} distance of 1.97 Å. Still, this bond is 0.13 Å longer than the one in the isolated dissociated molecule. On the other hand, Fe_B–O^w (2.09 Å) is 0.13 Å shorter than in the isolated flat molecule (1F). These differences are associated with the intermolecular interaction. An important feature is the predicted two distinct bond lengths Fe_B–O^w (2.09 Å) and Fe_B–O^{OH} (1.97 Å). This feature is supported by a quantitative LEED analysis.¹⁵

The formation of a hydrogen bond between the H₂O molecule and the neighboring OH group leads to a significantly elongated O^w–H distance of 1.10 Å. Furthermore, the O^{OH} exhibits a strong lateral shift from the on-top position toward the neighboring H₂O, which itself is strongly tilted as compared with the isolated molecule (Figure 2). The DOS in Figure 9 shows a much stronger broadening and splitting of the 3a₁ and 1b₁

states of H₂O compared with the isolated molecule case, indicating a stronger hybridization not only with the surface but also to the neighboring adsorbates. Likewise, the degeneracy of the 1 π MO of OH is lifted and exhibits a bonding/antibonding splitting. It is interesting to note that the PDOS of O^{OH} and O^W are very similar, especially in the range between -6 and -8.5 eV, illustrating that hydrogen is shared between H₂O and the neighboring OH. The hybridization to the substrate is expressed by a shift of the occupied 3d band of Fe_BS to lower energies.

The difference between the total energy of a free-standing adsorbate layer and the total energies of isolated OH and H₂O gives an estimate of the contribution due to hydrogen bonding to E_{ads} . We note that systematic studies^{34,35} have shown that the PBE¹⁸ functional gives a good description of hydrogen bonding w.r.t. equilibrium geometries with error bars of ± 0.02 eV. Both for 2M and 4M, we obtained ~ 0.37 eV per molecule. This emphasizes the contribution of hydrogen bonding in stabilizing the partial dissociation on the Fe₃O₄(001) surface.

3.5. Comparison between GGA and GGA+*U* Results.

Already for the clean Fe₃O₄(001) surface, the level of description of electronic correlations leads to significant qualitative differences in the electronic properties, albeit the energetic trends between different terminations are similar. Within GGA, states in the majority band gap lead to a metallic behavior at the surface.⁷ In contrast, GGA+*U* correctly describes the opening of an insulating band gap,^{8,15} as observed experimentally in scanning tunneling spectroscopy measurements.³⁷ In the case of water adsorption, we find that, especially for higher coverages, the trends within GGA and GGA+*U* are consistent (energy differences are within 0.2 eV; see Table 2).

However, there are some discrepancies in the case of an isolated molecule on the nondefective surface, which we would like to discuss in more detail in the following. Within GGA, the molecular adsorption where the water molecule is parallel to the surface with the hydrogen atoms pointing toward neighboring surface oxygens (1F) is found to be energetically most favorable (-0.70 eV), followed by the dissociative adsorption (-0.66 eV) and an adsorption in an upright position (1U) with the hydrogen atom pointing away from the surface (-0.62 eV). We note that, within GGA+*U*, the latter had a vanishing binding energy.

In contrast to transition-metal surfaces,^{31,33} where the Fermi level crosses the d band, here, both the adsorbate orbitals and the substrate majority 3d band are occupied. Therefore, the interaction is not expressed by a change of occupation of levels but mainly by broadening of molecular orbitals. The main feature that is observed within GGA for the upright adsorption (cf. Figure 10) is a significant broadening of the 1b₁ state. As the latter is closest to the Fermi level, it has a dominating influence on the stability. The hybridization with the broad Fe_B 3d band, which extends from -7 eV to the Fermi level, reduces the Pauli repulsion³² and stabilizes the molecular adsorption in an upright geometry within GGA. In contrast, within GGA+*U*, the 1b₁ level remains very narrow due to the lack of overlap with the narrow Fe 3d band whose main peak lies between -8 and -6 eV, thus favoring hybridization mainly with the 3a₁ state of the adsorbate.

A further issue concerns the adsorption of water on a defective surface: Although both GGA and GGA+*U* predict dissociation, the corresponding energies are 0.98 and 1.73 eV, respectively. The difference of 0.75 eV is ascribed to the different formation energies of a vacancy on the Fe₃O₄(001) surface: 1.67 eV (GGA) and 2.47 eV (GGA+*U*). This is related to the different degrees of localization of the electronic charge around the V_O and the

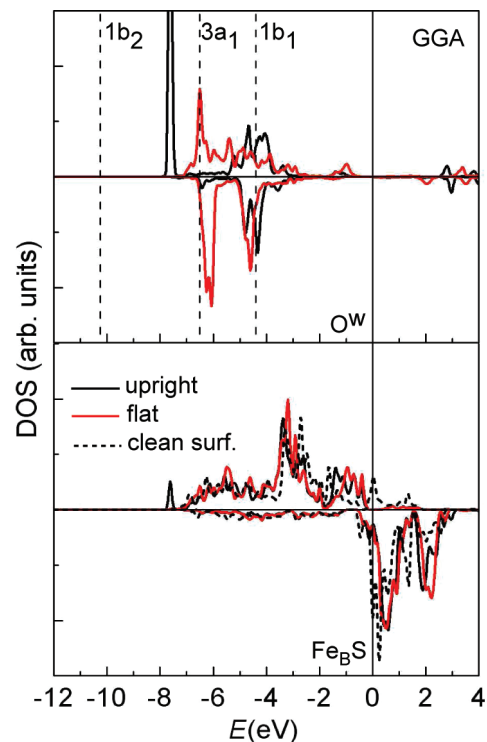


Figure 10. Total and projected DOS of 1U and 1F configurations obtained with GGA. The corresponding results within GGA+*U* are shown in Figure 2. The molecular orbitals of a gas-phase H₂O molecule are indicated by vertical dotted lines. For reference, the Fe 3d band of the clean surface is also shown with dashed lines.

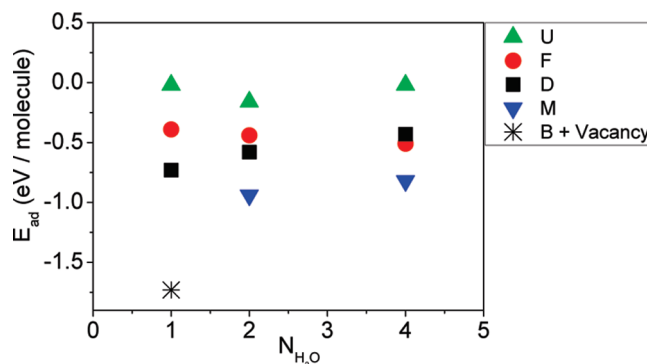


Figure 11. Adsorption energy (eV/molecule) obtained within GGA+*U* of different adsorbate systems as a function of the number of molecules per $(\sqrt{2} \times \sqrt{2})R45^\circ$ unit cell.

resulting structural relaxation. We note that an even larger variation of 1.5 eV between GGA and GGA+*U* was found for TiO₂(110).³⁶

The analysis of the bonding mechanism above suggests that GGA+*U* gives a more reliable description of the surface and adsorption properties of Fe₃O₄(001).

3.6. Adsorption Energy as a Function of Coverage. To obtain a full picture of the water interaction with Fe₃O₄(001), we discuss here the energetic trends as a function of water coverage. The adsorption energies for different coverages are plotted in Figure 11 and displayed also in Table 2. For an isolated molecule on a defect-free Fe₃O₄(001) surface, we find that the most stable adsorbate configuration is a dissociated molecule (-0.76 eV) where the released hydrogen forms an OH group with a surface oxygen. This is followed by a molecular adsorption in a flat geometry (-0.39 eV) with the hydrogens pointing toward neighboring surface oxygens. On a

defective surface, we find a strong tendency toward dissociation (GGA+*U*, -1.73 eV), where the OH group occupies the oxygen vacancy and the proton is bound at a more distant surface oxygen site. The high adsorption energy indicates that, as soon as water is present in the atmosphere, it will adsorb and dissociate at defect sites, thus eliminating surface defects. This is consistent with the observation of Kendelewicz et al.¹⁰ in the water pressure regime prior to extensive hydroxylation.

The adsorption of a second molecule results in an intermolecular bonding and a crossover to a partial dissociation (GGA+*U*, -0.94). In this case, the intact molecule forms a hydrogen bond to the neighboring OH group. A dissociative adsorption is 0.36 eV less favorable.

The mixed adsorption mode prevails also when a full saturation of the surface cation sites is reached after adsorption of four H₂O molecules. Here, the H₂O molecule is oriented with one hydrogen toward the next OH group and with the second pointing toward a surface oxygen, thus forming a 1D chain of alternating hydrogen-bonded flat water molecules and OH groups along the [110] direction. The two lone pairs of the water molecule play an important role by promoting the intermolecular hydrogen bonding, which can be comparable in strength to the water–substrate bonding.² A full dissociation is ~ 0.40 eV less favorable.

A common feature to all dissociated or partially dissociated configurations is that the proton attaches to a surface oxygen without a tetrahedral iron neighbor. Protonation of O^S with an Fe_A neighbor is highly unfavorable. With increasing coverage, we observe that the binding energy for the dissociative adsorption decreases slightly, indicating a repulsive adsorbate–adsorbate interaction. In the case of molecular flat/tilted adsorption, the adsorption energy slightly increases with coverage due to hydrogen bond formation.

Because of the stronger interaction with the surface, water is bound more strongly on oxide surfaces compared with transition and noble metal surfaces. In the latter case, adsorption energies are typically in the range between -0.1 and -0.5 eV.^{42,43} For oxide surfaces, the adsorption energy of a single water molecule ranges from -0.3 to -0.8 eV on Fe₂O₃(0001),⁴⁴ -0.57 eV on kaolinite,⁴⁵ -0.61 eV on NiO(001) (within GGA+*U*),⁴⁶ and -1.27 eV on zircon.⁴⁷ The adsorption energies for the mixed adsorption on Fe₃O₄(001) (-0.8 to -0.9 eV) found in this study are similar to values reported for TiO₂(110)³⁸ (-1.0 eV). On Fe₃O₄(111), an OH₃⁺–OH overlayer was reported with an adsorption energy of -0.85 eV within GGA+*U*.²⁸

4. Summary

In summary, we present a comprehensive DFT study of the initial adsorption of water on the Fe₃O₄(001) surface, analyzing also the underlying electronic mechanisms. We find that electronic correlations (described here within GGA+*U*) affect notably the width and position of the Fe³⁺ 3d band and thereby influence the hybridization with the MO of the adsorbate and the resulting binding strength. Our results establish that, for isolated molecules, a heterolytic dissociation is most favorable, especially at surface defect sites. Although the surface octahedral Fe ions remain in a 3+ valence state, the protonation of surface oxygen results in an electron transfer to a subsurface Fe that becomes Fe²⁺. On the nondefective surface, dissociation is followed in stability by a molecular adsorption where a flat/tilted molecule forms hydrogen bonds to surface oxygen. With increasing coverage, we obtain a crossover to a mixed adsorption where a hydrogen-bonded network forms between the alternating water molecules and OH groups. Such an adsorption mode has

been reported for several other oxide surfaces, for example, rutile TiO₂(110),³⁸ anatase TiO₂(001),³⁹ MgO(001),⁴⁰ and Al₂O₃(0001) surfaces.⁴¹ The partial dissociation leads to different surface species, that is, water molecules and OH groups on top of Fe_BS as well as OH groups involving a surface oxygen. These different functional groups and the induced electron transfer processes may have important implications for the adsorption of further molecules and the catalytic activity of Fe₃O₄(001).

Acknowledgment. We acknowledge discussions with W. Moritz, M.-L.-Bocquet, funding by the DFG/PE883/1-2 and a grant for computational time at the HLRBII supercomputer at the Leibniz Rechenzentrum.

References and Notes

- (1) Henderson, M. A. *Surf. Sci. Rep.* **2002**, *46*, 1.
- (2) Thiel, P. A.; Madey, T. E. *Surf. Sci. Rep.* **1987**, *7*, 211.
- (3) Ohe, K.; Tagai, Y.; Nakamura, S.; Oshima, T.; Baba, Y. *J. Chem. Eng. Jpn.* **2005**, *38*, 671.
- (4) Katsumata, H.; Kaneco, S.; Inomata, K.; Itoh, K.; Funasaka, K.; Masuyama, K.; Suzuki, T.; Ohta, K. *J. Environ. Manage.* **2003**, *69*, 187.
- (5) Martos, C.; Dufour, J.; Ruiz, A. *Int. J. Hydrogen Energy* **2009**, *34*, 4475.
- (6) (a) Tasker, P. W. *J. Phys. C: Solid State Phys.* **1979**, *12*, 4977. (b) Tasker, P. W. *Philos. Mag. A* **1979**, *12*, 4977.
- (7) Pentcheva, R.; Wendler, F.; Meyerheim, H. L.; Moritz, W.; Jedrecy, N.; Scheffler, M. *Phys. Rev. Lett.* **2005**, *94*, 126101.
- (8) Lodziana, Z. *Phys. Rev. Lett.* **2007**, *99*, 206402.
- (9) Reissner, R.; Schultze, M. *Surf. Sci.* **2001**, *482*, 285.
- (10) Kendelewicz, T.; Liu, P.; Doyle, C. S.; Brown, G. E., Jr.; Nelson, E. J.; Chambers, S. A. *Surf. Sci.* **2000**, *453*, 32.
- (11) Liu, P.; Kendelewicz, T.; Brown, G. E., Jr.; Nelson, E. J.; Chambers, S. A. *Surf. Sci.* **1998**, *417*, 53.
- (12) Peden, C. H. F.; Herman, G. S.; Ismagilov, I. Z.; Kay, B. D.; Henderson, M. A.; Kim, Y.-J.; Chambers, S. A. *Catal. Today* **1999**, *51*, 513.
- (13) Kundu, T. K.; Hanumantha Rao, K.; Parker, S. C. *J. Colloid Interface Sci.* **2006**, *295*, 364.
- (14) Rustad, J. R. *Geochim. Cosmochim. Acta* **2002**, *67*, 1001.
- (15) Mulakaluri, N.; Pentcheva, R.; Wieland, M.; Moritz, W.; Scheffler, M. *Phys. Rev. Lett.* **2009**, *103*, 176102.
- (16) Reuter, K.; Scheffler, M. *Phys. Rev. B* **2001**, *65*, 035406.
- (17) Blaha, P.; Schwarz, K.; Madsen, G. K. H.; Kvasnicka, D.; Luitz, J. *WIEN2k: An Augmented Plane Wave + Local Orbitals Program for Calculating Crystal Properties*; Karlheinz Schwarz, Technische Universität Wien: Wien, Austria, 2001; ISBN 3-9501031-1-2.
- (18) Perdew, J. P.; Burke, K.; Ernzerhof, M. *Phys. Rev. Lett.* **1996**, *77*, 3865.
- (19) Anisimov, V. I.; Solovyev, I. V.; Korotin, M. A.; Czyzyk, M. T.; Sawatzky, G. A. *Phys. Rev. B* **1993**, *48*, 16929.
- (20) Leonov, I.; Yaresko, A. N.; Antonov, V. N.; Korotin, M. A.; Anisimov, V. I. *Phys. Rev. Lett.* **2004**, *93*, 146404.
- (21) Jeng, H.-T.; Guo, G. Y.; Huang, D. J. *Phys. Rev. Lett.* **2004**, *93*, 156403.
- (22) Kurth, S.; Perdew, J. P.; Blaha, P. *Int. J. Quantum Chem.* **1999**, *75*, 889.
- (23) While the atomization energies of most molecules are well described within GGA, a larger error is observed for O₂.²² However, here, we are interested in energy differences between various adsorbate configurations, where the uncertainty in the description of these reference energies cancels out. Moreover, the energy of the oxygen molecule is used only for calculating the formation energy of oxygen vacancies on the defective Fe₃O₄(001) surface.
- (24) (a) Kresse, G.; Furthmüller, J. *Phys. Rev. B* **1996**, *54*, 11169. (b) Kresse, G.; Furthmüller, J. *Comput. Mater. Sci.* **1996**, *6*, 15. (c) Kresse, G.; Joubert, D. *Phys. Rev. B* **1999**, *59*, 1758.
- (25) Pentcheva, R.; Moritz, W.; Rundgren, J.; Frank, S.; Schrupp, D.; Scheffler, M. *Surf. Sci.* **2008**, *602*, 1299.
- (26) Foinin, M.; Pentcheva, R.; Dedkov, Yu., S.; Sperrlich, M.; Vyalikh, D. V.; Scheffler, M.; Rüdiger, U.; Güntherodt, G. *Phys. Rev. B* **2005**, *72*, 104436.
- (27) We have also performed calculations for a hydroxylated 0.5 Å-layer termination; however, it remained energetically unfavorable compared with systems containing a B layer.
- (28) Grillo, M. E.; Finnis, M. W.; Ranke, W. *Phys. Rev. B* **2008**, *77*, 075407.
- (29) Lang, N. D. *Solid State Commun.* **1971**, *9*, 1015.
- (30) Muscat, J. E.; News, D. M. *Surf. Sci.* **1978**, *74*, 355.

- (31) Carrasco, J.; Michaelides, A.; Scheffler, M. *J. Chem. Phys.* **2009**, *130*, 184707.
- (32) Nillson, A.; Pettersson, L. J. M.; Norksov, J. K. *Chemical Bonding at Surface and Interfaces*; Elsevier: Amsterdam, 2008.
- (33) Scheffler, M.; Stampfl, C. Theory of Adsorption on Metal Substrates. In *Handbook of Surface Science*, Vol. 2, Electronic Structure; Horn, K., Scheffler, M., Eds.; Elsevier: Amsterdam, 2000.
- (34) Santra, B.; Michaelides, A.; Scheffler, M. *J. Chem. Phys.* **2007**, *127*, 184104.
- (35) Santra, B.; Michaelides, A.; Fuchs, M.; Tkatchenko, A.; Filippi, C.; Scheffler, M. *J. Chem. Phys.* **2008**, *129*, 194111.
- (36) Morgan, B. J.; Watson, G. W. *Surf. Sci.* **2007**, *601*, 5034.
- (37) Jordan, K.; Cazacu, A.; Manai, G.; Ceballos, S. F.; Murphy, S.; Shvets, I. V. *Phys. Rev. B* **2006**, *74*, 085416.
- (38) Lindan, P. J. D.; Harrison, N. M.; Gillan, M. J. *Phys. Rev. Lett.* **1998**, *80*, 762.
- (39) Vittadini, A.; Selloni, A.; Rotzinger, F. P.; Gratzel, M. *Phys. Rev. Lett.* **1998**, *81*, 2954.
- (40) Odelius, M. *Phys. Rev. Lett.* **1999**, *82*, 3919.
- (41) Thissen, P.; Grundmeier, G.; Wippermann, S.; Schmidt, W. G. *Phys. Rev. B* **2009**, *80*, 245403.
- (42) Michaelides, A.; Ranea, V. A.; de Andres, P. L.; King, D. A. *Phys. Rev. Lett.* **2003**, *90*, 216102.
- (43) Ren, J.; Meng, S. *Phys. Rev. B* **2008**, *77*, 054110.
- (44) Yin, S.; Ma, X.; Ellis, D. E. *Surf. Sci.* **2007**, *601*, 2426.
- (45) Hu, X. L.; Michaelides, A. *Surf. Sci.* **2008**, *602*, 960.
- (46) Yu, N.; Zhang, W.-B.; Wang, N.; Wang, Y.-F.; Tang, B.-Y. *J. Phys. Chem. C* **2008**, *112*, 452.
- (47) Balan, E.; Mauri, F.; Muller, F.; Calasi, G. *Am. Mineral.* **2001**, *86*, 910.

JP100344N



Manuscript

Compensation mechanisms and functionality of transition metal oxide surfaces and Interfaces: A density functional theory study. In: High Performance Computing in Science and Engineering. (Eds.) S. Wagner, M. Steinmetz, A. Bode, and M. Brehm. Springer Berlin Heidelberg 2009, 709-717.
DOI: 10.1007/978-3-540-69182-2.

Compensation Mechanisms and Functionality of Transition Metal Oxide Surfaces and Interfaces: A Density Functional Theory Study

Rossitza Pentcheva, Narasimham Mulakaluri,
Wolfgang Moritz, Warren E. Pickett,
Hans-Georg Kleinhenz and Matthias Scheffler

Abstract The valence discontinuity at transition metal oxide surfaces and interfaces can lead to properties and functionality that are not observed in the respective bulk phases. In this contribution we give insight from density functional theory calculations on the emergence of conductivity and magnetism at the interfaces between (nonmagnetic or antiferromagnetic) insulators like LaTiO_3 and SrTiO_3 as well as LaAlO_3 and SrTiO_3 , and investigate systematically the influence of water adsorption on the surface properties of Fe_3O_4 . Additionally we present benchmarks for the performance of the full-potential linearized augmented plane wave method as implemented in the WIEN2k-code on HLRBI and HLRBII.

1 Introduction

The surfaces and interfaces of transition metal oxides represent a natural disruption of the bulk charge neutrality and a multitude of unexpected properties have been observed that differ substantially from the ones of the corresponding bulk materials. In

R. Pentcheva · N. Mulakaluri · W. Moritz
Department of Earth and Environmental Sciences, Section Crystallography, University of
Munich, Theresienstr. 41, 80333 Munich, Germany
e-mail: rossitza.pentcheva@lrz.uni-muenchen.de

W.E. Pickett
Department of Physics, University of California at Davis, One Shields Avenue, Davis,
CA 95616, USA
e-mail: pickett@physics.ucdavis.edu

H.-G. Kleinhenz
Leibniz-Rechenzentrum, Boltzmannstr. 1, 85748 Garching, Germany
e-mail: hgk@lrz.de

M. Scheffler
Fritz-Haber-Institut der Max-Planck-Gesellschaft, Faradayweg 4-6, 14195 Berlin,
Germany
e-mail: scheffler@fhi-berlin.mpg.de

order to understand naturally occurring phenomena as well as to selectively manipulate materials' properties like conductivity, magnetism and reactivity for technological applications, it is essential to gain a microscopic knowledge of the mechanisms of charge accommodation and the resulting structural and electronic relaxations at oxide surfaces and interfaces.

In the first part of the project, we have systematically investigated the surface termination of $\text{Fe}_3\text{O}_4(001)$ and have found that a hitherto ignored bulk termination containing oxygen and octahedral iron is stabilized [1, 2]. A Jahn-Teller distortion was identified as the origin of the observed $(\sqrt{2} \times \sqrt{2})R45^\circ$ -reconstruction. Experimental evidence is given by scanning tunneling microscopy [3] as well as x-ray and low electron energy diffraction (XRD and LEED) measurements and quantitative analysis [1, 4]. The interaction of water with a mineral surface can be used as a probe of the surface reactivity and is a fundamental process both in nature and technology. In Sect. 4.1 we investigate how the adsorption of water influences the surface reconstruction, stability and properties of $\text{Fe}_3\text{O}_4(001)$.

Recently, the conductivity measured at the interfaces between the Mott insulator LaTiO_3 (LTO) and the band insulator SrTiO_3 (STO) but also between the two simple band insulators LaAlO_3 (LAO) and STO [5, 6] has fueled intensive research both on the theoretical and experimental side. In Sect. 4.2 we show how the charge mismatch at these interfaces together with electronic correlations can lead to the stabilization of novel charge, orbital and magnetically ordered phases [7, 8].

Prior to presenting the scientific results, we briefly describe the method in Sect. 2 and discuss the performance of WIEN2k-code on HLRBI and HLRBII in Sect. 3.

2 Method

Density functional theory (DFT) is a powerful tool to study the physical properties of crystals and surfaces. However, the high accuracy goes hand in hand with a high numerical demand, thus restricting DFT calculations to system sizes of the order of 10^2 atoms and 1000 electrons. Transition metal oxide surfaces and interfaces represent a particularly challenging task due to their complex structure, strong relaxations and surface reconstructions, the treatment of $3d$ electrons, the localized orbitals of oxygen and magnetism. The method we have chosen is the full-potential augmented plane waves (FP-LAPW) method in the WIEN2k-implementation [9]. As an all-electron method with atom-centered basis functions around the nuclei with a well defined angular momentum and plane waves in the interstitial region it is particularly suitable for the questions of interest. In order to investigate charge ordering phenomena at oxide surfaces and interfaces and to explore the role of electronic correlations, the LDA+U method in the fully localized limit [10] is used.

As generally known, DFT is a ($p = 0$ Pa, $T = 0$ K) method. Combining DFT with thermodynamics allows us to extend the predictive power of DFT to finite temperatures and pressures in the atmosphere. In the previous project period we have applied the *ab initio* thermodynamics formalism [11, 12] to investigate the influence of the oxygen pressure and temperature on the surface termination of $\text{Fe}_3\text{O}_4(001)$.

In the current project we extend the phase diagram to account for the presence of hydrogen and water in the atmosphere. The lowest energy configuration of a surface in thermodynamic equilibrium with a humid environment with partial pressure p_{O_2} , $p_{\text{H}_2\text{O}}$ and temperature T minimizes the surface energy, $\gamma(T, p)$, which depends on the Gibbs free energy of the surface and the chemical potentials of the constituents:

$$\gamma(T, p) = \frac{1}{2A} [G_{\text{Fe}_3\text{O}_4(001)}^{\text{slab}} - N_{\text{Fe}}\mu_{\text{Fe}}(T, p) - N_{\text{O}}\mu_{\text{O}}(T, p) - N_{\text{H}_2\text{O}}\mu_{\text{H}_2\text{O}}(T, p)]. \quad (1)$$

Applying the line of argument stated in Ref. [12] we can substitute the terms in (1) by quantities accessible to DFT-calculations. As mentioned above to solve the all-electron Kohn-Sham equations we use the full-potential augmented plane waves (FP-LAPW) method in the WIEN2k-implementation [9] and the generalized gradient approximation (GGA) in the parameterization of Perdew, Burke and Ernzerhof [13].

3 Performance of WIEN2k on HLRBI and HLRBII

The fine grain parallel version of the WIEN2k-code was ported to and optimized for the Hitachi-SR8000 in collaboration with the Leibniz Rechenzentrum (LRZ). A detailed report of the optimization steps and the extensive benchmarks on SR8000 and IBM Regatta (RZ Garching) is given in Ref. [2].

The migration to the HLRBII SGI-Altix 4700 was completed in the last two years again in close collaboration with the LRZ. Currently both the fine grain parallel version (MPI) and the k -point parallelization scheme are used in the production. A hardware description of the HLRBI and HLRBII is given in Table 1. Here, we have done detailed benchmarks of the performance on HLRBII (second stage) and have compared these to previous ones on the HLRBI.

We have used two systems for the benchmarks: A 0.5 ML A-termination of $\text{Fe}_3\text{O}_4(001)$ containing 70 atoms in the unit cell to compare with previous benchmarks on HLRBI. Here the cutoff for the plane wave basis set was set to $E_{\text{cut}} = 19$ Ry which corresponds to a matrix size of 15000. The second benchmark case is a typical system used currently to study the water adsorption on $\text{Fe}_3\text{O}_4(001)$. With

Table 1 Hardware Description of HLRBI (Hitachi's SR8000) and HLRBII (SGI Altix 4700—second stage) and performance of `lapw1`

	Hitachi SR8000	SGI Altix 4700
Clock rate	0.375 GHZ	1.6 GHZ
Peak/core	1.5 GFlop/s	6.4 GFlop/s
Memory BW/core	0.5 GBytes/s	2.12 GBytes/s
Performance of <code>diag</code> per core (8 cores)	0.450 GFlops/s	1.87 GFlop/s
Percent of peak performance	30	28(38-BW)

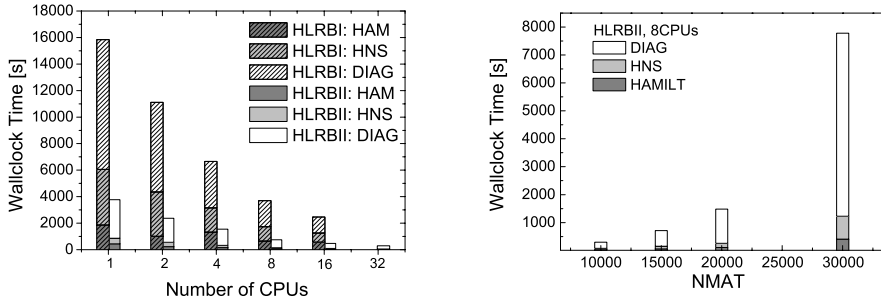


Fig. 1 *Left panel:* Comparison of running times for the different parts of `lapw1` (`hamilt`, `hns` and `diag`) for $N_{mat} = 15000$ as a function of N_{CPU} on Hitachi SR-8000 and SGI Altix 4700. *Right panel:* Running times of `lapw1` for different matrix sizes on 8 cores on HLRBII

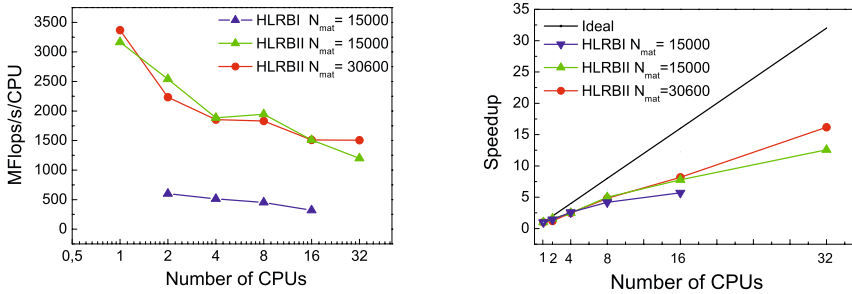


Fig. 2 *Left panel:* Performance of `lapw1` per core as a function of N_{CPU} . *Right panel:* Speedup on HLRBI ($N_{mat} = 15000$) and HLRBII ($N_{mat} = 15000$ and 30600)

its 130 atoms and 1050 electrons per unit cell, it corresponds to the biggest systems currently under consideration. The adsorption of water on the $\text{Fe}_3\text{O}_4(001)$ -surface represents a computational challenge—due to the short O-H-bond the muffin tin radii of oxygen (and hydrogen) have to be substantially reduced. The consequence is that a much higher cutoff parameter for the wave functions and potential is needed in order to achieve the same accuracy as for the clean $\text{Fe}_3\text{O}_4(001)$ -surface. This leads to a matrix dimension of $N_{mat} = 30600$.

The results of the benchmarks are displayed in Figs. 1, 2 and Table 1. The most time-consuming step in WIEN2k is `lapw1` where approximately 80–90% of the computational time is spent. As can be seen from Fig. 1 (right panel), the latter scales exponentially with the size of the matrix. Generally, the computational time in `lapw1` is reduced by a factor of 4–5 on HLRBII compared to HLRBI. To a large extent this can be attributed to the change of core clock rate (375 MHz vs 1600 MHz). `lapw1` contains the set up of the Hamiltonian (subroutine `hamilt`), its non-spherical part (subroutine `hns`) and the diagonalization (subroutine `diag`). Reprogramming of the MPI parallelization in the last version (07.03) of WIEN2k led to a substantial reduction of the computational time of `hns` from up to 30% on HLRBI to approx. 10% in the current version on HLRBII. On Hitachi SR-8000

`lapw1` showed an acceptable scaling up to 8 CPUs (one node) which however breaks down when using more than one node (cf. Fig. 2). The scaling behavior of the fine grain parallel version on HLRBII is much better and preserves a nearly linear behavior beyond 8 CPUs, especially for large system sizes of $N_{mat} = 30600$.

As can be seen from Table 1 the peak performance per core of HLRBII is four times higher than Hitachi's SR8000. We find that the effective performance of `diag` is about 30% of the peak performance on both HLRBI and II, which is an excellent value for this type of code. We have experienced that the memory bandwidth has influence on the performance of the major routines of `lapw1`. Partitions with low density blades (2 cores per memory path) show a further performance improvement of 25% compared to the high density blades (4 cores per memory path) given in Table 1. The performance on the low density blades is 2.4 Gflop/s per core or 38% of peak performance.

4 Scientific Results

4.1 Adsorption of Water on $\text{Fe}_3\text{O}_4(001)$

The interaction of water with a mineral surface is a fundamental process both in nature and technology (e.g. catalysis) and a first step in understanding surface reactivity. Magnetite plays an important role in the adsorption and reduction of heavy metal ions (Cr, As) and other contaminants [14, 15]. These processes typically take place in aqueous solutions. Therefore, it is important to understand how water adsorption influences the stability and properties of the $\text{Fe}_3\text{O}_4(001)$ -surface.

Magnetite crystallizes in the inverse spinel structure, where in [001]-direction B-layers, containing oxygen and octahedral iron, alternate with A-layers with tetrahedral iron. Starting from the modified B-layer, found to be most stable on the clean surface [1] and shown in Fig. 3(a) as well as an A-layer termination where every second tetrahedral iron is missing (0.5 A-layer), we have varied the degree of hydroxylation of the surface. These calculations are computationally very involved, because due to the short OH-bond length the muffin tin of hydrogen is very small ($R_{mt}^H = 0.6$ a.u., $R_{mt}^O = 1.1$ a.u.), and this requires a very high plane wave cutoff to obtain good convergence (currently $E^{wf} = 25$ Ry). Because surface relaxations involve deeper layers and to avoid spurious interaction between the surface layers we are using a slab containing seven B-layers and 10–12 Å of vacuum to separate the surfaces in z -direction. On the average, the considered systems contain 130 atoms and 1050 electrons which results in matrix sizes of 30600. On 8 CPUs the computational time for the setup and diagonalization of the Hamiltonian matrix (`lapw1`) is 6553 s/core (on 8 cores). In spin-polarized calculations `lapw1` is performed for both spin directions separately and we use 4 k_{II} -points for the integration in the irreducible part of the Brillouin zone (IBZ). The full geometry optimization of each system requires on the average 10 geometry steps and for each geometry step approximately 20–40 iterations are needed to reach convergence of the energy and electron density.

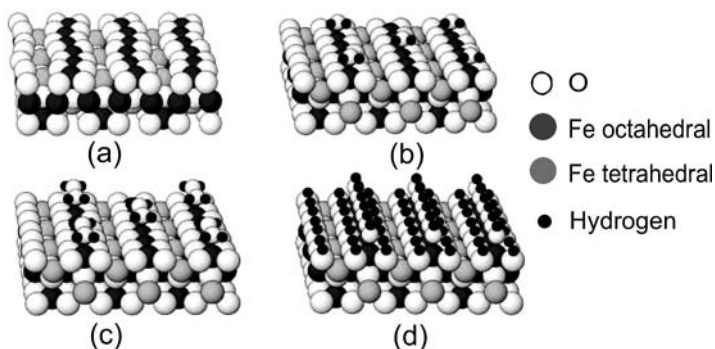


Fig. 3 Models of the $\text{Fe}_3\text{O}_4(001)$ -surface (a) clean surface showing the Jahn-Teller distorted B-layer termination; (b) and (c) B-layer termination covered by one or two H_2O molecules per unit cell; (d) a fully hydroxylated B-layer termination

One aspect that we want to resolve is the mode of adsorption of water: molecular versus dissociative. Therefore we are also studying different adsorption mechanisms of a single water molecule as well as two H_2O molecules in the surface unit cell. Some adsorbate geometries are shown in Fig. 3(b) and (c). Preliminary results indicate that molecular adsorption (Fig. 3(b)) is more favorable for low coverages but already for two water molecules per surface cell the two mechanisms (molecular and dissociative) have close energies. To compare the stability of the different configurations, the surface phase diagram of the clean $\text{Fe}_3\text{O}_4(001)$ -surface [1] is extended to account for both the O_2 and H_2O partial pressure. We find that a completely hydroxylated B-layer with OH-groups on top of octahedral iron and all surface oxygen being substituted by OH-groups, shown in Fig. 3(d), is the most stable configuration at water rich conditions. The results of the structural optimization reveal that the adsorption of water tends to suppress and even lift up the $(\sqrt{2} \times \sqrt{2})R45^\circ$ -reconstruction observed on the clean surface. Preliminary LEED measurements performed in parallel to the calculations support this interesting prediction. The geometries obtained from DFT are currently used as a starting point for a quantitative LEED-analysis as already done for the clean surface [4].

4.2 Charge Accommodation at Digital Perovskite Superlattices

The fabrication of perovskite superlattices with an atomic control of the number of layers of each material was recently demonstrated using pulsed laser deposition [5]. This achievement of today's growth techniques has invigorated intensive research. The reason is that the interfaces, that are generated, show novel properties that do not exist in the parent compounds. Examples are the two-dimensional electron gas (2DEG) measured at the interfaces between the Mott insulator LaTiO_3 (LTO) and the band insulator SrTiO_3 (STO) [5], but also between the two simple band insulators LaAlO_3 (LAO) and STO [6]. Perovskites possess a natural charge modula-

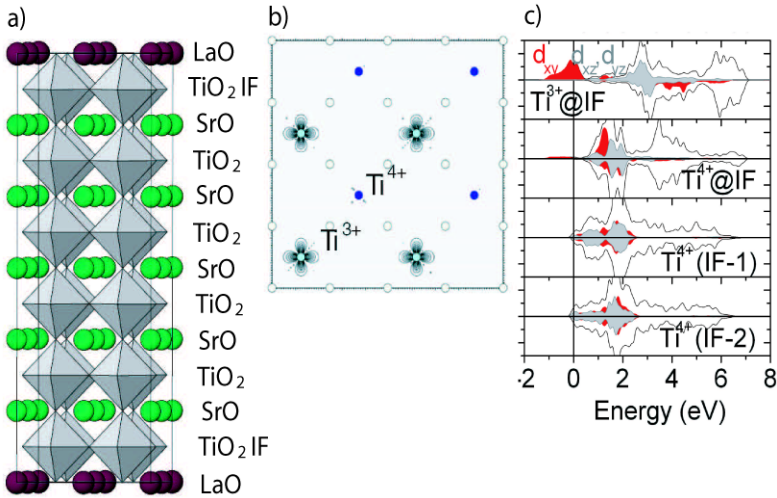


Fig. 4 (a) Side view of a (LTO)₁/STO₅ superlattice; (b) charge distribution of the 3d states in the interface TiO₂-layer, showing a charge and orbitally ordered checkerboard arrangement of Ti³⁺ and Ti⁴⁺; (c) layer resolved density of states showing the Ti 3d states across the interface for a relaxed (LTO)₁/STO₅ superlattice (from Ref. [8])

tion in the [001]-direction, e.g. in LTO positively charged (LaO)⁺ layers alternate with negatively charged (TiO₂)⁻, while in STO both the SrO and TiO₂-layers are neutral. Thus the interface (IF) between these two insulators represents a simple realization of a polar discontinuity and poses the question of how charge mismatch is accommodated and whether insulating behavior can be preserved. In the other system, LAO/STO, both the A and B sublattice cations in the perovskite structure change across the interface giving rise to two different types of interfaces: an *n*-type between a LaO and a TiO₂-layer, that was found conducting with a high electron mobility and a *p*-type between a SrO and an AlO₂-layer that showed insulating behavior despite the charge mismatch [6].

In order to investigate the compensation mechanism using the material specific insight from first principles and in particular to explore the role of electronic correlations, we have performed DFT calculations including a Coulomb repulsion *U* [10] for a variety of LTO_{*n*}/STO_{*m*} and LAO_{*n*}/STO_{*m*} superlattices. Here, we have varied the number of layers (*n*, *m*) of each material. These systems contain so far up to 100 atoms and 800 electrons (*N_{mat}* = 14500). The computational time of `lapw1` per CPU (on 8 CPUs) per *k*-point is 2800 s. We note that all cases are spin-polarized and that at least 6 *k_{IF}*-points are used in the IBZ.

Figure 4(a) shows a side view of a LTO₁/STO₅. Our LDA+*U* calculations [8] predict that the charge mismatch at this interface is accommodated by a charge disproportionation: A charge and orbitally ordered IF-layer is found with Ti³⁺ and Ti⁴⁺ ordered in a checkerboard manner (see Fig. 4(b)). At the Ti³⁺-sites the *d_{xy}*-orbital is occupied. While the system is insulating for the structure with bulk positions of the atoms, lattice relaxations lead to the experimentally observed conducting

behavior. A similar compensation mechanism is found also for the n -type interface of LAO and STO [7]. Although both LAO and STO are nonmagnetic and LTO is an antiferromagnet of G-type, a new magnetic phase emerges at the IF with diluted Ti^{3+} -spins that have a slight preference to antiferromagnetic coupling (with a larger periodicity than LTO bulk) [7, 8]. Brinkman et al. recently found first experimental indications for localized magnetic moments at the n -type LAO/STO IF [16] supporting our prediction. Since these superlattices are strained due to the lattice mismatch between the bulk compounds, we are currently investigating the effect of interlayer relaxations on the properties of the interface.

At the p -type LAO/STO interface (AlO_2 -layer next to a SrO-layer at the interface) we have investigated two compensation mechanisms: (i) at a structurally ideal interface, as suggested by the initial results of Ohtomo and Hwang [6], insulating behavior can only be obtained by a charge disproportionation on the oxygen sublattice with a charge and magnetically ordered OP_π hole localized at a quarter of the oxygens in the AlO_2 -layer [7]; (ii) oxygen vacancies, suggested in several more recent experimental studies (e.g. [17]), are a natural way to compensate the excess hole at the interface. We have studied vacancies in the AlO_2 - and SrO-layer and find that in both cases the Fermi level lies in a dip of the density of states.

These results show that in materials with multivalent ions charge disproportionation offers an additional, correlation driven compensation mechanism, unanticipated e.g. in polar semiconductor interfaces.

Acknowledgements We acknowledge support by the German Science Foundation, European Science Foundation within EUROMINSCI and the Bavaria California Center of Technology (BaCaTeC). N.M. acknowledges a fellowship by the Max-Planck Society. A grant for computational time at the supercomputer HLRBII at the Leibniz Rechenzentrum through project h0721 is gratefully acknowledged.

References

1. R. Pentcheva, F. Wendler, H.L. Meyerheim, W. Moritz, N. Jedrecy, M. Scheffler, *Phys. Rev. Lett.* **94**, 126101 (2005)
2. R. Pentcheva, F. Wagner, W. Moritz, M. Scheffler, Structure, energetics and properties of $\text{Fe}_3\text{O}_4(001)$ from first principles, in *High Performance Computing in Science and Engineering*, Munich, 2004 (Springer, Heidelberg, 2005), pp. 375–381
3. M. Fonin, R. Pentcheva, Yu.S. Dedkov, M. Sperrlich, D.V. Vyalikh, M. Scheffler, U. Rüdiger, G. Güntherodt, *Phys. Rev. B* **72**, 104436 (2005)
4. R. Pentcheva, W. Moritz, J. Rundgren, S. Frank, D. Schrupp, M. Scheffler, A combined DFT/LEED-approach for complex oxide surface structure determination: $\text{Fe}_3\text{O}_4(001)$. *Surf. Sci.* **602**, 1299 (2008)
5. A. Ohtomo, D.A. Muller, J.L. Grazul, H.Y. Hwang, *Nature* **419**, 378 (2002)
6. A. Ohtomo, H.Y. Hwang, *Nature* **427**, 423 (2004)
7. R. Pentcheva, W.E. Pickett, *Phys. Rev. B* **74**, 035112 (2006)
8. R. Pentcheva, W.E. Pickett, *Phys. Rev. Lett.* **99**, 016802 (2007)
9. P. Blaha, K. Schwarz, G.K.H. Madsen, D. Kvasnicka, J. Luitz, *WIEN2k, an Augmented Plane Wave + Local Orbitals Program for Calculating Crystal Properties* (Karlheinz Schwarz, Techn. Univ. Wien, Wien, 2001). ISBN 3-9501031-1-2

10. V.I. Anisimov, I.V. Solovyev, M.A. Korotin, M.T. Czyzyk, G.A. Sawatzky, *Phys. Rev. B* **48**, 16929 (1993)
11. C.M. Weinert, M. Scheffler, in *Defects in Semiconductors*, ed. by H.J. Bardeleben. Mat. Sci. Forum, vols. 10–12 (1986), p. 25
12. K. Reuter, M. Scheffler, *Phys. Rev. B* **65**, 035406 (2002)
13. J.P. Perdew, K. Burke, M. Ernzerhof, *Phys. Rev. Lett.* **77**, 3865 (1996)
14. K. Ohe, Y. Tagai, S. Nakamura, T. Oshima, Y. Baba, *J. Chem. Eng. Jpn.* **38**(8), 671 (2005)
15. H. Katsumata, S. Kaneco, K. Inomata, K. Itoh, K. Funasaka, K. Masuyama, T. Suzuki, K. Ohta, *J. Environ. Manag.* **69**, 187 (2003)
16. A. Brinkman, M. Huijben, M. van Zalk, J. Huijben, U. Zeitler, J.C. Maan, W.G. van der Wiel, G. Rijnders, D.H.A. Blank, H. Hilgenkamp, *Nature Mater.* **6**, 493 (2007)
17. N. Nakagawa, H.Y. Hwang, D.A. Muller, *Nature Mater.* **5**, 204 (2006)

Acknowledgements

At the outset I thank my supervisor PD Dr. Rossitza Pentcheva and Prof. Dr. Wolfgang Moritz for providing me an opportunity to pursue doctoral studies at the department of crystallography, Ludwig-Maximilians-Universität, Munich.

Dr. Rossitza's thorough guidance throughout my studies enabled me to understand and assimilate modern computational materials science and other techniques useful for the successful completion of the work assigned to me. I really appreciate her dedication and patience shown towards me and my work and I am ever grateful to her. I am also grateful to Prof. Wolfgang Moritz for teaching me low energy electron diffraction (LEED) technique and supporting our project with experimental results.

I take this opportunity to thank my co-supervisor Prof. Dr. Matthias Scheffler for his constant support to our project. I got many valuable inputs from him apart from financial support in terms of a Max-Planck fellowship from Fritz-Haber-Institute, Berlin.

I am also thankful to Dr. M.-L. Bocquet for very useful scientific discussions.

I should mention Master student Maria Wieland for doing a set of LEED experiments for us and Dr. Olga Zakhariyeva for helping me with the Gaussian code. I am thankful to Carmen Elena Quiroga for helping me in formatting the thesis.

I thank all members of the institute for being so friendly and helpful to me. I wish all the best to my friends/colleagues who made my stay in Germany enjoyable: Casjen Merkel, Maike Luebbe, Hasan Sadat Nabi, Melanie Kaliwoda, Christoph Schlueter, Nuria Sanchez Pastor, Katrin Otte, Andreas Götze, Shekar Burada, Sundar and Ganesh Kumar.

I am also thankful to DFG for funding me in the early stages of my project.

I am specially grateful to my family members without whose encouragement this step in my life would not have been possible.

Curriculum Vitae

Personal Data:

Narasimham Mulakaluri
Date of Birth 10.01.1980, India
Nationality: Indian
Family status: Single

Education:

2006 - present PhD thesis, Ludwig-Maximilians-Universität, Munich & Fritz-Haber-Institut (MPI), Berlin, Germany
2001 - 2003 MSc in Physics
Indian Institute of Technology Madras, Chennai, India
1998 - 2001 BSc, Osmania University, Hyderabad, India
Specialisation: Physics, Electronics and Mathematics

Research Experience:

Apr. 2006 present PhD thesis
Titled: Density functional theory investigation of H₂O adsorption on Fe₃O₄(001)
Supervisor: PD Dr. Rossitza Pentcheva
Aug.2004 Mar. 2006 Junior Research Fellow at University of Pune.
Title: Feasibility study of Aluminium nanoclusters in HTPB and DOA matrix
Prof. Dr. Anjali Kshirsagar
Dec.2002-Apr.2003 Masters Thesis
Title: Study of Electrospinning:
A Process used to produce polymer nanofibers
Prof. Dr. T. S. Natarajan

Publications

- Adsorbate Induced Semiconductor-Half Metal Transition at the Fe₃O₄(001) Surface, G. S. Parkinson, **N. Mulakaluri**, Y. Losovyj, P. Jacobson¹, R. Pentcheva and U. Diebold, **Phys. Rev. B** 82, 115420 (2010).
- Coverage dependent adsorption mode of water on Fe₃O₄(001): Insights

from first principles. **N. Mulakaluri**, R. Pentcheva and M. Scheffler, **J. Phy. Chem. C** 114, 11148 (2010).

- Partial dissociation of water on $\text{Fe}_3\text{O}_4(001)$: Adsorbate induced charge and orbital order. **N. Mulakaluri**, R. Pentcheva, M. Wieland, W. Moritz, and M. Scheffler, **Phys. Rev. Lett.** 103, 176102 (2009).
- Compensation mechanisms and functionality of transition metal oxide surfaces and Interfaces: A density functional theory study. *In: High Performance Computing in Science and Engineering.*, R. Pentcheva, R., **N. Mulakaluri**, W.E. Pickett, H.-G. Kleinhenz, W. Moritz, and M. Scheffler: Editors-(Eds.) S. Wagner, M. Steinmetz, A. Bode, and M. Brehm. Springer Berlin Heidelberg 2009, 709-717.
- Theoretical evidence of a mixed adsorption mode of water on $\text{Fe}_3\text{O}_4(001)$. **N. Mulakaluri**, R. Pentcheva, M. Wieland, W. Moritz, and M. Scheffler, **Geochim. Cosmochim. Acta** 73(13), A913.
- **N. Mulakaluri** (2003), Study of Electrospinning: A Process used to produce polymer nanofibers. Masters Thesis at IITM Chennai, India

Manuscripts in preparation

- Photoemission study of the reaction of water vapor with the $\text{Fe}_3\text{O}_4(001)$ Surface at near ambient conditions, T. Kendelewicz, S. Kaya, J. E. Newberg, H. Bluhm, **N. Mulakaluri**, R. Pentcheva, W. Moritz, A. Nilsson, and G. E. Brown, Jr.

Scientific contributions presented at national and international conferences

- *Partial dissociation of Water on $\text{Fe}_3\text{O}_4(001)$: Adsorbate Induced Charge and Orbital Order.* American Physical Society spring meeting, Portland, USA, 15 March, 2010
- *H and H_2O adsorption on $\text{Fe}_3\text{O}_4(001)$: Adsorbate induced charge and orbital order.* German Physical Society spring meeting, Regensburg, Germany, 22 March, 2010
- *Theoretical evidence for mixed adsorption of water on $\text{Fe}_3\text{O}_4(001)$.* German Physical Society spring meeting, Dresden, Germany, 24 March, 2009
- *Water adsorption on $\text{Fe}_3\text{O}_4(001)$: Insights from first Principles.* European Conference on Surface Science, Liverpool, UK, Jul.27-Aug.1, 2008

-
- *Water adsorption on $Fe_3O_4(001)$: A first principles Study.* German Physical Society spring meeting, Berlin, Germany, 29 March, 2008
 - ICMR-JNCASR joint winter school on chemistry and physics of materials, Bangalore, India, Dec.6-13, 2007
 - German Physical Society spring meeting, Regensburg, Germany, March, 2007